NASA/CR—2002-212104

Experimental Investigation of Transition to Turbulence as Affected by Passing Wakes

Richard W. Kaszeta and Terrence W. Simon
University of Minnesota, Minneapolis, Minnesota

December 2002

The NASA STI Program Office . . . in Profile

Since its founding, NASA has been dedicated to the advancement of aeronautics and space science. The NASA Scientific and Technical Information (STI) Program Office plays a key part in helping NASA maintain this important role.

The NASA STI Program Office is operated by Langley Research Center, the Lead Center for NASA's scientific and technical information. The NASA STI Program Office provides access to the NASA STI Database, the largest collection of aeronautical and space science STI in the world. The Program Office is also NASA's institutional mechanism for disseminating the results of its research and development activities. These results are published by NASA in the NASA STI Report Series, which includes the following report types:

- TECHNICAL PUBLICATION. Reports of completed research or a major significant phase of research that present the results of NASA programs and include extensive data or theoretical analysis. Includes compilations of significant scientific and technical data and information deemed to be of continuing reference value. NASA's counterpart of peer-reviewed formal professional papers but has less stringent limitations on manuscript length and extent of graphic presentations.

- TECHNICAL MEMORANDUM. Scientific and technical findings that are preliminary or of specialized interest, e.g., quick release reports, working papers, and bibliographies that contain minimal annotation. Does not contain extensive analysis.

- CONTRACTOR REPORT. Scientific and technical findings by NASA-sponsored contractors and grantees.

- CONFERENCE PUBLICATION. Collected papers from scientific and technical conferences, symposia, seminars, or other meetings sponsored or cosponsored by NASA.

- SPECIAL PUBLICATION. Scientific, technical, or historical information from NASA programs, projects, and missions, often concerned with subjects having substantial public interest.

- TECHNICAL TRANSLATION. English-language translations of foreign scientific and technical material pertinent to NASA's mission.

Specialized services that complement the STI Program Office's diverse offerings include creating custom thesauri, building customized databases, organizing and publishing research results . . . even providing videos.

For more information about the NASA STI Program Office, see the following:

- Access the NASA STI Program Home Page at ***http://www.sti.nasa.gov***

- E-mail your question via the Internet to help@sti.nasa.gov

- Fax your question to the NASA Access Help Desk at 301–621–0134

- Telephone the NASA Access Help Desk at 301–621–0390

- Write to:
  NASA Access Help Desk
  NASA Center for AeroSpace Information
  7121 Standard Drive
  Hanover, MD 21076

NASA/CR—2002-212104

Experimental Investigation of Transition to Turbulence as Affected by Passing Wakes

Richard W. Kaszeta and Terrence W. Simon
University of Minnesota, Minneapolis, Minnesota

Prepared under Cooperative Agreement NCC3–652

National Aeronautics and
Space Administration

Glenn Research Center

December 2002

Acknowledgments

This project was supported by NASA Glenn Research Center. The contract monitor was David Ashpis. His guidance, through review and coordination of researchers on the NASA LP Turbine Program, is greatly appreciated. Support was also given by the National Science Foundation Research Fellowship Fund and the University of Minnesota Graduate School, Graduate Research Fellowship and Dissertation Fellowship Funds. Special thanks also to Professor Ralph Volino, U.S. Naval Academy, and William Solomon, General Electric Company, for their help on spectral measurements and turbulence intermittency calculations. The authors would like to also thank Mr. Bob Nelson and Mr. Patrick Nelsen at the Mechanical Engineering Department Research Shop for their excellent help with fabrication of the test facility.

The Aerospace Propulsion and Power Program at
NASA Glenn Research Center sponsored this work.

Available from

NASA Center for Aerospace Information
7121 Standard Drive
Hanover, MD 21076

National Technical Information Service
5285 Port Royal Road
Springfield, VA 22100

Available electronically at http://gltrs.grc.nasa.gov

Contents

List of Figures

List of Tables

Nomenclature

B	Barometric pressure
B_1, B_2	Hot-wire relationship coefficients
b	Hot-wire offset calibration factor
C	Mayle model proportionality constant
C_1, C_2	Hot-wire calibration coefficients
C_f	Temperature correction factor
C_p	Pressure coefficient
C_{T_r}	Non-dimensional turbulence threshold parameter
D	Intermittency criterion function
d	Wake generator rod diameter
d_s	Anemometer sensor diameter
E	Anemometer bridge output voltage
E_u	Power density function of u'
E_v	Power density function of v'
E_w	Power density function of w'
f	Frequency
$FSTI$	Freestream turbulence intensity
H	Yaw coefficient
i	Index variable used to describe algorithms
K	Pitch coefficient

k	Turbulent kinetic energy, $0.5(\overline{u'u' + v'v' + w'w'})$
K_t	Dimensionless acceleration parameter
k_w	Wills near-wall velocity correction factor
L	True chord length
ℓ_1	Inlet channel width
ℓ_2	Wake generator streamwise length
ℓ_3	Wake generator upstream flap length
ℓ_4	Wake generator downstream flap length
ℓ_5	Suction surface bleed slot width
ℓ_6	Pressure surface bleed slot width
ℓ_7	Distance from the inlet plane to the point mid-span between the leading edges
L_r	Rod spacing along sled axis
L_u	Energy length scale
L_x	Axial chord length
L_z	Airfoil span length
L_{ss}	Suction surface length
l	Distance along the blade's true chord
M	Number of data points used in the autocorrelation
m	Hot-wire slope calibration factor
N	Number of data points in the sample
n	Hot-wire relation exponent
$\hat{n}$	Dimensionless turbulent spot production rate
P	Airfoil pitch
P_s	Static pressure
P_t	Total pressure
P_v	Pressure head from the pitot tube
$P_{s,exit}$	Static pressure at passage exit

$Q_{u,i}$	Auto-correlation of u' at point i
R	Anemometer control resistance
R_0	Platinum RTD calibration resistance
R_s	Hot-wire sensor resistance
R_{RTD}	Platinum RTD resistance
$Re_{\theta,t}$	Reynolds number based on momentum thickness at the location of onset of transition and local velocity at the edge of the boundary layer
$Re_{L_{ss}}$	Reynolds number based on suction surface length, L_{ss}, and passage exit velocity
Re_L	Reynolds number based on chord length, L, and passage inlet velocity
S	Wake Strouhal number, fL_x/u_x
s	Distance along the blade's suction surface
T	Absolute temperature, or wake passing period
T_0	Platinum RTD calibration temperature
T_c	Calibration flow operating temperature
T_f	The fluid temperature
T_s	Hot-wire sensor operating temperature
t	Time
t_{bl}	Boundary layer eddy time scale
t_w	Windowing time
TI	Turbulence intensity
U_b	Velocity component normal to the hot-wire sensor, perpendicular to the plane of the mounting prongs (binormal)
U_e	Effective velocity of air past the hot-wire sensor
U_n	Velocity component normal to the hot-wire sensor and in the plane of the mounting prongs
U_t	Velocity component tangent to the hot-wire sensor and normal to the plane of the mounting prongs
u	Streamwise component of velocity

u_r	Rod velocity
u_x	Axial component of inlet velocity
U_{fs}	Freestream Velocity, velocity at the edge of the near-wall viscous zone
x	Axial distance from blade leading edge
y	Normal distance from the suction surface
z	Spanwise distance from the measurement plane

Greek:

α	Inclination angle of the hot-wire
α_{RTD}	Platinum RTD calibration scale factor
β_1	Airfoil inlet angle
β_2	Airfoil outlet angle
δ	Boundary layer thickness
$\delta_{1,2,3}$	Relative angles between hot-wire sensors
ϵ	Dissipation of turbulence kinetic energy
γ	Turbulence intermittency
λ	Taylor microscale
λ_θ	Dimensionless pressure gradient parameter
Λ	Integral length scale of turbulence
$\Lambda_{u,x}$	Integral length scale of u' in streamwise direction
$\Lambda_{v,x}$	Integral length scale of v' in streamwise direction
$\Lambda_{w,x}$	Integral length scale of w' in streamwise direction
μ	Viscosity
ν	Kinematic viscosity
ρ	Density
σ	Emmons spot propagation parameter
τ	Turbulence weighting factor
τ_w	Wall shear stress, $\mu \left.\frac{\partial u}{\partial y}\right\|_{y=0}$

θ	Momentum thickness, Phase Angle
υ	Kolmogorov velocity scale, $(\epsilon\nu)^{1/4}$

Sub/Superscripts:

$1, 2, 3$	Designates one of the three hot-wire sensors
$\bar{}$	Time-average
$\tilde{}$	Phase-average
$'$	Fluctuation about mean value
t	Quantity at onset of transition

Chapter 1

Introduction

1.1 Motivation

Low Pressure (LP) turbines of gas turbine systems are commonly used in the aerospace and power industries. In aircraft, they are used primarily to provide input shaft power for fan and compressor components of the turbine engine. For the power industry, they are used to generate shaft power. Turbine design engineers are constantly working towards achieving increased turbine efficiency, decreased weight, and reduced part count while simultaneously reducing cost.

An important component of this effort is obtaining a better understanding of the aerodynamics of turbine stages, which allows the turbine designer to estimate and optimize aerodynamic performance.

Traditional analysis of turbine blades treated the flow through the turbine as a steady, turbulent flow. This is reasonable due to the high turbulence of the flow entering the turbine stage from the upstream components such as the combustion chamber and upstream turbine stages with features such as blade wakes, film cooling, endwall cooling, and surface roughness.

However, in low pressure turbines, due to a combination of relatively high free-stream fluid temperature and relatively low pressures, the Reynolds numbers of these flows are relatively low compared to those of high pressure turbines. Therefore the turbine designer must account for flow viscous effects when designing the turbine stage. These effects include viscous boundary layer growth, laminar to turbulent

transition, and boundary layer separation, all of which significantly affect the aerodynamic performance of the turbine engine.

Transition is important in the high pressure turbine as well, for accurate prediction is needed to properly describe the convective heat transfer coefficient distribution over the airfoil surfaces. The thermal environment of the high pressure turbine is extreme and prediction of the heat transfer rates is critical to proper thermal design.

Though the disturbance environments of both the high and low pressure turbines are still being characterized, there is evidence that the low pressure turbine sees lower disturbance to the flow.

The present study investigates boundary layer development, flow transition, and separation of the boundary layer flow over low-pressure turbine surfaces.

Laminar to turbulent transition in a very low-disturbance environment is a well-studied topic. An excellent summary of these efforts is presented by Mayle (1991). He observed that the majority of experimental work had focused upon laminar to turbulent transition under steady flow conditions. The actual flow present in turbine engines has significant unsteadiness resulting from wake shedding by the preceding blade stages; thus, Mayle suggested that experimental investigations should be conducted to determine design criteria for the effects of wakes upon transition over turbine blade surfaces. Mayle also expressed concern that the majority of existing experimental works at that time focused upon laminar to turbulent transition under low turbulence and steady flow conditions, neither of which is appropriate for turbomachinery flows, as the actual flow present in turbine engines has turbulence levels ranging from 2–10%, with significant unsteadiness due to wakes. Considerable work has been done since the 1991 paper was written. Much of this research was reviewed by Simon and Kaszeta (2000).

1.1.1 Unsteady Wake Flows in Turbine Engines

In a turbine engine, the rotor is rotating relative to the stator, moving the turbine blades through the turbulent wakes produced by the upstream stators. The impact of these turbulent wakes upon the turbine blade creates a series of turbulent spots appearing on the turbine blade, which eventually coalesce into turbulent "strips" which grow and travel along the surface of the blade. The wake trajectories are shown

conceptually in Figure 1.1. Between these turbulent wakes, laminar to turbulent transition can occur in the separated flow zone should the boundary layer separate or by bypass transition in the boundary layer if there is no separation. Thus, at any given time, the surface of a turbine blade may include laminar flow, turbulent strips due to wake passage, separation, transition in the separated flow, bypass transition of an attached boundary layer, and re-attachment of a separated flow.

1.2 Relevant Transitional Literature

A considerable body of literature is dedicated to the study of laminar to turbulent transition. However, much of this literature is dedicated to transition to turbulence of a laminar boundary layer subjected to infinitesimal disturbances. For these flows, transition to turbulence occurs through fundamental instabilities in the laminar boundary layer which result in the amplification of small disturbances and in the growth of Tollmien-Schlichting (T-S) waves. Such waves are two-dimensional, with vorticity perpendicular to the flow. They further disturb the flow, creating higher-order modes of instability, leading to randomly-oriented vorticity. This eventually triggers transition to full turbulence. This mechanism is referred to as "natural transition," and is described in detail by Schlichting (1979).

However, for a flow to pass into turbulence via this mechanism, the level of flow disturbance must be quite small. In flows with high levels of free-stream turbulence, it has often been observed that the free stream turbulent fluctuations can directly create turbulent spots in the boundary layer, resulting in a transition to turbulence without any observable disturbance amplification process as seen in T-S induced transition. Turbulent spots were first described by Emmons (1951), who identified such a transition process in water-table experiments. Morkovin (1978) hypothesized that in cases of large turbulence levels the free-stream could create such turbulent spots in the boundary layer and labelled this phenomenon "Bypass Transition," implying bypassing of the normal instability amplification processes during transition to turbulence. Additionally, while the original discussion of bypass transition concerned transition under high free-stream turbulence, the bypass mechanism appears to occur in flows with surface roughness and unsteady wake flows in which passing turbulent wakes lead to the formation of turbulent spots in the boundary layer.

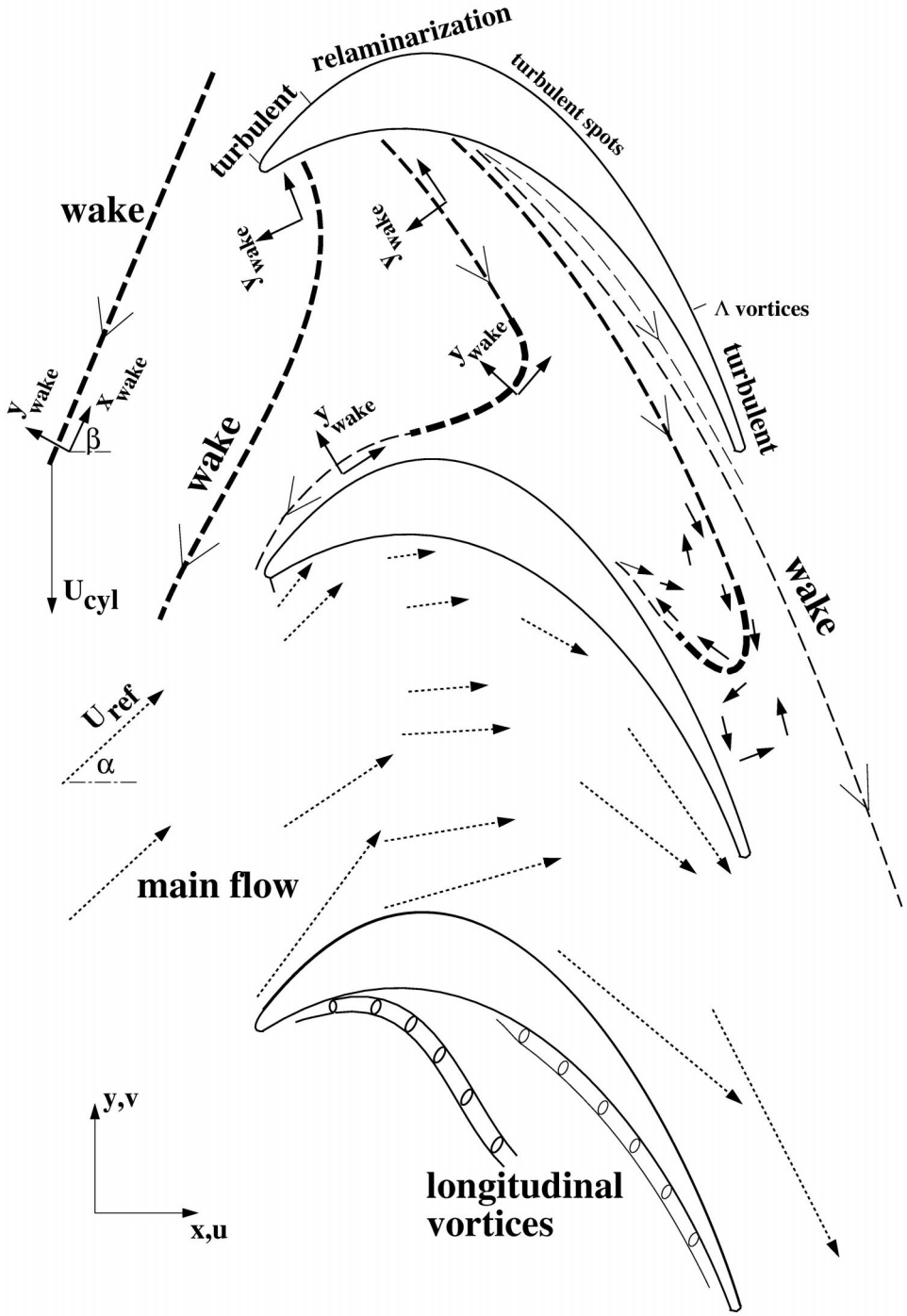

Figure 1.1: Sketch of the observed wake distortion, wake induced transition and flow velocity vectors, from Wu and Durbin (2000a)

Finally, a third mode of transition that occurs in turbomachinery flows is "Separated Shear Transition." Though the stability considerations are a bit different, transition to turbulence occurs in shear flows, like a free jet or the shear flow which resides over a separation bubble on a surface. The latter is important to turbine design as it is also commonly observed in low Reynolds number turbomachinery flows.

1.2.1 Transition in Turbomachinery Flows

While transition to turbulence has been widely investigated, transition in highly-disturbed environments such as those seen in engine flows is not well documented. For example, in turbomachinery flows, combustor turbulence, rotor-stator interaction, and high surface roughness result in flow subject to elevated disturbance levels and periodic unsteadiness. These high levels of free-stream turbulence often result in earlier and shorter transition to turbulence than with lower turbulence levels. In many cases, this transition often delays or completely prevents boundary layer separation on the surface of the turbine blade; without transition the strong streamwise pressure gradient imposed on the boundary layer would have induced separation.

The periodic unsteadiness created by rotor-stator interactions similarly affects the flow. The wakes create a periodic change in velocity over the blade surface, creating temporal pressure gradients which may influence boundary layer separation similar to the influence of spatial pressure gradients. Additionally, the wakes create periodic strips of turbulence which can induce early transition to turbulence and eliminate separation in much the same manner as induced by increased free-stream turbulence in steady-state flows without wakes.

1.2.2 Modeling Efforts

The prediction of transition due to bypass transition mechanisms has proven to be extremely difficult. Indeed, the predictions have proven difficult enough that the predominant method to date has been the use of empirical or semi-empirical correlations.

The most notable correlation is that presented by Abu-Ghannam and Shaw (1980). Based upon both their own experimental observations and earlier correlations developed by Hall and Gibbings (1972), the authors developed a series of empirical relations for steady flow, correlating the location of onset of transition to effects of

pressure gradient and free-stream turbulence intensity, in terms of the turbulent spot production rate versus the following non-dimensional pressure gradient:

$$\lambda_\theta = \left(\theta^2/\nu\right) \cdot \frac{dU}{dx}, \tag{1.1}$$

in which θ is the local momentum thickness of the boundary layer, U is the local velocity at the boundary layer edge, and ν is the kinematic viscosity of the fluid.

Blair (1982), found better predictive capabilities if the model were based instead on the non-dimensional acceleration parameter,

$$K_t = \left(\nu/U_t^2\right) \left(\mathrm{d}U/\mathrm{d}x\right)_t \tag{1.2}$$

evaluated at transition as indicated by the subscript. U is the local velocity at the boundary layer edge.

Similar correlation techniques incorporating both pressure gradient and free-stream turbulence effects, and an overview of other predominant transition correlations, such as Narasimha (1985), are presented in Gostelow and Walker (1990).

More recently, the problem of predicting bypass transition in turbomachinery flows was addressed by Mayle (1991). Mayle hypothesized that at the level of turbulence and pressure gradient present in gas turbine flows, a prediction correlation of

$$Re_{\theta,t} = 4000\, TI^{-5/8} \tag{1.3}$$

produced good results. Like the Abu-Ghannam and Shaw (1980) model, this model was also widely used to predict transition, with fair success. A similar correlation is reported by Hourmouziadis (1989).

Mayle's correlation is notable, as it suggests that transition to turbulence is strongly affected by free-stream turbulence and its effects on the pre-transitional laminar boundary layer. Researchers have taken multiple approaches to developing better correlations relating free-stream turbulence to transition. Johnson and Ercan (1996) suggest that low frequency disturbances are most likely to cause transition. Conversely, Mayle and Schulz (1997) suggest that transition to turbulence is most strongly influenced by the higher frequencies of the free stream turbulence, which

induce instabilities in the near-wall region due to pressure fluctuations. This led directly to Mayle (1998), in which a theory for predicting the turbulent spot generation rate is developed (both onset and length of transition to turbulence). The model is based upon turbulence in the boundary layer leading to the production of turbulent spots at the rate:

$$\hat{n}\sigma = C(\upsilon/U)Re_{\theta,t}^{-1}, \tag{1.4}$$

where C is a proportionality constant derived from the data.

By statistical analysis of hot-wire results, Johnson and Dris (2000) developed a simple analytical model that supports the conclusions of Johnson and Ercan (1996) and Mayle (1998), suggesting that pressure fluctuations induced by free-stream turbulence perturb the near-wall velocity creating small pockets of transient separation and turbulent spots. Similar conclusions were reached by Dietz (1999), who investigated the receptivity of a Blasius boundary layer to disturbances from a vibrating ribbon.

Recently, fundamental bypass transition modeling continues to see significant contributions. Steelant and Dick (1996a, 1999a,b) model transition to turbulence by using the Navier-Stokes equations combined with transport equations which they derive for turbulence intermittency, γ, and a turbulence weighting factor, τ. The model covers the physics of both free-stream turbulence diffusion and turbulent spot generation.

Dorney et al. (1999) investigated various prediction techniques by comparing an unsteady Navier-Stokes solver, a two-layer algebraic turbulence model and transition models to data for transition in turbines. They found that, despite its deficiencies, the Abu-Ghannam and Shaw (1980) transition model produced the most reliable predictions.

Roach and Brierley (2000) developed a bypass transition model which incorporates turbulence level and scale effects, noting that the model shows sensitivity to the level of turbulence at the leading edge of the test surface, not to the turbulence locally outside of the boundary layer, suggesting that flow history effects are more significant than the local free-stream turbulence effects.

1.2.3 Steady Flow Experiments

Much of the early work concerning transition in turbomachinery flows focused primarily upon compressor blade passages. Evans (1978) is representative of this early work, presenting hot-wire boundary layer measurements on a compressor stator blade. Similar investigations were conducted in compressor passages by Hodson (1984) (hot-wire) and Deutsch and Zierke (1987) (single-component LDV).

However, due to the complex flow patterns resulting from variations in combustor outlet distributions, endwall cooling, surface roughness, wakes, and rotational effects, a number of research efforts have focused on simplified geometries representative of a reduced set of all the effects of LP turbine flows. Notable works include Blair (1982), Baughn et al. (1995), Jonas (1997), Chakka and Schobeiri (1999b), and Funazaki et al. (1999a,b).

A common simplification used to simulate turbine passages is to use a flat plate subjected to high inlet free-stream turbulence intensity flow and an imposed pressure gradient. Matsubara et al. (1998) used smoke visualization over a such a flat plate geometry subjected to various levels of free-stream turbulence intensity to document the longitudinal structures that form in the boundary layer, leading to turbulent streaks. Their results show also that T-S wave theory doesn't satisfactorily account for the observed flow physics in free-stream turbulence-disturbed boundary layers.

Sohn et al. (1998) provided extensive hot-wire measurement and also used smoke visualization over a flat plate with imposed pressure gradients to simulate the suction side of a LP turbine blade, subjecting the boundary layer to various levels of free-stream turbulence intensity, documenting transition due to both separated shear layer transition and the formation of intermittent turbulent spots in the laminar boundary layer.

Volino and Hultgren (2000) conducted a similar study with a flat plate and imposed pressure gradients, investigating separation and transition with a single-sensor hot-wire anemometer. They concluded that, while laminar to turbulent transition is strongly influenced by the Reynolds number and free-stream turbulence intensity, the location of boundary layer separation is controlled by the pressure profiled and is fairly insensitive to Re and $FSTI$ unless these two parameters are high enough that the flow fully transitions to turbulence before separation occurs.

Many research efforts have attempted to represent the geometry of turbine blade passages using simplified curved geometries and linear cascades. Volino and Simon (1997a,b,c) investigated the flow over a curved surface with various pressure gradients imposed. Modifying the same facility, Qiu and Simon (1997) and Simon et al. (2000) used a simulated cascade composed of a single pressure surface and a single suction surface, simulating a single turbine blade passage, to investigate the effects of free-stream turbulence intensity and Reynolds number on both the onset of transition and separation.

Murawski et al. (1997) used a three-vane, four-passage linear cascade to assess the effects of changes in Reynolds number and free-stream turbulence on separation and transition. Additionally, this study investigated the wakes created downstream of a turbine blade under steady flow conditions.

Boyle et al. (1998) used a three-vane, four-passage linear cascade to compare steady-state hot-wire velocity surveys with various two-dimension prediction codes in order to identify flow scenarios in which common transition models displayed shortcomings.

Schreiber et al. (2000) used a three-blade, two-passage cascade to show the effects of Reynolds number and free-stream turbulence on transition for a controlled-diffusion compressor airfoil, noting that for increased free-stream turbulence, the transition location moved upstream and the thin pre-transitional boundary layer flow became more sensitive to surface roughness.

Recently, Alfredsson and Matsubara (2000) used both PIV and visualization techniques in a flat plate boundary layer under high free-stream turbulence to conclude that free-stream turbulence oscillations penetrate into the transitioning boundary layer.

Other research efforts have focused on flow control to promote transition to turbulence to prevent or delay separation. In one such investigation, Bons et al. (2000) introduced vortex generators into transitional boundary layers on a turbine surface, noting a reduction in aerodynamic losses. Similarly, Lake (1999) and Lake et al. (2000) investigated the effects of adding dimples, V-grooves and trips to the surface in an attempt to prevent boundary layer separation.

1.2.4 Unsteady Flow Studies

Like the steady-flow investigations, much of the early work involving the effects of unsteadiness in turbomachinery flows started with compressor studies. In one such study, Dong and Cumpsty (1990a,b), hot-wire data from a compressor cascade allowed comparing the effects of wakes to the effects of increased levels of turbulence, both resulting in early transition to turbulence. It was suggested that the incorporation of wakes be treated as a special case to existing bypass transition models.

It is important to note that in turbine passage flows made unsteady by the passage of wakes, there are several wake phenomena: (1) an oscillating free-stream velocity component due to the wake, (2) an oscillating angle of attack and (3) wake turbulence. All of these have separate effects upon transition and separation in the turbine flow, as discussed by Mayle and Schulz (1997) and Lou and Hourmouziadis (2000).

In an attempt to represent the unsteady flowfield in turbine passages, researchers have used both rotating rigs and wake simulators. Boundary layer profile measurements inside of rotating turbomachines are difficult to take, therefore such experimental data in actual rotating turbomachinery are limited. The primary research efforts conducted in such facilities include Halstead et al. (1997a,b,c,d), Tiedemann and Kost (1999), Kost et al. (2000), and Solomon (2000).

Halstead et al. (1997a,b,c,d) used a rotating rig to provide a comprehensive picture of the unsteady flowfield in LP turbines and compressors, including both compressor and turbine passage flows. In Halstead et al. (1997c), by using hot-wire and surface-mounted hot-film anemometry, the researchers concluded that in order to accurately model the actual upstream disturbance present in real turbomachines, simulations should use at least two upstream blade rows. Doing so would correctly account for all significant clocking effects. The researchers also document the existence of significant calmed regions occurring behind each turbine wake, which, if accounted for by turbine designers, may allow more aggressive blade loading than allowed by conventional analyses. In these cases, the airfoil loading was low and the boundary layers do not separate in the base case.

Tiedemann and Kost (1999) used a similar rotating rig instrumented with hot-film sensors mounted along the pressure and suction surfaces of the passage to measure

time-resolved profiles of surface pseudo-shear stress. From their results, the authors determined that between wakes, turbine passage transition occurs as separated flow transition followed by bypass transition, while underneath the wakes, the flow fully transitions to turbulence by bypass mechanisms before separation can occur. Kost et al. (2000) used the same facility with a PIV technique to measure 2D velocity distributions and wake trajectories. They showed that as the wakes move through the turbine passage, they spread to cover a much larger portion of the suction surface than the wake spreading in the free-stream flow would predict.

Solomon (2000) used a low-speed research turbine to investigate the effects of passing wakes and elevated free-stream turbulence for two different blade spacings. He noted that the effects of turbulence on the transition onset location were smaller when the solidity was reduced. He also noted an optimum clocking of the rotor, or most effective wake passage timing, for effecting transition before separation.

In place of rotating rigs, a number of researchers have instead used a variety of wake simulators. A complete review and evaluation of wake-generation techniques is presented in Yuan (1999). Most researchers used some variation of passing solid rods in front of either a flat plate or turbine passage simulator to simulate the wakes coming from an actual series of stator vanes.

Funazaki and Kitazawa (1997) and Funazaki et al. (1999a,b) used a flat plate with imposed pressure gradients and wakes from a rotating, spoked-wheel wake generator, documenting the velocity field of the boundary layer. Funazaki and Aoyama (2000) used this same facility in conjunction with a split-film thermal anemometer to obtain two-component velocity profiles of a wake-disturbed boundary layer, documenting the secondary flow and Reynolds shear stress distributions of the boundary layer responding to varying free-stream turbulence levels.

Schobeiri et al. (1998) used a five-blade, four-passage linear cascade along with a timing-chain driven wake generator to document the effects of unsteady wakes on aerodynamic and heat transfer characteristics of a turbine blade. From these results, the authors concluded that transition in wake-disturbed turbine passages shifts between natural transition and bypass transition, depending on the prominence of the wake-induced turbulence in the free-stream. Schobeiri et al. (1995) and Chakka and Schobeiri (1999a,b) previously used this facility with a curved wall flow disturbed by wakes generated by a squirrel-cage wake generator to measure boundary layer

distributions of velocity. From these results, they observed that, for wake-disturbed flows, an increase in wake passing frequency resulted in a high frequency scale activity in the boundary layer with small time scales dominant throughout the transition process.

Kittichaikarn et al. (1999) used a heated flat plate test section coated with liquid crystals in a water tunnel to visualize the process of wake-induced transition. From these visualizations, they confirmed the presence of turbulent spots in the transition region and found good agreement between their experimental results and the correlation presented by Mayle (1991)

Lou and Hourmouziadis (2000) documented separation bubble transition on a flat plate, contouring the opposite wall to create the appropriate pressure gradient on the test wall. By using a downstream rotating valve, they were able to create a periodic acceleration/deceleration pattern in the flow and identify characteristic instability frequencies in the shear layer over a separation bubble. The resulting flow is similar to a wake-disturbed flow, except that the periodic acceleration/deceleration of the fluid is not accompanied by increased turbulence, as would occur in a wake-disturbed flow.

Brunner et al. (2000), Stadtmüller et al. (2000) and Teusch et al. (2000) used a high-speed, low-pressure, seven-blade cascade with timing-belt-mounted rods to generate wakes. Brunner et al. used surface-mounted hot films to qualitatively map the distribution of transition over the blade surface. They noted a loss reduction of 34% and 28% in two airfoil profiles due to the unsteady inlet flow associated with passing wakes. Stadtmüller et al. collected similar data and compared them with calculations of wall shear stress, showing good agreement. From these results, they showed that the wake effect on the reduction of losses depends on the frequency and strength of the wake. Teusch et al. documented results similar to Dong and Cumpsty (1990b), showing a 20% reduction in losses under low Reynolds number conditions due to wakes, but a 20% rise in losses due to wakes at higher Reynolds numbers where the separation bubble is small.

A summary of the data set to be documented in the present report has been presented in the literature (Kaszeta et al., 2001).

1.2.5 Analysis and Computation

In order to better predict the onset and length of transition to turbulence, a number of computational techniques have been used, included Reynolds-Averaged Navier-Stokes (RANS) equations coupled with various transport equations, Large Eddy Simulation (LES), and, increasingly, Direct Numerical Simulation (DNS).

A number of research efforts have focused explicitly on bypass transition. Notable efforts include Simon and Ashpis (1996), Savill (1993b), Suzen and Huang (2000a), Dorney et al. (2000a,b), Kang and Lakshminarayana (1997), Chakka and Schobeiri (1999a), and Kim and Crawford (2000). Large eddy and direct numerical simulations of transitional flows have been made by Rai and Moin (1993), Madavan and Rai (1995), Berlin and Henningson (1999), Wu et al. (1999), and Alam and Sandham (2000). Rai and Moin initiated their computations with random inlet values and allowed sufficient streamwise distance to let them develop into proper turbulence. This was shown to require considerable computation time and some compromise in grid resolution. The Wu et al. study includes DNS simulation of the effects of passing wakes.

In McDaniel and Hassan (2000), transition was treated with turbulence modeling. Correlations taken from the literature were used for the transition length and the intermittency distribution through transition. The turbulent diffusivity was determined by the turbulence model.

Alam and Sandham (2000) showed by DNS the development of a separating flow where transition is via oblique modes and vortex-induced breakdown.

Müller et al. (2000) investigated the modeling of separated flow transition to find that a combined onset model of Mayle (1998) and spot production rate model of Walker et al. (1988) was best. The chosen model performed well on the pressure side but calculated the transition location to be too far downstream on the suction surface.

Enomoto et al. (2000) showed by computation and experimentation that the process of laminar flow separation, reattachment and subsequent flow transition at low Reynolds numbers is dominated by relatively large eddies near the wall which can be simulated with unsteady numerical codes. Hobson and Weber (2000) described

the application of Navier-Stokes solvers to the computation of controlled-diffusion compressor blades.

Dorney et al. (2000b) made calculations on the PAK-B turbine blade to show the effects of turbulence and boundary layer trips. The authors showed that the Baldwin-Lomax turbulence model produced satisfactory results as compared with data for low Reynolds number cases. An intermittency transport equation formulated by Suzen and Huang (2000a,b) from the works of Steelant and Dick (1996b) and Cho and Chung (1992) was shown to be successful against the transition data assembled by Savill (1993a,b).

Davies et al. (2000) compared computational results from a Renormalization Group (RNG) model of turbulence with experiments, discussing the results in terms of the entropy generation rate. Details of the boundary layer measurements were given in O'Donnell and Davies (2000).

Wu and Durbin (2000a,b) presented detailed DNS results of simulated wakes sweeping past a low pressure turbine cascade. In their results, the authors present evidence of longitudinal vortices arising from the turbulent wakes as they are distorted by their travel through the turbine passage. A sketch from their results is shown in Figure 1.1.

1.3 Research at the University of Minnesota

The Heat Transfer Laboratory at the University of Minnesota has a long history of experimental investigation of transitional flows. The transitional flow program began with studies by Wang (1984) and Kim et al. (1992), who investigated the effects of both curvature (by comparison of flat plate and concave curved wall geometries) and varying free-stream turbulence intensity levels upon transition. Their work concluded that both concave curvature and increased *FSTI* resulted in earlier transition to turbulence.

These data were later reprocessed by Volino and Simon (1994) using a technique called "octant analysis," in which the values of the streamwise velocity, cross-stream velocity and temperature fluctuations were used to segregate their measurements into octant classifications, allowing various eddy motions, such as bursting, occurring within the boundary layer to be identified. These results showed a distinct difference

in structure between transitional and fully turbulent flow, with a wider distribution of scales present in the turbulent flow. They also concluded that large scales were more important in transitional flows, a conclusion similar to that of Johnson and Ercan (1996).

Volino and Simon (1995a) later investigated transition in boundary layer flows subjected to high *FSTI* and mild acceleration, finding that for mild acceleration levels, transition was little influenced by acceleration. Volino and Simon (1995b) presented a similar study with strong acceleration effects, showing that at strong levels of acceleration, the acceleration had a significant effect in lengthening the transition zone. Additionally, they found that strong acceleration tended to have a strong enough stabilization effect on the boundary layer that reverse transition occurred.

Qiu (1996), Qiu and Simon (1997), and Simon et al. (2000) followed this work with a study of both temporal and spatial acceleration effects upon laminar to turbulent transition. In the first part of the study, Qiu used a Stirling engine heater tube simulator to produce a zero-mean oscillatory flow to investigate the effect of temporal acceleration upon laminar to turbulent transition. The author found that in this oscillating flow, transition is triggered by the arrival of highly turbulent flow generated upon entry to the test section. In the second part of the study, Qiu investigated spatial acceleration effects by utilizing a one-passage cascade simulator (using the PAK-B blade profile), subjecting the flow to various *FSTI* values (ranging from 0.5 to 10%) and suction surface length Reynolds numbers (ranging from 50,000 to 300,000). The author found that for a combination of high *FSTI* and high *Re*, the boundary layer transitioned to turbulence early enough that boundary layer separation was eliminated. For lower values of *FSTI* and *Re*, it was found that transition in these flows occurred by the following process:

1. Laminar boundary layer development
2. Strong growth rate as a laminar boundary layer until the adverse pressure gradient is reached
3. Laminar separation
4. Transition of the shear layer over the separation bubble

5. Turbulent flow established throughout the shear-layer and near-wall region

6. Possible re-attachment and growth as an attached turbulent boundary layer.

Figure 1.2 (from Simon et al. 2000) shows these results graphically.

1.4 Overview of the Current Study

While a large body of experimental data which documents the flow field and transition in turbomachinery flows exists, much of the research has been conducted under steady-state conditions. Of the unsteady-flow experimental studies, the majority of the studies primarily investigated surface measurements, such as thermal properties or surface shear stress through the use of hot-film sensors—few measurements within the boundary layer flow have been presented. The present study addresses this by using hot-wire anemometry to collect wall-normal, time-resolved records of velocity.

The study utilizes a modified version of the cascade simulator used in Qiu (1996), Qiu and Simon (1997), and Simon et al. (2000). A linear wake generator, modified from a design developed by Yuan (1999), is used to introduce periodic wakes into the flow upstream of the turbine blade leading edge, simulating the wakes created by rotor-stator interaction. The wake generator operates by sliding a rack of rods through the flow development section. Through the use of a photogate mounted on the sliding rack, the rods' positions can be recorded, allowing ensemble averaging of individual wakes and their influence on the LP turbine near-wall flow. By analyzing these results, ensemble-averaged, wall-normal profiles of velocity, turbulence intensity and turbulence intermittency can be measured over the turbine passage suction surface. Both the experimental geometry and the results are amenable to comparison with wake-disturbed, LP turbine computational works, such as those of Dorney et al. (2000a), Wu and Durbin (2000a,b) and Suzen and Huang (2000b).

The objectives of this study are as follows:

1. Document the development of boundary layers in a simulated turbine passage under the influence of rod-generated wakes, collecting ensemble-averaged profiles of velocity, turbulence intensity, and turbulence intermittency.

2. By comparing these data with steady-state data collected on the same facility, identify the effects of these wakes on laminar to turbulent transition in the flow passing over the suction surface.

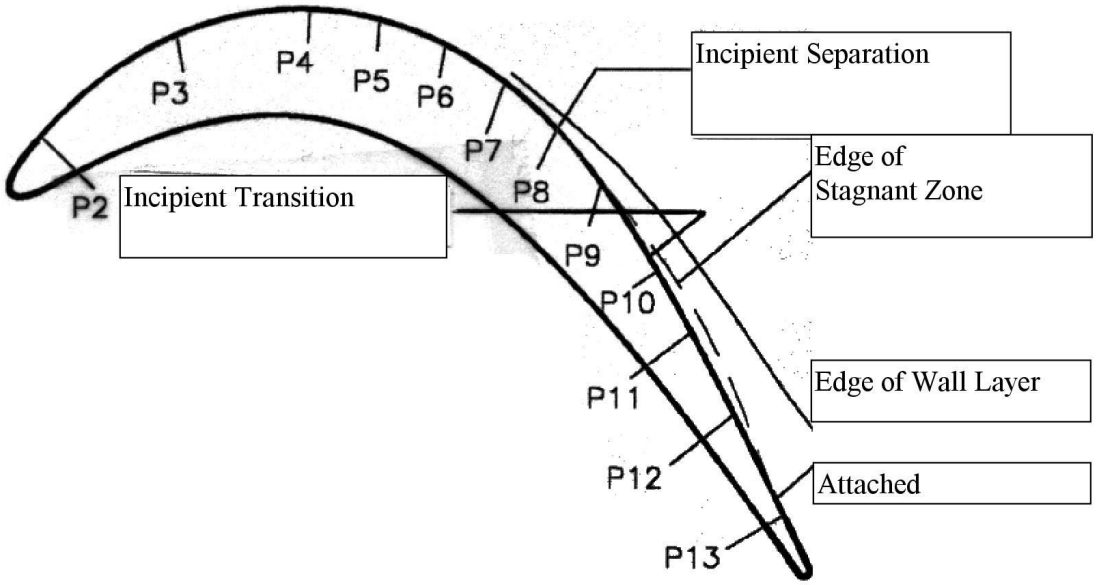

Figure 1.2: Sketch of PAK-B airfoil under steady flow, with $Re_{L_{ss}} = 50{,}000$ and $TI = 2.5\%$, showing approximate locations of separation and transition, (Simon et al., 2000)

Chapter 2

Experimental Test Facility

2.1 The Experimental Facility

The experimental facility consists of a low-speed wind tunnel, a wake generator, and a turbine cascade simulator. Each of these will be discussed, in turn.

2.1.1 The Low Speed Wind Tunnel

All experiments were done using the low-speed, open-return, blown-type wind tunnel, shown schematically in Figure 2.1. This facility was initially designed and built by Wang (1984) and modified by Kim (1990). It consists of a filter box, a blower, a redistribution section, an oblique header, a heat exchanger, a conditioning section, a nozzle, and a developing section.

The filter box is used to prevent large particles from entering the test section. Particles larger than 5 μm, which could damage the hot wire sensor in the test section, are eliminated from the flow.

The flow is driven by a centrifugal fan (New York Blower, model 244) with a capacity of 5500 scfm. The fan is driven by a 3-phase, 10 HP electric motor, driven with a Lancer 10 HP variable-frequency motor controller.

Downstream of the blower, a series of grids and a honeycomb matrix are located to remove swirl and improve uniformity before the flow enters the heat exchanger. For these experiments, the flow is not heated, but for long-duration data collection, the

heat exchanger is used to provide thermal control and uniformity of flow temperature. This heat exchanger is capable of maintaining a spatial variation of temperature of less than 0.1 °C. The heat exchanger is connected to a 40 gallon storage reservoir and a 3/4 HP centrifugal pump (Dayton 98K588) which circulates water through the heat exchanger.

Following the heat exchanger is a flow conditioning segment with a settling chamber and a 24 mesh size screen pack. This reduces the turbulence entering the 10.7:1 contraction ratio nozzle, with an inlet area of $0.914\,\mathrm{m} \times 0.914\,\mathrm{m}$ and an outlet exit area of $0.685\,\mathrm{m} \times 0.114\,\mathrm{m}$. By using a high aspect ratio of 6 for the nozzle, end wall effects can be minimized.

Finally, a development section of the same cross-sectional area as the wind tunnel nozzle exit is located in the flow, allowing measurement of the free stream parameters entering the wake generator and the insertion of turbulence generation devices. Without any turbulence generation devices added to the development section, the exit flow has a *FSTI* of approximately 0.5%. By inserting a passive rod grid composed of a series of eleven evenly-spaced, 0.95 cm diameter steel rods (two evenly-spaced vertical rods and nine evenly-spaced horizontal rods), a *FSTI* of approximately 2.5% can be produced. The turbulence generator geometry is shown in Figure 2.2.

2.1.2 The Wake Generator

The wake generator, shown in Figures 2.3 through 2.10, was designed by Yuan (1999) to simulate the wakes emerging from the upstream turbine stages in a low pressure turbine. It consists of a moving sled assembly containing the wake generating objects (for the cases presented here, the objects are 0.635 cm stainless steel rods), an H-beam rail upon which the sled slides, a speed-controlled motor assembly, transmission assembly (shown schematically in Figure 2.6), a push-bar, a deceleration device, a pulley-rope driving system and a support frame. The wake generator is designed so that the existing rods can be removed and replacement wake generation objects (such as airfoils, rods with tailboards, or other shapes) can be inserted.

In order to avoid leakage from the wind tunnel when the wake-generating rods enter and leave the upstream passage, plastic flaps attached to wood blocks (not shown) mounted outside the flow passage reduce the gap in the wind tunnel flow

development section to slightly larger than the rod diameter. This scheme is shown in Figure 2.7.

Additionally, an infrared photogate detector and a picket-fence linear encoder are mounted on the upper sled, allowing the position, speed and acceleration of the sled to be measured. This linear encoder is used also to trigger data acquisition by noting when each wake generating bar enters the channel.

A complete description of the design and the performance testing of the wake generator are presented in Yuan (1999). However, a number of substantial modifications were required to make the facility suitable for this study.

First, the original design built by Yuan was manually operated. To obtain a sufficient number of wakes to adequately calculate ensemble-averages, it was necessary to devise a technique for automating the wake generator transmission. This was accomplished by the addition of a Bimba, 3/4 inch diameter, 8 inch stroke air cylinder (Model H-095-DUZ) shown in Figure 2.8. The air cylinder is operated by compressed air and is computer controlled through the use of a 120 VAC solenoid valve which, in turn, is driven by a Crydom D1210 solid state relay. The relay is controlled using an IEEE-488-enabled, HP 59501B Programmable Power Supply. This modification allows the experiment to be completely automated during data collection.

Second, the wake generator transmission was found to have significant wear problems between the forward wheel shaft and the return friction wheel (similar wear problems between the drive shaft and the forward friction wheel were reported by Yuan). This portion of the friction drive mechanism was replaced by gears (shown in Figure 2.10), eliminating the wear problems. Also, a number of oil taps were added to some of the bushing and linkages to reduce operating heat and wear.

Finally, the operation of the wake generator is violent enough that the vibrations from the sled passage were causing the test section and anemometer to vibrate, since the test section and probe support were attached to the wake generator support frame. To address this problem, a new stand for the test section was developed which was completely detached from the wake generator, resulting in the test section being vibrationally isolated from the source of vibrations. Additionally, a series of diagonal braces was added to the test section and the wake generator to further stiffen them. The braces are shown in Figures 2.5 and 2.9.

2.1.3 The Test Section

The turbine blade passage, shown in Figure 2.11, is a cascade simulator, in which two half blades (one representing the pressure surface, the other representing the suction surface) are bolted onto acrylic endwalls to create a flow passage.

With pressure bleeds outside the leading edges of each half-blade, the flow can be adjusted so that when no wakes are present, the approaching flow stagnates at the leading edge of each half-blade. Furthermore, the entire pressure profile along the suction surface can be adjusted by the addition of tailboards which allows the design pressure profiles of the blade to be matched. Based on the study by Qiu (1996), it was decided to not use the tailboards in the present study.

The suction surface is machined from a piece of epoxy phenolic laminate (this material was selected for its low thermal conductivity and excellent machining characteristics) with a series of 13 pressure taps spaced along the blade surface. The tap locations are listed in Table 2.1. While assembling this report, it was discovered that there were slight measurement errors in the s values reported in Table 2.1 of Simon et al. (2000). Table 2.1 gives the corrected values. For each pressure tap location, velocity data were collected at each of thirty y locations, spaced starting at $\Delta y = 0.01\,\text{cm}$ near the wall, increasing gradually to $\Delta y = 0.10\,\text{cm}$ as the probe enters the freestream flow. These y values are shown in Table 2.2.

The pressure surface is fabricated from a thin Lexan sheet supported by a series of machined ribs. The pressure surface is divided into two pieces of the same height, with a separation gap of 0.8 cm (not shown) at the middle of the span to allow hot-wire probes to be placed into the turbine passage. During data collection, exposed portions of this access slot are covered with tape to prevent leakage.

2.1.4 The Test Surface

The airfoil surface geometry was obtained from the PAK-B airfoil shape offered for research by Pratt and Whitney. The important geometrical parameters for this flow are shown in Fig. 2.12. Note that the experimental configuration only models a single turbine passage, so the airfoil surfaces outside of the single turbine passage are not modeled, and are thus indicated as dashed lines in Fig. 2.12. Velocity profiles

Table 2.1: Profile locations on the suction surface

Tap No.	x (cm)	x/L_x (%)	l (cm)	l/L (%)	s (cm)	s/L_{ss} (%)
p01	0.00	0.00	0	0.00	0.00	0.00
p02	0.41	3.94	0.07	0.61	0.79	5.19
p03	2.17	20.98	1.08	9.45	3.02	19.78
p04	3.90	37.62	2.48	21.70	4.79	31.36
p05	4.80	46.35	3.36	29.40	5.71	37.35
p06	5.65	54.59	4.28	37.45	6.62	43.34
p07	6.43	62.04	5.18	45.32	7.54	49.33
p08	7.10	68.54	6.04	52.84	8.45	55.33
p09	7.67	74.08	6.88	60.19	9.37	61.32
p10	8.40	81.13	8.05	70.43	10.74	70.31
p11	8.83	85.23	8.78	76.82	11.63	76.11
p12	9.38	90.55	9.73	85.13	12.83	84.00
p13	10.02	96.71	10.87	95.10	14.28	93.49

Table 2.2: Wall-normal measurement locations

Station	y	Station	y	Station	y
1	0.010 cm	11	0.260 cm	21	0.840 cm
2	0.020 cm	12	0.300 cm	22	0.920 cm
3	0.030 cm	13	0.350 cm	23	1.000 cm
4	0.050 cm	14	0.400 cm	24	1.080 cm
5	0.070 cm	15	0.450 cm	25	1.170 cm
6	0.090 cm	16	0.510 cm	26	1.260 cm
7	0.120 cm	17	0.570 cm	27	1.350 cm
8	0.150 cm	18	0.630 cm	28	1.450 cm
9	0.180 cm	19	0.700 cm	29	1.550 cm
10	0.220 cm	20	0.770 cm	30	1.650 cm

were measured on the mid-plane of the test section, where the access slot on the concave wall allows hot-wire probe access.

2.2 Data Acquisition Equipment

The data acquisition system used in this study consists of a triple-wire probe, a boundary layer single-wire probe, anemometer bridges, an analog-to-digital converter and a computer. Each of these components will be discussed, in turn.

2.2.1 The Anemometer

A four-channel, hot-sensor anemometer bridge (TSI model IFA 100) was used to operate the thermal anemometers. For the boundary layer measurements, separate channels were used for the straight and boundary-layer style probes to eliminate the need for re-calibration when switching between sensors. For flow qualification using the triple-sensor probe, one channel was dedicated to each hot-film sensor. For all measurements, each sensor's output was low-pass filtered at 20 kHz using the anemometer bridge's built-in filters. Additionally, for the boundary layer measurements, a gain of 4.0 was applied to the bridge output signal to allow more effective use of the voltage resolution of the analog-to-digital converter.

2.2.2 Analog-to-Digital Converter

The output voltages of both the anemometer bridge and the photogate linear encoder were sampled using a pair of IOTech ADC-488/8SA analog-to-digital converters. These ADCs are each capable of sampling with 16-bit resolution at a rate of 100 kHz. Each voltage signal was sampled 60,000 times at 100 kHz for a total sampling time of 0.6 seconds, long enough to capture a complete passage of the wake generation sled through the wake generator with a generous amount of pre- and post-wake signal collected as well. To make best utilization of the ADCs' resolution, the hot-wire signal (nominally 1.05 V) was amplified by a factor of 4.0 with the anemometer bridge and the signal was sampled using the IOtechs' 5 volt range. The digitized voltage values for both the anemometer bridge and the linear encoder were transferred to the computer via an IEEE-488 bus. Both IOTechs were configured to begin sampling simultaneously upon an external trigger provided by the photogate linear encoder.

2.2.3 Stepper Motor

The stepper motor assembly consists of a Modulynx SCA 311 system controller, a PDM155 Motor Driver, and a SLO-Syn M063-LF-401 stepping motor, all provided by Superior Electric, Inc. The stepper motor has a resolution of 5 μm per step. The motor is controlled separately from the main data acquisition routine, using the program `superior.c`, listed in Appendix C.

2.2.4 Computer and Data Acquisition Bus

A 500 MHz Pentium-III Debian Linux computer was used for data communication and experimental control. The computer has a National Instruments IEEE-488 communications card, allowing it to communicate with the IOTech 488/8SA units, the power supply driving the air cylinder solenoid, the Fluke multimeter driving the platinum RTD (discussed in section 3.4) and the stepper motor assembly.

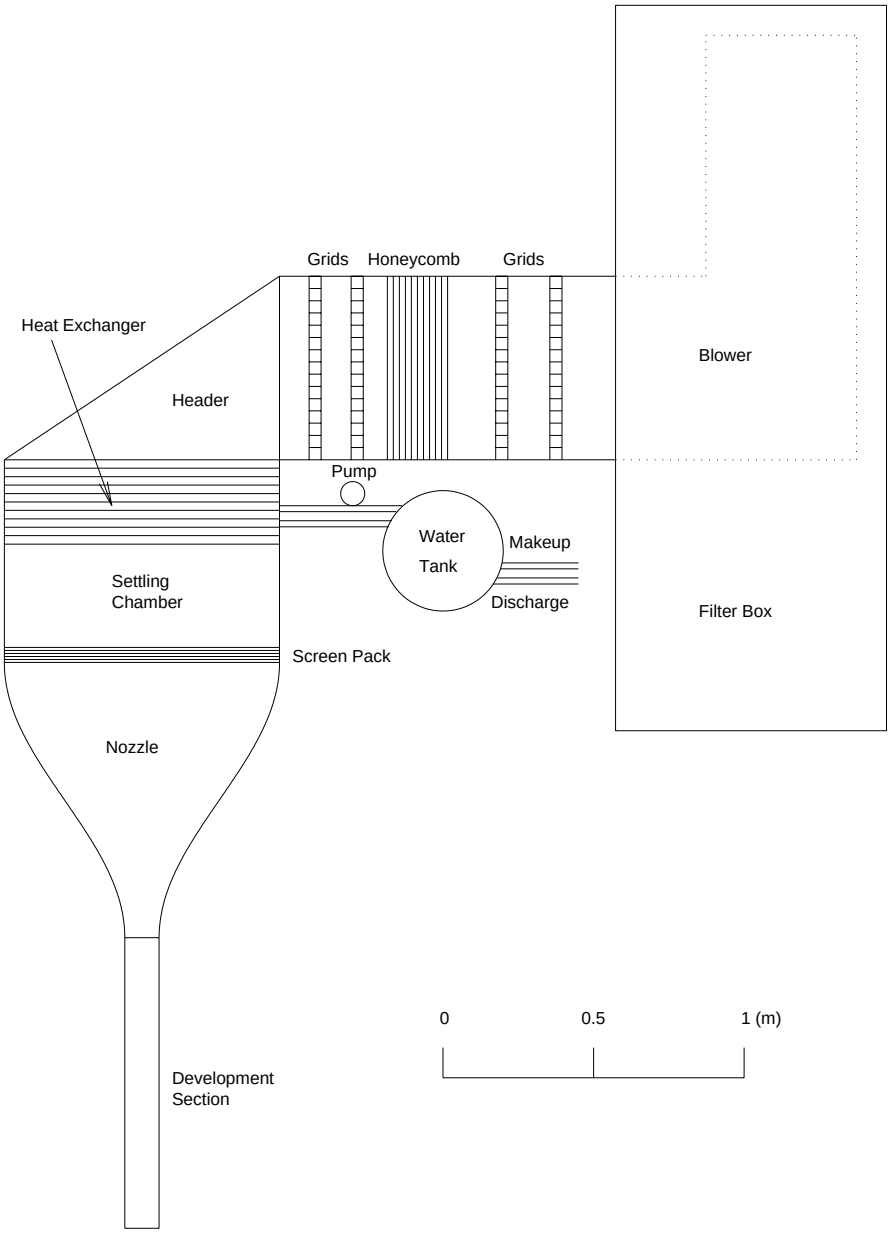

Figure 2.1: The low speed wind tunnel (Yuan, 1999)

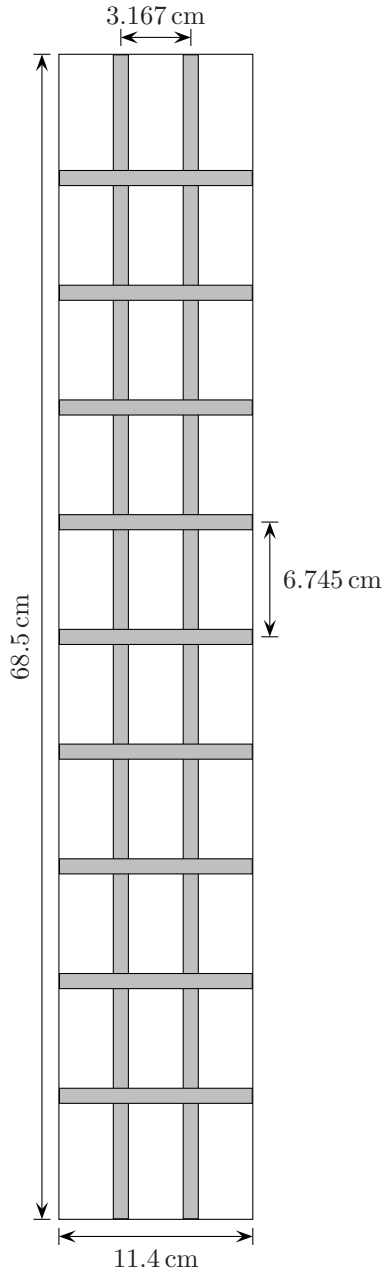

Figure 2.2: Rod-grid turbulence generator used for $FSTI = 2.5\%$. Each rod is 0.95 cm in diameter

.

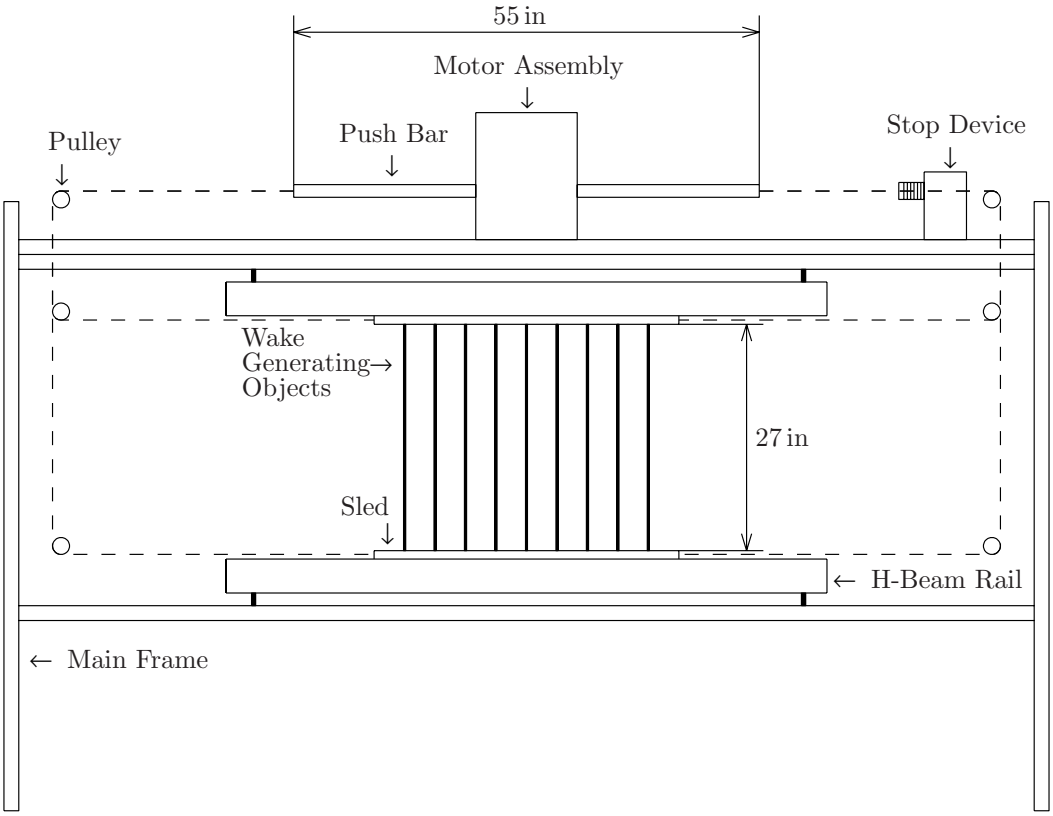

Figure 2.3: A side-view schematic of the wake generator (Yuan, 1999).

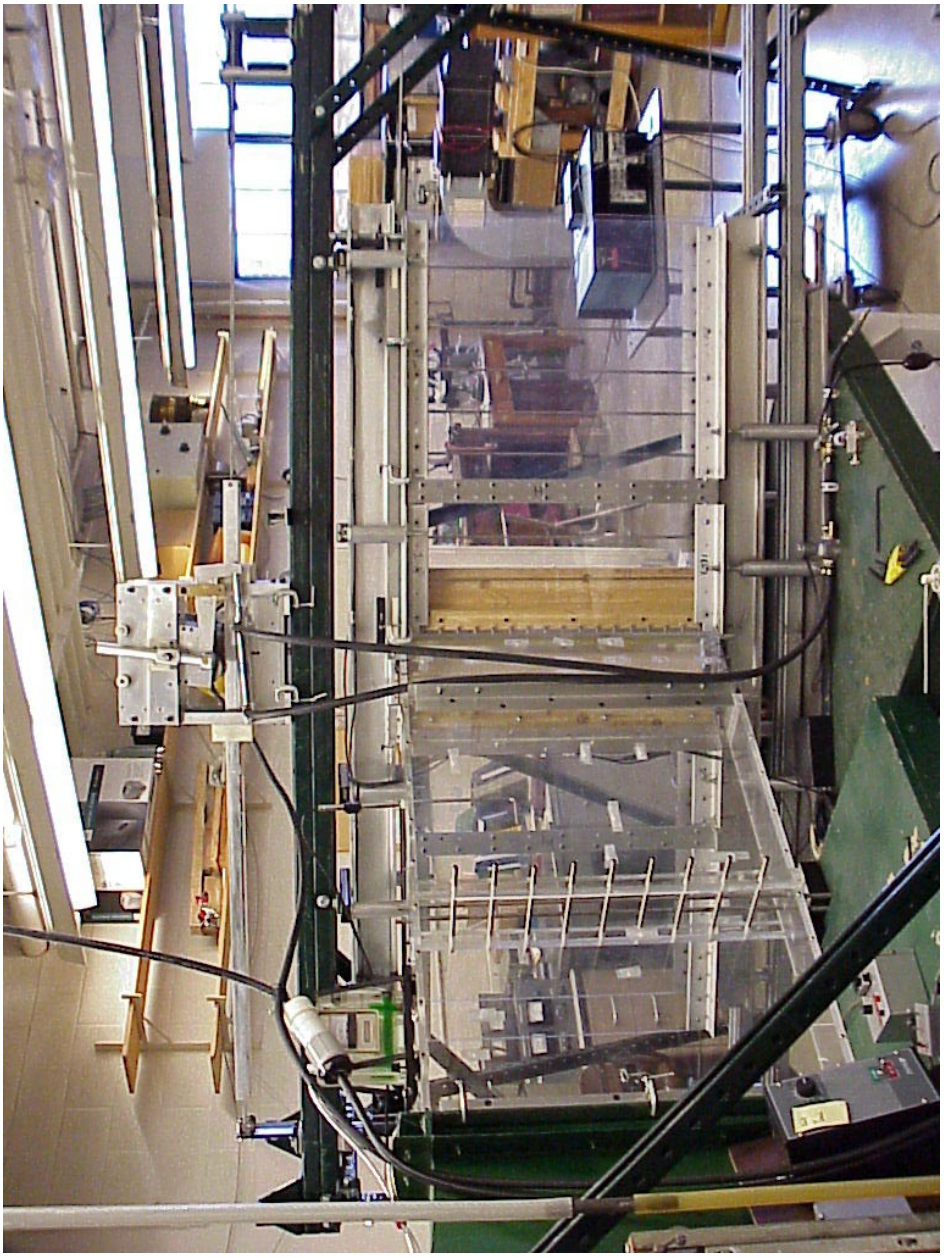

Figure 2.4: Test facility, upstream side. Note the turbulence-generation grid.

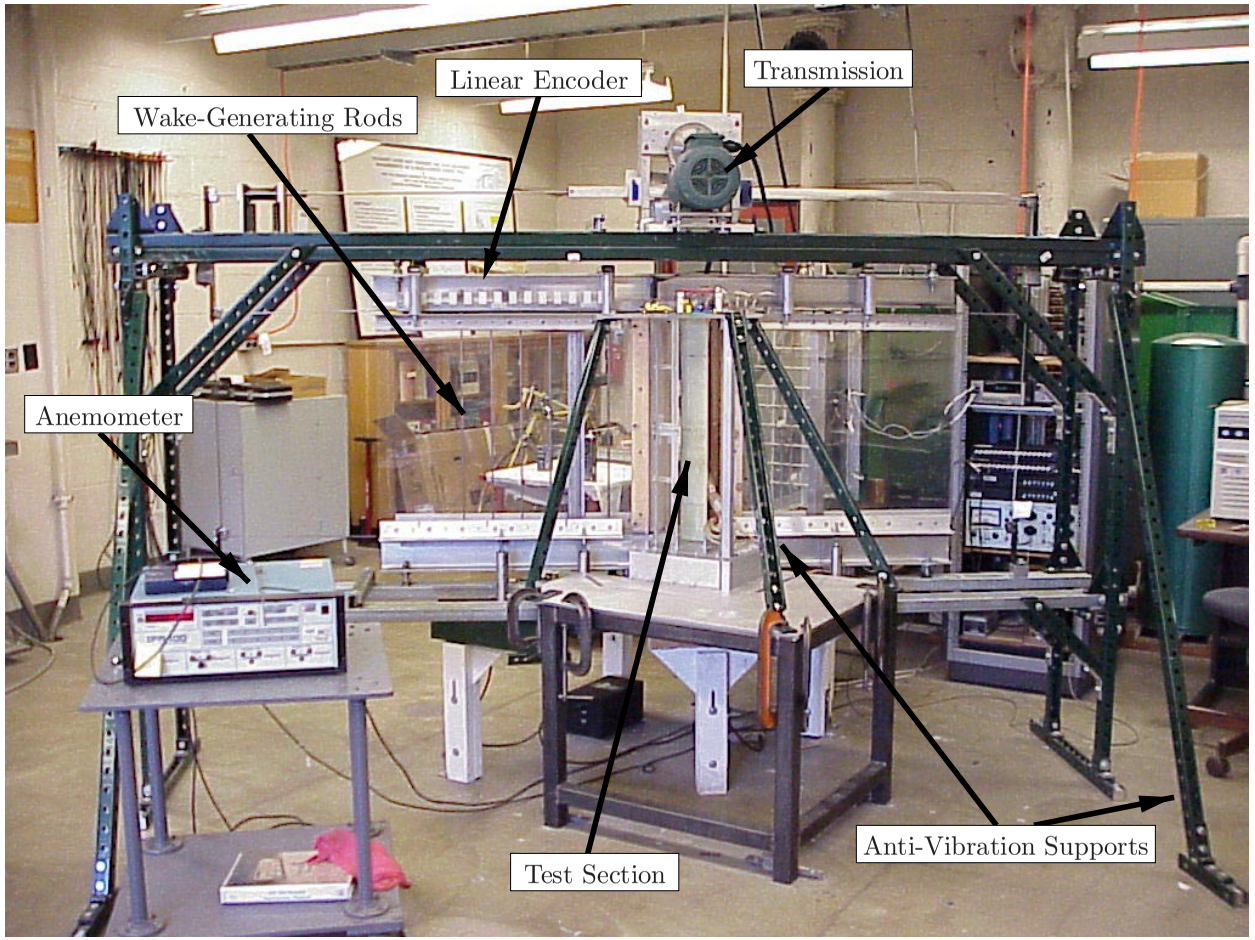

Figure 2.5: Test facility, downstream side. Note vibration bracing, as well as the wake generator sled from Figure 2.3 in the background.

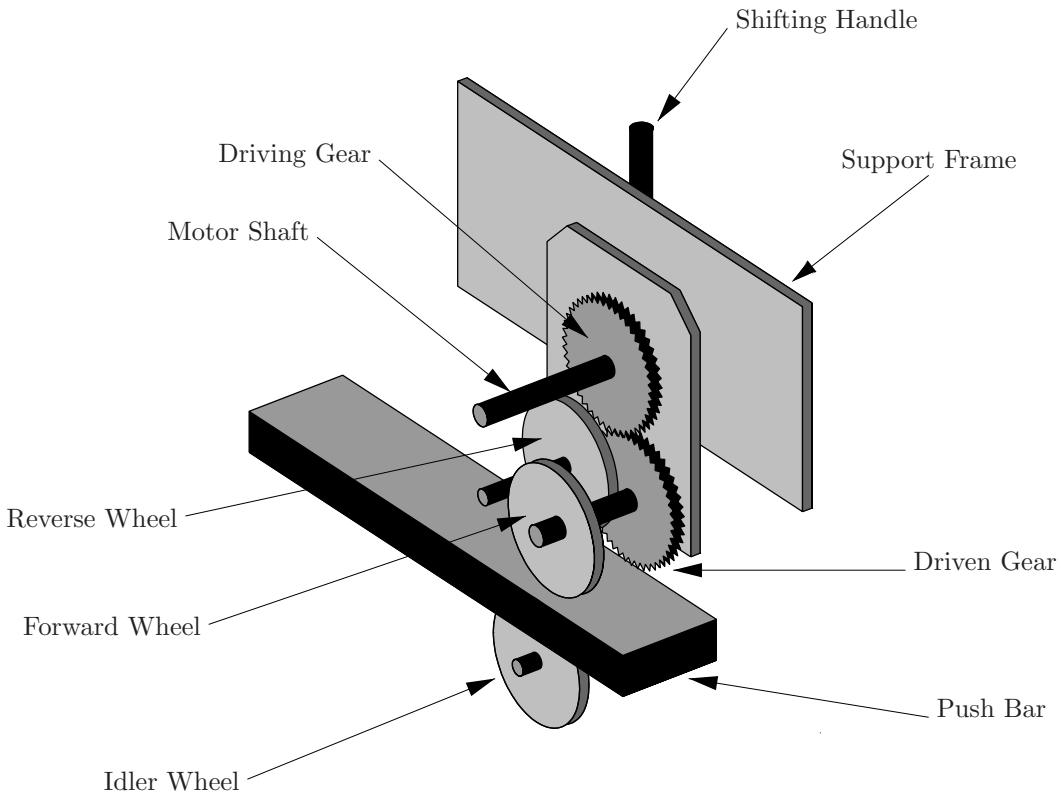

Figure 2.6: A schematic view of the wake generator transmission (Original design, from Yuan (1999)).

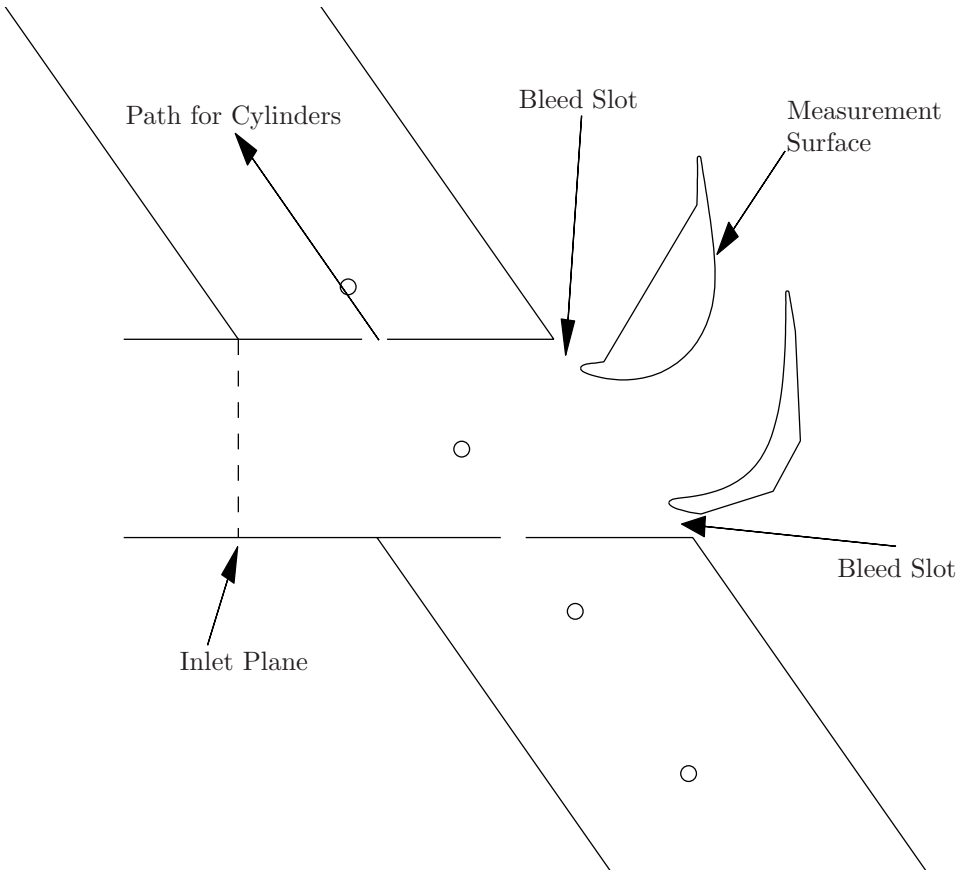

Figure 2.7: Cross-sectional view of the wake generator.

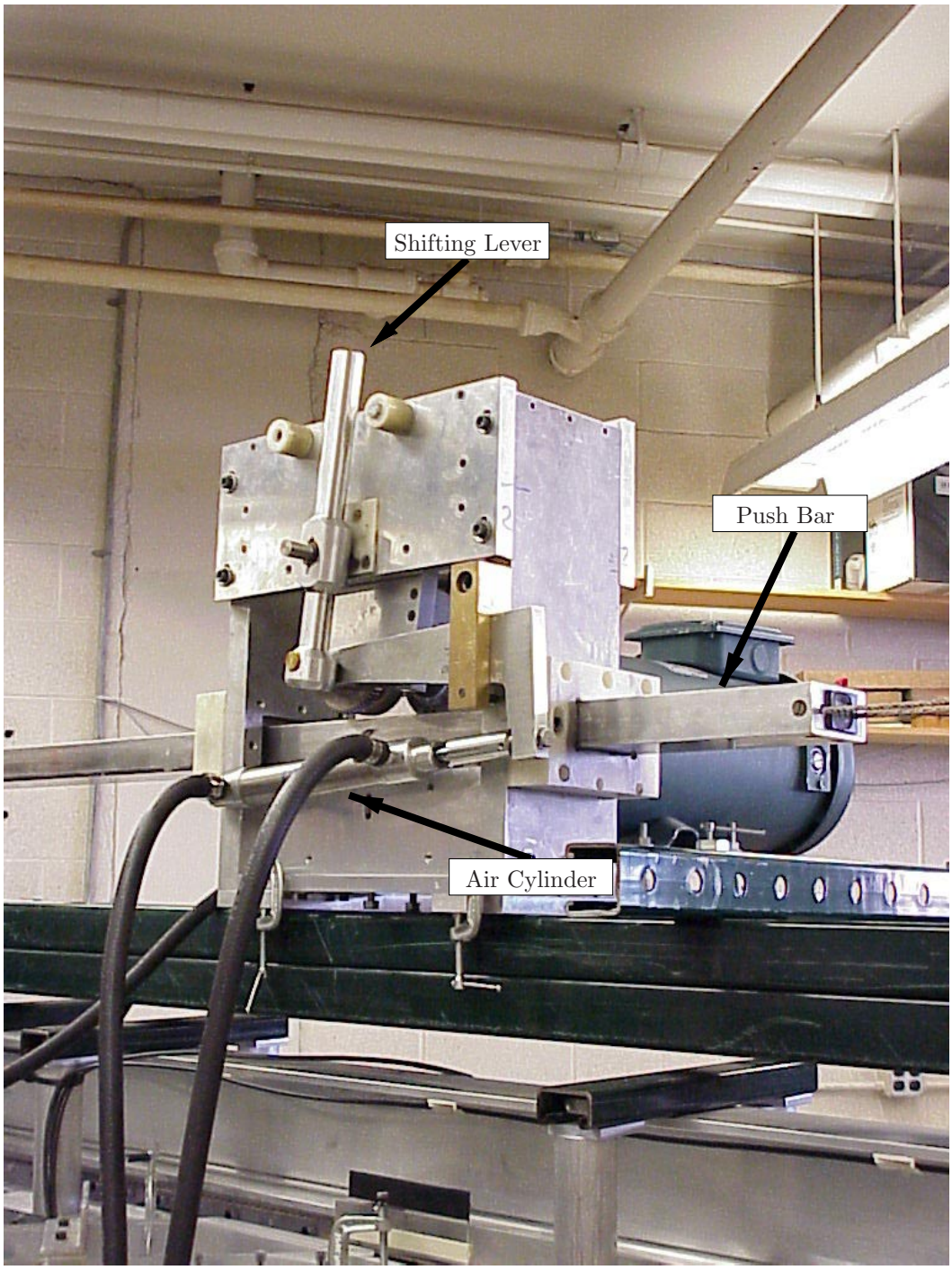

Figure 2.8: Photo of the wake generator transmission with air cylinder actuator added

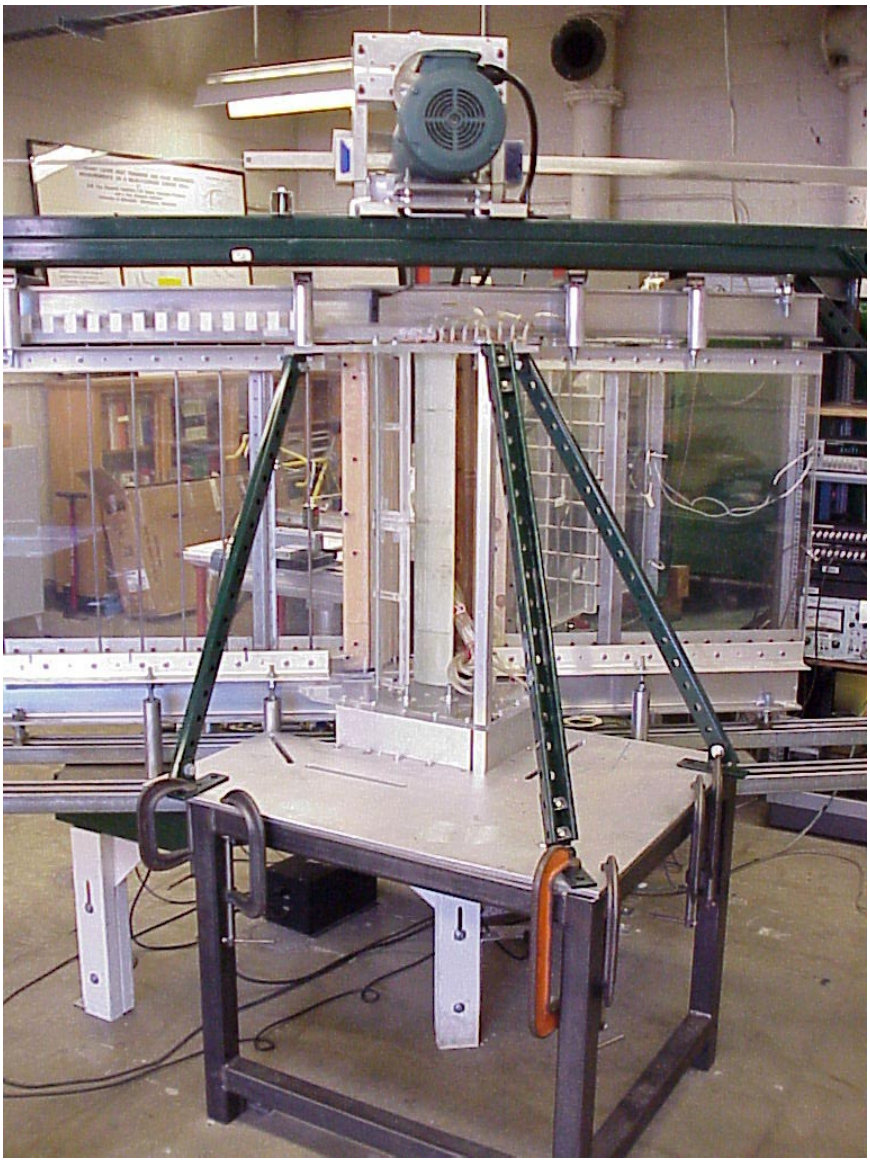

Figure 2.9: Test section isolation table, showing braces added to reduce vibration.

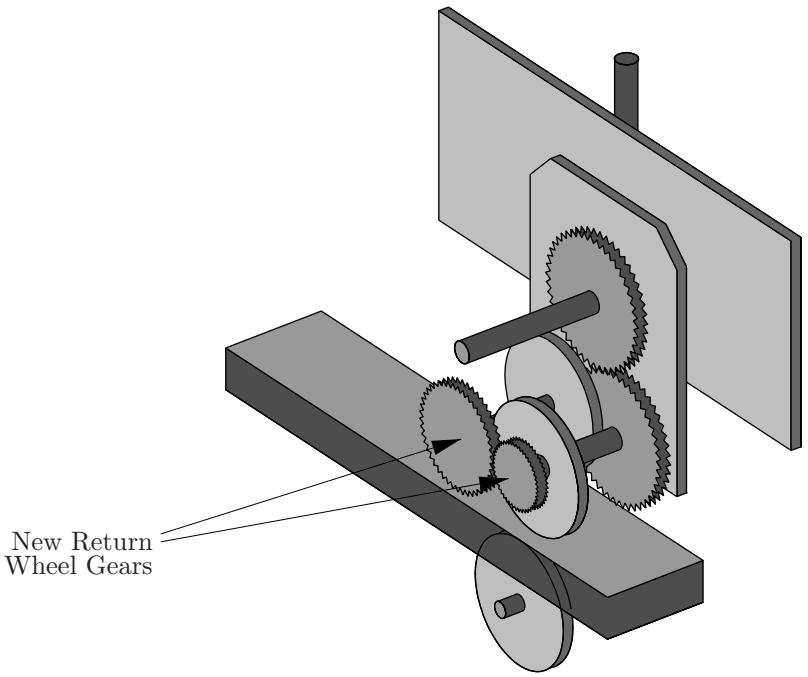

Figure 2.10: A schematic view of the wake generator transmission (New design with return wheel gears).

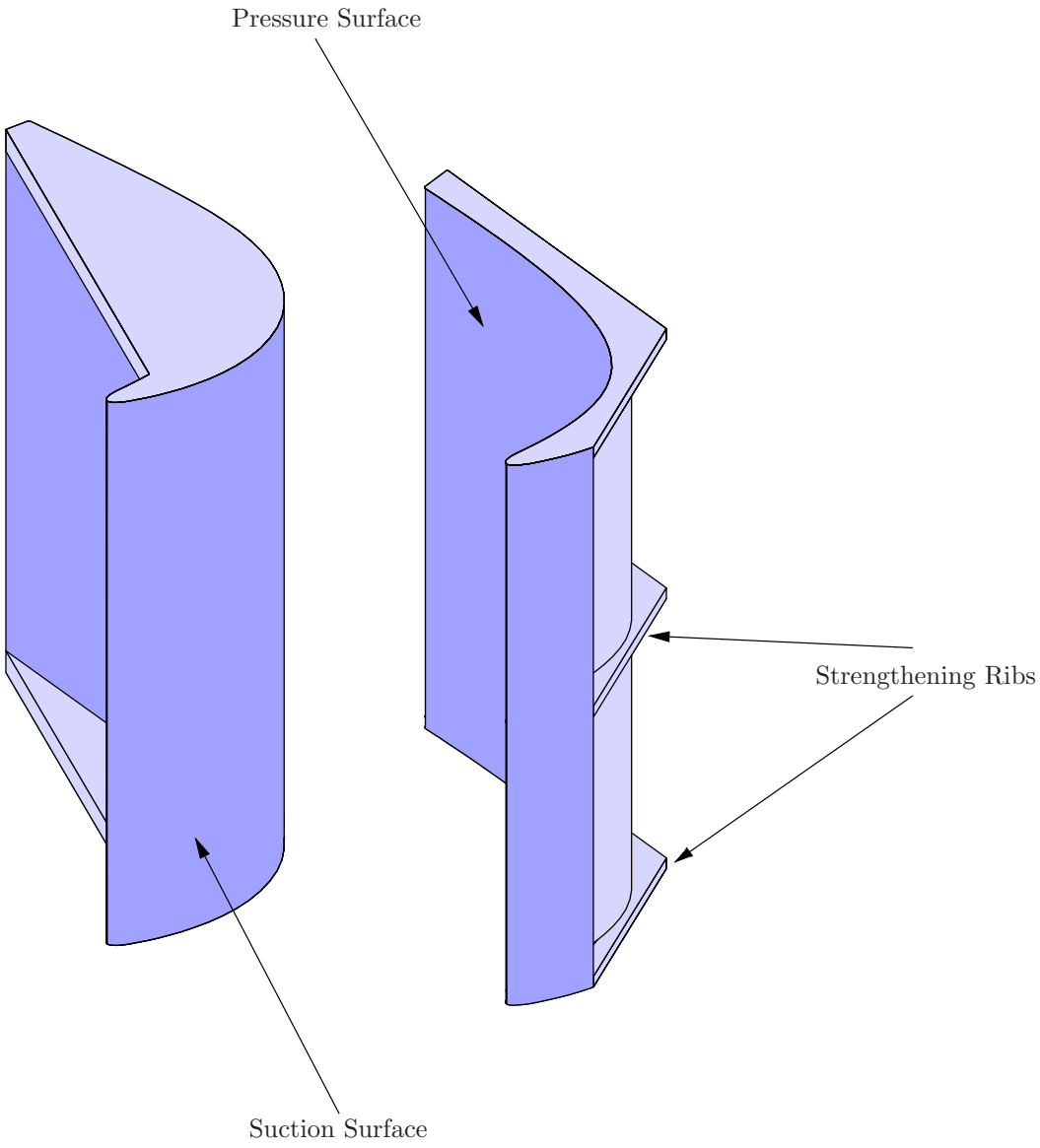

Figure 2.11: The cascade simulation test section.

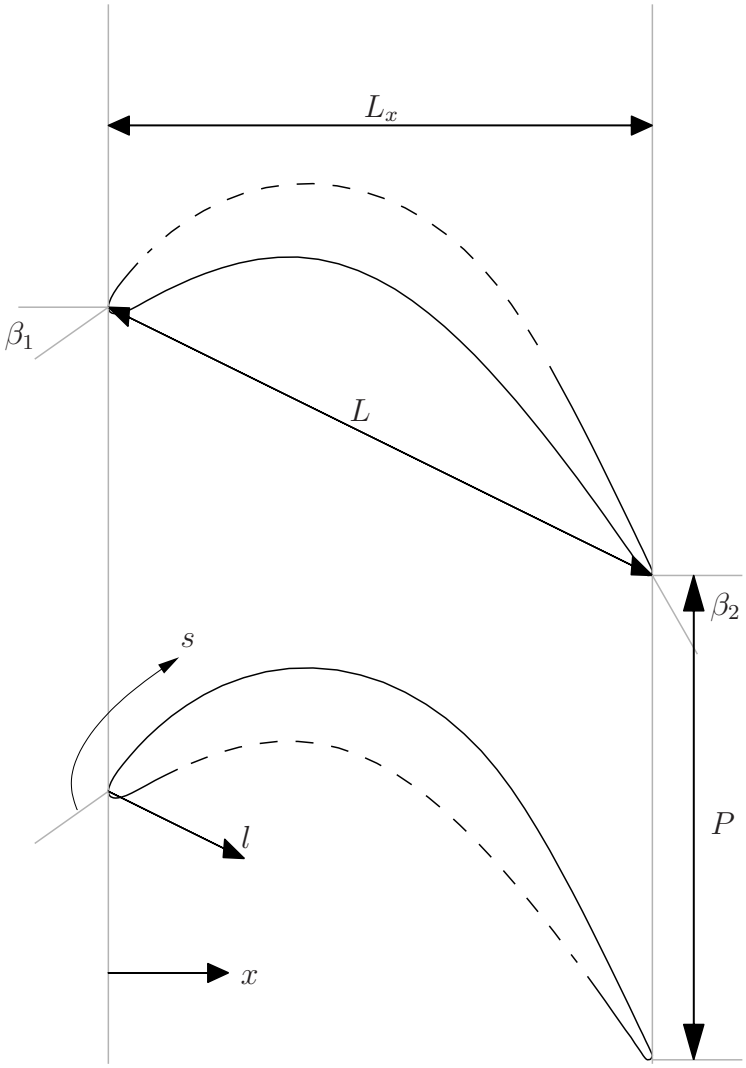

Chord length, L:	114.3 mm
Axial chord length, L_x:	103.57 mm
Suction surface length, L_{ss}:	152.76 mm
Axial chord to chord ratio, L_x/L:	0.906
Pitch to chord ratio, P/L:	0.8
Aspect ratio (span/chord), L_z/L:	6.0
Blade inlet angle, β_1:	35°
Blade outlet angle, β_2:	−60°
Rod velocity to axial velocity ratio, u_r/u_x:	~ 0.70
Rod spacing to airfoil pitch ratio, L_r/P:	1.0

Figure 2.12: PAK-B airfoil geometry

Chapter 3

Experimental Procedures and Data Processing

3.1 Thermal Anemometry

Thermal anemometry techniques were used in this study to obtain instantaneous time-series measurements of velocity and velocity fluctuations. Thermal anemometry sensors are advantageous for use in turbulent flows because they have excellent frequency response, allow accurate measurement of instantaneous velocities in flows with up to 30% turbulence intensity and provide DC electrical signals which are easily processed. The instantaneous velocity waveforms provided by the sensors also allow analyses such as spectral analysis and correlation of velocity components (to obtain turbulent shear stresses). The primary disadvantages of thermal anemometry are the inability to measure flow reversal, the intrusive nature of the probe, and, for multi-sensor probes, the inability to correctly measure flows approaching the sensor outside of the approach angle of the sensor (>30° approach angle for triple-sensor anemometers). Flow reversal does occur in the present data set but the error in detecting the flow direction of these locations did not represent a problem. The intrusiveness of the probe was also not a problem to the moderate to high levels of turbulence in the flow—even the 2.5% *FSTI* was sufficient to allow the probe to not influence the transition measurements.

A thermal anemometer is a small resistance element, typically either a tungsten wire or a coated quartz element (a "film") which is maintained at a constant

temperature using an anemometer bridge. The rate at which heat is removed from the sensor is directly related to the velocity of the fluid flowing over the sensor and the temperature of the sensor. In this study, two forms of thermal anemometry are used: single-sensor anemometry, in which a single heated element is used to measure a single velocity component of the flow and triple-sensor anemometry, in which three orthogonally-mounted sensors are used to simultaneously measure all three components of the flow.

For single-sensor anemometry, either a straight, single-sensor hot-wire (TSI Model 1210-T1.5, shown in Figure 3.1(a)) or a boundary-layer style, single-sensor hot-wire (TSI Model 1218-T1.5, shown in Figure 3.1(b)) was used, depending on the geometry and probe access available in different portions of the flow. Both sensors are tungsten wires. The ends of the tungsten wire are copper-coated, which isolates the sensing portion of the wire from the supports. With a diameter of 4 μm and an active length of 2 mm, the overall length-to-diameter ratio is approximately 500.

For 3-D anemometry, a triple-sensor, hot-film probe (TSI Model 1299BM-20, shown in Figure 3.1(c)) was used. Each hot-film sensor in this probe uses a thin film of platinum deposited on a thin cylindrical quartz cylinder. The overall diameter of the sensor is 50.8 μm and the overall length-to-diameter ratio of the active surface of each probe is approximately 20. The active area of the hot film represents approximately one fourth the total length of the cylinder.

3.1.1 Single-Sensor Anemometry

3.1.1.1 Single-Sensor Anemometry Theory

As air passes over a hot-wire sensor, it cools the sensor at a rate that is proportional to the mass flux of fluid past the sensor. The relationship between the effective velocity past the sensor, U_e, and the bridge voltage, E, is given by:

$$\frac{E^2 R}{(R + R_s)^2} = \left[B_1 + B_2(\rho U_e)^{1/n}\right](T_s - T_f) \tag{3.1}$$

The value of n depends on the type of hot-film, the medium and the flow speed, but is typically close to 2.3. As mentioned earlier, the hot-film is maintained at a constant temperature of 250 °C during the experiments.

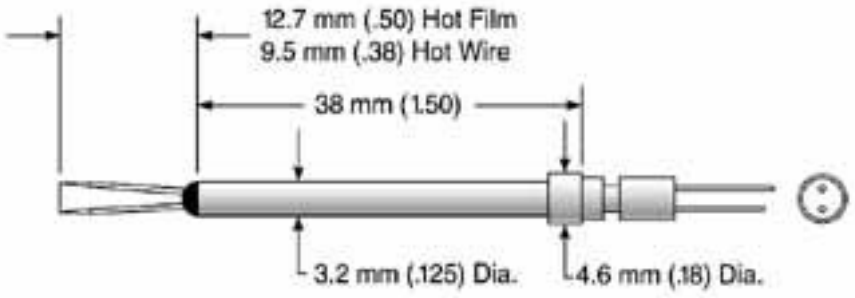

(a) Model 1210 Anemometer

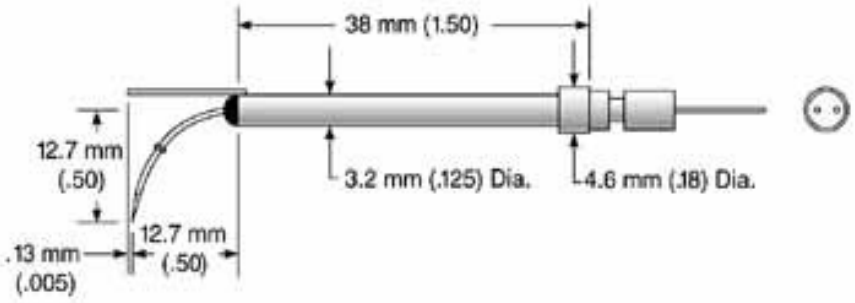

(b) Model 1218 Anemometer

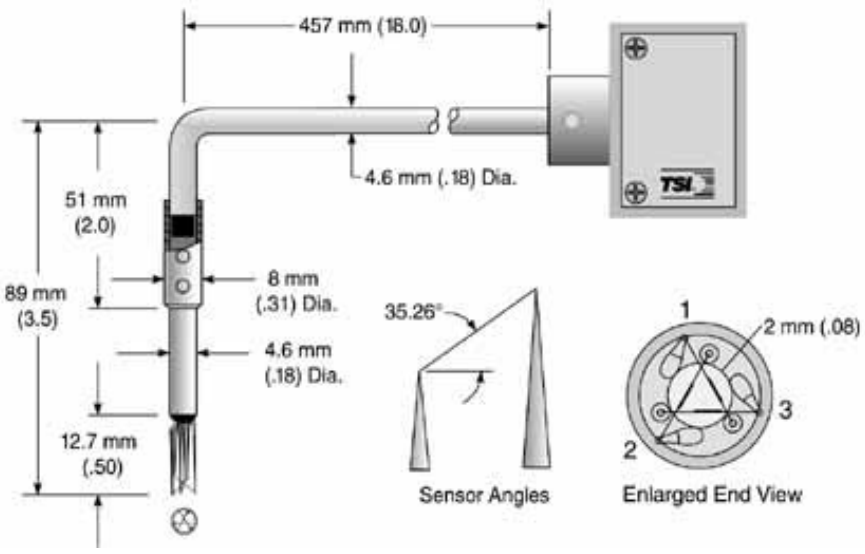

(c) Model 1299BM Anemometer

Figure 3.1: TSI thermal anemometers (TSI, Inc., 1999)

If the hot-wire surface temperature and flow temperatures were maintained at constant values and the film and control resistances of the anemometer were known, Eqn. 3.1 provides a near-linear relationship between the square root of effective velocity and the square of the bridge voltage, a relationship commonly known as King's law. Experimentally,

$$E^2 = C_1 + C_2 U_e^{0.435} \tag{3.2}$$

tends to provide a suitable curve fit for the hot-wire response. The values of the constants C_1 and C_2 are obtained during calibration of the hot-wire sensor.

3.1.1.2 Single-Sensor Hot-Wire Calibration

To calibrate the single-sensor probe, the voltage vs. velocity response curve must be calculated. This is done by introducing the sensor to a flow of known velocity and recording the output voltage seen on the anemometer bridge. In this study, the flow development section upstream of the turbine cascade simulator is used to provide such a steady flow. The velocity of this flow is measured with a Pitot tube, as discussed in section 3.3.

The sensor is exposed to a range of effective velocities from 0.5 m/s (the lowest reliable calibration velocity available in the tunnel) to 9 m/s (slightly above the highest effective velocities anticipated during data collection). By measuring the voltage response of the sensor at a series of different velocities in this range, calibration constants for the approximated hot-wire response, Eqn. 3.2 can be calculated using a least-squares linear curve fit. An example of such a calibration is shown in Figure 3.2 The C program used to calibrate the anemometer is included as `pitotsingle-cal.c` in Appendix C.

3.1.1.3 Single-Sensor Hot-Wire Temperature Correction

The thermal anemometer was calibrated in a fixed-temperature flow. Most of the production measurements were taken over intervals of more than four hours. Though the heat exchanger in the facility was effective in reducing temperature changes during this period, there were some slight changes in operating temperature over the course of each experimental run.

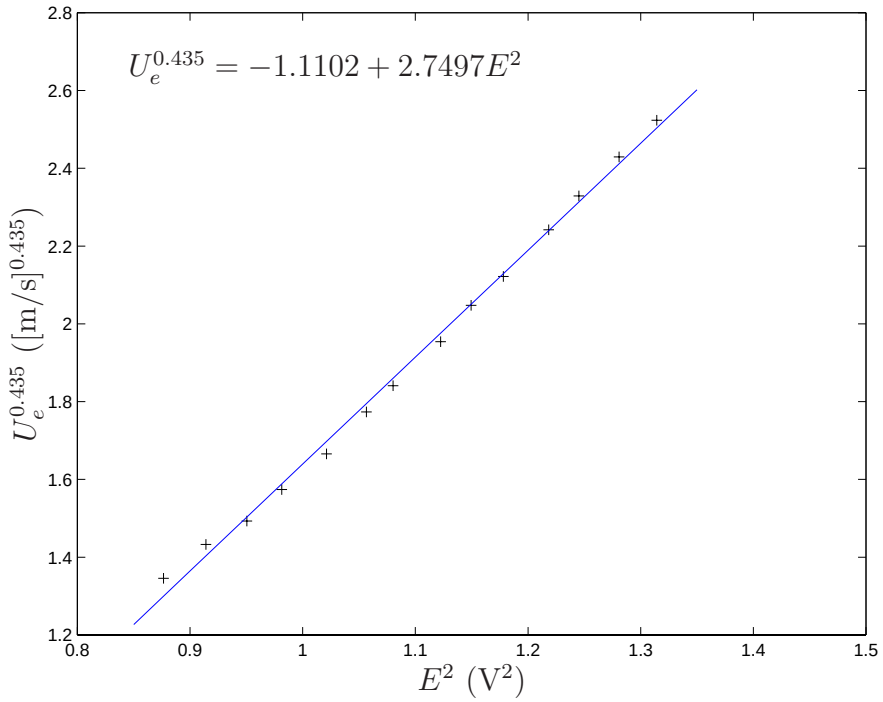

Figure 3.2: Sample single-wire calibration curve

Since the hot-wire voltage response, Eqn. 3.1, is a function of both the ambient temperature and the mass flux around the sensor, it is necessary to correct for temperature variations during the experiment. This is accomplished using a first-order temperature correction scheme in which the measured bridge voltage is multiplied by a correction factor based on the sensor temperature, the calibration temperature and the current flow temperature:

$$C_f = \sqrt{\frac{T_s - T_c}{T_s - T_f}} \tag{3.3}$$

To apply this correction, the fluid temperature was monitored and the correction factor adjusted continuously during the experiment. Additionally, if environmental changes result in temperature changes more than 2–3 °C the triple-wire calibration is repeated with a new calibration temperature to minimize errors due to this first order correction.

Changes in other environmental factors such as pressure and humidity generally do not have a significant effect on the hot-wire voltage response, so no correction is

necessary for these changes. The range of pressure in the room varies less than 4%, and usually is stable to with 0.25%. For large changes in humidity (over 25% relative humidity), the anemometer is recalibrated to account for changes in response.

3.1.1.4 Wall Finding Technique

The collection of boundary layer velocity profiles requires that the position of the hot-wire probe relative to the test surface be accurately known. The probe was mounted on a stepper motor traverse system (described in section 2.2.3) with 5 μm per step resolution, but at the onset of data collection, the actual location of the wall is unknown. In order to correctly determine the location of the wall, the hot-wire probe was manually adjusted until the wire of the probe was in slight visible contact with the test surface. The probe was then backed away from the wall in 5 μm increments. When the probe was in contact with the wall, the recorded velocity of the probe was essentially constant. However, when the probe finally broke contact with the wall, there was a noticeable and immediate increase in the recorded velocity. The position of this velocity increase was taken to be one wire radius (2 μm for the probe used in this study) from the wall. Since this was the major bias error in y-position, an overall uncertainty in y of approximately 2 μm was assigned. This procedure was repeated for every y-profile collected.

3.1.1.5 Near-Wall Velocity Corrections

Since the hot-wire sensor measures velocity from the heat flux out of the sensor surface, care must be taken to correct for conduction losses which cause extra heat loss from the sensor, yielding artificially high values of velocity. As the hot-wire sensor is used at locations very near the wall (distances less than approximately 0.4 mm), conduction losses between the hot-wire sensor and the wall become high enough that they begin to influence the velocities reported by the hot-wire sensor.

A number of techniques have been proposed for correcting the measured velocities to eliminate the velocity bias resulting from this extra conduction. A review of such techniques is provided by Chew et al. (1995). Most techniques involve corrections based on the sensor size, wall-normal distance, shear velocity, wall conductivity or surface shear stress. However, due to the periodic-unsteady nature of the flow being measured and the difficulty of accurately estimating the time-varying boundary

layer thickness and wall shear stress, many of the techniques are inappropriate for this flow.

The most promising near-wall correction scheme is an empirical one, developed by Wills (1962) and refined for use in turbulent flows by Kim (1990). For this study, the Wills correction is used for laminar flow:

$$u_{corrected} = \left[u_{uncorrected}^{0.45} - \left(\frac{\nu}{d_s}\right)^{0.45} k_w \right]^{\frac{1}{0.45}} \tag{3.4}$$

$$k_w = 0.9 - 7.2 \times 10^{-2} \left(\frac{2y}{d_s}\right) + 2.89 \times 10^{-3} \left(\frac{2y}{d_s}\right)^2 - 6.15 \times 10^{-5} \left(\frac{2y}{d_s}\right)^3 + 6.51 \times 10^{-7} \left(\frac{2y}{d_s}\right)^4, \text{when } 2y/d_s < 50 \tag{3.5}$$

$$k_w = 0.54 - 2.42 \times 10^{-2} \left(\frac{2y}{d_s}\right) + 5.01 \times 10^{-4} \left(\frac{2y}{d_s}\right)^2 - 5.36 \times 10^{-6} \left(\frac{2y}{d_s}\right)^3 + 2.85 \times 10^{-8} \left(\frac{2y}{d_s}\right)^4, \text{when } 2y/d_s > 50 \tag{3.6}$$

where d_s is the sensor diameter, $4\,\mu$m.

The work of Kim suggests that for turbulent flow, a correction equal to 84% of the Wills correction should be used, yielding the following:

$$u_{corrected} = 0.84 \left[u_{uncorrected}^{0.45} - \left(\frac{\nu}{d_s}\right)^{0.45} k_w \right]^{\frac{1}{0.45}} + 0.16 u_{uncorrected}. \tag{3.7}$$

The obvious disadvantage of this technique is that since it is an instantaneous correction technique, it requires that the flow be correctly identifies as being laminar or turbulent before the correction is applied. Thus, the actual corrected velocities must be calculated after the intermittency is calculated, which will be discussed in section 3.2.

3.1.1.6 Single-Sensor Uncertainty Analysis

To ascertain our ability to accurately measure velocities using the hot-wire anemometer, an uncertainty analysis was required. Since many of the relationships used in calculating the velocity are nonlinear, the traditional propagation of errors

analysis was replaced with a Monte Carlo method. In this method, the characteristic uncertainties of the quantities used to compute the velocity were estimated and a computer code (written in MATLAB, included as `monte.m` in Appendix C) was written that randomly varied the inputs within the range of estimated uncertainties to produce a histogram of output values showing the anticipated variation of output values given the input uncertainties.

In addition to producing a highly accurate estimation of uncertainty, the computational engine developed for this technique is suitable for calculating the relative sensitivity of the measured experimental quantities to changes in the input quantities.

As an example of this technique, the uncertainty in the measured velocity reported by the hot-wire is calculated.

The measured velocity, u, obtained from the hot-wire is given by the expression

$$u = \left[b + m \left(\frac{T_{sensor} - T_c}{T_s - T_f} \right) \left(E^2 \right) \right]^{2.29885} \tag{3.8}$$

where b and m are found through calibrating the sensor at a room temperature T_c, E is the output voltage of the anemometer, T_s is the operating temperature of the anemometer, and T_f is the fluid temperature during data collection.

Based upon standard estimation techniques, the single-point, single measurement error (expressed at 95% confidence level) for each quantity is:

$$\begin{aligned} \delta E &\approx 0.001\,\mathrm{V} \\ \delta b &\approx 0.04 \\ \delta m &\approx 0.004 \\ \delta(T_c) &\approx 0.2\,^{\circ}\mathrm{C} \\ \delta(T_f) &\approx 0.2\,^{\circ}\mathrm{C}. \end{aligned}$$

Using these input uncertainties, the `monte.m` code was run for 1 million trials. Using the above error estimations as inputs to Eqn. 3.8, the resulting distribution of calculated velocity values, can be used to calculate a level of uncertainty (with 95% confidence) of $\delta u/u \approx 4.7\%$, quite acceptable for measurement of boundary layer profiles.

3.1.2 Triple-Sensor Anemometry

3.1.2.1 Triple-Sensor Anemometry Theory

For triple-sensor anemometry, a series of three orthogonally-mounted films are used to measure all three components the instantaneous flow-field. This means that at a given instant, at least two of the hot-film sensors are not perpendicular to the approaching flow. The extent of cooling of the hot-film is dependent on the angle with which the flow is incident upon the probe. The effective velocity, U_e, seen by the the sensor is a function of the three components of velocity relative to the sensor (shown in Figure 3.3). The relationship between these velocity components and the effective velocity is given by Jorgensen's equation:

$$U_e^2 = U_n^2 + K^2 U_t^2 + H^2 U_b^2. \tag{3.9}$$

In this study, an orthogonal triple-sensor probe was used. A perfectly constructed orthogonal probe (Figure 3.4) has each sensor orthogonal to the other two sensors. Each sensor is aligned 35.26° to the normal, and the angle of each sensor is 60° from the other two sensors when viewed along the probe axis. Additionally, the sensors are placed such the there is no wake interference between them when the flow is approaching from the octant that includes the vector parallel to and in the direction of the probe support. Also, it was previously determined by Russ and Simon (1990) that flow must approach the sensor from an angle of less than 30°. Beyond this, instantaneous flow reversal over one or more of the sensors is too frequent, resulting in incorrect measurements. Each of the three sensors gives the local effective velocity seen by that sensor, which can, in turn, be transformed to yield the three instantaneous principal velocity components.

To determine the transformation between the effective velocities seen by each sensor and the principal velocity components, we start by relating the effective velocities seen by each sensor to the normal, binormal and tangential velocities at each sensor using Eqn. 3.9:

$$U_{e1}^2 = U_{n1}^2 + K_1^2 U_{t1}^2 + H_1^2 U_{b1}^2 \tag{3.10a}$$

$$U_{e2}^2 = U_{n2}^2 + K_2^2 U_{t2}^2 + H_2^2 U_{b2}^2 \tag{3.10b}$$

$$U_{e3}^2 = U_{n3}^2 + K_3^2 U_{t3}^2 + H_3^2 U_{b3}^2. \tag{3.10c}$$

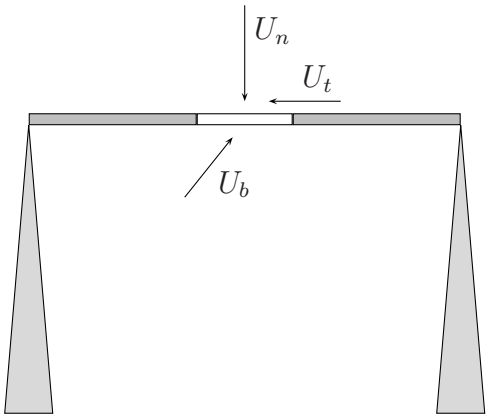

Figure 3.3: Velocity components for a hot-film sensor

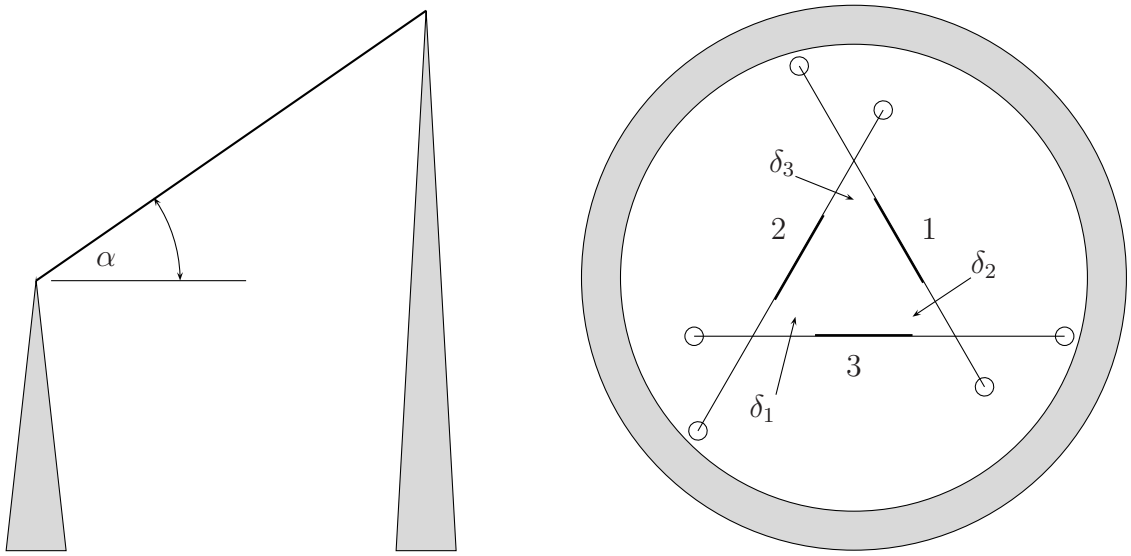

(a) Sensor Side View

(b) Probe End View

Figure 3.4: An orthogonal triple-sensor probe

These normal, binormal and tangential velocities can then be related to the principal velocities u, v, and w through simple geometric relations:

$$\begin{aligned}
U_{e1} =& \Big\{ u\cos(\alpha_1) + \big[w\cos(\delta_2) + v\sin(\delta_2) \big] \sin(\alpha_1) \Big\}^2 \\
&+ K_1^2 \Big\{ u\sin(\alpha_1) - \big[w\cos(\delta_2) + v\sin(\delta_2) \big] \cos(\alpha_1) \Big\}^2 \\
&+ H_1^2 \Big\{ v\cos(\delta_2) - w\sin(\delta_2) \Big\}^2
\end{aligned} \tag{3.11a}$$

$$\begin{aligned}
U_{e2} =& \Big\{ u\cos(\alpha_2) + \big[w\cos(\delta_1) - v\sin(\delta_1) \big] \sin(\alpha_2) \Big\}^2 \\
&+ K_2^2 \Big\{ u\sin(\alpha_2) - \big[w\cos(\delta_1) - v\sin(\delta_1) \big] \cos(\alpha_2) \Big\}^2 \\
&+ H_2^2 \Big\{ v\cos(\delta_1) + w\sin(\delta_1) \Big\}^2
\end{aligned} \tag{3.11b}$$

$$\begin{aligned}
U_{e3} =& \Big\{ u\cos(\alpha_3) - w\cos(\alpha_3) \Big\}^2 \\
&+ K_3^2 \Big\{ u\sin(\alpha_3) + w\cos(\alpha_3) \Big\}^2 \\
&+ H_3^2 v^2.
\end{aligned} \tag{3.11c}$$

These relationships apply in general to all triple-sensor probes, and are not specific to the orthogonal triple-sensor probe. However, the orthogonal relationship between the sensors in the triple-sensor probe allows these relationships to be greatly simplified. Although slight non-orthogonality typically occurs as a result of misalignments during manufacture, the error resulting from this non-orthogonality is slight (Russ and Simon, 1990). Since the sensors are orthogonal, a velocity component that is tangential to one sensor will be normal to the other two sensors. Thus, we can relate the tangential, normal and binormal velocity components thusly:

$$U_{t1}^2 + U_{t2}^2 = U_{b3}^2 + U_{n3}^2 \tag{3.12a}$$

$$U_{t2}^2 + U_{t3}^2 = U_{b1}^2 + U_{n1}^2 \tag{3.12b}$$

$$U_{t1}^2 + U_{t3}^2 = U_{b2}^2 + U_{n2}^2. \tag{3.12c}$$

Additionally, if the yaw coefficients, H_1, H_2, and H_3, are assumed to be unity (a reasonable assumption for a cylindrical sensor), then we can substitute these expressions

into Eqn. 3.10 to directly relate the effective and tangential velocities at each wire:

$$U_{e1}^2 = K_1^2 U_{t1}^2 + U_{t2}^2 + U_{t3}^2 \tag{3.13a}$$

$$U_{e2}^2 = K_2^2 U_{t2}^2 + U_{t1}^2 + U_{t3}^2 \tag{3.13b}$$

$$U_{e3}^2 = K_3^2 U_{t3}^2 + U_{t1}^2 + U_{t2}^2. \tag{3.13c}$$

If the pitch coefficients, K_1, K_2, and K_3, are known, then this set of equations can easily be inverted to yield the tangential velocities. Once the tangential velocities have been calculated, simple geometric relations based on Figure 3.4 can be used to relate u, v, and w to the tangential velocities:

$$U_{t1} = u\sin(35.26^\circ) - \left[w\cos(60^\circ) + v\sin(60^\circ)\right]\cos(35.26^\circ) \tag{3.14a}$$

$$U_{t2} = u\sin(35.26^\circ) - \left[w\cos(60^\circ) - v\sin(60^\circ)\right]\cos(35.26^\circ) \tag{3.14b}$$

$$U_{t3} = u\sin(35.26^\circ) + w\cos(35.26^\circ). \tag{3.14c}$$

Like Eqn. 3.13, these equations can be easily inverted to yield a series of linear equations giving u, v, and w when the tangential velocities are known.

3.1.2.2 Triple-Sensor Hot-Film Calibration

To calibrate the triple-sensor probe, the voltage vs. velocity response curves must be calculated for all three sensors on the probe. This calibration is done in the same manner as the single-sensor probe calibration, by placing the triple-sensor probe in a flow of known velocity.

By carefully aligning the probe so that its axis is parallel to the bulk flow, all three sensors can be calibrated at the same time. Since each sensor is aligned 35.26° to the calibration jet, the relative tangential and normal components of the velocity over each sensor can be calculated. By using Jorgensen's equation, Eqn. 3.9, the effective velocity seen by each sensor can then be calculated. Each sensor is exposed to a range of effective velocities from 0.5 m/s (the lowest reliable calibration velocity available in the tunnel) up to 15 m/s (slightly above the highest effective velocities anticipated during data collection). By measuring the voltage response of each sensor at a series of different velocities in this range, calibration constants for the approximated hot-

film response, Eqn. 3.2 can be calculated using a least-squares linear curve fit. These curves appear similar to those shown in Figure 3.2. The C program used to calibrate the triple-sensor probe is `pitottriple-cal.c`, included in Appendix C.

3.1.2.3 Triple-Sensor, Hot-Film Temperature Correction

Since the response of each sensor in the triple-sensor probe has a response similar to that of the single-wire probes, the same temperature correction scheme presented in section 3.1.1.3 can be used for the triple-sensor probe.

3.2 Intermittency Calculation

The thermal anemometers used in this study have a sufficiently high frequency response to allow them to follow the high-frequency velocity fluctuations associated with turbulence.

By analyzing the velocity signal provided by the anemometer bridge, the flow can be characterized as either being non-turbulent or turbulent. This quantity for characterization of the signal is called the intermittency, γ, and is defined as the percentage of time the observed flow is turbulent. For this study, we will be investigating the "transitional intermittency"—the intermittency associated with the transition from a laminar to a turbulent boundary layer. By calculating the intermittency at each location in the flow, the onset and length of transition in the flow can be determined. For the current study, the flow is periodically unsteady, and, thus, the onset location and length of transition vary with time. At any given point in the flow, γ will be a function of time.

There exists a wide variety of techniques for calculating intermittencies. Early techniques are described by Townsend (1949) and comprehensive reviews of various intermittency techniques are presented by Hedley and Keller (1974), Narasimha (1985) and Solomon (1996). An ideal intermittency calculation technique meets the following conditions:

1. Due to the large volume of collected data, the system must be automatically applied to the flow data, with a minimal amount of manual intervention.

2. Since many of the flow parameters, such as boundary layer thickness, freestream

velocity, and freestream turbulence level vary with time due to the periodic unsteady nature of the flow, the technique should rely on characteristics of the flow to filter the signal into turbulent and non-turbulent components instead of relying on empirical parameters such as threshold settings, filter coefficients, and user-selected adjustments.

3. The technique must be applicable over a wide range of spatial and temporal pressure gradients and shear wall stresses.

4. The technique should provide some safeguarding against transient short-term false turbulence identification (known as "spiking"), as well as false laminar flow identification (known as "dropouts").

5. The technique must be applicable to single-component anemometry.

The technique selected for this study is the Turbulent Energy Recognition Algorithm (TERA) technique, developed by Falco and Gendrich (1990) and further refined and described by Walker and Solomon (1992) and Solomon (1996). Although developed as a technique for measuring turbulent bursting, the technique was found to be quite useful for the transitional flow data by Solomon. This technique is well-suited to this study, since it meets all of the above criteria except for item 2. The TERA algorithm still requires that the user define a criterion function, $D(t)$, a threshold level, T_r, and a windowing time t_w. Each of these is described below.

Selecting a proper criterion function is essential in discriminating between laminar and turbulent flow. Ideally, a criterion function should represent a feature of the flow particular to turbulence, such as fluctuations in velocity, temperature, vorticity, shear stress, or a combination of these. Keller and Wang (1995) discuss in depth the issue of selecting criterion functions, recommending criterion functions based upon shear stress, such as $(\partial(uv)/\partial t)^2$.

However, for single-component unheated flows, the choice of criterion function is rather limited, since temperature, shear stress, or vorticity measurements are not available. For this study, we selected the criterion function recommended by Falco and Gendrich, $D(t) = |u \cdot \partial u/\partial t|$, as it shows the time rate of change of the streamwise component of turbulent kinetic energy. Use of this criterion function tends to reduce dropouts since for a non-turbulent flow, if $u(t)$ is low then $\partial u/\partial t$ is high (for example,

consider the sinusoidally oscillating flow $u(t) = \sin(t)$, with $^{\partial u}/_{\partial t} = \cos(t)$), and vice versa, reducing smoothing requirements.

The threshold level, T_r, is set such that when $D(t) > T_r$, the flow is turbulent. With the TERA algorithm, the level of T_r is usually set empirically, the only characteristic of the TERA algorithm that cannot be directly determined from flow parameters. Falco and Gendrich recommend choosing the threshold based upon the rms value of the flow signal, such that

$$T_r = C_{T_r} \left(u \frac{\partial u}{\partial t} \right)_{rms} \tag{3.15}$$

By observing sample calculations of γ while varying C_{T_r}, it was found that for the current study a value of $C_{T_r} = 2.75$ seemed to provide the most reliable and stable (i.e. small changes in C_{T_r} wouldn't appreciably affect the resulting intermittency) calculation of intermittency.

The windowing time, t_w, is the time scale used to smooth the raw intermittency scale so that spikes and dropouts are eliminated. Ideally, the windowing time should be chosen to reflect the largest characteristic time scales associated with the largest turbulent eddies present in the boundary layer. This time scale, t_{bl}, can be defined from the boundary layer thickness and freestream velocity,

$$t_{bl} = \frac{\delta}{U_{fs}}. \tag{3.16}$$

Based upon recommendations of Blair (1991), the windowing time was set to be $t_w = 2.5 t_{bl}$.

The basic algorithm for this technique, shown in Table 3.1, is based upon this description.

An example calculation of $\gamma(t)$ is shown in Figure 3.5. The top plot shows the raw velocity signal, $u(t)$. This velocity trace is typical of the data collected in this investigation. The flow starts as a steady, low (2.5% nominal) turbulence flow. Then, as each of the seven wakes created by a single passage of the wake generator passes the sensor, the wake introduces turbulence. Examining the figure, one can clearly see seven packets of turbulence created by the wakes. Following the wakes, the flow again settles to a steady, non-turbulent signal.

Table 3.1: The TERA intermittency detection algorithm, as described by Solomon (1996)

while $(i < n)$ **do**
  if $(D(t) > T_r)$ **then**
    $t_d = (i - i_{end})\Delta t$
    if $(t_d > t_w)$ **then**
      (assume a new event is starting)
      $i_{start} = i$
    else
      (assume this is a continuation of a new event)
      $i_{start} = i_{end}$
    end if
    while (event_continues) **do**
      (calculate the average value of $D(t)$ over the window, $D(t)_{ave}$)
      if $(D(t)_{ave} > T_r)$ or $(D(t) > T_r)$ **then**
        event_continues = true
      else
        $i_{end} = i$
        event_continues = false
      end if
      $i = i + 1$ (next point)
    end while
    $t_d = (i_{start} - i_{end})\Delta t$
    if $(t_d > t_w)$ **then**
      (fill γ with 1s back to i_{start})
      $i_{end} = i$
    else
      (event was too short, ignore)
      $i_{end} = i_{start}$
    end if
  end if
  $i = i + 1$ (next point)
end while

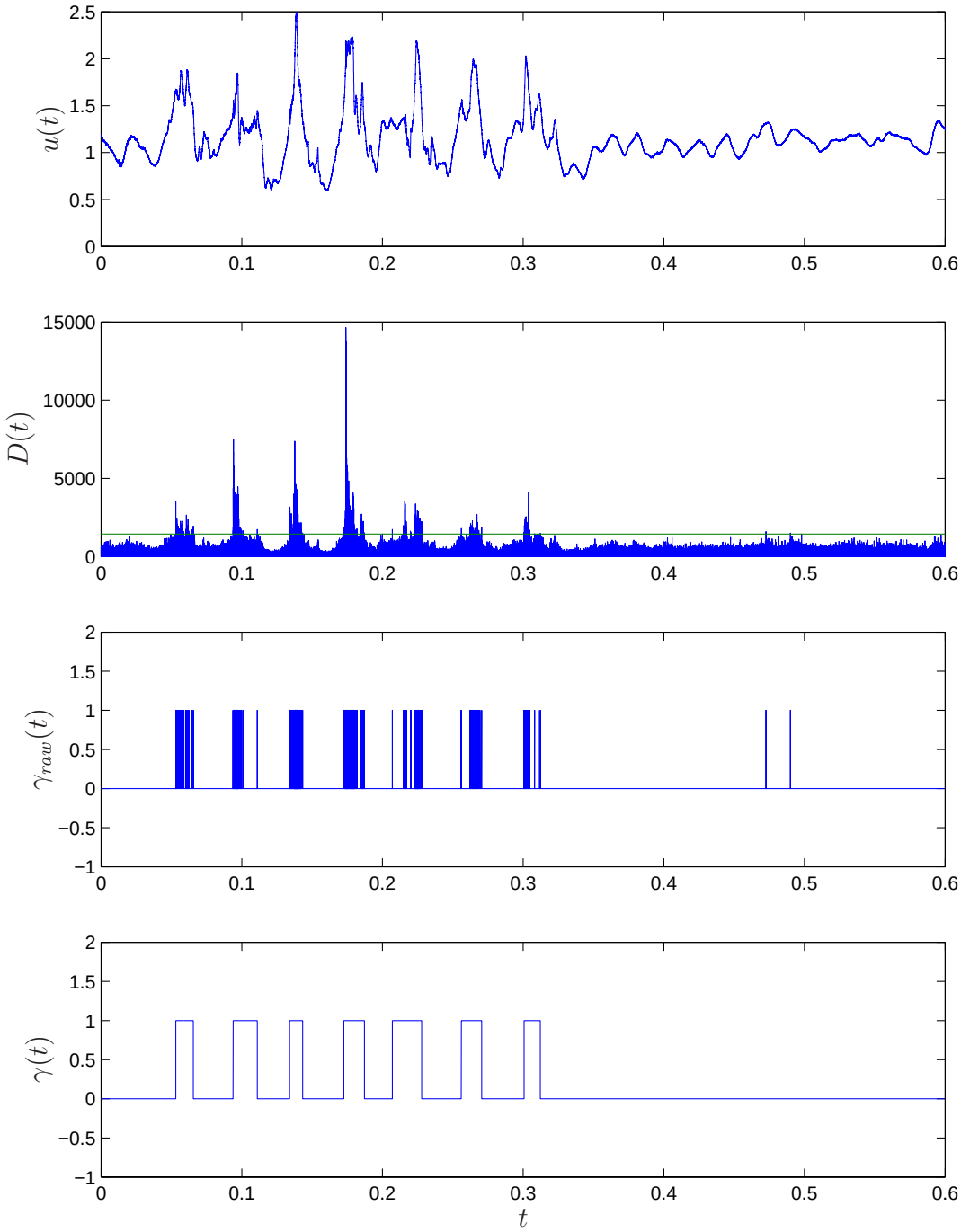

Figure 3.5: Sample intermittency calculation, at $p05$, $y = 0.01\,\text{cm}$, and $FSTI = 2.5\%$, showing the velocity $u(t)$ (top trace), criterion function $D(t)$ (second trace), Raw intermittency $\gamma_{raw}(t)$ (third trace), and smoothed intermittency $\gamma(t)$ (bottom trace)

The second plot shows the intermittency criterion function, $D(t) = |u \cdot {}^{\partial u}/_{\partial t}|$. Also, a line is drawn on the plot showing the threshold value, T_r. Note that for each of the wakes observed in the velocity signal, $D(t)$ shows a distinct peak. The third plot shows all points in the flow where $D(t) > T_r$, producing the "raw intermittency," $\gamma_{raw}(t)$. Note that this signal shows two characteristic problems of many intermittency calculating techniques: multiple "dropouts" of the intermittency in the middle of some of the wakes, as well as two "spikes" of false turbulence occurring in the steady flow.

By applying the algorithm from Table 3.1 with an appropriate windowing time, we can remove the spikes and dropouts and smooth out the signal, resulting in the intermittency trace, $\gamma(t)$, in the fourth plot. Note that each of the regions where $\gamma = 1$ closely matches the portions of the $u(t)$ figure that would qualitatively be identified as turbulent.

It is important to note, however, that it is very difficult to develop an intermittency calculation technique that is able to discern turbulence generated during laminar-to-turbulent transition from high-frequency fluid oscillations resulting from unsteady flow phenomena such as passing wakes or vortex shedding. A result of this difficulties is that, in this flow, the intermittency algorithm used cannot tell the difference between turbulence produced in the boundary layer flow during the transition processes, and the high-frequency oscillations of the wakes.

3.3 Upstream Flow Conditions

3.3.1 Flow Velocity

The flow velocity in the development section was determined by using an Airflow 9020184 telescopic elliptic-nose Pitot-static tube, with the Pitot and static pressures measured with a Dwyer Microtector water-column micromanometer. The flow velocity, U, is given by the relationship

$$U = 4.05\sqrt{\frac{762}{B} \times \frac{T}{293} \times \frac{10,363}{10,363 + P_s} \times P_v} \tag{3.17}$$

where U is the velocity in m/s, B is the barometric pressure in mmHg, T is the absolute temperature in K, P_s is the static pressure in mmH_2O, and P_v is the velocity (or dynamic) pressure in mmH_2O.

3.4 Experimental Conditions

Small corrections were made for approach flow conditions, including pressure, temperature and relative humidity during each experimental run. Since the thermal anemometer calibration is temperature-dependent, it is important to measure the temperature of the developing flow in order to apply the first-order anemometer temperature correction, Eqn. 3.3. This temperature was measured using a calibrated Rosemount Model 1050B Platinum Resistance Temperature Detector (RTD) mounted on the wall of flow development section. This sensor is 1 cm × 1 cm and has a time constant of approximately 4 s. However, since the developing flow is steady and the upstream air temperature is essentially constant, neither the relatively large surface area nor the long time constant of the sensor is of concern.

For a calibrated platinum RTD, temperature is a function of the resistance of the sensor film, given by

$$T = \frac{R_{RTD}/R_0 - 1}{\alpha_{RTD}} + T_0 \tag{3.18}$$

where R_{RTD} is the measured four-wire resistance of the RTD, R_0 is the four-wire resistance of the RTD at T_0, and α_{RTD} is the temperature coefficient of resistance, a scale factor. R_0, T_0, and α_{RTD} are determined by calibration (in this case, provided by the manufacturer). For this experiment, the four-wire resistance of the film is measured using an IEEE-488-controlled Fluke 8840A Multimeter in four-wire mode. Due to the high precision and accuracy of RTD films and the calibrations provided, the uncertainty of these temperature measurements is essentially the uncertainty in measuring the four-wire resistance. For the Fluke 8840A multimeter, this results in an overall uncertainty of 0.02 °C in the developing flow. The C code which implements these calculations is included in `automate2.c` and `speed.c`, in Appendix C.

Similarly, in order to ensure that the inlet velocity Pitot tube measurements are correct, the room pressure must also be measured. The room pressure was measured using a calibrated Setra 470 digital pressure transducer. This sensor measures absolute pressure and is calibrated with an overall uncertainty of less than 0.02%.

Upstream temperature and pressure were continually monitored during data collection, and the appropriate correction factor, Eqn. 3.3, was applied to the anemometer measurements.

3.5 Wake Data Collection Procedure

Due to the large number of instruments and the maintenance requirements of the wake generator, very detailed setup and operating procedures for the wake generator were developed. In order for the reader to understand fully the procedure used to collect the experimental data, the setup and data collection procedures are briefly described.

3.5.1 Setup Procedure

1. The air cylinder linkage and main shaft of the wake generator are lubricated with heavy machine oil.
2. The push-rod and friction wheels of the wake generator are cleaned with alcohol to remove any lubricant residue which may impede operation.
3. The water loop and circulating pump are started, with water circulating until the reservoir comes to a steady temperature.
4. The wind tunnel is started at the nominal operating velocity.
5. The wind tunnel and room are allowed to settle to a steady temperature.
6. The velocity in the flow development section is verified through the use of a Pitot tube.
7. The solenoid valve controlling the air cylinder on the wake generator is closed.
8. Shop air is connected to the solenoid valve.
9. The wake generator motor is turned on and set to the desired operating speed.

3.5.2 Operating Procedure

For each passage of the wake generating sled, seven wakes are generated, one for each rod mounted on the sled. Due to concerns about initial conditions, the first wake from each passage is discarded, yielding 6 wakes per passage. However, during analysis of the data, it was discovered that the last two wakes generated during each passage were also non-representative, since they are located on the end of the wake generation sled and arrive in the turbine passage after the flow is no longer periodic.

Thus, these wakes were discarded as well, leaving a total of 4 wakes per passage. From preliminary results, it was determined that the wake profiles converged for ensembles of 75 or more wakes. For our final data, the wake generator is run for 35 sled passages for each data point. At 4 wakes per passage, this results in a total of 140 wakes for each y station.

As described in section 2.1.2, the wake generator is computer-automated through the use of IEEE-488-capable instrumentation. The procedure used to run the wake generator, which includes error checks to ensure that the data collection process is stopped if any malfunctions occur, is listed in Table 3.2. This procedure was implemented in C using the program `automate2.c` listed in Appendix C.

Table 3.2: The data collection procedure

for (each of 30 y locations) **do**
  (initialize both IOTech ADCs, Fluke DVM, and HP power supply for activating air supply)
  (measure room temperature and pressure)
  (turn off power supply to close air supply)
  (create the directories in which the data will be stored)
  for (each of 35 trials) **do**
    (Measure photogate limit switches to make sure that the wake is in the correct starting position)
    (Exit if photogate states are incorrect)
    (Prepare both IOTech to collect data on external trigger)
    (Turn on power supply to open solenoid, activating wake generator)
    (Data collection on IOTech is triggered by photogate signals)
    (Write photogate and hot-wire voltage traces to file)
    (Measure photogate limit switches to make sure that the wake is in the correct ending position)
    (Exit if photogate states are incorrect)
    (Turn off power supply to close solenoid, resetting wake generator)
    (Move to next y position using the stepper motor)
  end for
end for

3.6 Data Reduction

Unlike the previous studies conducted using this facility, in which the flow was essentially steady, the turbine passage is now subject to periodic wake disturbances.

Thus, in place of the time-averaging techniques used in previous studies, the current results must be analyzed using ensemble averaging techniques.

From the wake generator facility, for each wake we obtain from the digitizer a time record of the velocity measured by the hot wire. By repeatedly running the wake generator, we can collect a series of wakes from which we can calculate the ensemble-average (or "phase-average") velocity, $\tilde{u}(t)$, turbulence intensity, $\widetilde{TI}(t)$, and intermittency, $\tilde{\gamma}(t)$, distributions.

Each wake is represented as a velocity signal over the time range $0 < t < T$, where T is the wake passing period. To non-dimensionalize the results, the ensemble-averaged data are presented as a function of non-dimensionalized time, $0 < t/T < 1$. Since the wake data are periodic in nature, it is sometimes useful to present the data as a function of phase angle, θ, such that over the range $0 < t/T < 1$ the phase will range from $0 < \theta < 360°$.

To calculate the ensemble averages, each wake passing period signal was broken down into 90 segments, each representing 4° of the wake period. The signal was broken down into 4° segments to reduce the computational complexity and increase convergence of the resulting ensemble averages. For each component of the cycle, all $u(t)$ data points from that segment for all 140 wakes were ensemble-averaged together to obtain the ensemble-average velocity $\tilde{u}$. The rms fluctuation of all points in the segment about the ensemble-average velocity $\tilde{u}$ is taken to be the ensemble-average turbulence intensity, $\widetilde{TI}$. Similarly, all $\gamma(t)$ data points from that segment are averaged together to obtain the ensemble-average intermittency, $\tilde{\gamma}$.

The overall computational procedure is shown in Table 3.3. This procedure was implemented in MATLAB. A sample data reduction script, `p09.m`, is listed in Appendix C.

Table 3.3: The data reduction procedure

for (each pressure station) **do**
  for (each y location station) **do**
    for (each sled passage) **do**
      (load photogate data from file)
      (load velocity data from file)
      (calculate the intermittency signal, γ, from the velocity data)
      (apply the near-wall anemometry velocity corrections based upon whether the flow is laminar or turbulent)
      (locate the state changes in the photogate data, identifying the beginning of each wake)
      (separate the velocity and γ into distinct wakes)
    end for
    (ensemble-average the wakes together to obtain the phase-averaged velocity $\tilde{u}(y,t)$, the phase-averaged turbulence intensity $\widetilde{TI}(y,t)$, and the phase-averaged intermittency, $\tilde{\gamma}(y,t)$)
  end for
  (save reduced information to file so that it can be re-plotted without recalculation)
end for

Chapter 4

Documentation of Flow Parameters

4.1 Operating Parameters

This test facility is designed to produce flow conditions simulating a low pressure turbine environment. As discussed in section 2.1, the experimental facility is capable of operating over a large range of inlet parameters. Particularly, the facility can operate with suction surface length Reynolds numbers ranging from $Re_{L_{ss}} = 25{,}000$ to 300,000 and with free-stream turbulence intensities ranging from 0.5 to 10%. However, the wake generator only has an operating speed range corresponding to approximately $Re_{L_{ss}} = 25{,}000$ to 62,500.

Based upon both this constraint and the steady-state experimental results from Qiu (1996), an operating state of $Re_{L_{ss}} = 50{,}000$ with a turbulence intensity of 2.5% was chosen, since this case showed a combination of both separation and boundary layer transition (see Figure 1.2), and serves as an acceptable base for comparison with the steady-state data.

Based upon the turbine passage simulator geometry (Figure 2.12), this operating state corresponds to an axial inlet velocity of nominally $u_x = 3.03\,\mathrm{m/s}$, and a wake generating sled velocity of

$$u_r = 0.7u_x = 2.12\,\mathrm{m/s} \tag{4.1}$$

which corresponds with a wake frequency of 23.184 Hz. With a rod spacing of

91.44 mm and an axial chord length, L_x, of 103.57 mm, this yields a wake Strouhal number, S, of 0.792. The inlet turbulence intensity of 2.5% was achieved by the use of a passive rod grid, as described in section 2.1.1.

4.2 Inlet Flow Conditions

The freestream uniformity of the approach velocity and turbulence level was measured using a series of two single-sensor anemometer surveys of the approach flow: a coarse 2-dimensional survey across the entire flow development section and a detailed 1-dimensional survey along the mid-span plane. Both were taken at the inlet plane, shown as a dashed line on Figure 4.1, located 18.25 cm upstream from the point mid-span between the leading edges. Additionally, a series of surveys with a triple-sensor anemometer was used to document the inlet turbulence parameters.

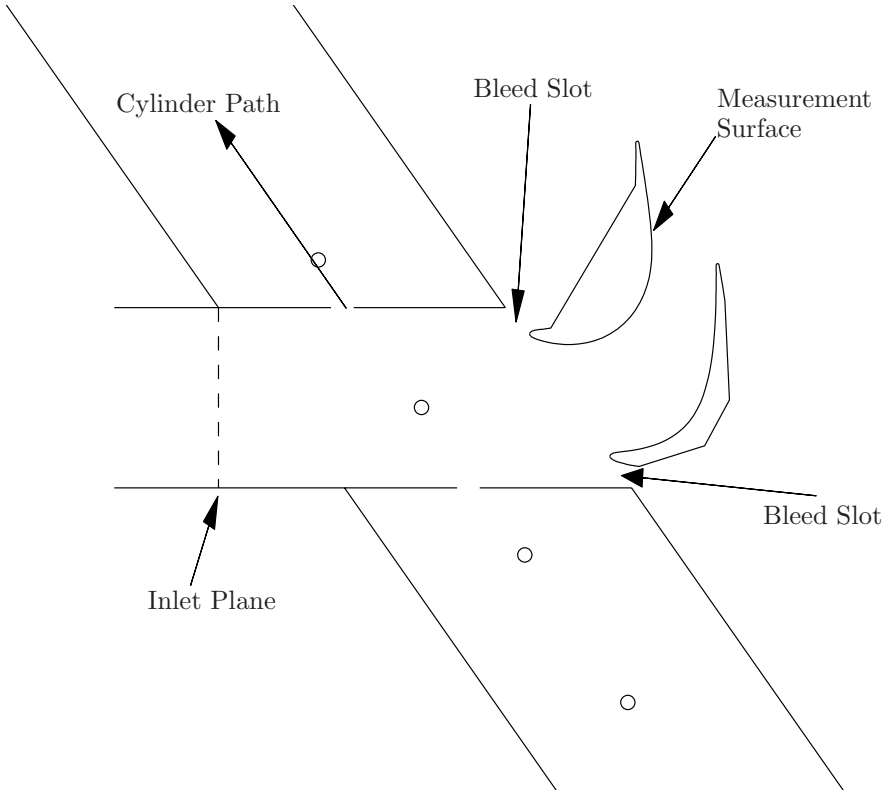

Figure 4.1: Cross-sectional view of the wake generator passage, showing the inlet plane location.

The two-dimensional survey results along the inlet plane are shown in Figure 4.2. The largest deviations in uniformity are due to the side-walls' boundary layers. Examining the velocity distribution, Figure 4.2(a), we can see that the velocity varies between 93.3% and 104.1% of the mean inlet value. However, if we restrict ourselves to the region of interest (between the leading edges), the maximum deviation from the mean velocity drops to less than 4%.

Similarly, Figure 4.2(b) shows the turbulence intensity distribution at the same location. Including the near-wall region, the turbulence intensity ranges from 2.86% in the near center of the channel to over 7.5% in the boundary layer. However, if we restrict ourselves to the region between the leading edges, the flow turbulence intensity is nearly uniform, varying from 3.00% to 3.02%.

To more fully document the upstream flow, a second, high-resolution, 1-D survey is taken of the inlet plane at the z-plane where the boundary layer measurements are taken. These results are shown in Figure 4.3, in which $\bar{u}$ is the time-averaged velocity, and $\overline{\overline{u}}$ is the mean velocity in the channel. The locations of the leading edges of both the pressure surface and suction surface are shown in the figures. Note that the profiles are near-uniform in the region of interest between the leading edges. Also note that, due to slight leakage through the hot-wire access hole, there is some slight error in the pressure side profile data (note the slight scatter in the data), so it may be more desirable to treat the pressure surface half inlet flow as being a mirror image of the suction surface flow. From these plots, we can report a nominal average velocity of 3.03 $^{\mathrm{m}}/_{\mathrm{s}}$, and a turbulence intensity of 3%, which decays to approximately 2.5% by the time the flow reaches the test section leading edge.

From the profile data at the inlet plane, a momentum boundary layer thickness on the side wall upstream of the suction surface of $\theta = 0.1464\,\mathrm{cm}$ was calculated.

4.2.1 Turbulence Quantities

In order to document the turbulent scales upstream of the wake generator, one-dimensional power spectra of u', v', and w' were measured using the triple-sensor anemometer probe described in section 3.1.2. These power spectral measurements were collected at the same location as the single-wire surveys in the previous section, 14.7 cm upstream of the turbine passage inlet. The power spectral measurements were collected by sampling 2,097,152 (2^{21}) data points at 2 kHz (low-pass filtered

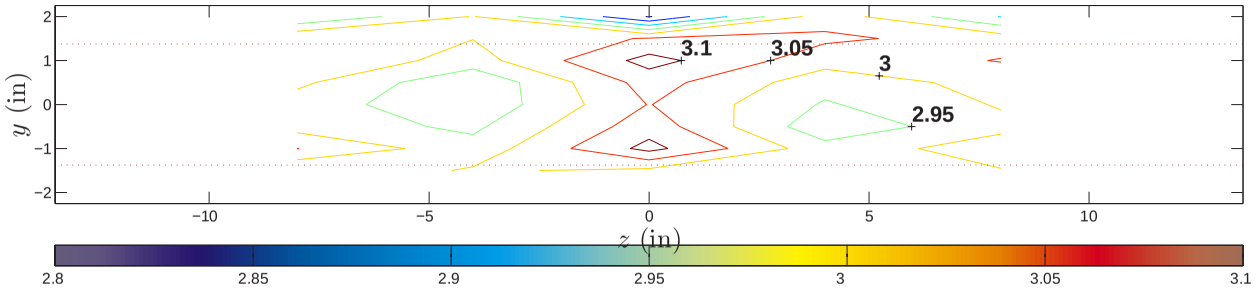

(a) $\bar{u}(y, z)$

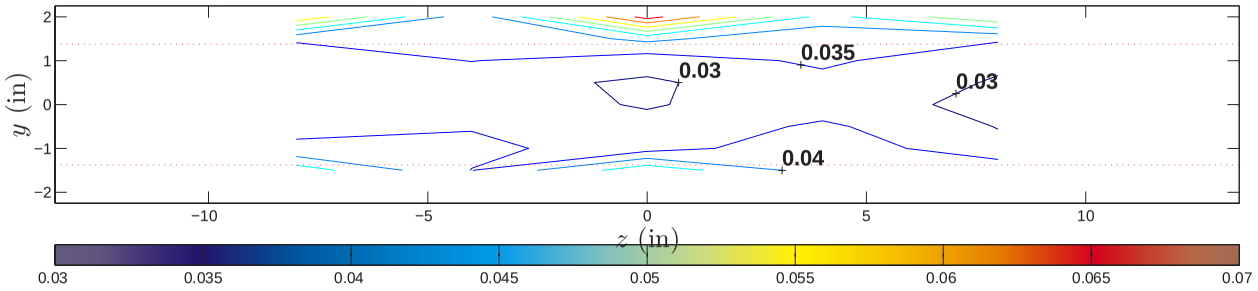

(b) $TI(y, z)$

Figure 4.2: Inlet flow 2-D single-sensor hot-wire survey. The dotted lines indicate the location of the test section airfoil leading edges.

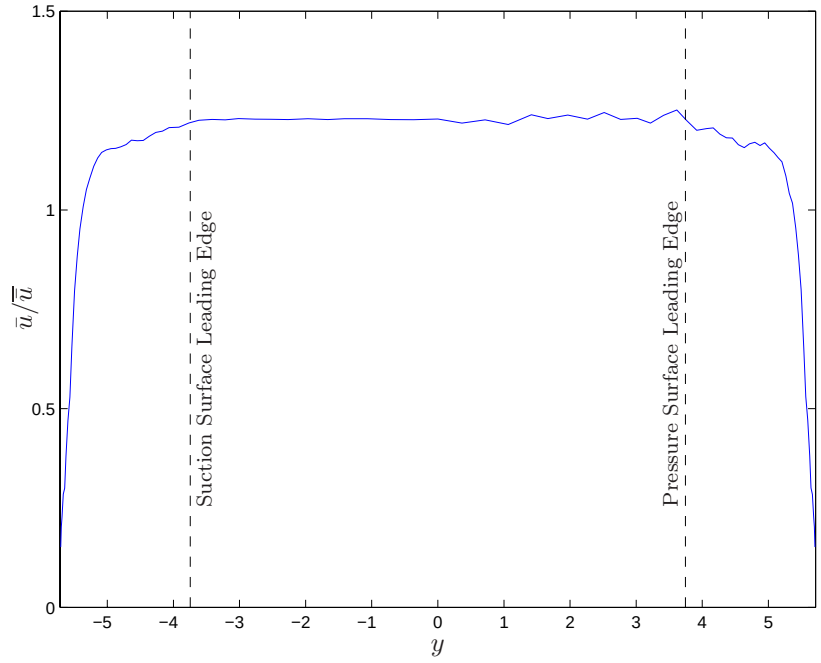

(a) Mean Velocity, $\bar{u}/\overline{\bar{u}}$

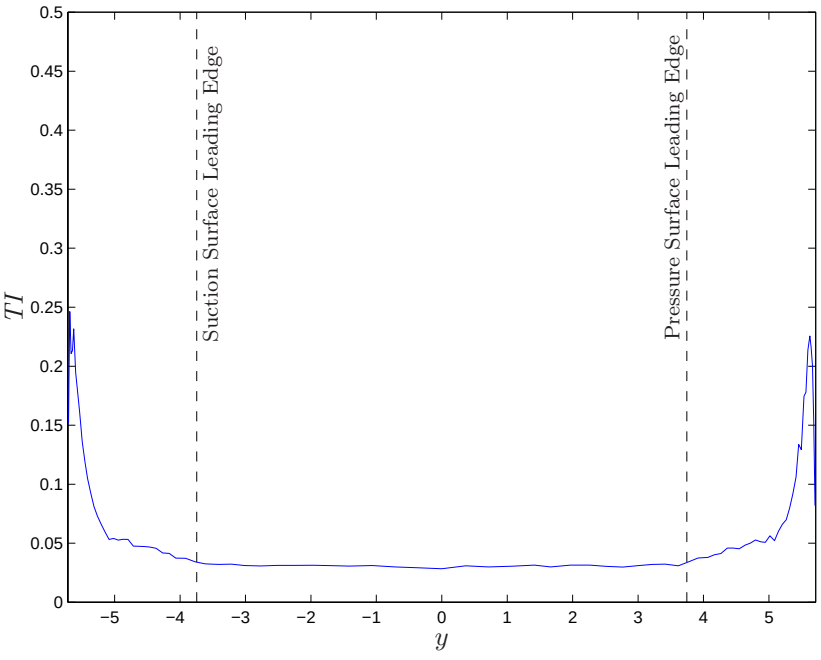

(b) Turbulence Intensity TI

Figure 4.3: Inlet flow velocity and turbulence intensity distributions

at 500 kHz), for a total sampling time of 17.47 minutes. The power spectral distribution were computed using MATLAB, using the script `lengthscale.m` included in Appendix C.

The power spectra are presented in Figure 4.4. In Figure 4.5, they are plotted versus energy coordinates. From these data, the integral length scales of the flow, $\Lambda_{u,x}$, $\Lambda_{v,x}$, and $\Lambda_{w,x}$, can be calculated. Using relations developed by Hinze (1975), the integral length scales can be calculated by extrapolating the PSD values in Figure 4.4 to $f = 0$ and using the following formulas:

$$\Lambda_{u,x} = \frac{\bar{u}E_u(f=0)}{4u'^2_{rms}} \tag{4.2a}$$

$$\Lambda_{v,x} = \frac{\bar{u}E_v(f=0)}{4v'^2_{rms}} \tag{4.2b}$$

$$\Lambda_{w,x} = \frac{\bar{u}E_w(f=0)}{4w'^2_{rms}}. \tag{4.2c}$$

From these results, integral length scales of $\Lambda_{u,x} = 4.44\,\text{cm}$, $\Lambda_{v,x} = 1.21\,\text{cm}$, and $\Lambda_{w,x} = 0.99\,\text{cm}$ were calculated.

For comparison, the integral length scales can also be calculated by using the autocorrelation of the velocity signal. From Hinze:

$$\Lambda_{u,x} = \frac{1}{u'^2_{rms}} \int_0^\infty Q_u(x)dx = \frac{\bar{u}}{u'^2_{rms}} \int_0^\infty Q_u(t)dt = \frac{\bar{u}}{u'^2_{rms}} \sum_{i=1}^{N} Q_{u,i} \tag{4.3}$$

where $Q_{u,i}$, the auto-correlation of u', is calculated using

$$Q_{u,i} = \sum_{j=1}^{N-i} u_j u_{i+j} \Delta t. \tag{4.4}$$

Combining Eqn. 4.3 and Eqn. 4.4, we obtain

$$\Lambda_{u,x} = \frac{\bar{u}\Delta t}{u'^2_{rms}} \sum_{i=1}^{M} \sum_{j=1}^{N-1} u_j u_{i+j} \tag{4.5a}$$

Similarly, equations for $\Lambda_{v,x}$ and $\Lambda_{w,x}$ can be derived:

$$\Lambda_{v,x} = \frac{\bar{u}\Delta t}{{v'^2}_{rms}} \sum_{i=1}^{M} \sum_{j=1}^{N-1} v_j v_{i+j} \tag{4.5b}$$

$$\Lambda_{w,x} = \frac{\bar{u}\Delta t}{{w'^2}_{rms}} \sum_{i=1}^{M} \sum_{j=1}^{N-1} w_j w_{i+j} \tag{4.5c}$$

where N is the number of data points in the signal and M is the number of data points after which the autocorrelation has had its first zero-crossing. Using this technique, integral length scales of $\Lambda_{u,x} = 4.19\,\text{cm}$, $\Lambda_{v,x} = 1.04\,\text{cm}$, and $\Lambda_{w,x} = 1.04\,\text{cm}$ were calculated, reasonably consistent with the PSD-derived values.

Similarly, the spectra in Figure 4.4 can be used to estimate the turbulence dissipation rate, ϵ, by fitting a $-5/3$ sloped line to the power spectrum in the inertial subrange and using the Kolmogoroff spectrum law (Hinze, 1975):

$$E_u(f) = 0.6545\pi^{-2/3}\epsilon^{2/3}(\bar{u})^{2/3}(2f)^{-5/3}. \tag{4.6}$$

yielding a value of ϵ of $0.049\,\text{m}^2/\text{s}^3$.

Also, the dissipation, ϵ can be calculated directly by measuring the turbulent kinetic energy, k, at two streamwise location, simplifying the k-ϵ equations, assuming one-dimensional, isotropic flow:

$$U_{fs}\frac{\partial k}{\partial x} = -\epsilon. \tag{4.7}$$

By measuring k at two locations in the flow which are sufficiently close to assume linearity but sufficiently separated to minimize error, we can estimate $\partial k/\partial x$ using finite differences. Calculating k at the measurement plane used above and at a point 10.16 cm upstream of the measurement plane, we can estimate ϵ to be $0.050\,\text{m}^2/\text{s}^3$, reasonably consistent with our results obtained from the PSD.

Table 4.1: Turbulence quantities for the inlet flow with a suction surface length Reynolds number, $Re_{L_{ss}}$, of 50,000 and $TI = 2.5\%$

Quantity:	**Value:**
Turbulence Length Scale, $\Lambda_{u,x}$ from PSD:	4.44 cm
Turbulence Length Scale, $\Lambda_{v,x}$ from PSD:	1.21 cm
Turbulence Length Scale, $\Lambda_{w,x}$ from PSD:	0.99 cm
Turbulent Dissipation, ϵ, from PSD:	$0.049\,{}^{\mathrm{m}^2}/_{\mathrm{s}^3}$
Energy Length Scale, L_u:	1.25 cm
Taylor Microscale, λ:	5.05 mm

Once calculated, ϵ can then be used to calculate both the energy length scale, L_u, and the Taylor microscale, λ:

$$L_u = 1.5\frac{\left(u'_{rms}\right)^3}{\epsilon} \tag{4.8}$$

$$\lambda = \left(\frac{15\nu u'^2_{rms}}{\epsilon}\right)^{1/2}. \tag{4.9}$$

Using these relations, $\epsilon = 0.049\,{}^{\mathrm{m}^2}/_{\mathrm{s}^3}$, $L_u = 1.25$ cm, and $\lambda = 5.05$ mm. The turbulence quantities of the flow are summarized in Table 4.1

4.3 Pressure Profile

In order to assure that the general flow pattern in this facility matches both the design angle of attack and the steady state studies presented by Qiu (1996), the pressure bleed slots in the facility were adjusted so that at steady state:

1. The incoming flow to the passage stagnates as closely as possible to the leading edge stagnation line at pressure tap p01, to assure the proper angle of attack.

2. The static pressure distribution measured over the 13 pressure taps located on the suction surface matches the pressure distribution of Qiu for the same $Re_{L_{ss}}$ and $FSTI$ as closely as possible.

After the facility's bleed slots were adjusted to correct the angle of attack, the local static pressure was measured at each of the 13 pressure stations. From these measurements, the local pressure coefficient at each station was calculated,

$$C_p = -\frac{P_t - P_s}{P_t - P_{s,exit}} \tag{4.10}$$

where P_t is the total pressure, P_s is the local static pressure, and $P_{s,exit}$ is the static pressure downstream of the test section as computed from $P_{s,inlet}$, the flow exit area to inlet area ratio, and the assumption of inviscid flow. For this calculation, it was assumed that the flow leaves the passage at the blade exit camber angle, β_2.

The measured values of C_p, as well as those reported by Qiu and the High-Re design C_p distribution for the PAK-B airfoil are shown in Figure 4.6. Examining this figure, one sees that the measured C_p distribution for the current study closely matches the C_p distribution reported by Qiu (1996), suggesting that, despite facility modifications, the steady flow through the turbine passage is essentially the same. It is also useful to note that, starting at $x/L_x = 60\%$, the pressure profile begins to vary significantly from the design calculation profile, suggesting that the boundary layer is beginning to rapidly thicken and the flow is beginning to separate. Between this location and $x/L_x = 96\%$, it appears that the flow has separated, possibly re-attaching just before the trailing edge of the airfoil. These results are supported by the velocity profiles presented by Qiu (1996).

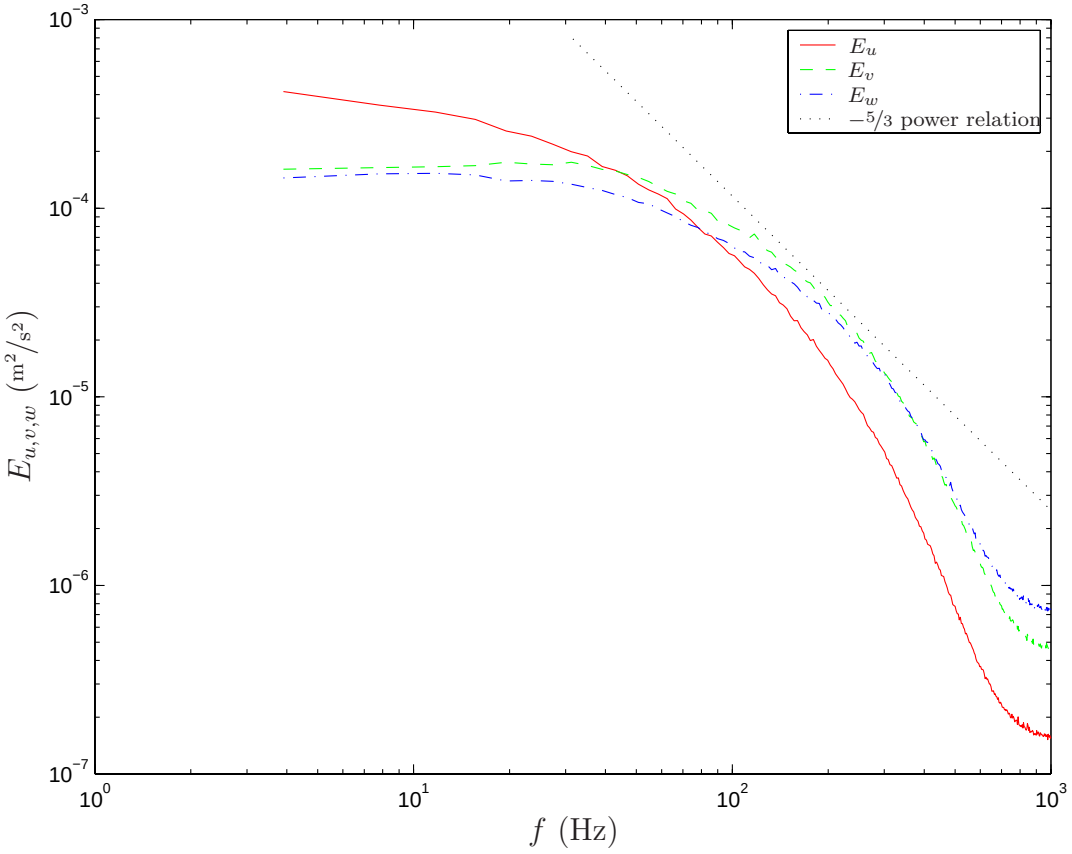

Figure 4.4: Power spectral distributions of turbulence in the x, y, and z directions at the inlet plane.

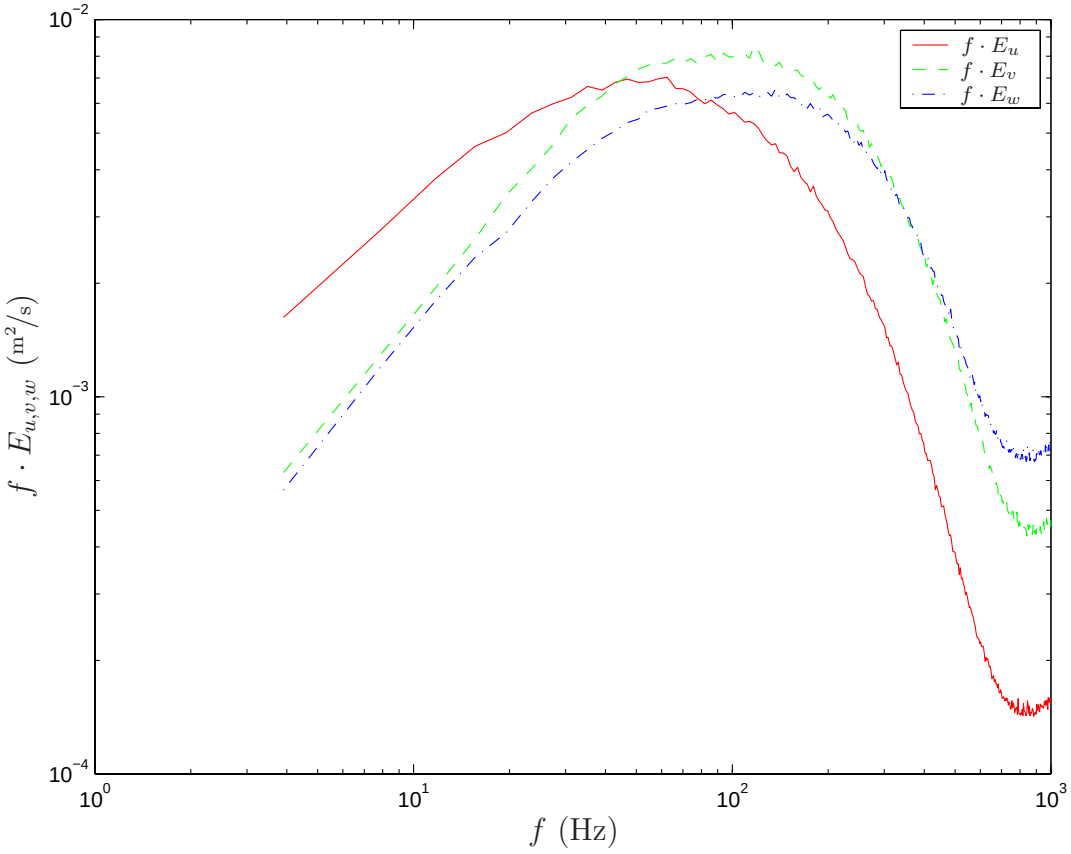

Figure 4.5: Power spectral distributions of turbulence in the x, y, and z directions at the inlet plane, plotted in energy coordinates..

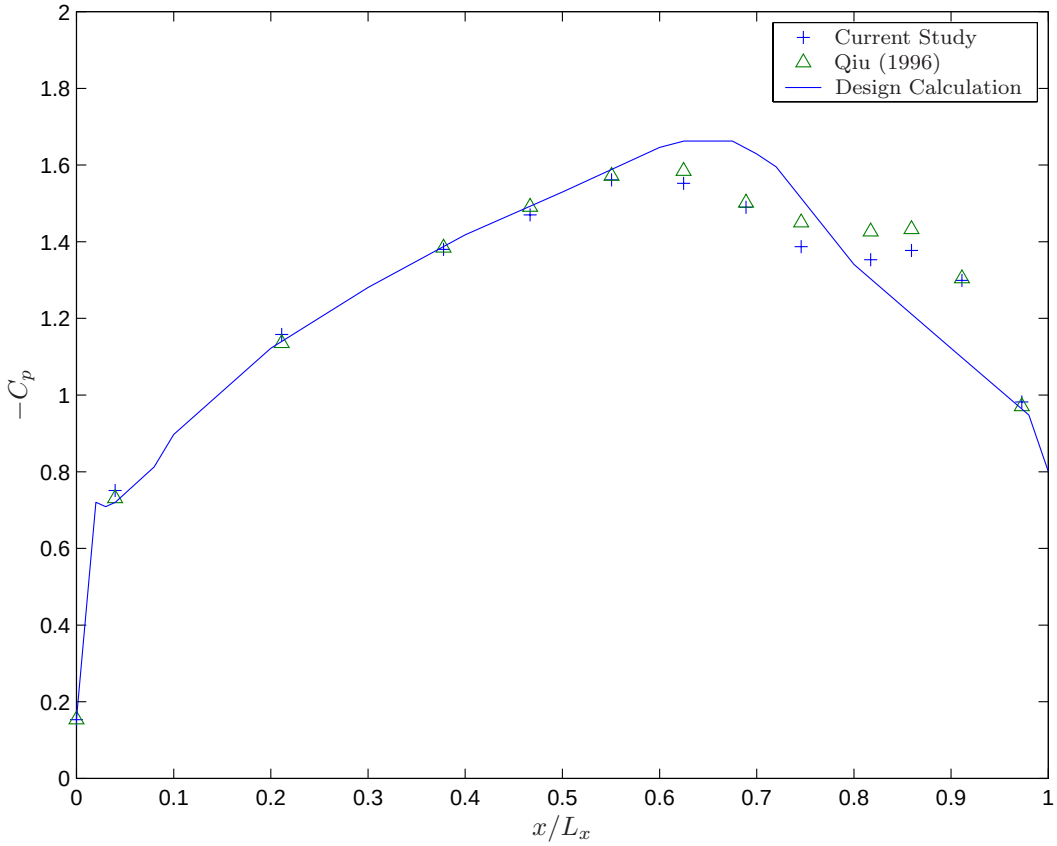

Figure 4.6: Pressure Coefficient Distribution at $Re_{L_{ss}} = 50{,}000$ and $TI = 2.5\%$

Chapter 5

Results and Discussion

The boundary layer profiles are presented in two sections. The first section is devoted to documentation and characterization of the wakes generated by the wake generator. Here, the wakes are compared to those presented by other researchers.

The second section documents the flow in the turbine passage, as affected by the wakes entering from the wake generator. Wall-normal profiles of velocity, rms velocity fluctuation, turbulence intensity, and intermittency are presented. The effects of the wakes upon the flow are presented, with flow transition and separation identified.

5.1 Wake Characterization

The ensemble-average velocity, $\tilde{u}(t)$, and turbulence intensity, $\widetilde{TI}(t)$ of the incoming wakes are shown in Figure 5.1.

These data were collected at the midpoint between the leading edges of the pressure and suction surfaces, and represent the ensemble averages of 600 wakes (4 wakes per sled passage, 150 sled passings). Examining Figure 5.1(a), we see that the minimum velocity of the wake is approximately 87.5% of the average value, which matches the work of Halstead (1996) in which a rotating airfoil stage (simulating a rotating turbine stage) was used to create wake profiles. Examining the turbulence intensity profile (Figure 5.1(b)), however, we see that it peaks at 17.5%, more than twice that reported by Halstead. This may be consistent with Halstead's assertion that rods seem to produce more turbulence than airfoils of the same loss coefficient.

It should be noted, however, that the flows over the airfoils of the Halstead study were not separated and a highly loaded airfoil, such as the one describe here, would be inclined to separate at the lower Reynolds numbers typical of the present case and, thus, the wakes of the present case should contain higher levels and larger scales of turbulence. In the regions between the wakes, the turbulence intensity is approximately 2.5–3%, consistent with the level recommended by Halstead. However, at the streamwise position of the test section, the wakes have begun to merge and the minimum turbulence intensity between wakes has risen to 5% (Figure 5.1(b)).

The wakes from this facility also compare favorably with wakes reported by other researchers. Comparing the wakes in Figures 5.1 with wakes reported by Ou et al. (1994) in Figure 5.2, we can see that the wakes of the present study have approximately the same velocity deficit and peak turbulence intensity values as those reported by Ou et al. for a Reynolds number based on chord length and inlet velocity of $Re_L = 300{,}000$, a turbulence level of $FSTI = 5\%$ and a Strouhal number of $S = 0.1$. The most appreciable difference between the wakes generated in this facility from those presented by Ou et al. is that the present wakes are much broader in time, taking up almost the entire wake period (Figure 5.1(a)). This is, most likely, due to the large difference in Strouhal numbers between the two cases (the current study has $S = 0.792$, while the Strouhal number of the Ou et al. study is $S = 0.1$). The wakes of the present study also show a similar velocity deficit, turbulence level, and general shape as the wakes presented by Murawski et al. (1997) and Dullenkopf et al. (1991).

5.2 Experimental Results

As discussed in section 3.6, due to the periodic unsteady nature of this flow, the results of the experiment are presented as phase-averaged quantities.

The large volume of data produced in this experiment proves to be not only difficult to collect and calculate, but difficult to present, as well. For some types of interpretation, it is useful to plot the data as a function of both the wall-normal distance y and wake phase angle θ (as mentioned previously in section 3.6, the phase angle θ serves as a non-dimensional time, ranging from 0° to 360° over the wake-passing period $0 < t < T$), while for others it is more intuitive to present the data as a series of plots showing the wall-normal profiles at varying values of θ. Thus, all the

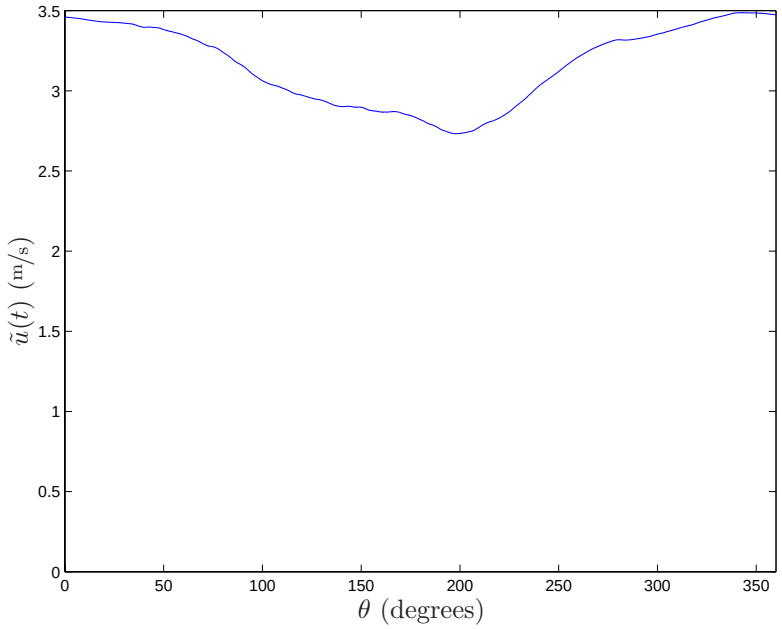

(a) $\tilde{u}(t)$

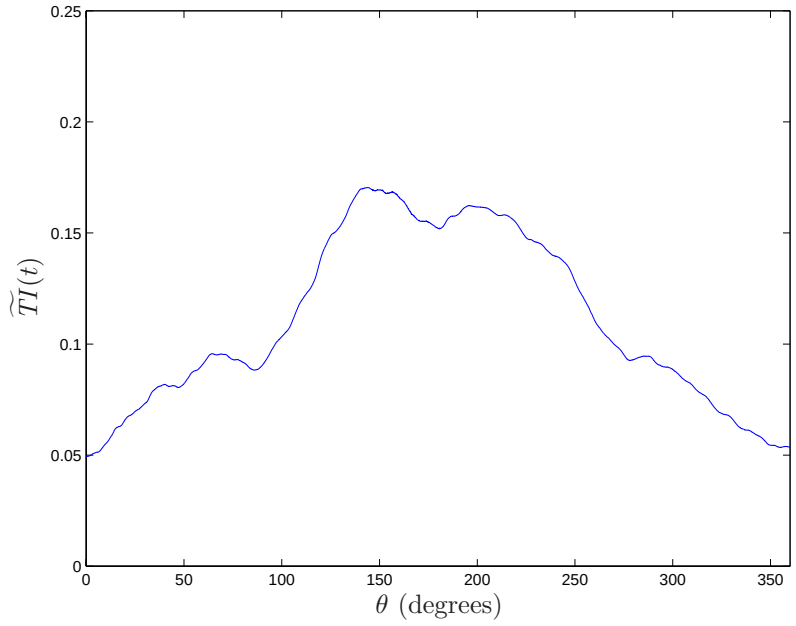

(b) $\widetilde{TI}(t)$

Figure 5.1: Ensemble-average velocity and TI of 600 wakes, taken at the midpoint between the leading edges of the pressure and suction surfaces.

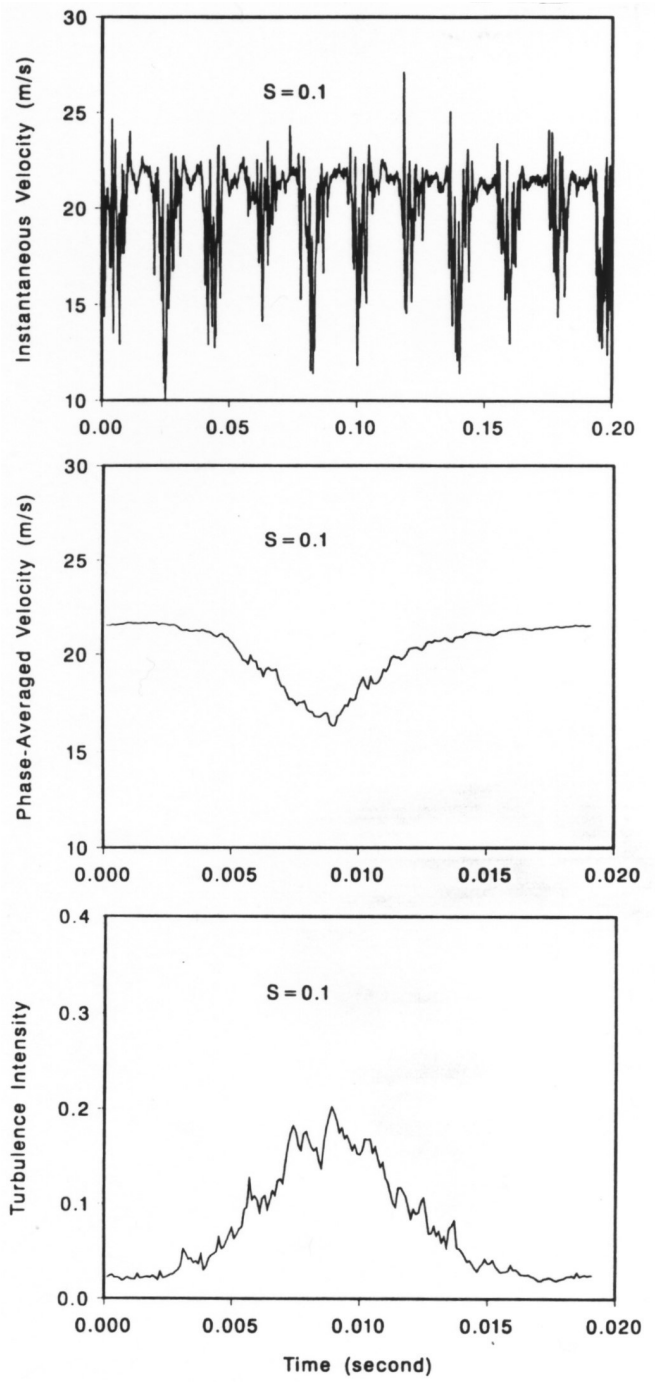

Fig. 7 Typical wake flow profiles for S = 0.1 at Re = 3 × 10^5

Figure 5.2: Wakes reported by Ou et al. (1994)

data are presented in multiple formats. For example, Figures 5.10, 5.14, and 5.18 all present the same data, $\tilde{u}(y,\theta)$, but in three different manners.

Additionally, in wake-disturbed flows, it is common to present results as pseudo-color plots of the data as a function of the suction surface position, s, and the non-dimensional time t/T. Viewing the data in this manner allows the passage of wakes across the blade surface as time passes to be easily visualized. Figures 5.3, 5.4 and 5.5 are examples of this data presentation style.

The data are presented in order of pressure tap number. For each pressure tap, the data are first presented as a series of pseudo-color plots representing the velocity, velocity rms, the turbulence intensity, and the intermittency. Examples of each of these plots are given in Figure 5.10 ($\tilde{u}(y,\theta)$), Figure 5.11 ($\widetilde{u_{rms}}(y,\theta)$), Figure 5.12 ($\widetilde{TI}(y,\theta)$), and Figure 5.13 ($\tilde{\gamma}(y,\theta)$). For each of these figures, the horizontal axis represents a single wake, presented as the phase angle, θ, while the vertical axis represents the wall-normal distance, y. Thus, each figure represents the ensemble average of the series of wakes at a fixed location on the suction surface.

Next, the same data are presented again, with each quantity now represented as a series of plots showing the wall-normal distribution of each quantity at different time intervals. Examples of each of these plots are shown in Figure 5.14 ($\tilde{u}(y,\theta)$), Figure 5.15 ($\widetilde{u_{rms}}(y,\theta)$), Figure 5.16 ($\widetilde{TI}(y,\theta)$), and Figure 5.17 ($\tilde{\gamma}(y,\theta)$). For each of these figures, each set of axes represents the wall-normal distribution of the quantity at a fixed value of θ, with the horizontal axis designating the plotted quantity, and the vertical axis representing the wall-normal distance, y. Unlike the pseudo-color plots, presenting the data in this fashion allows the near-wall values of the data and the overall shape of the boundary layer profiles to be more easily visualized.

Finally, for each pressure tap location, the ensemble-average velocity $\tilde{u}(y,\theta)$ is presented as a series of plots showing the ensemble-average velocity at different values of y. An example of this style of plot is shown in Figure 5.18. For this figure, the horizontal axis represents the phase angle, θ, while the vertical axis represents the velocity, $\tilde{u}(y,\theta)$. The different colors indicate different wall-normal distances. Again, this manner of presentation allows the phase shift between the near-wall and freestream flows to be more easily identified.

The data are presented in this manner for each pressure station, located at the

end of the chapter, starting on page 96. A table summarizing the data presentation is included as Table 5.1. Additionally, visualization animations and this report with higher-resolution versions of the figures an are included, as discussed in Appendix D.

5.2.1 The Pre-Separation Flowfield

In this section, the basic features of the unsteady flowfield are discussed. As mentioned previously, the introduction of wakes into the approach flow greatly disturbs the flow from that of the steady state case. The passage of wakes across the turbine blade suction surface introduces a number of significant flow phenomena:

1. The velocity deficit created by the wake results in an oscillating free-stream velocity component, which adds a temporal acceleration effect to the flow in addition to the spatial acceleration effects resulting from the turbine passage geometry.

2. Similarly, this periodic oscillation in freestream velocity results in the turbine airfoil undergoing a periodic oscillation in its angle of attack; thus, the effective "origin" of boundary layer development at the leading edge moves as a function of time and the pressure distribution over the test surface changes accordingly. However, the nature of the data presented here does not allow us to directly document this effect.

3. The passing of the turbulent wake creates a "turbulent strip" which is convected through the passage, increasing the local turbulence as the wakes passes.

To understand the basic nature of the wakes' effects on the turbine passage flow, plots of $\tilde{u}(s,t)$ and $\widetilde{u_{rms}}(s,t)$ are presented in Figures 5.3 and 5.4, respectively. Examining either of these figures, one sees that the wakes appear as diagonal bands of increased turbulence and reduced velocity going from the lower left to the upper right of the figure—as time passes (t increases), and the wake passes along the surface of the blade (s increases). In Figure 5.3, one observes that as the wake travels along the blade surface, the velocity defect of the wake is clearly visible. Similarly, in Figure 5.4, the high turbulence levels contained in the wake can be seen as diagonal strips of high rms velocity fluctuation. At an early stage of the research project, the distributions of $\tilde{u}$ and $\widetilde{u_{rms}}$ at each location were examined to determine whether

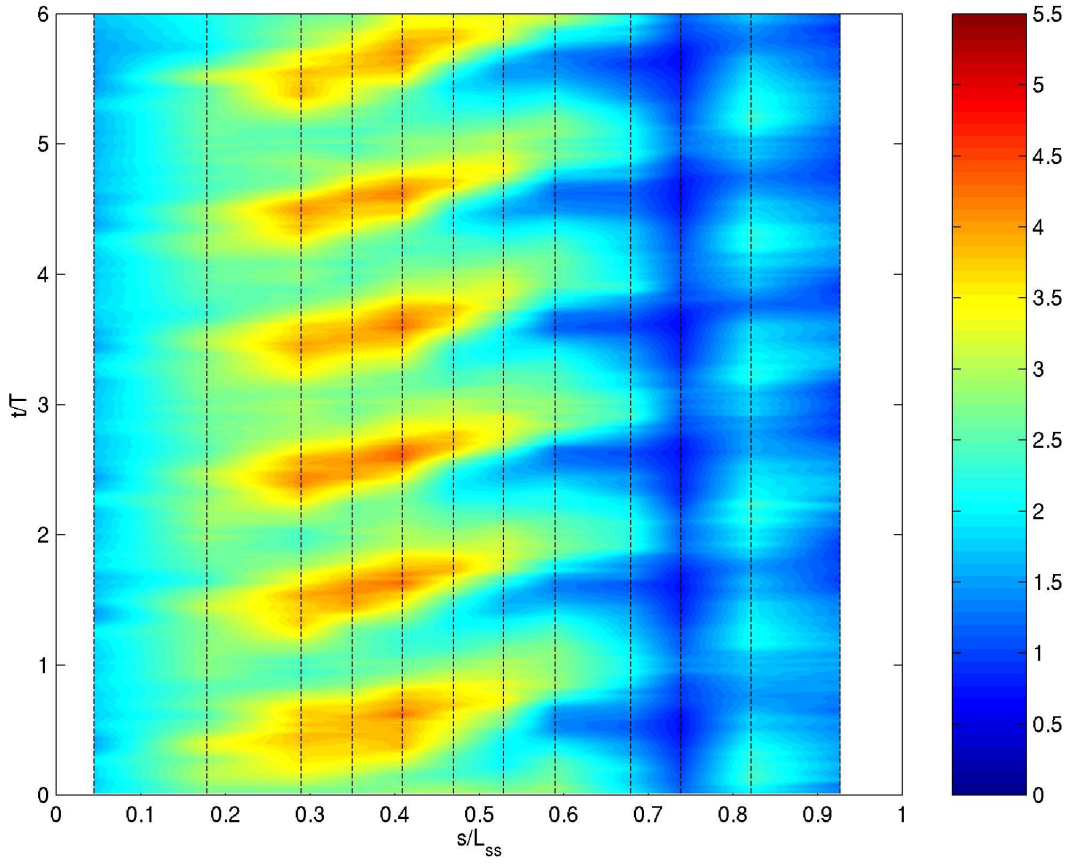

Figure 5.3: Ensemble-average velocity $\tilde{u}$ as a function of suction surface length s and non-dimensional time t/T at $y =$ 0.070 cm. Dashed lines indicate the locations of pressures stations p02 through p13.

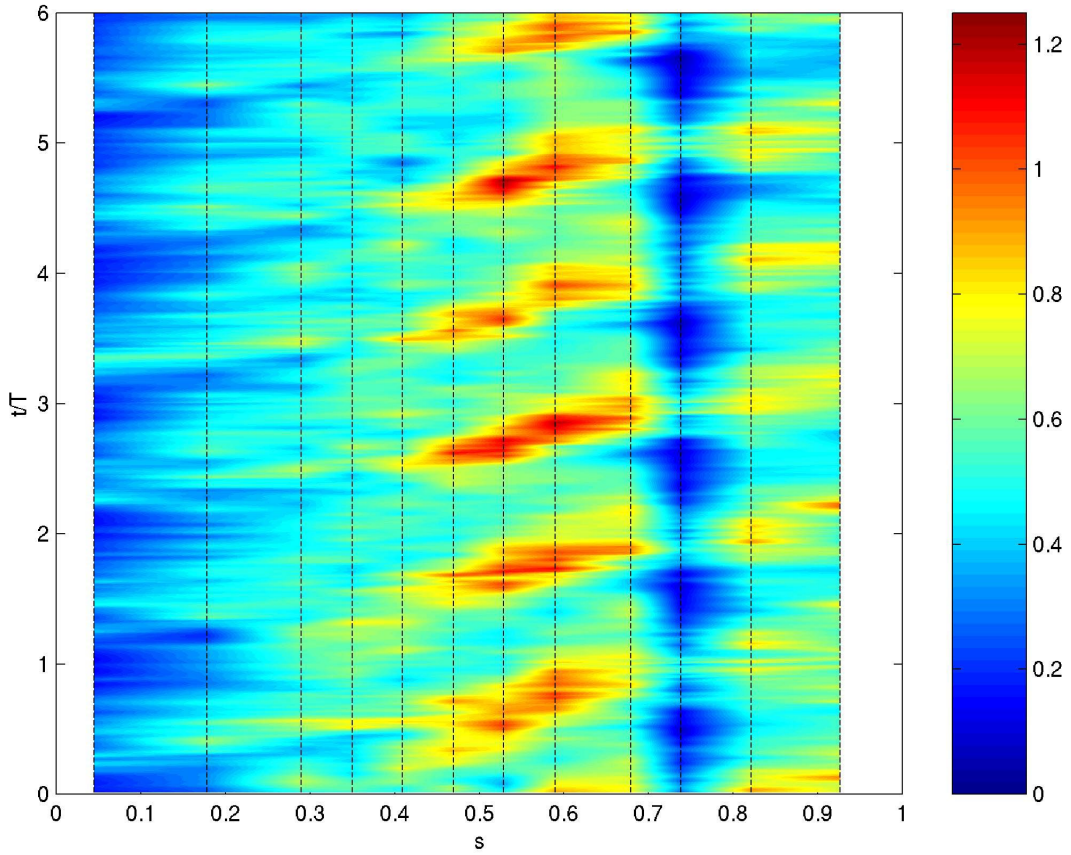

Figure 5.4: Ensemble-average velocity fluctuation $\widetilde{u_{rms}}$ as a function of suction surface length s and non-dimensional time t/T at $y = 0.070\,\text{cm}$. Dashed lines indicate the locations of pressures stations p02 through p13.

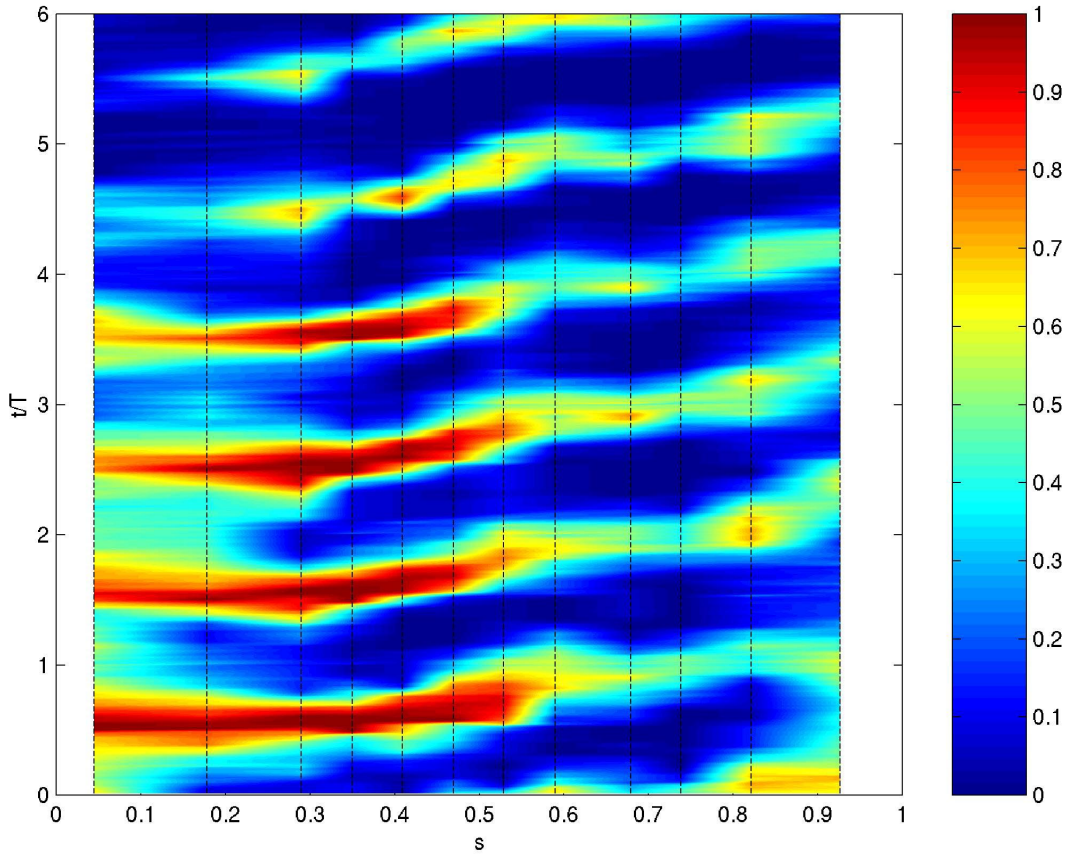

Figure 5.5: Ensemble-average intermittency $\tilde{\gamma}$ as a function of suction surface length s and non-dimensional time t/T at $y = 0.070\,\text{cm}$. Dashed lines indicate the locations of pressures stations p02 through p13.

the wake generator was creating wakes of acceptable repeatability and periodicity. From these preliminary results, it was decided that of the seven wakes generated by each pass of the wake generator, the last six would be used to calculate ensemble averages. This decision was supported by results such as those shown in Figures 5.3 and 5.4. However, once the data were collected and the intermittency profiles were calculated, differences between the early wakes (bars 2 through 5) and later wakes (bars 6 and 7) became apparent. Examining the phase-average intermittency, $\tilde{\gamma}(s,t)$, shown in Figure 5.5, we can see distinct differences between the early wakes and the later wakes, where the later wakes have a remarkably lower intermittency. The explanation for this follow: The distance between the wake generator and the test surface (see Figure 4.1) is sufficiently large that by the time the wakes generated by the last two rods on the wake generation sled arrive at the measurement locations, the upstream channel through which the rods normally pass no longer has any rods passing through it. The wakes generated by each rod represent a significant flow blockage in the channel, reducing mean flow in the channel by $\sim$15%. The loss of acceleration and deceleration associated with this change in mean flow represent a significant change in upstream boundary conditions between the results obtained for the first four wakes and those of the last two wakes shown in Figure 5.5. Turbulence is typically more responsive to the deceleration phase than the acceleration phase. It is hypothesized that this change in upstream conditions results in a sudden withdrawal of the acceleration and deceleration of the flow after the last wake generating rods have left the upstream flow, which causes stabilization of the flow and a concomitant reduction of $\tilde{\gamma}$, as shown in Figure 5.5.

Based upon these observations, the ensemble averaged quantities were recalculated, discarding the last two wakes due to their variation from the other wakes. For the remainder of the figures presented here, the ensemble average values of $\tilde{u}$, $\widetilde{u_{rms}}$, $\widetilde{TI}$, and $\tilde{\gamma}$ were calculated using only the center four wakes from each pass of the sled. For these four wakes, the results showed good periodicity and repeatability.

Since the wake effects are primarily convected by the flow in the turbine passage, the wake propagation speed varies throughout the passage. This is an important property of the flow. Over the test surface, this is seen as an increase in velocity with decreasing y outside of the viscous zone due to wall convex curvature and as a decrease in velocity with decreasing y within the viscous zone. This is shown most clearly when plotting the phase average velocity, $\tilde{u}(y,\theta)$, as a series of slices through

various y values. For example, examine the distribution of $\tilde{u}(y,\theta)$ at p07 (located at $s = 49.33\%$ of the suction surface length), shown in Figure 5.63. In the free-stream, the center of the wake (point of maximum velocity deficit) is located at approximately $\theta = 0°$. However, as we approach the wall, the mean velocity decreases, and thus the wake travels more slowly, arriving at p07 at increasingly large values of θ. The wake is centered at $\theta \approx 140°$. Thus, using convection arguments alone, one can expect a distinct time lag between the occurrences of events in the free-stream flow and the corresponding events occurring in the near-wall region. This is consistent with the flat plate boundary layer results of Lou and Hourmouziadis (2000), in which the temporal location of the wakes were phase-shifted with respect to the wake activity in the free-stream flow.

Examining Figure 5.63 further, we can see also that, for the Strouhal number studied here ($S = 0.792$), by the time the wake has traveled from the wake generator to the suction surface, the wakes are no longer distinct—the flow has not had a chance to fully recover from one wake before the next wake arrives. Examining the freestream velocity flow in either Figure 5.55 or 5.63, we can see that from approximately $y =$ 0.6 cm to the freestream, the flow has essentially become sinusoidally oscillating. This is quite an interesting feature of the flow, because it suggests comparison between the turbulent wakes presented here, and the low-turbulence oscillating flows presented by Lou and Hourmouziadis (2000) on a plate and the profiles presented by Qiu (1996) in a pipe. These comparisons will be discussed in section 5.2.2.

Examining these same data as plotted in Figure 5.55, we can see another time lag between the freestream flow and the near-wall region flow. For example, examining Figures 5.55, 5.59 and 5.63, we can see that the freestream flow accelerates from $\theta = 8°$ to approximately $\theta = 192°$, and then begins to decelerate at $\theta = 200°$. However, examining the same figure, the thickening of the boundary layer due to the deceleration of the free-stream flow doesn't commence until approximately $\theta = 275°$. Similarly, as the flow accelerates, starting at approximately $\theta = 8°$, the boundary layer thickness doesn't respond by thinning until approximately $\theta = 120°$. This lag between acceleration and the integrated response of the boundary layer is well documented. This is discussed for spatial acceleration for turbulent boundary layer flows in Chapter 11 of Kays and Crawford (1993).

This phase difference between changes in the free-stream flow and the near-wall flow's response to these changes occurs due to the boundary layer requiring time to respond to changes in freestream conditions. It is affected by the difference in wake propagation speed between the freestream and near-wall regions. This is an important observation since it means that at any given moment, an instantaneous "snapshot" of a phase-averaged velocity profile doesn't necessarily give a good representation of the flow behavior. Thus, integral parameters, such as the momentum thickness, energy thickness, or displacement thickness give an indication of the integrated effects, but do not give a full representation of the state of the near-wall flow. At any given moment, the near-wall flow is retarded in time from the free-stream flow and has not yet had a chance to respond to the changing free-stream conditions. Thus, transition models based upon quantities such as the momentum thickness Reynolds number at transition, Re_{θ_t}, may not perform so well in a wake-disturbed flow, such as in the present study, as they do for steady flow. Additional consideration is needed to address these effects.

The results from station p07 also allow the identification of some interesting features of the turbulence distribution in the flow. At any given point in the flow, the turbulence level can result from a number of sources: (1) turbulence convected in from upstream, (2) turbulence generation due to boundary layer transition, (3) turbulence generated due to passage of the wake's "turbulent strip", and (4) turbulence generation due to other mechanisms, such as shear layer transition. Examining the intermittency, Figure 5.58, we can clearly see the "turbulent strip" generated from the wake generator, shown by the high values of $\tilde{\gamma}(y,\theta)$ in the range $130^\circ < \theta < 300^\circ$ at $y = 1.65\,\text{cm}$. However, in the near wall region, the high intermittency values associated with the wake don't appear until $\theta \approx 250^\circ$ at $y = 0.07\,\text{cm}$. While it is natural to assume that this time delay is a result of the difference in wake propagation times between the free-stream flow and the near-wall flow, an examination of the intermittency distributions from earlier pressure stations (Figures 5.22 and 5.31) shows that the turbulent strip from the wake doesn't penetrate much into the near-wall boundary layer. Instead, in the corresponding $\widetilde{u_{rms}}(y,t)$ distribution (Figure 5.56), it appears that a region of high velocity fluctuation occurs, peaking at approximately $y = 0.07\,\text{cm}$ between $100^\circ < \theta < 275^\circ$, concurrent with the turbulent strip appearing overhead. This region of high rms velocity fluctuation starts to dissipate just as the turbulent intermittency in Figure 5.58 begins to climb. Thus, in the portion of

the flow preceding separation, it appears that the turbulent strip in the free-stream flow introduces fluctuations in the boundary layer beneath it, producing a region of highly unsteady flow (high $\widetilde{u_{rms}}$). This unsteadiness eventually causes the flow to transition to turbulence, resulting in the turbulent strip seen in the near-wall region in Figure 5.58, from $250° < \theta < 300°$. Then, as the turbulent strip passes and the flow begins to accelerate, the boundary layer flow returns to laminar flow ($\theta > 300°$). A similar pattern of intermittencies and velocity fluctuations can be observed at the other pre-separation locations (stations p02 through p06).

This supports the theories presented by Johnson and Ercan (1996) and Mayle and Schulz (1997), who both hypothesized that the location of turbulent spot generation (and hence the onset point of transition) is influenced primarily by pressure oscillations in the free-stream flow. However, it is important to note that there is a short time delay between when the flow is first affected by the turbulent strip passage and when the flow begins to undergo transition, an effect not captured by the models of either Johnson and Ercan or Mayle and Schulz. This suggests that before the flow can begin to transition into turbulence and turbulence spots can begin to form and grow, the flow must undergo an amplification process in which the rms velocity fluctuation begins to increase. This is akin to normal (non-bypass) transition of a boundary layer, in which the first instabilities present in the boundary layer (before the appearance of T-S waves) must undergo a process of slow amplification before higher-order modes of instability begin to affect the flow. The difference here, beside the higher turbulence levels, is the presence of a destabilizing, adverse gradient due to deceleration during the time.

The discussion so far has focused entirely upon wall-normal surveys at p07. However, an examination of the distributions of $\tilde{u}(y,\theta)$, $\widetilde{u_{rms}}(y,\theta)$, $\widetilde{TI}(y,\theta)$, and $\tilde{\gamma}(y,\theta)$ for pressure stations p02 through p08 (Figures 5.10 through 5.72) show essentially the same flow properties as at p07 (it is important to mention, however, that the profiles at p02 and p03 were taken with a straight hot-wire probe instead of a boundary layer probe due to geometry restrictions, and have a much higher uncertainty in the wall-normal position y, perhaps as high as 0.025 cm). From stations p04 to p08, we can see that, as expected, the boundary layer thickens significantly (see Figures 5.28, 5.37, 5.55, and 5.64, in order). Examining the rms velocity fluctuation and intermittency profiles for stations p02 to p08, we see similar results to those shown for p07—the turbulent strip generated by the wakes (high $\tilde{\gamma}$ values in the free-stream flow) induces

some fluctuations in the near-wall boundary layer (high $\widetilde{u_{rms}}$ occurring over the same θ range as for the freestream turbulent strip), which develop and eventually trigger transition to turbulence in the near-wall boundary layer (as evidenced by the large $\tilde{\gamma}$ values in the near-wall region occurring soon after the large region of $\widetilde{u_{rms}}$ and laminar near-wall flow for the portions of the wake-passing period during which the wake is not present in the external flow).

5.2.2 Separating Flow

At lower (cruise) Reynolds numbers, LP turbine flows are subject to separation. For example, the steady state results reported by Qiu and Simon (1997) and Simon et al. (2000) (see Figure 1.2) for $Re_{L_{ss}} = 50{,}000$ and $FSTI = 2.5\%$ indicate that under these conditions, the boundary layer separates from the suction surface at approximately 50% of the suction surface length (between stations p07 and p08). Although the introduction of wakes into this flow greatly changes the flow turbulence and instantaneous pressure gradients, it is still reasonable to expect the flow to separate.

The distribution of phase-average velocity, $\tilde{u}(y,t)$ at p10 is shown in Figure 5.86. In general, the boundary layer behavior is similar to that shown for p07, with the oscillating freestream velocity inducing a thinning, then thickening of the near-wall boundary layer. However, unlike the p07 profiles shown earlier, there is strong evidence of separation of the flow at this location. Examining the figure, we see normal turbulent boundary layer profiles, initially ($0° < \theta < 100°$). Unlike the upstream pressure stations p02 through p08, in which the flow merely thickens and thins in response to the velocity oscillations of the free-stream flow, as the wake arrives at p10, deceleration due to the wake passing destabilizes the flow to the point that the profile becomes inflectional and the flow separates from the wall (starting at $\theta = 168°$). The wake passes this station and the flow begins to accelerate and restabilize until it reattaches (at $\theta = 312°$). Similar results are seen at stations p09 through p13. These observations are consistent with Lou and Hourmouziadis (2000), who noted similar oscillations in the location and length of separation as a function of phase angle.

This separation can be observed also by looking at the s-t plot of $\widetilde{u_{rms}}(s,t)$ at $y = 0.07\,\text{cm}$, shown in Figure 5.4. From $s = 0.4$ to 0.7, we can see the regions of high rms velocity fluctuation induced by the passage of the wakes' turbulent strips, as

discussed in section 5.2.1. However, starting at approximately $s = 0.6$, we see a sharp drop in the level of rms velocity fluctuation, directly corresponding to the regions of separated flow seen at pressure stations p09 through p11 ($s = 0.53$ to 0.75). This drop in rms velocity fluctuation is due to the detachment of the boundary layer, which is now flowing over the separation bubble. This is supported by the shear stress plots to be introduced in Section 5.2.3.

By the time the flow reaches p12 and p13, the boundary layer has grown significantly due to upstream flow separation. Due to the very high turbulence levels ($TI > 40\%$ in Figure 5.106), the near-wall ($y < 0.5\,\text{cm}$) data at these locations are not accurate, due to unacceptably high hot-wire uncertainties. Turbulence levels in the high range of this figure may be somewhat higher than indicated. Examining Figures 5.104 and 5.113, we can see that, like the steady-state results of Qiu, the wake-disturbed boundary layer shows evidence of attached flow throughout the wake passage period, and thus, reattachment of the flow between the wakes on the suction surface at pressure stations p12 and p13 (compare the near-wall profiles of $\tilde{u}$ in Figures 5.95 (p11), 5.104 (p12), and 5.113 (p13)).

Examining the distributions of $\widetilde{u_{rms}}$ and $\tilde{\gamma}$ at stations p09 through p13 (seen in Figures 5.74, 5.83, 5.92, 5.101, 5.110, 5.76, 5.85, 5.94, 5.103, and 5.112), we can see the same interrelation between the passage of the turbulent strip and near-wall transition: the turbulent strips generated by the wakes induce some instabilities in the near-wall boundary layer, which eventually trigger transition to turbulence in the near-wall boundary layer. However, if we examine the profiles of $\widetilde{u_{rms}}$ and $\tilde{\gamma}$ carefully, we can see some differences from the pre-separational flow. Since the flow has separated from the wall over p09 through p11, the near-wall portion of the boundary layer has effectively become a shear layer, which is more susceptible to disturbances from the free-stream than was the attached boundary layer. As a result, the passage of the turbulent strip generates larger fluctuations in velocity than it did in the pre-separation flow (compare the size of the high $\widetilde{u_{rms}}$ regions in the pre-separation flow in Figure 5.56 to the post-separation flow in Figure 5.83). Likewise, the shear layer's increased sensitivity to disturbances results also in a faster transition to turbulence. This can be by comparing the lag in intermittency between the wake flow and the near-wall flow at station p07 (Figure 5.58) and the lag at station p10 (Figure 5.85).

5.2.3 Shear Stress Measurements

From the near-wall distributions of the ensemble-average velocity, $\tilde{u}(y,\theta)$, we can calculate an estimate of the wall shear stress on the suction surface. The first three points on the ensemble-average wall-normal velocity profile are used to spline-fit a near-wall, $\tilde{u}(y)$ profile which is extrapolated to the wall to produce a wall shear stress value of

$$\tau_w = \mu \left. \frac{\partial u}{\partial y} \right|_{y=0} . \tag{5.1}$$

These results are presented in Figure 5.6. Examining the figure, we can see evidence of separation as an abrupt drop-off in surface shear stress, ranging from $s/L_{ss} \approx 0.5$ to $s/L_{ss} \approx 0.7$ as the wakes passes. However, these data must be used with caution, since the uncertainties in the measurements are quite high ($\sim 30\%$) in some of the more severe locations. Additionally, the use of hot-wire anemometry to measure velocities means that for high-TI and reversing flow, the measured velocity (and hence the calculated shear stress) can be incorrect. We will be able to identify regions of low wall shear stress but we cannot measure the directions or magnitudes of near-zero values with accuracy. Finally, previous measurements in the steady flow (Simon et al., 2000) showed that separation and reattachment points taken from such shear stress distribution maps which were computed from near-wall flow velocities differed, somewhat, from separation and reattachment points taken directly from surface shear stress direction measurements. Ideally, the location of separation should be determined using surface measurement techniques, such as surface-mounted hot films. The development of techniques applicable under unsteady flow conditions is underway.

5.3 Discussion

It is also useful to compare the results presented here with the wake-disturbed flows reported by other researchers. Figure 5.7 shows the distribution of intermittency (obtained from surface-mounted hot-film sensors) in s-t coordinates presented by Solomon (1996), while Figure 5.8 shows intermittencies from the present study calculated at the y-location closest to the wall, $y = 0.01\,\text{cm}$. While the studies are conducted at different $Re_{L_{ss}}$ ($\sim$86,000 for Solomon vs. 50,000 for the present study),

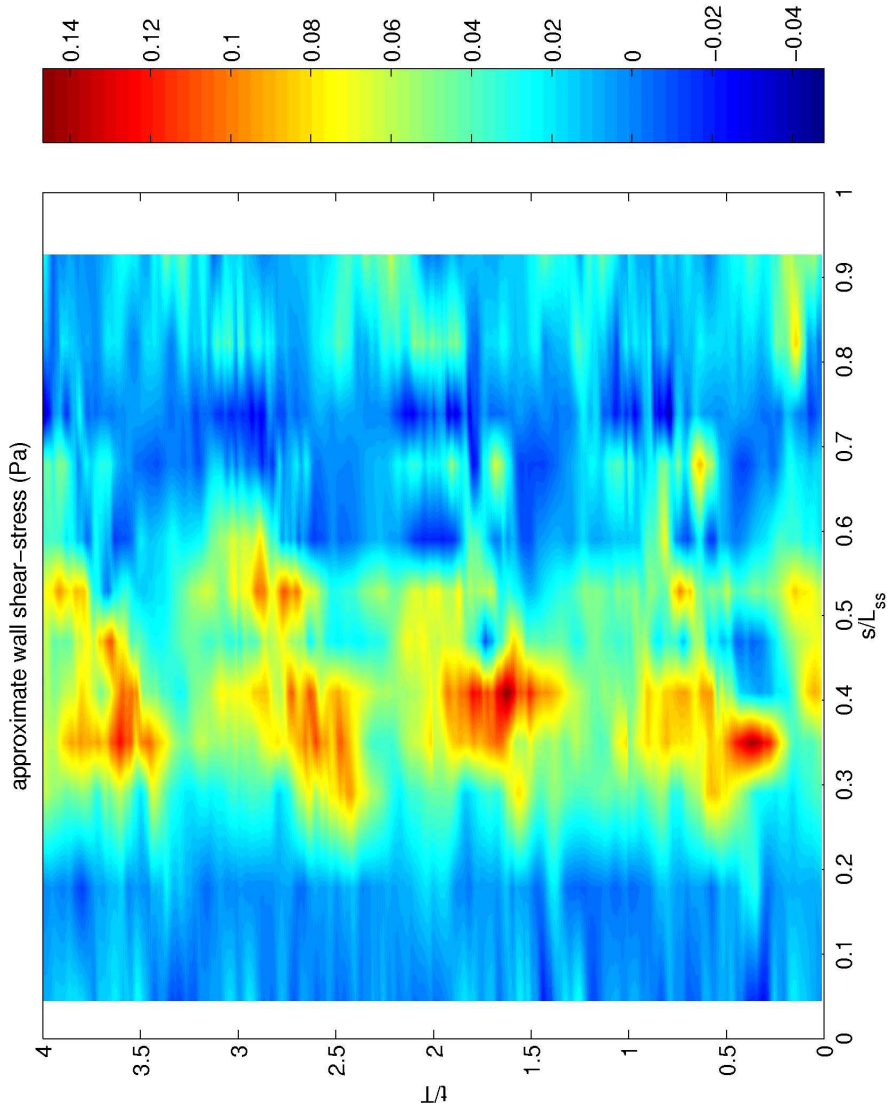

Figure 5.6: Approximate wall shear stress obtained from the ensemble-averaged velocity profiles.

both show the passage of turbulent wakes from the leading edge to trailing edge (the reader is cautioned that the scales of the figures are significantly different). However, the observed profiles show some differences. The most significant difference between the results is that while Figure 5.8 shows high intermittency values, Figure 5.7 shows near-zero intermittencies until around $s = 0.3$. This has a number of likely causes. The first cause may be the difference in y-planes at which the data are presented—the results of Solomon are from surface measurements, while Figure 5.8 is located further away from the wall, at $y = 0.01$ cm. Especially at the locations closest to the leading edge, the boundary layer is very thin and slight differences in wall-normal distance can have a significant impact on results. Also, the surface-mounted hot-films will be restrained by the wall thermal inertia and are therefore not inclined to display the high frequencies associated with the intermittency function threshold.

This difference between the two may also be a result of the different intermittency strategies used to calculate these results. The results of Solomon were calculated using a Peak-Valley-Counting method with surface mounted hot-films, and, hence, are calculated from the quasi-shear stress at the wall, while the results of Figure 5.8 are calculated directly from velocity data. Finally, any intermittency-detection scheme is susceptible to the identification of highly disturbed unsteady (but non-turbulent) flow as "turbulent." Clearly, the disturbance levels carried by the wake are interpreted to be turbulence with the present scheme. For the results presented here, the "intermittency" identified near the leading edge in Figure 5.9 may simply be high-frequency or small-scale vorticity, which creates high-level, high-frequency velocity fluctuations as the wakes tend to wrap around the leading edge, and pass. This stretching of the wake around the leading edge is shown by Wu and Durbin (2000a) in Figure 1.1.

Additionally, the results differ due to separation of flow from the surface in the present study, starting at approximate $s = 0.50$, as noted in section 5.2.2. The results presented by Solomon, as well as similar results presented by Halstead (1996), do not indicate evidence of separation. However, due to the relatively low turbulence intensity, and low $Re_{L_{ss}}$ of the present flow, the boundary layer is rather susceptible to separation. Based upon his work, Halstead determined a theoretical process for describing transition in LP turbines when the flow remains attached (Figure 5.9). The blade geometry and $Re_{L_{ss}}$ used by Halstead are different from the present study—the blade curvature in the Halstead study is weaker, the Reynolds numbers are significantly higher $Re_{L_{ss}} > 120{,}000$, and the flow did not separate. Nevertheless, some

comparisons between the two cases can be made. Referring back to Figure 5.4, we can see for the current study that while in the pre-separational portion of the flow ($s < 0.5$), the rms fluctuations show a similar distribution to those suggested by Halstead. The flow separates, however, before either any significant calming of the flow by acceleration or between-wake boundary layer growth or transition can be observed. Thus, a study similar to the present one, but with a less aggressive blade curvature, higher $Re_{L_{ss}}$, or higher $FSTI$ to decrease the likelihood of separation would provide much better comparisons with the Halstead or Solomon data.

Conclusions from this data set are summarized in Chapter 6 (p. 180) which follows the figures discussed above.

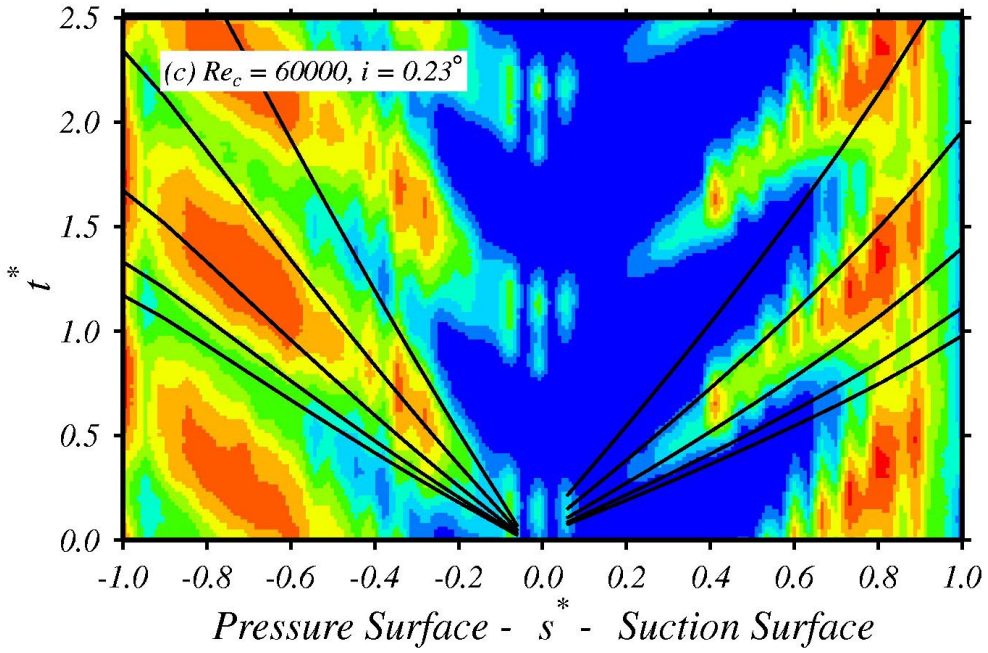

Figure 5.7: s-t plot of ensemble average intermittency from Solomon (1996). s^* is equivalent to s/L_{ss} used in the current study, and t^* is equivalent to t/T.

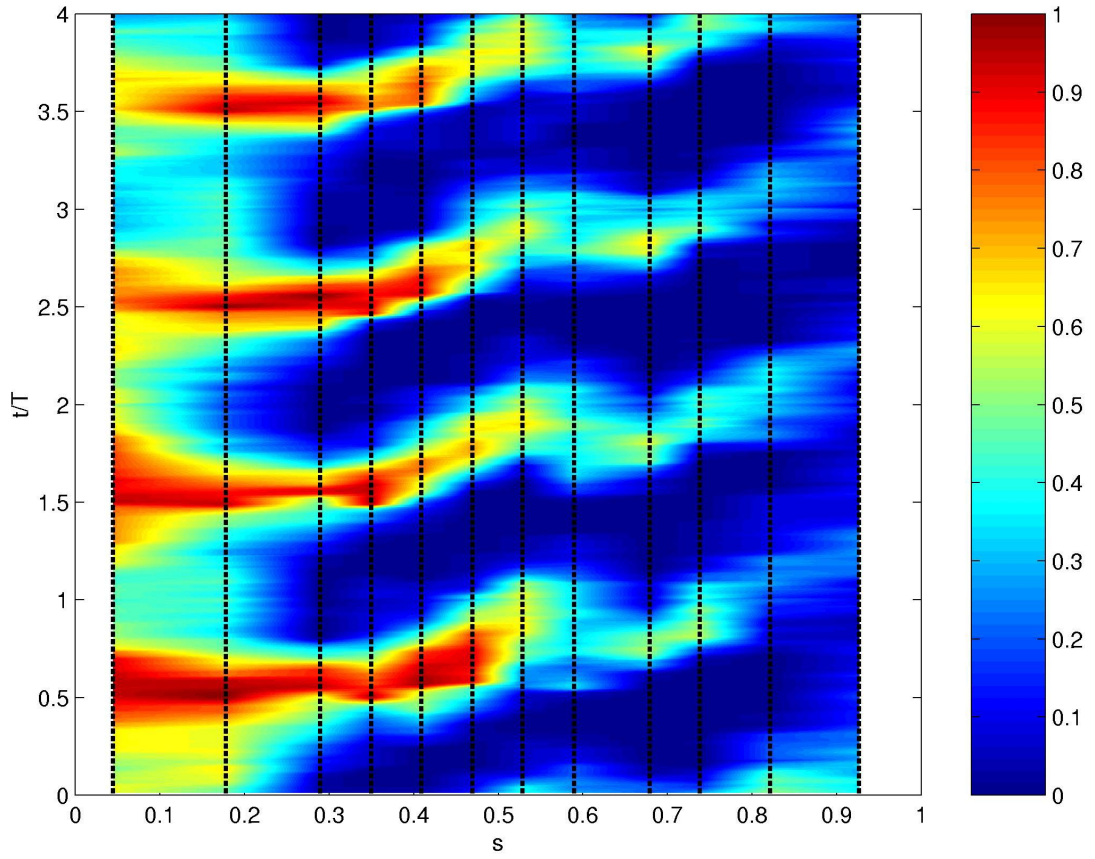

Figure 5.8: s-t plot of ensemble average intermittency, $\tilde{\gamma}(s,t)$. at $y = 0.01$ cm, from the present study

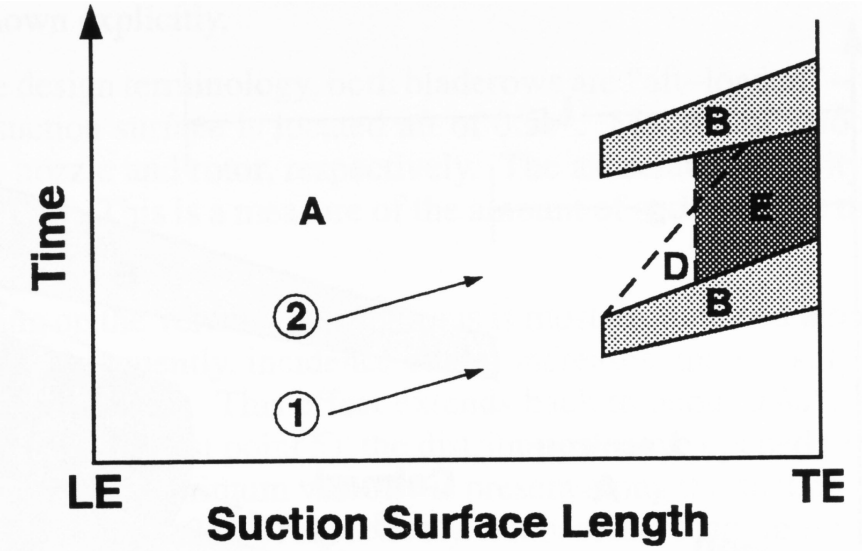

Figure 5.9: Boundary layer development at Low Re, in s-t coordinates, from Halstead (1996). The lines labeled (1) and (2) represent wake-disturbed and between-wake flow, respectively. The region marked "A" is laminar, the region marked "B" is transitional due to wake passage, the region marked "D" is the calmed region, and the region "E" indicates between-wake boundary layer growth and transition.

Table 5.1: Summary of presented data

Station:	**Quantity:**	**Figures:**
p02:	$\tilde{u}(y,\theta)$	Figures 5.10 (page 96), 5.14 (page 98), and 5.18 (page 102)
	$\widetilde{u_{rms}}(y,\theta)$	Figures 5.11 (page 96) and 5.15 (page 99)
	$\widetilde{TI}(y,\theta)$	Figures 5.12 (page 97) and 5.16 (page 100)
	$\tilde{\gamma}(y,\theta)$	Figures 5.13 (page 97) and 5.17 (page 101)
p03:	$\tilde{u}(y,\theta)$	Figures 5.19 (page 103), 5.23 (page 105), and 5.27 (page 109)
	$\widetilde{u_{rms}}(y,\theta)$	Figures 5.20 (page 103) and 5.24 (page 106)
	$\widetilde{TI}(y,\theta)$	Figures 5.21 (page 104) and 5.25 (page 107)
	$\tilde{\gamma}(y,\theta)$	Figures 5.22 (page 104) and 5.26 (page 108)
p04:	$\tilde{u}(y,\theta)$	Figures 5.28 (page 110), 5.32 (page 112), and 5.36 (page 116)
	$\widetilde{u_{rms}}(y,\theta)$	Figures 5.29 (page 110) and 5.33 (page 113)
	$\widetilde{TI}(y,\theta)$	Figures 5.30 (page 111) and 5.34 (page 114)
	$\tilde{\gamma}(y,\theta)$	Figures 5.31 (page 111) and 5.35 (page 115)
p05:	$\tilde{u}(y,\theta)$	Figures 5.37 (page 117), 5.41 (page 119), and 5.45 (page 123)
	$\widetilde{u_{rms}}(y,\theta)$	Figures 5.38 (page 117) and 5.42 (page 120)
	$\widetilde{TI}(y,\theta)$	Figures 5.39 (page 118) and 5.43 (page 121)
	$\tilde{\gamma}(y,\theta)$	Figures 5.40 (page 118) and 5.44 (page 122)
p06:	$\tilde{u}(y,\theta)$	Figures 5.46 (page 124), 5.50 (page 126), and 5.54 (page 130)
	$\widetilde{u_{rms}}(y,\theta)$	Figures 5.47 (page 124) and 5.51 (page 127)
	$\widetilde{TI}(y,\theta)$	Figures 5.48 (page 125) and 5.52 (page 128)
	$\tilde{\gamma}(y,\theta)$	Figures 5.49 (page 125) and 5.53 (page 129)
p07:	$\tilde{u}(y,\theta)$	Figures 5.55 (page 131), 5.59 (page 133), and 5.63 (page 137)
	$\widetilde{u_{rms}}(y,\theta)$	Figures 5.56 (page 131) and 5.60 (page 134)
	$\widetilde{TI}(y,\theta)$	Figures 5.57 (page 132) and 5.61 (page 135)
	$\tilde{\gamma}(y,\theta)$	Figures 5.58 (page 132) and 5.62 (page 136)
p08:	$\tilde{u}(y,\theta)$	Figures 5.64 (page 138), 5.68 (page 140), and 5.72 (page 144)
	$\widetilde{u_{rms}}(y,\theta)$	Figures 5.65 (page 138) and 5.69 (page 141)
	$\widetilde{TI}(y,\theta)$	Figures 5.66 (page 139) and 5.70 (page 142)
	$\tilde{\gamma}(y,\theta)$	Figures 5.67 (page 139) and 5.71 (page 143)
p09:	$\tilde{u}(y,\theta)$	Figures 5.73 (page 145), 5.77 (page 147), and 5.81 (page 151)
	$\widetilde{u_{rms}}(y,\theta)$	Figures 5.74 (page 145) and 5.78 (page 148)
	$\widetilde{TI}(y,\theta)$	Figures 5.75 (page 146) and 5.79 (page 149)
	$\tilde{\gamma}(y,\theta)$	Figures 5.76 (page 146) and 5.80 (page 150)
p10:	$\tilde{u}(y,\theta)$	Figures 5.82 (page 152), 5.86 (page 154), and 5.90 (page 158)
	$\widetilde{u_{rms}}(y,\theta)$	Figures 5.83 (page 152) and 5.87 (page 155)
	$\widetilde{TI}(y,\theta)$	Figures 5.84 (page 153) and 5.88 (page 156)
	$\tilde{\gamma}(y,\theta)$	Figures 5.85 (page 153) and 5.89 (page 157)
p11:	$\tilde{u}(y,\theta)$	Figures 5.91 (page 159), 5.95 (page 161), and 5.99 (page 165)
	$\widetilde{u_{rms}}(y,\theta)$	Figures 5.92 (page 159) and 5.96 (page 162)
	$\widetilde{TI}(y,\theta)$	Figures 5.93 (page 160) and 5.97 (page 163)
	$\tilde{\gamma}(y,\theta)$	Figures 5.94 (page 160) and 5.98 (page 164)
p12:	$\tilde{u}(y,\theta)$	Figures 5.100 (page 166), 5.104 (page 168), and 5.108 (page 172)
	$\widetilde{u_{rms}}(y,\theta)$	Figures 5.101 (page 166) and 5.105 (page 169)
	$\widetilde{TI}(y,\theta)$	Figures 5.102 (page 167) and 5.106 (page 170)
	$\tilde{\gamma}(y,\theta)$	Figures 5.103 (page 167) and 5.107 (page 171)
p13:	$\tilde{u}(y,\theta)$	Figures 5.109 (page 173), 5.113 (page 175), and 5.117 (page 179)
	$\widetilde{u_{rms}}(y,\theta)$	Figures 5.110 (page 173) and 5.114 (page 176)
	$\widetilde{TI}(y,\theta)$	Figures 5.111 (page 174) and 5.115 (page 177)
	$\tilde{\gamma}(y,\theta)$	Figures 5.112 (page 174) and 5.116 (page 178)

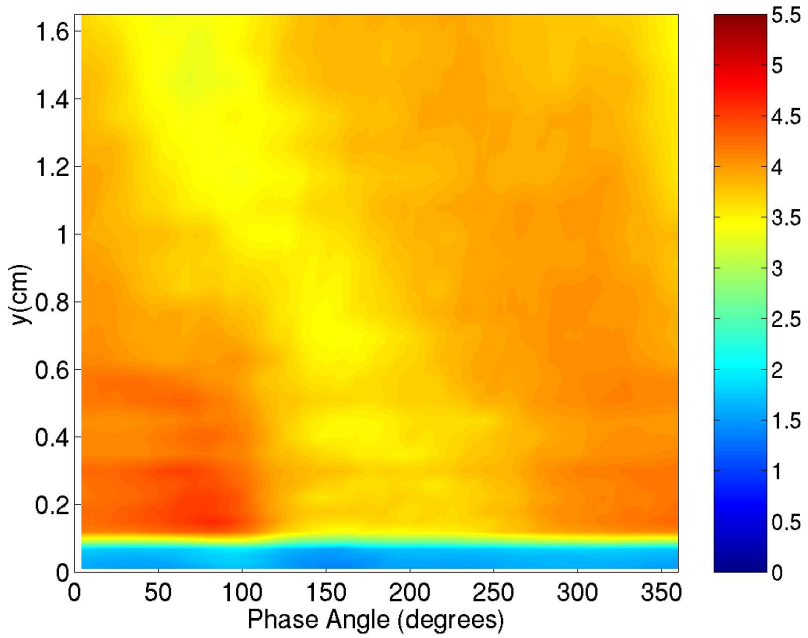

Figure 5.10: Phase average velocity $\tilde{u}(y,\theta)$ at p02, $s/L_{ss} = 5.19\%$.

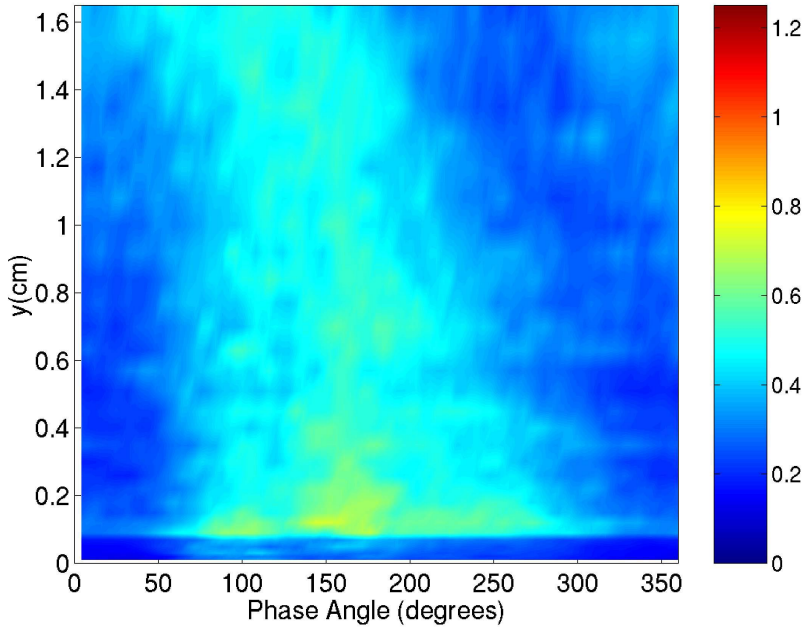

Figure 5.11: Phase average rms velocity fluctuation $\widetilde{u_{rms}}(y,\theta)$ at p02, $s/L_{ss} = 5.19\%$.

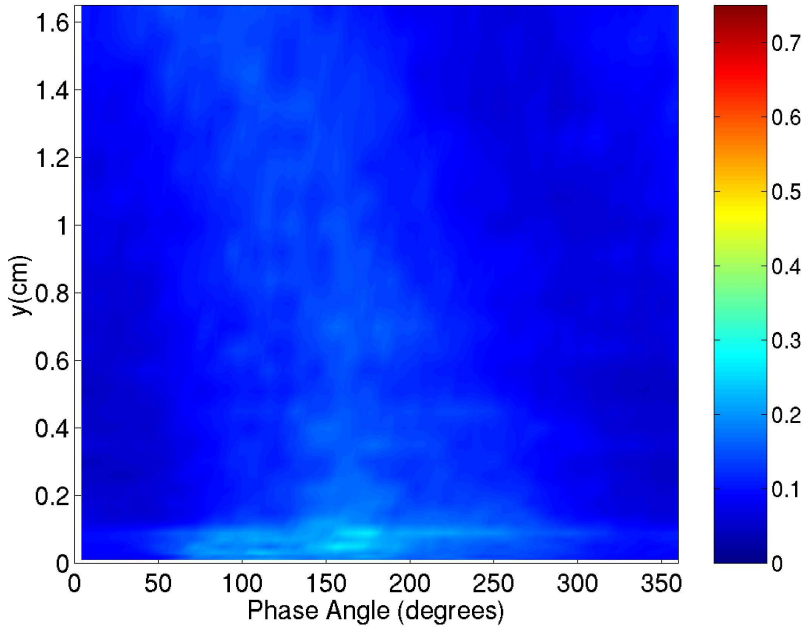

Figure 5.12: Phase average turbulence intensity $\widetilde{TI}(y,\theta)$ at p02, $s/L_{ss} = 5.19\%$.

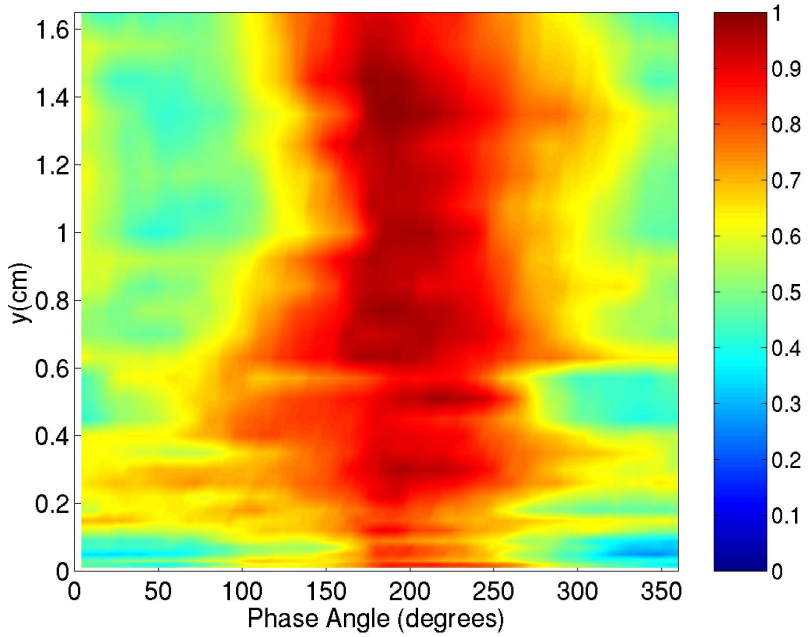

Figure 5.13: Phase average intermittency $\tilde{\gamma}(y,\theta)$ at p02, $s/L_{ss} = 5.19\%$.

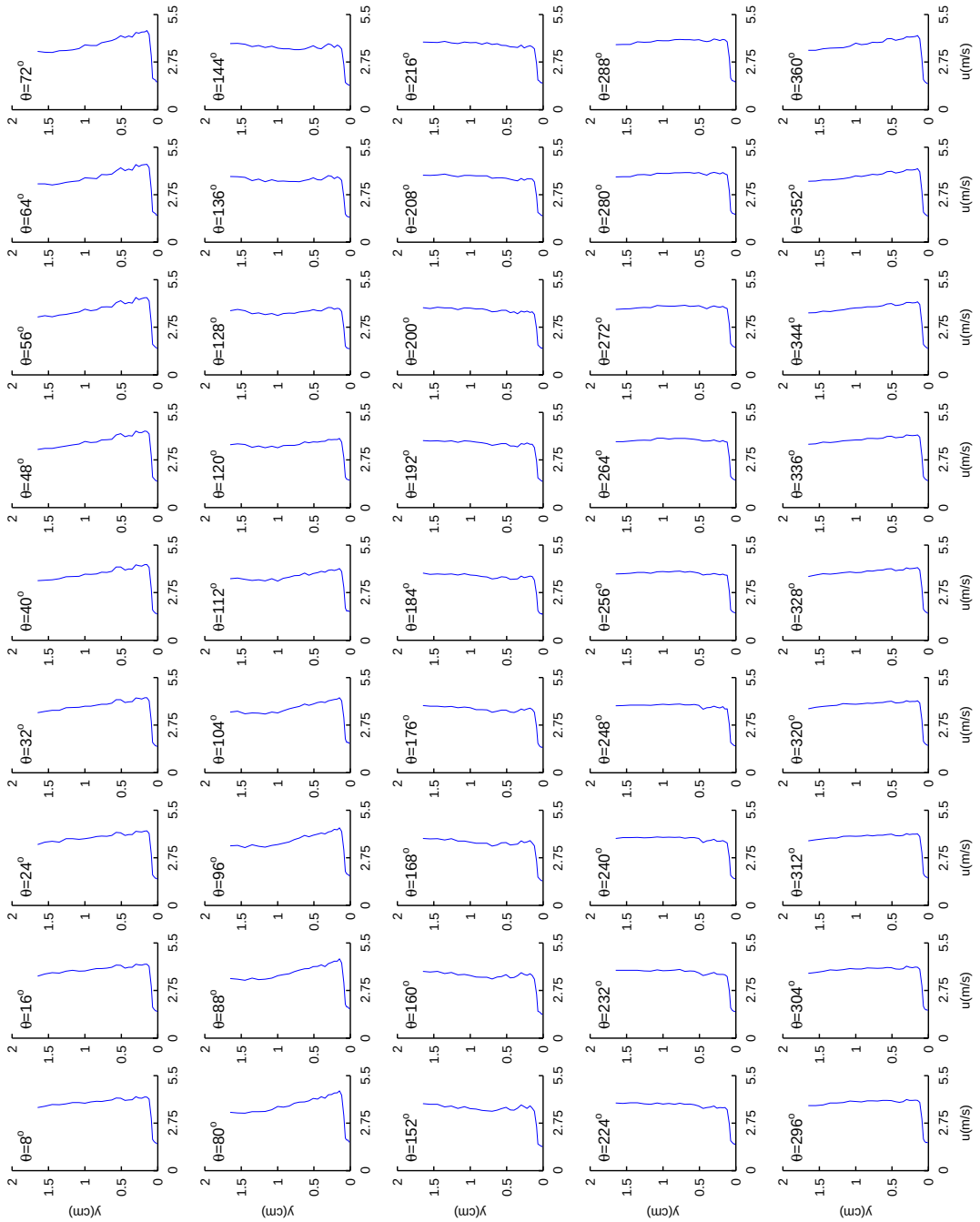

Figure 5.14: Phase average velocity $\tilde{u}(y, \theta)$ at p02, presented as a function of θ.

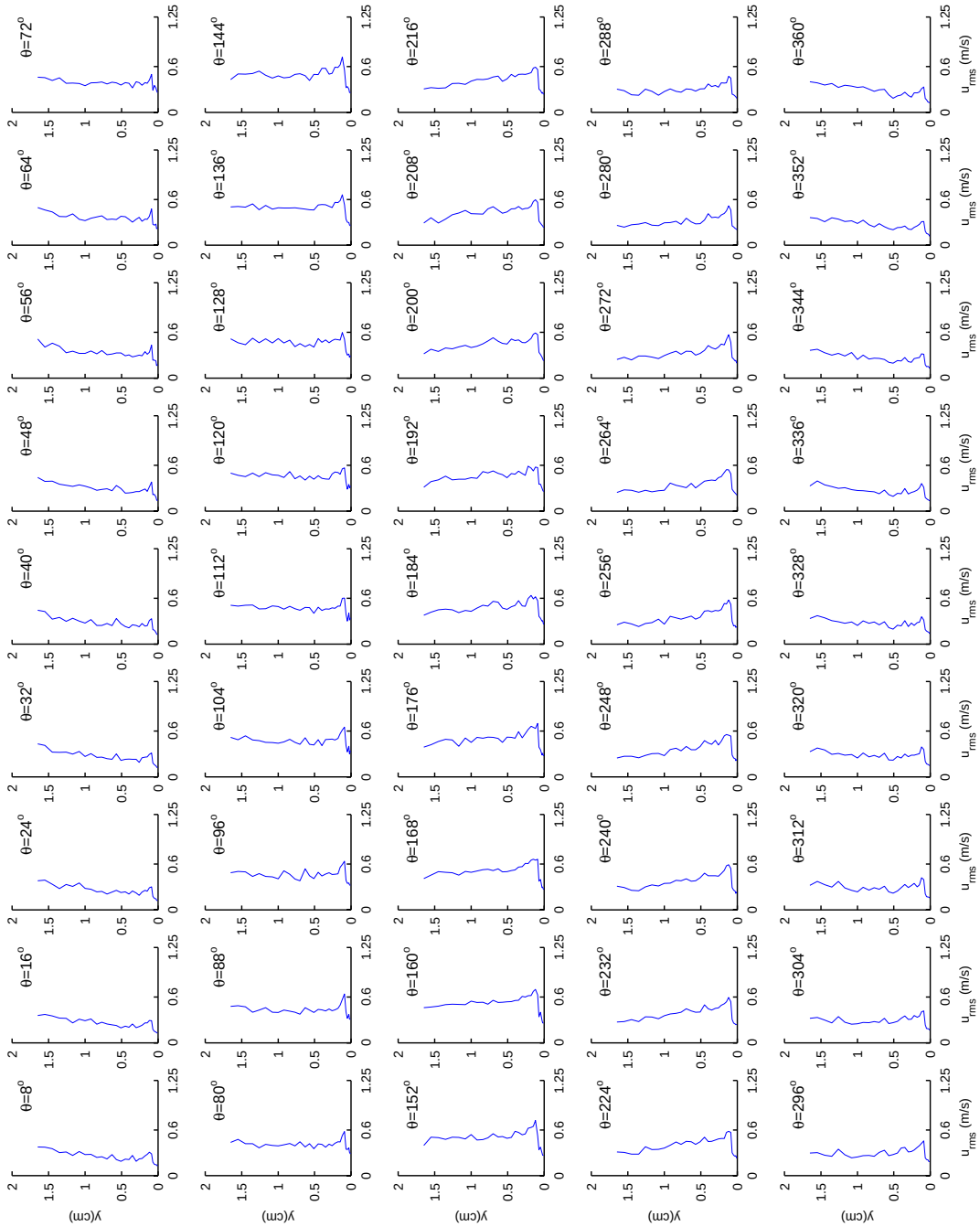

Figure 5.15: Phase average rms velocity fluctuation $\widetilde{u_{rms}}(y, \theta)$ at p02, $s/L_{ss} = 5.19\%$, presented as a function of θ.

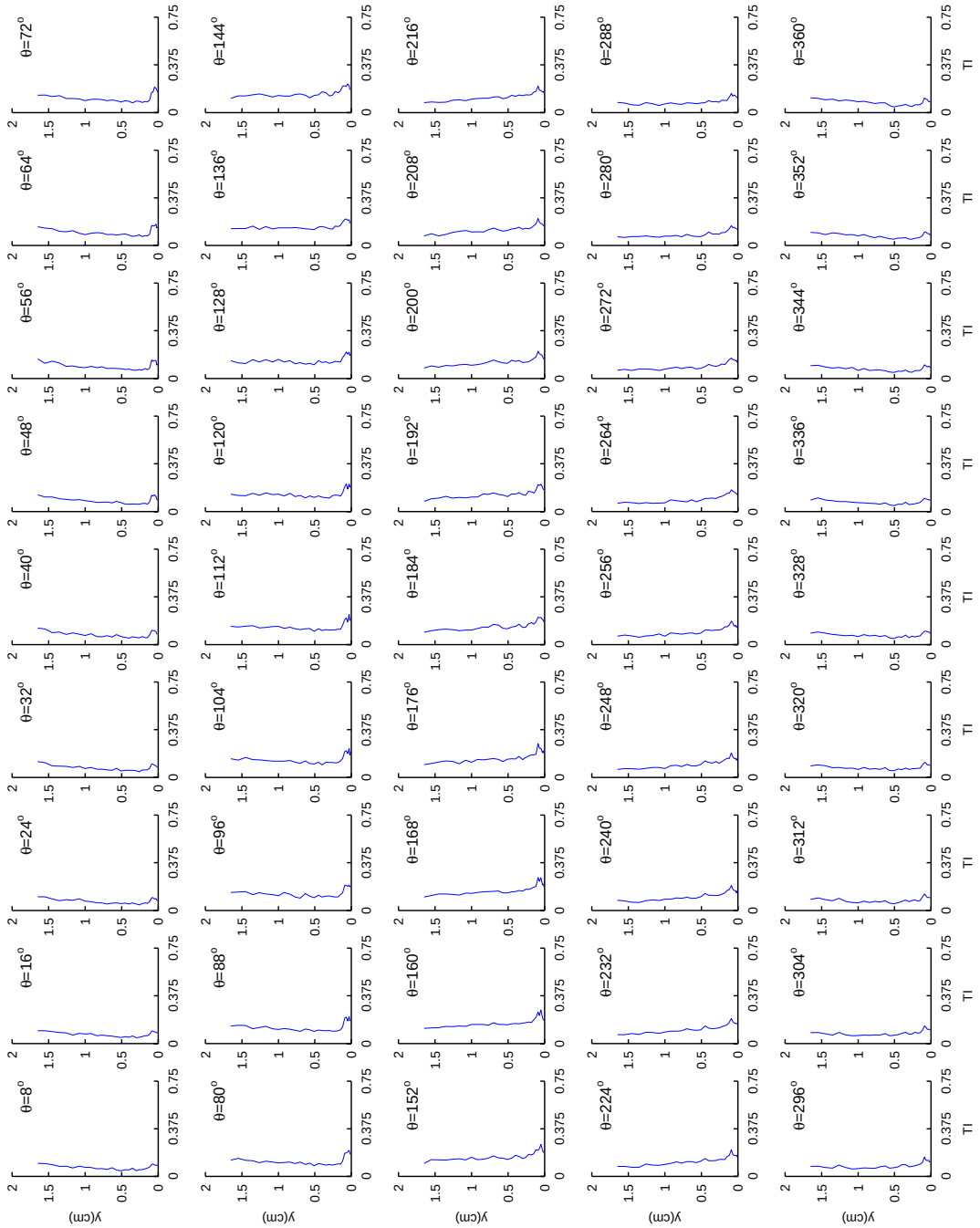

Figure 5.16: Phase average turbulence intensity $\widetilde{TI}(y,\theta)$ at p02, $s/L_{ss} = 5.19\%$, presented as a function of θ.

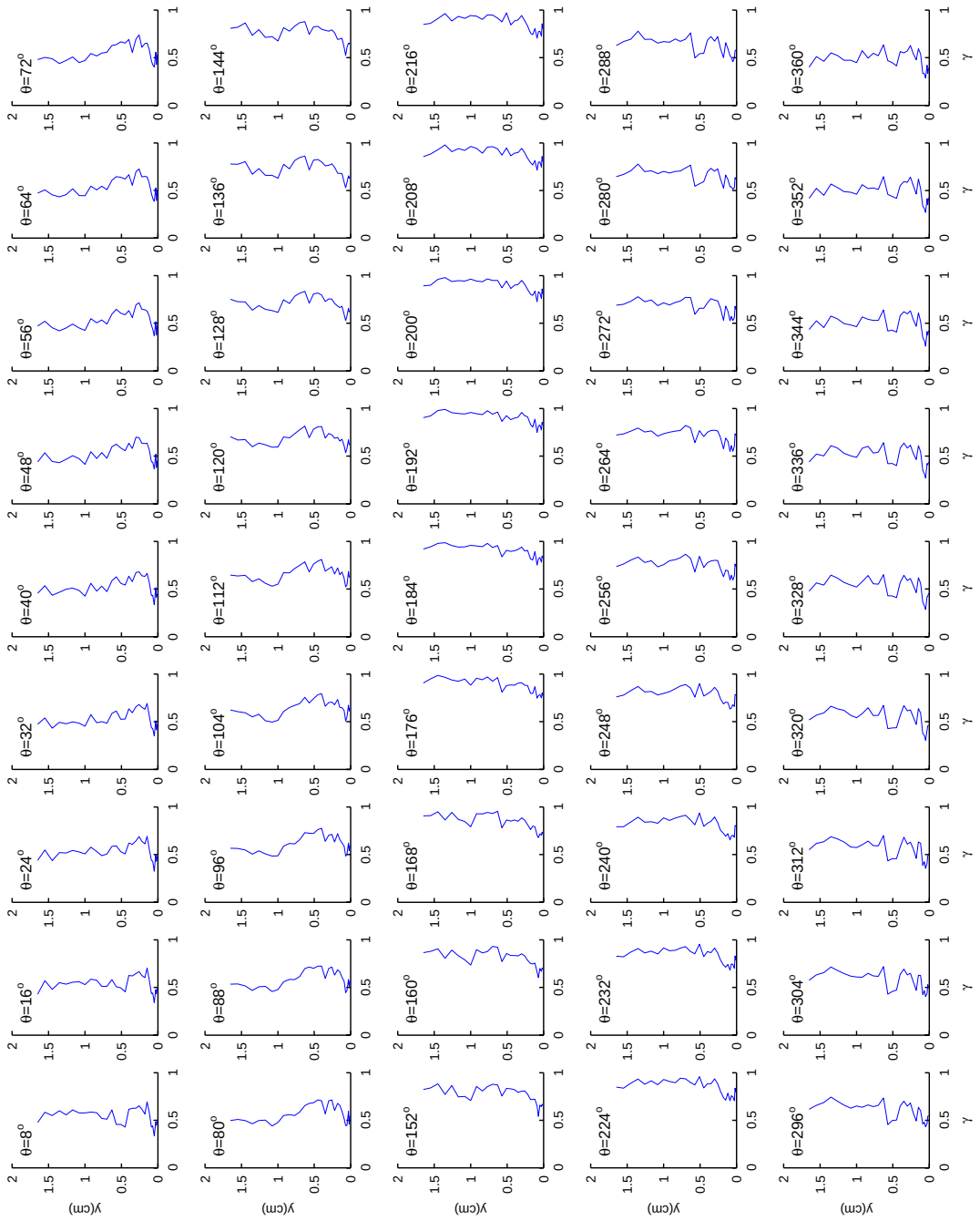

Figure 5.17: Phase average intermittency $\tilde{\gamma}(y, \theta)$ at p02, $s/L_{ss} = 5.19\%$, presented as a function of θ.

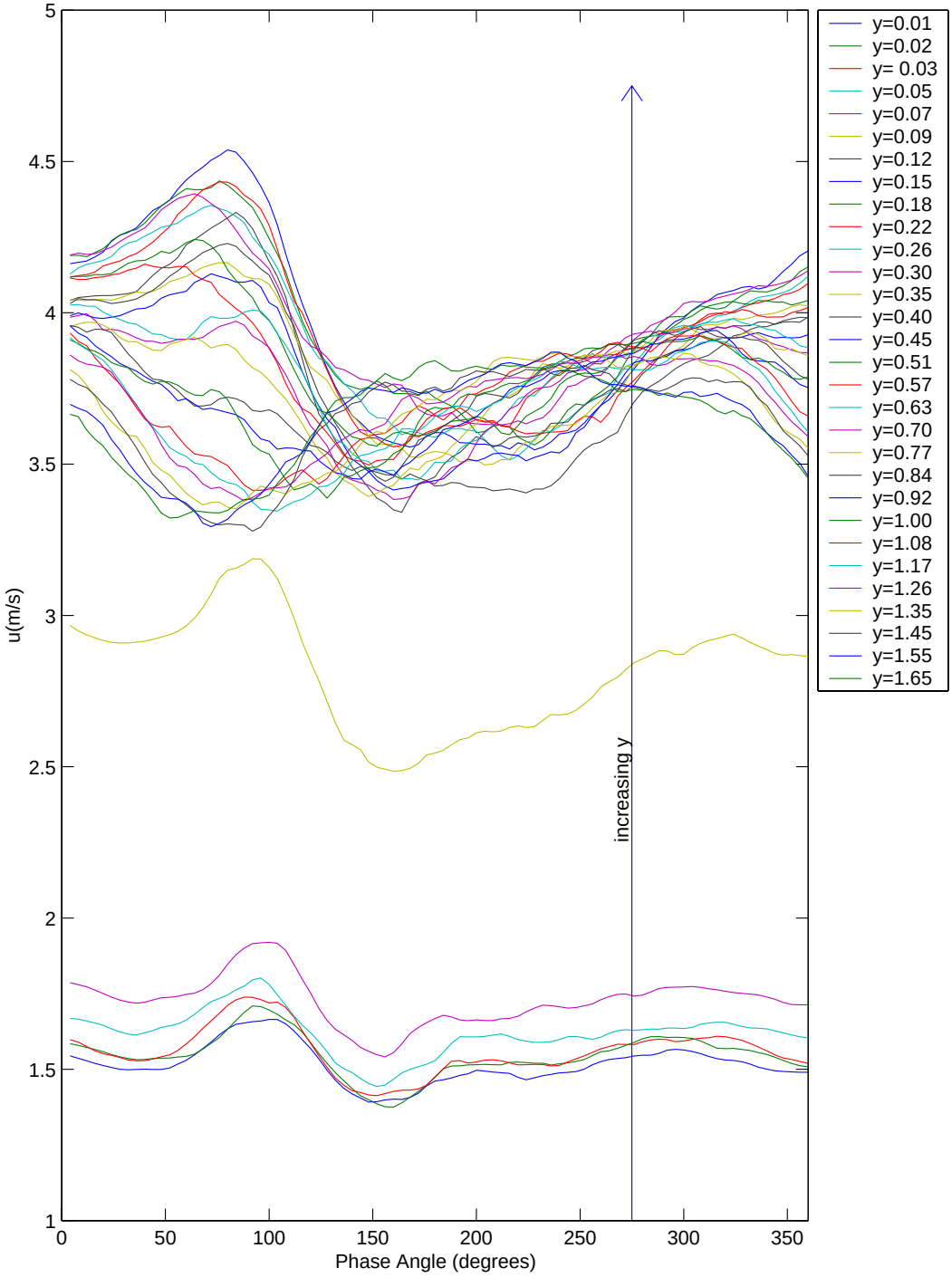

Figure 5.18: Phase average velocity $\tilde{u}(y, \theta)$ at p02, $s/L_{ss} = 5.19\%$, presented as a function of y (y-values are in cm).

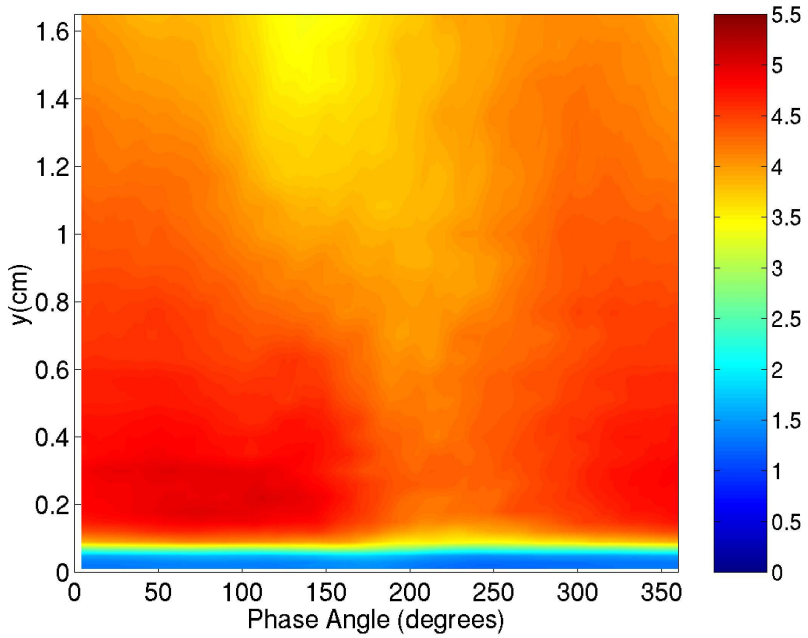

Figure 5.19: Phase average velocity $\tilde{u}(y, \theta)$ at p03, $s/L_{ss} = 19.78\%$.

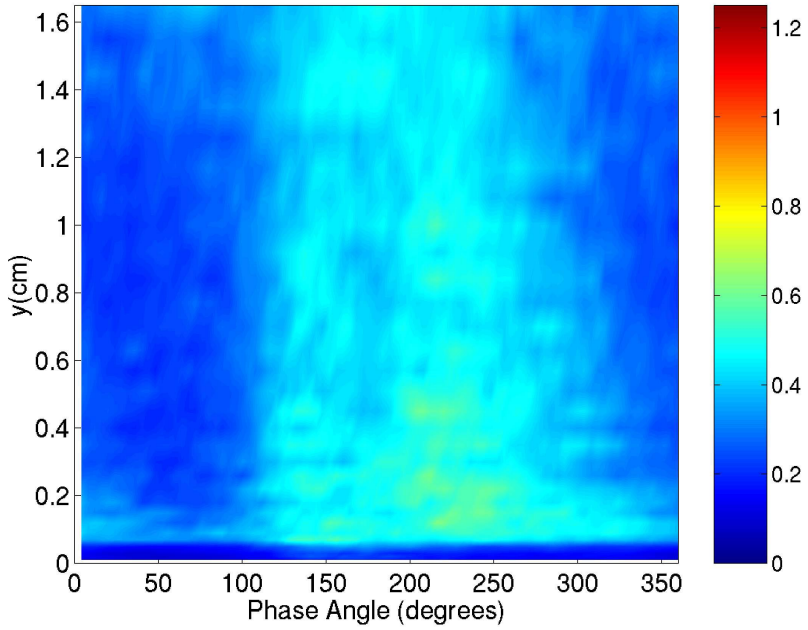

Figure 5.20: Phase average rms velocity fluctuation $\widetilde{u_{rms}}(y, \theta)$ at p03, $s/L_{ss} = 19.78\%$.

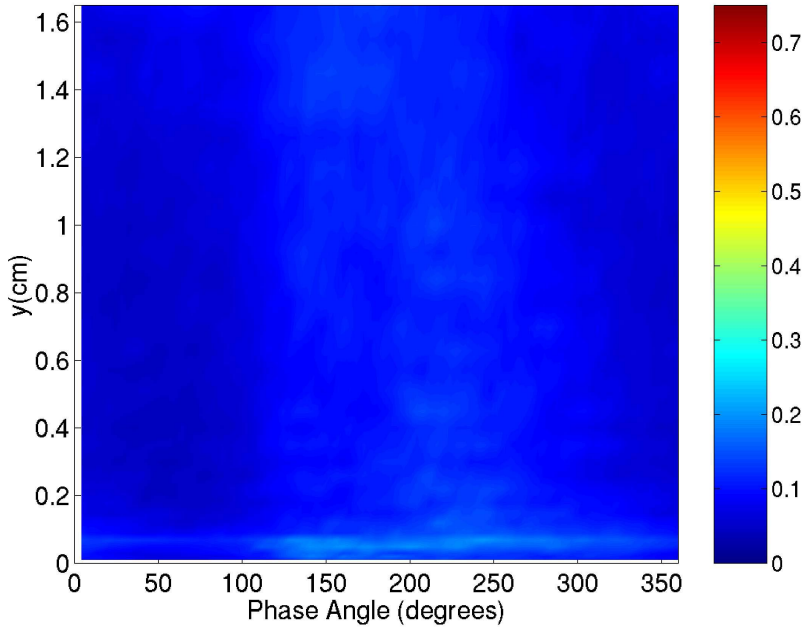

Figure 5.21: Phase average turbulence intensity $\widetilde{TI}(y,\theta)$ at p03. $s/L_{ss} = 19.78\%$.

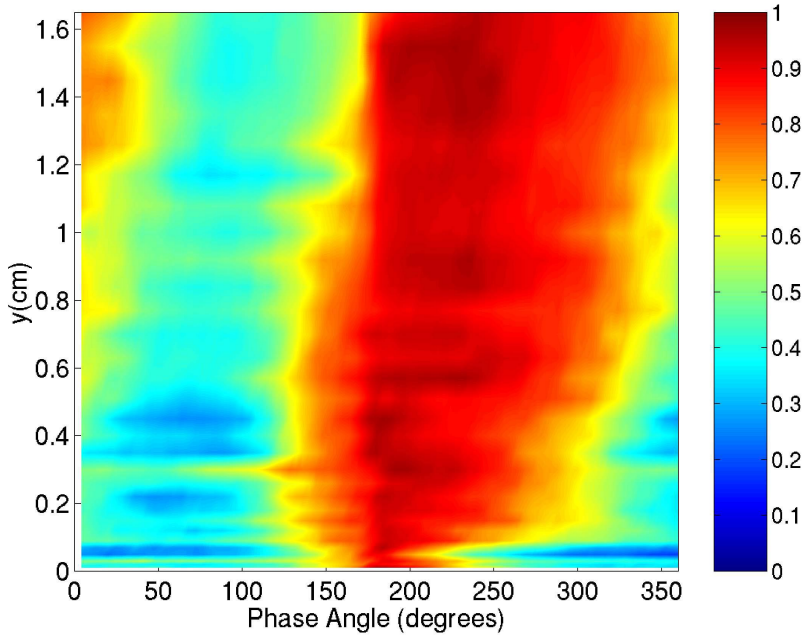

Figure 5.22: Phase average intermittency $\tilde{\gamma}(y,\theta)$ at p03, $s/L_{ss} = 19.78\%$.

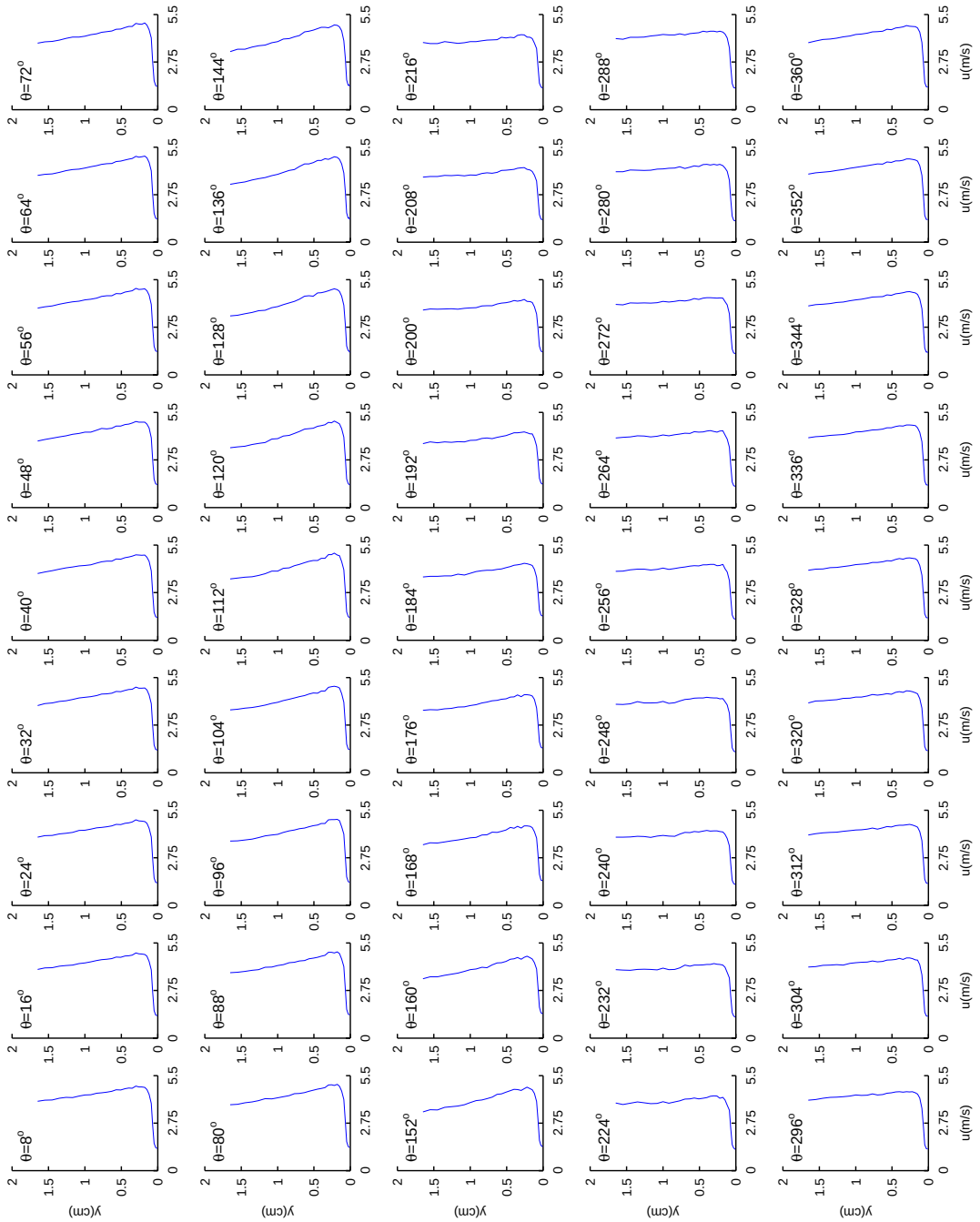

Figure 5.23: Phase average velocity $\tilde{u}(y, \theta)$ at p03, $s/L_{ss} = 19.78\%$, presented as a function of θ.

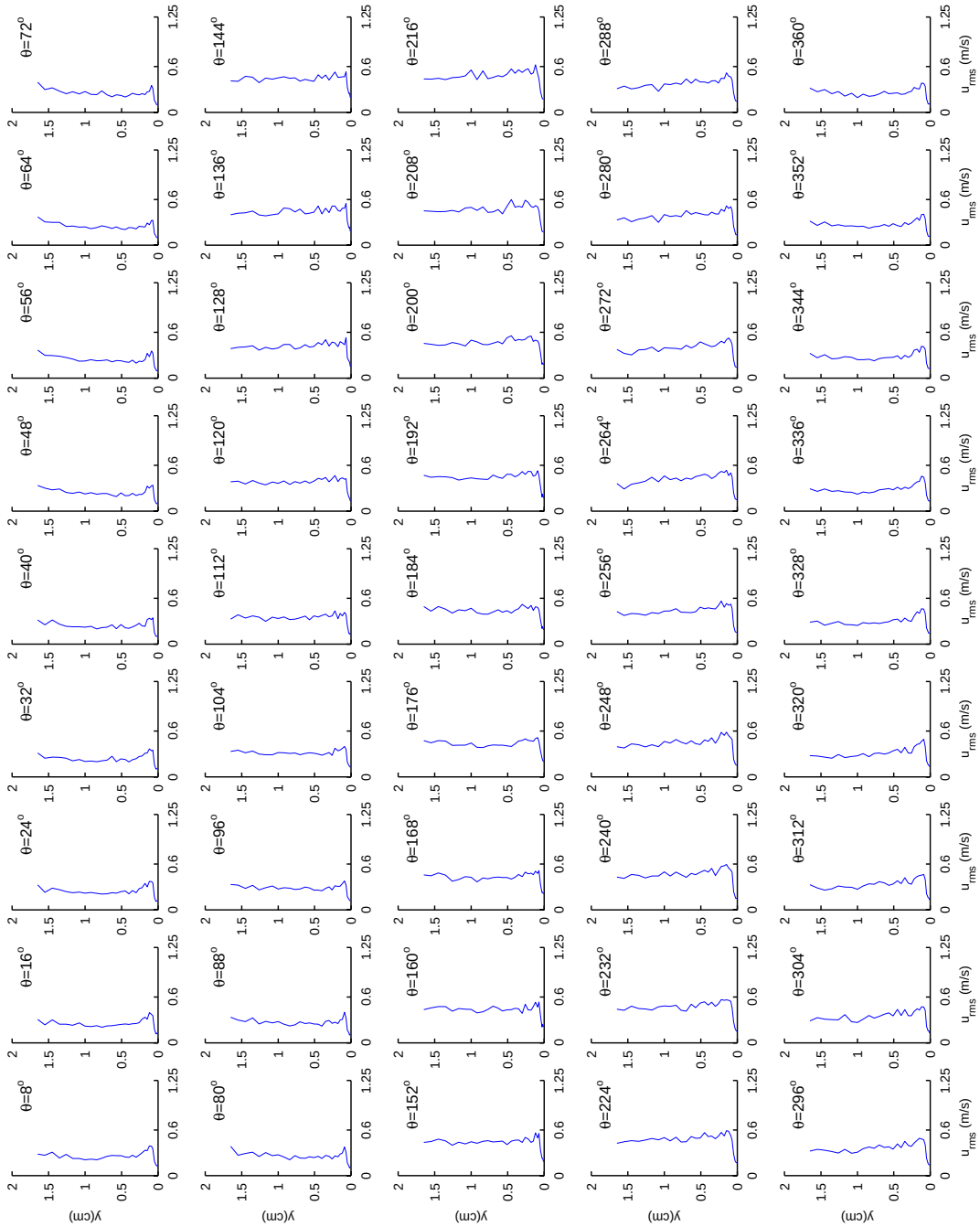

Figure 5.24: Phase average rms velocity fluctuation $\widetilde{u_{rms}}(y, \theta)$ at p03, $s/L_{ss} = 19.78\%$, presented as a function of θ.

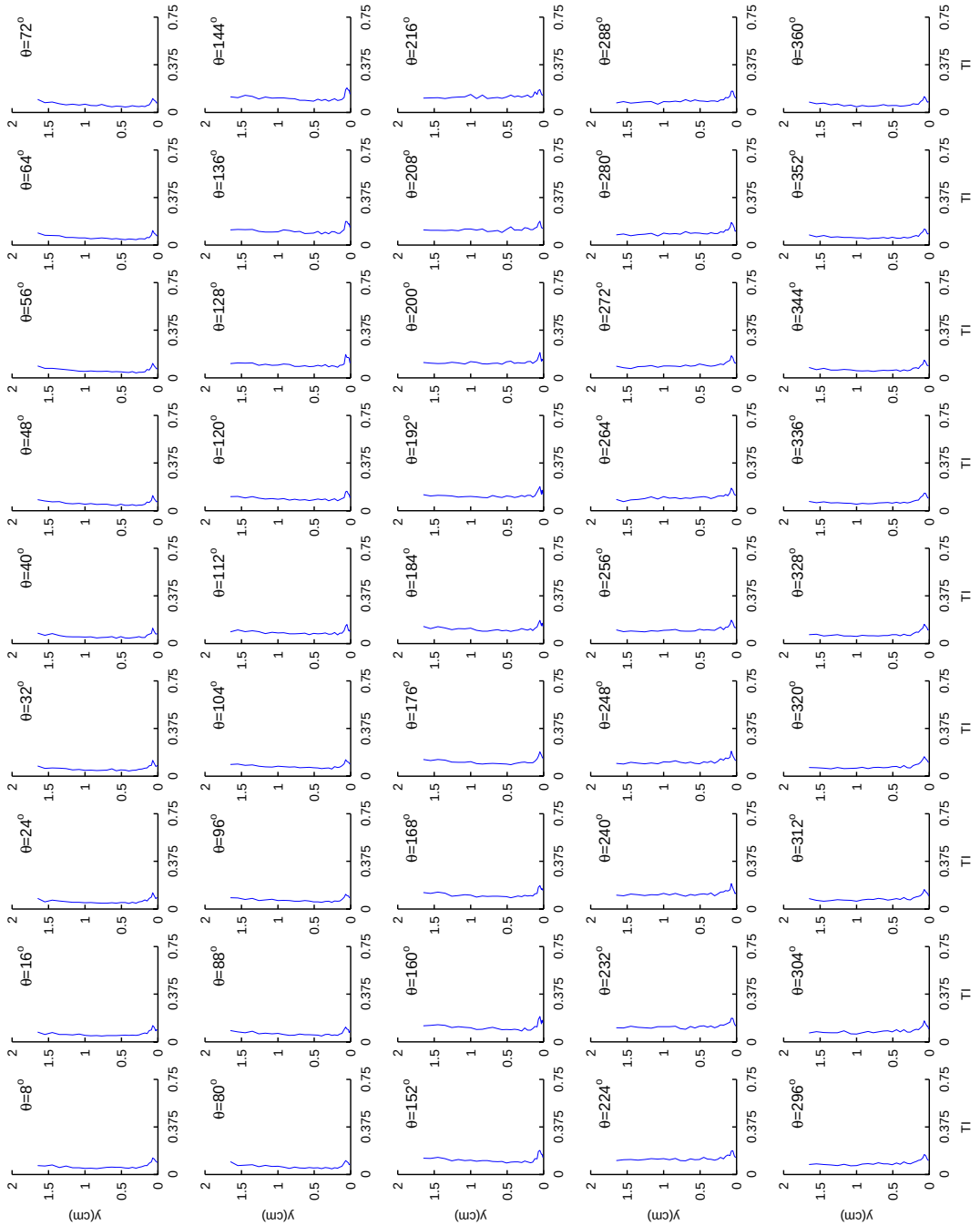

Figure 5.25: Phase average turbulence intensity $\widetilde{TI}(y,\theta)$ at p03, $s/L_{ss} = 19.78\%$, presented as a function of θ.

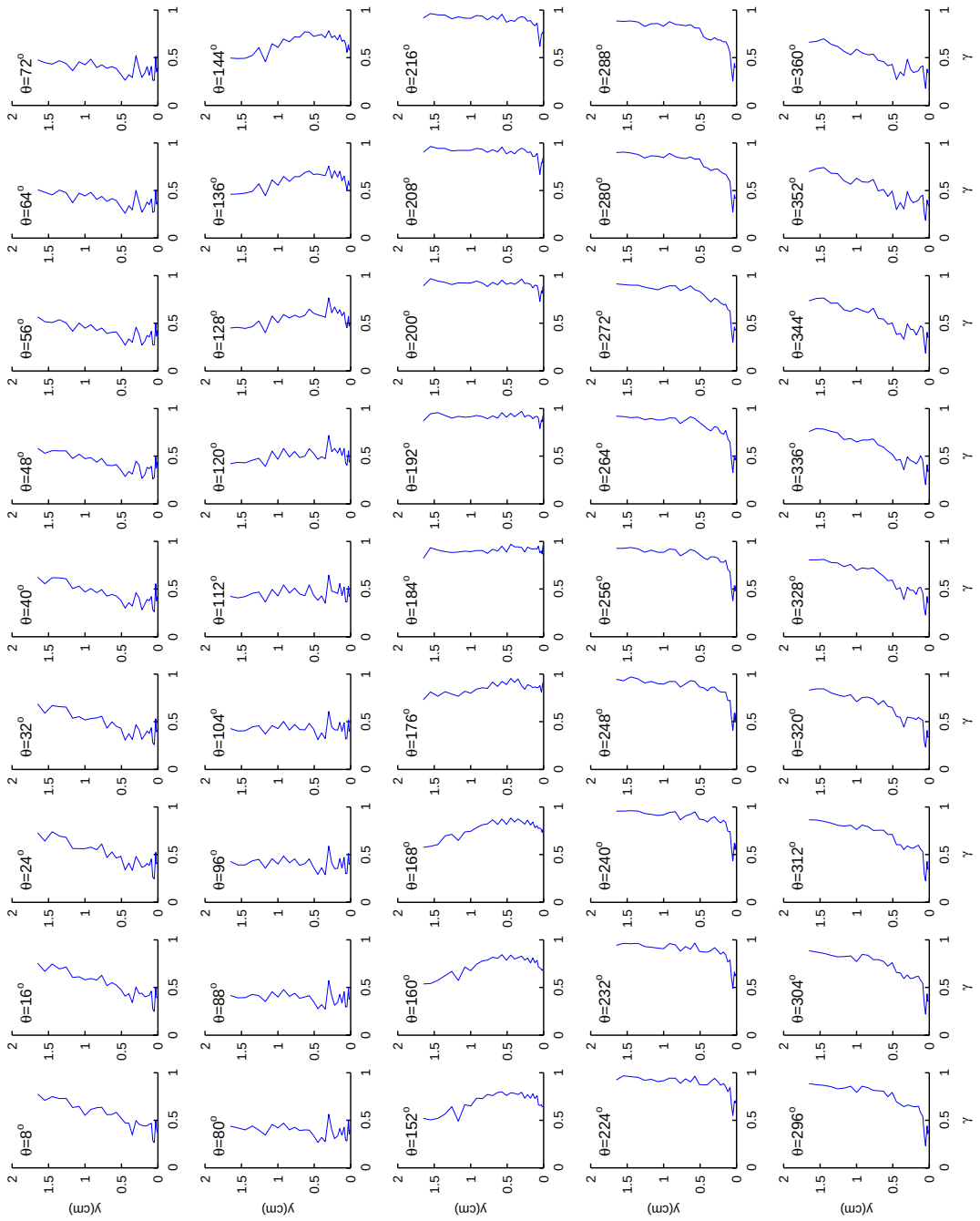

Figure 5.26: Phase average intermittency $\tilde{\gamma}(y, \theta)$ at p03, $s/L_{ss} = 19.78\%$, presented as a function of θ.

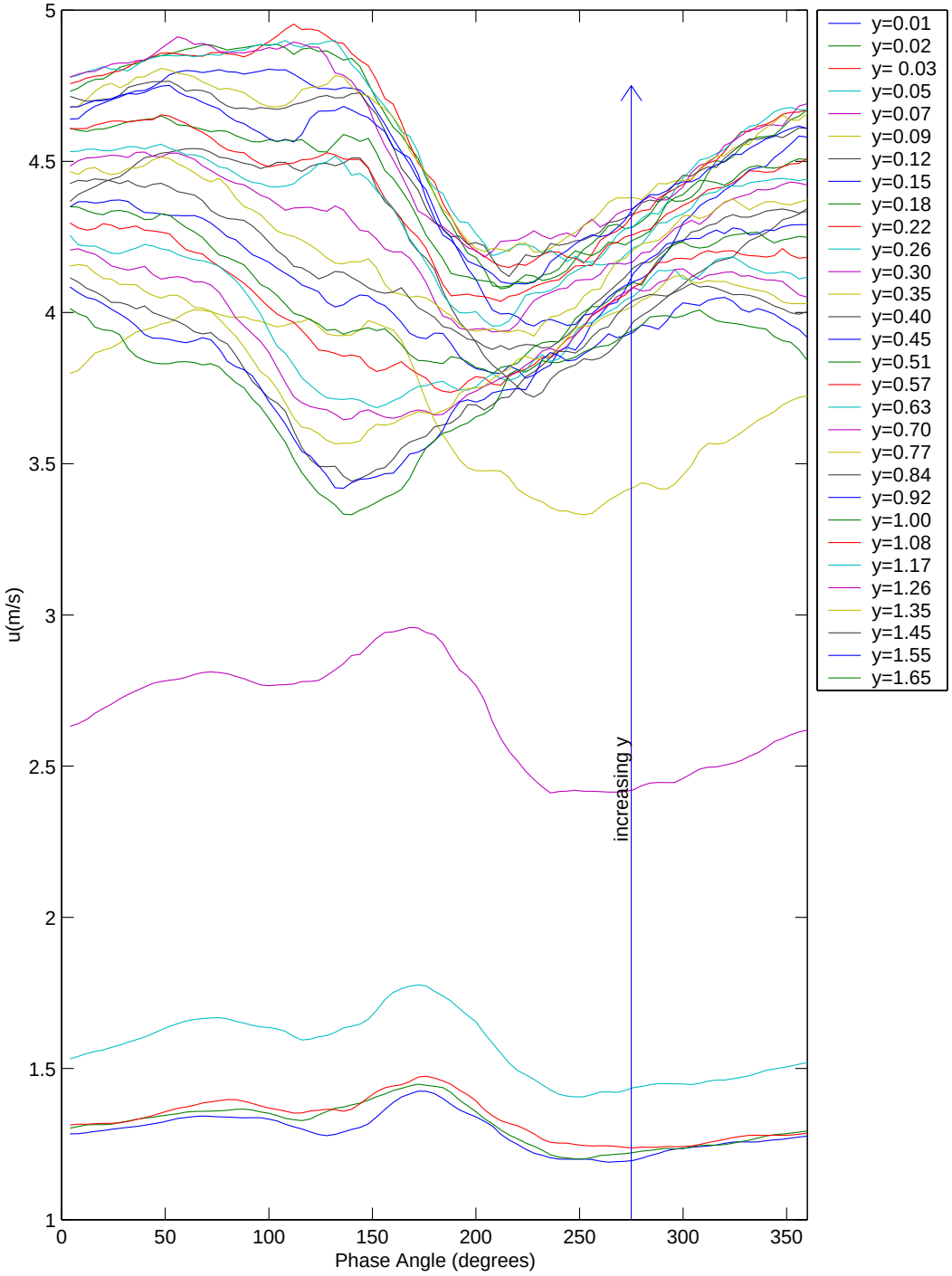

Figure 5.27: Phase average velocity $\tilde{u}(y, \theta)$ at p03, $s/L_{ss} = 19.78\%$, presented as a function of y (y-values are in cm).

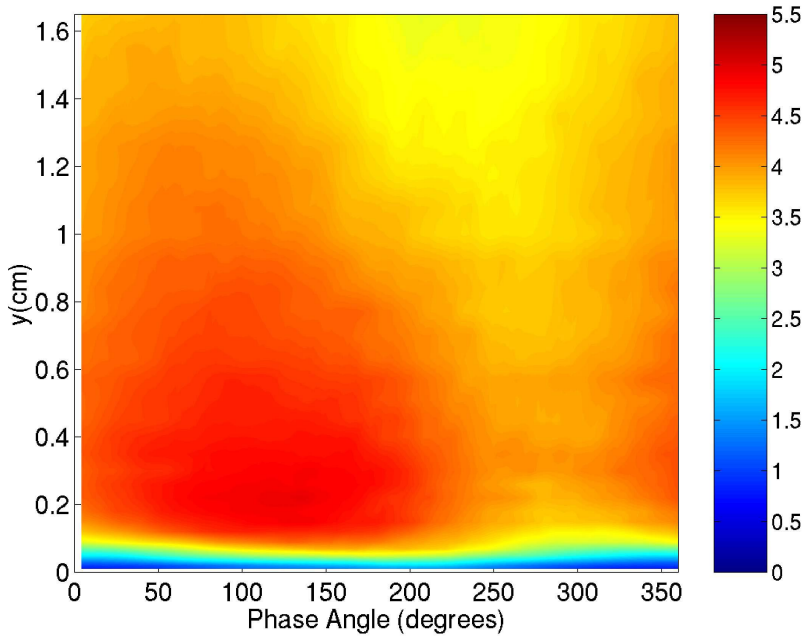

Figure 5.28: Phase average velocity $\tilde{u}(y, \theta)$ at p04, $s/L_{ss} = 31.36\%$.

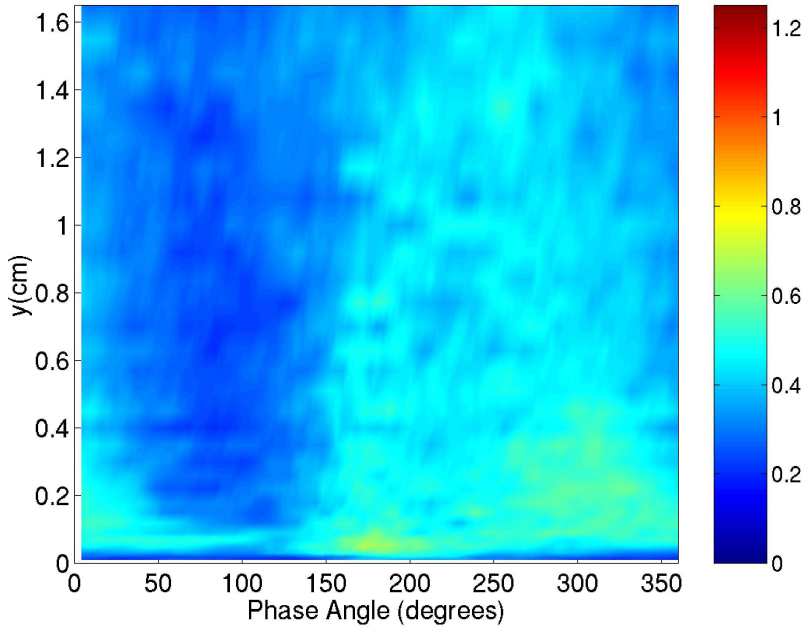

Figure 5.29: Phase average rms velocity fluctuation $\widetilde{u_{rms}}(y, \theta)$ at p04, $s/L_{ss} = 31.36\%$.

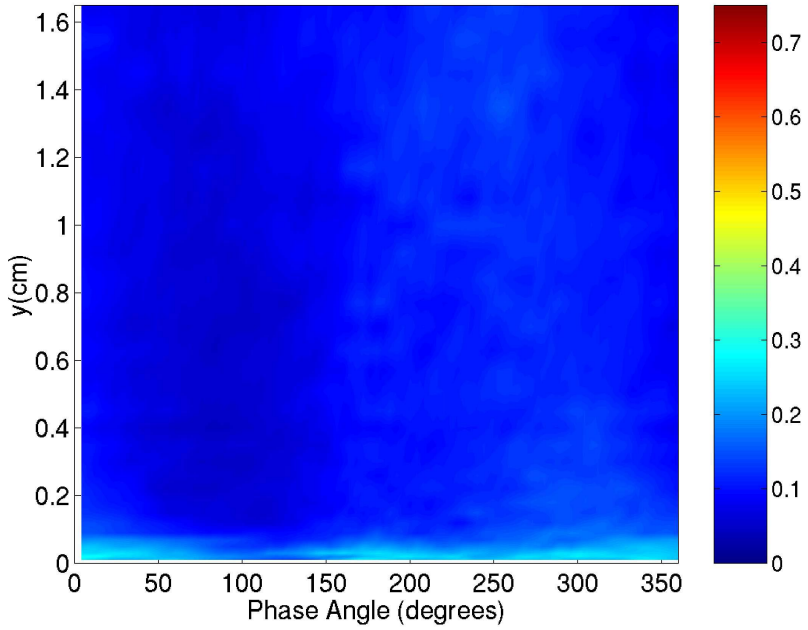

Figure 5.30: Phase average turbulence intensity $\widetilde{TI}(y,\theta)$ at p04, $s/L_{ss} = 31.36\%$.

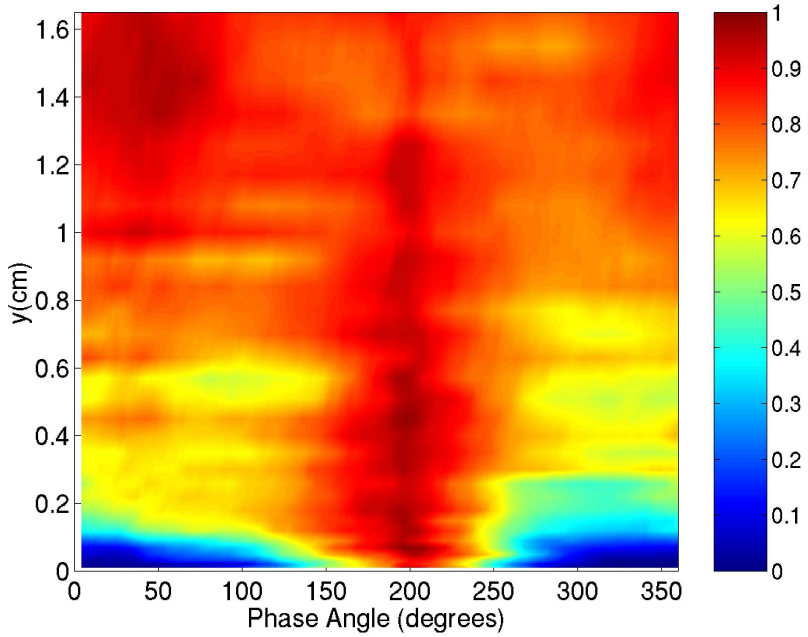

Figure 5.31: Phase average intermittency $\tilde{\gamma}(y,\theta)$ at p04, $s/L_{ss} = 31.36\%$.

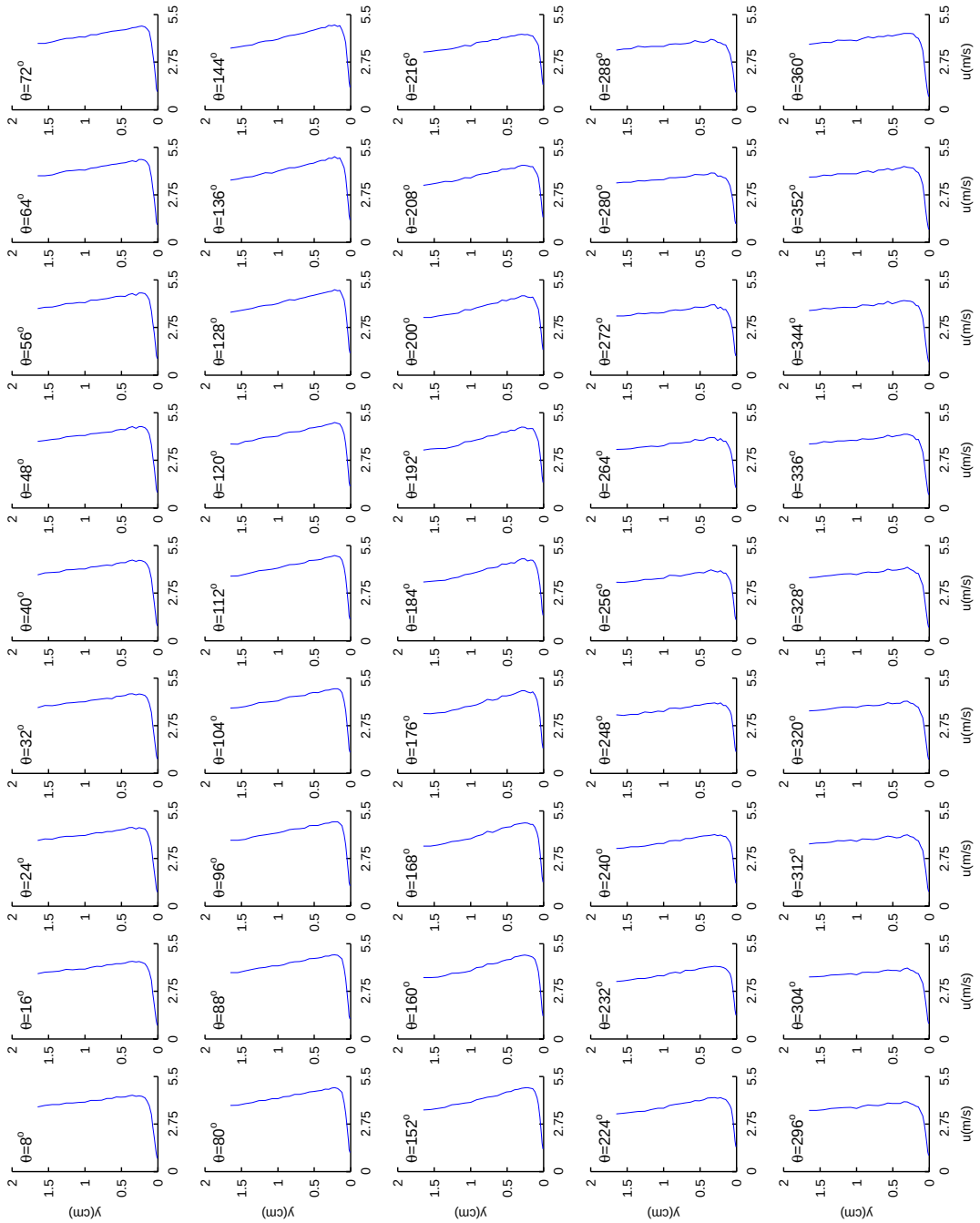

Figure 5.32: Phase average velocity $\tilde{u}(y, \theta)$ at p04, $s/L_{ss} = 31.36\%$, presented as a function of θ.

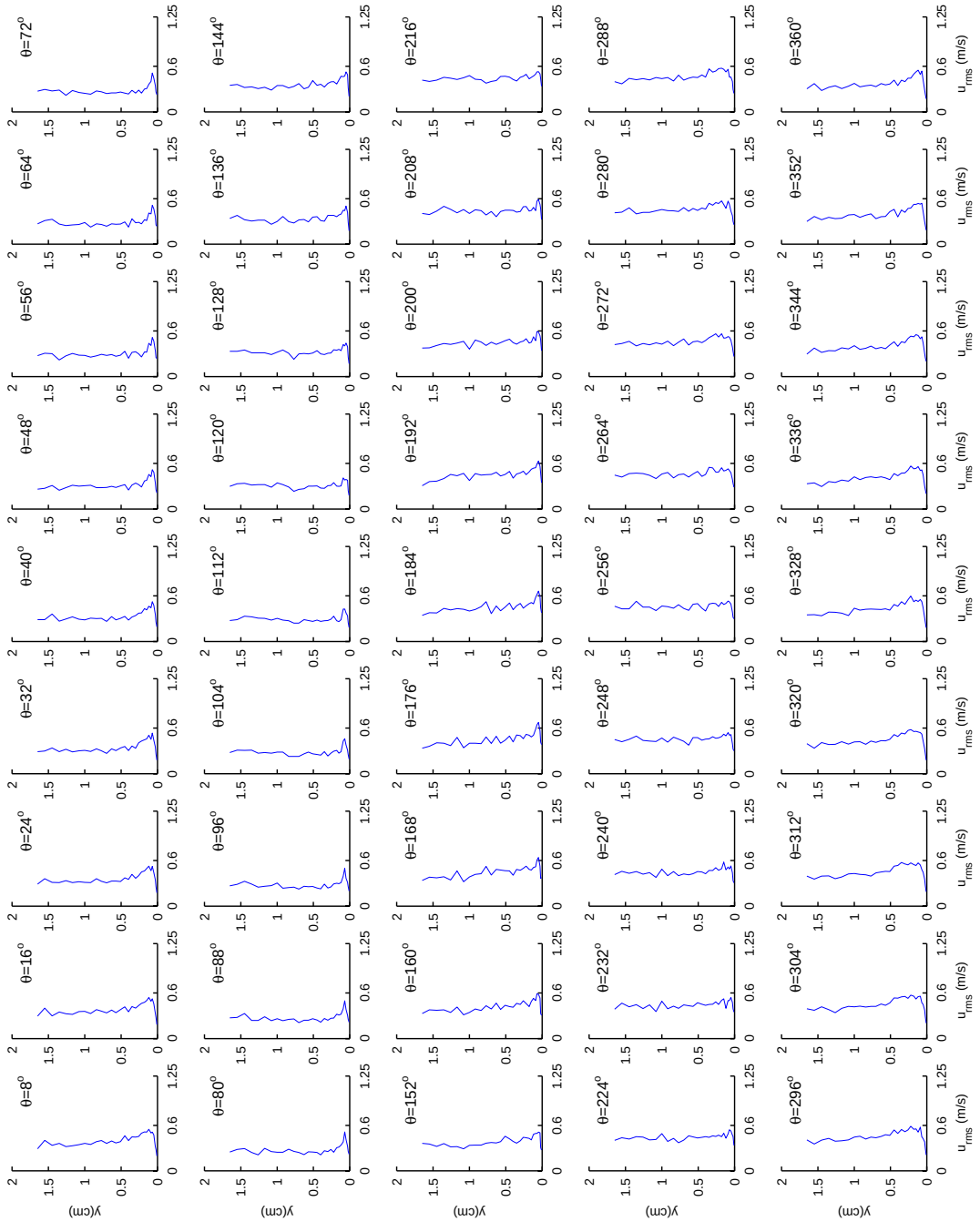

Figure 5.33: Phase average rms velocity fluctuation $\widetilde{u_{rms}}(y, \theta)$ at p04, $s/L_{ss} = 31.36\%$, presented as a function of θ.

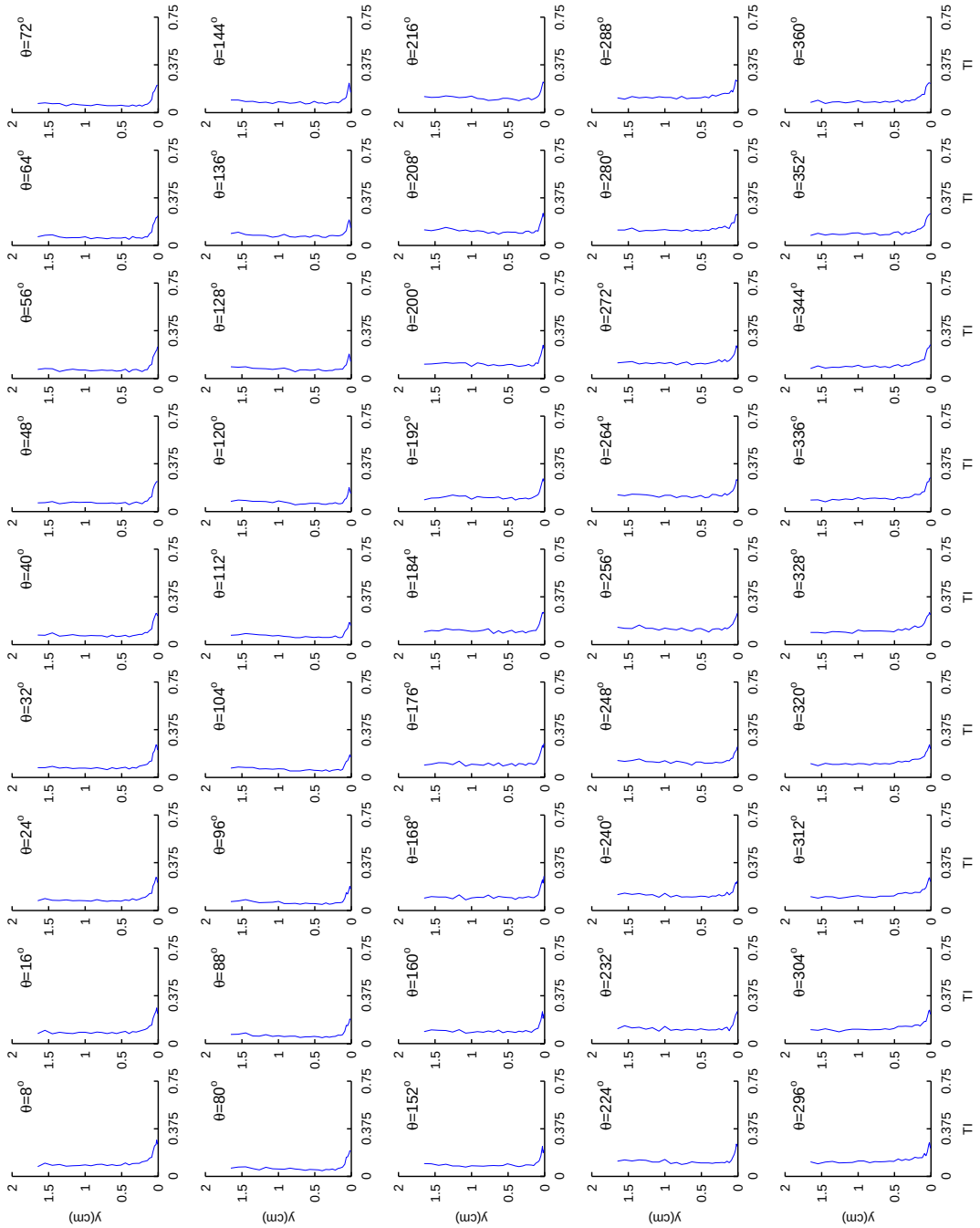

Figure 5.34: Phase average turbulence intensity $\widetilde{TI}(y,\theta)$ at p04, $s/L_{ss} = 31.36\%$, presented as a function of θ.

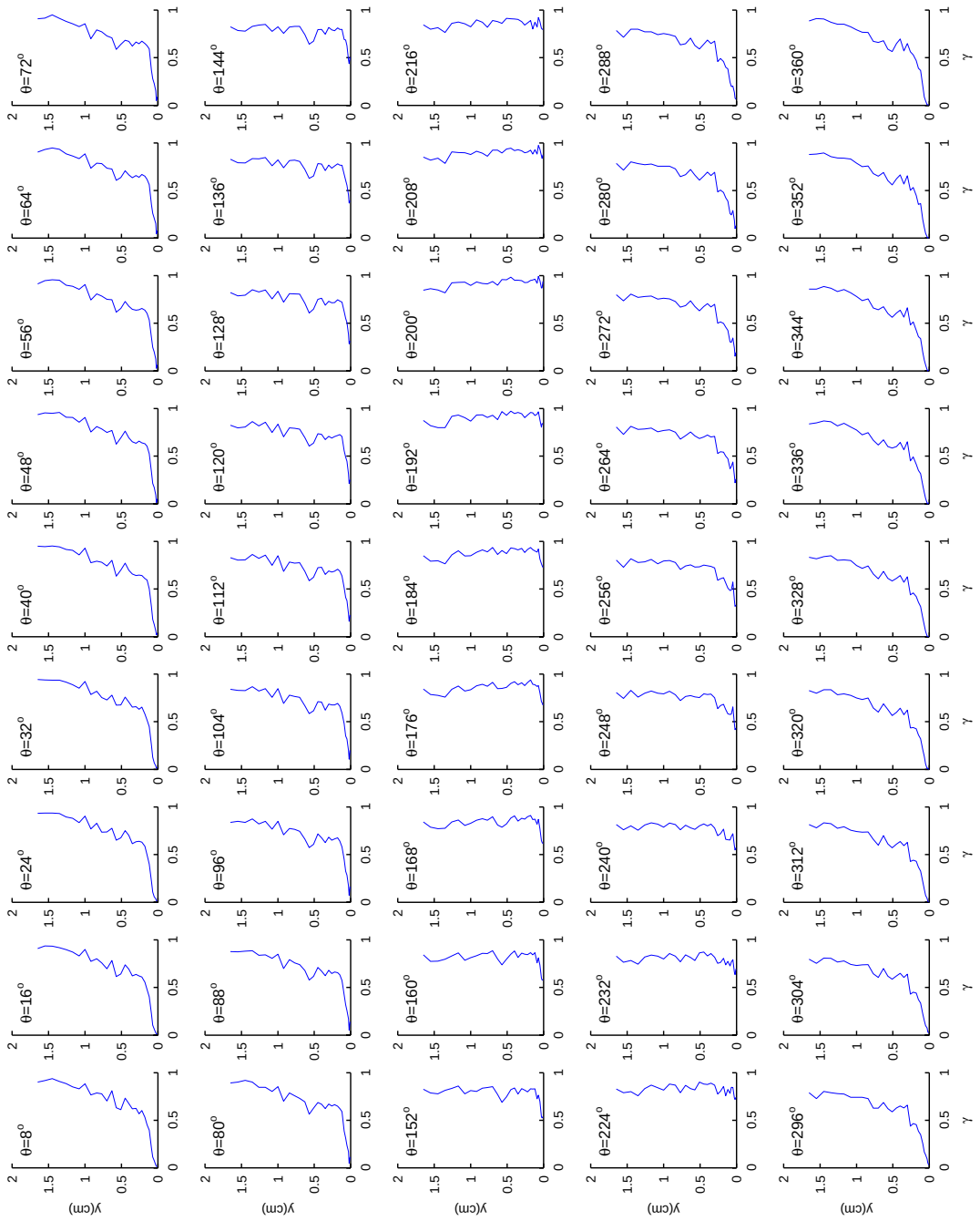

Figure 5.35: Phase average intermittency $\tilde{\gamma}(y, \theta)$ at p04, $s/L_{ss} = 31.36\%$, presented as a function of θ.

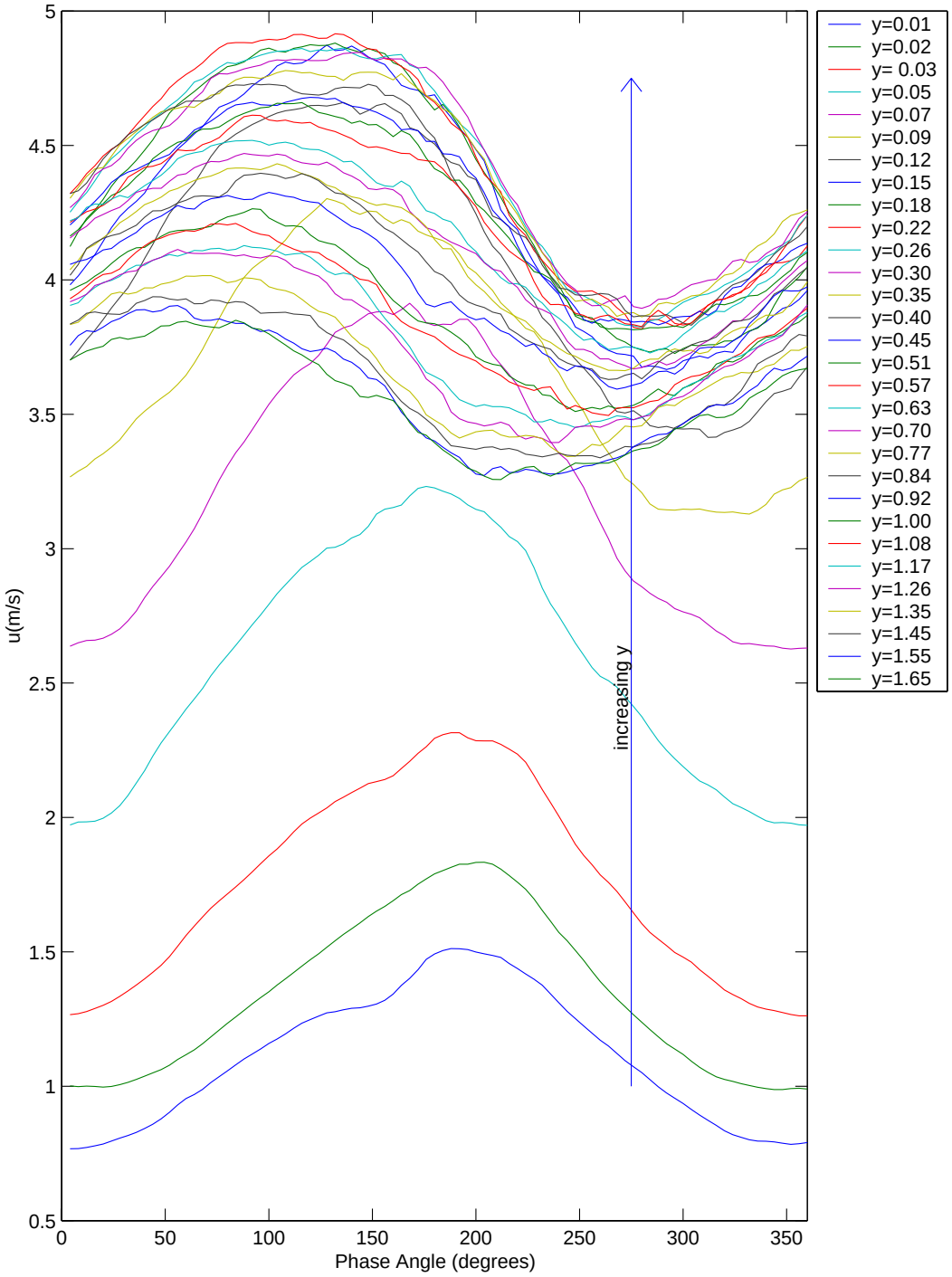

Figure 5.36: Phase average velocity $\tilde{u}(y, \theta)$ at p04, $s/L_{ss} = 31.36\%$, presented as a function of y (y-values are in cm).

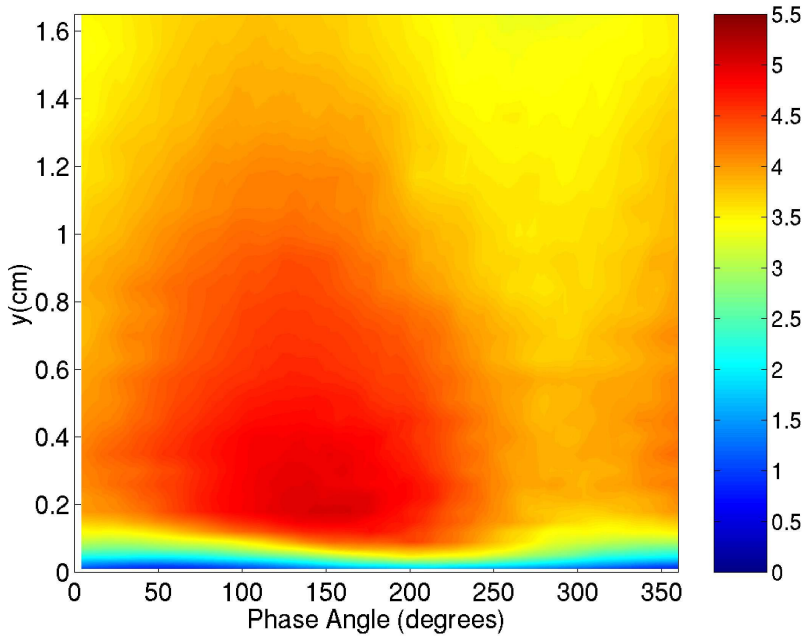

Figure 5.37: Phase average velocity $\tilde{u}(y,\theta)$ at p05, $s/L_{ss} = 37.35\%$.

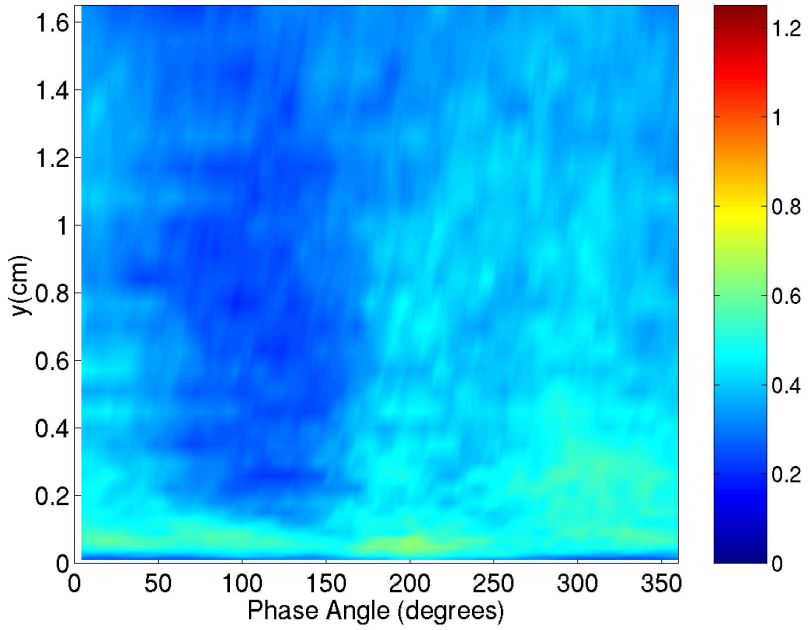

Figure 5.38: Phase average rms velocity fluctuation $\widetilde{u_{rms}}(y,\theta)$ at p05, $s/L_{ss} = 37.35\%$.

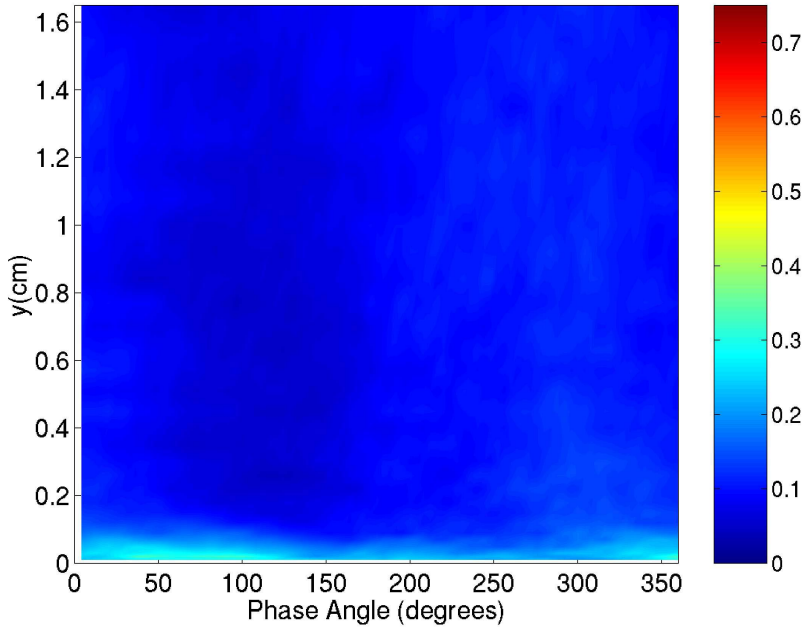

Figure 5.39: Phase average turbulence intensity $\widetilde{TI}(y,\theta)$ at p05, $s/L_{ss} = 37.35\%$.

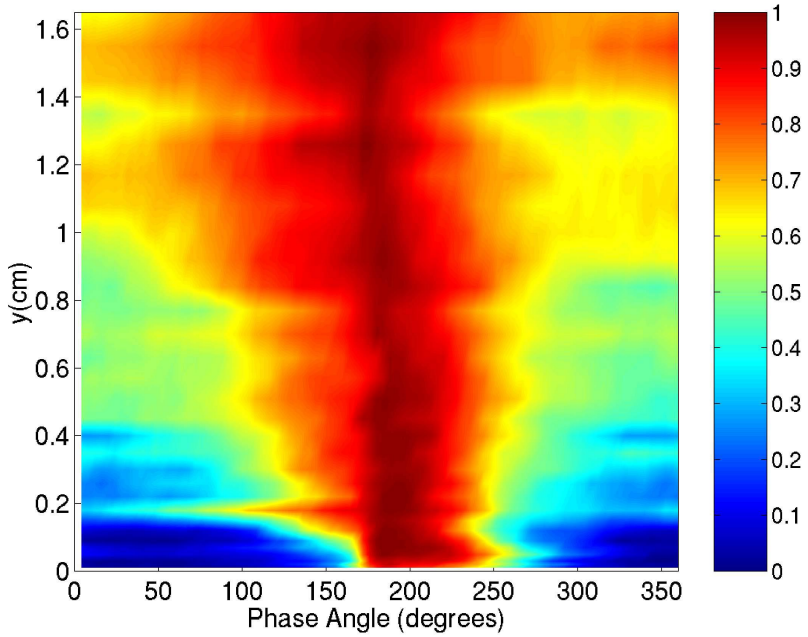

Figure 5.40: Phase average intermittency $\tilde{\gamma}(y,\theta)$ at p05, $s/L_{ss} = 37.35\%$.

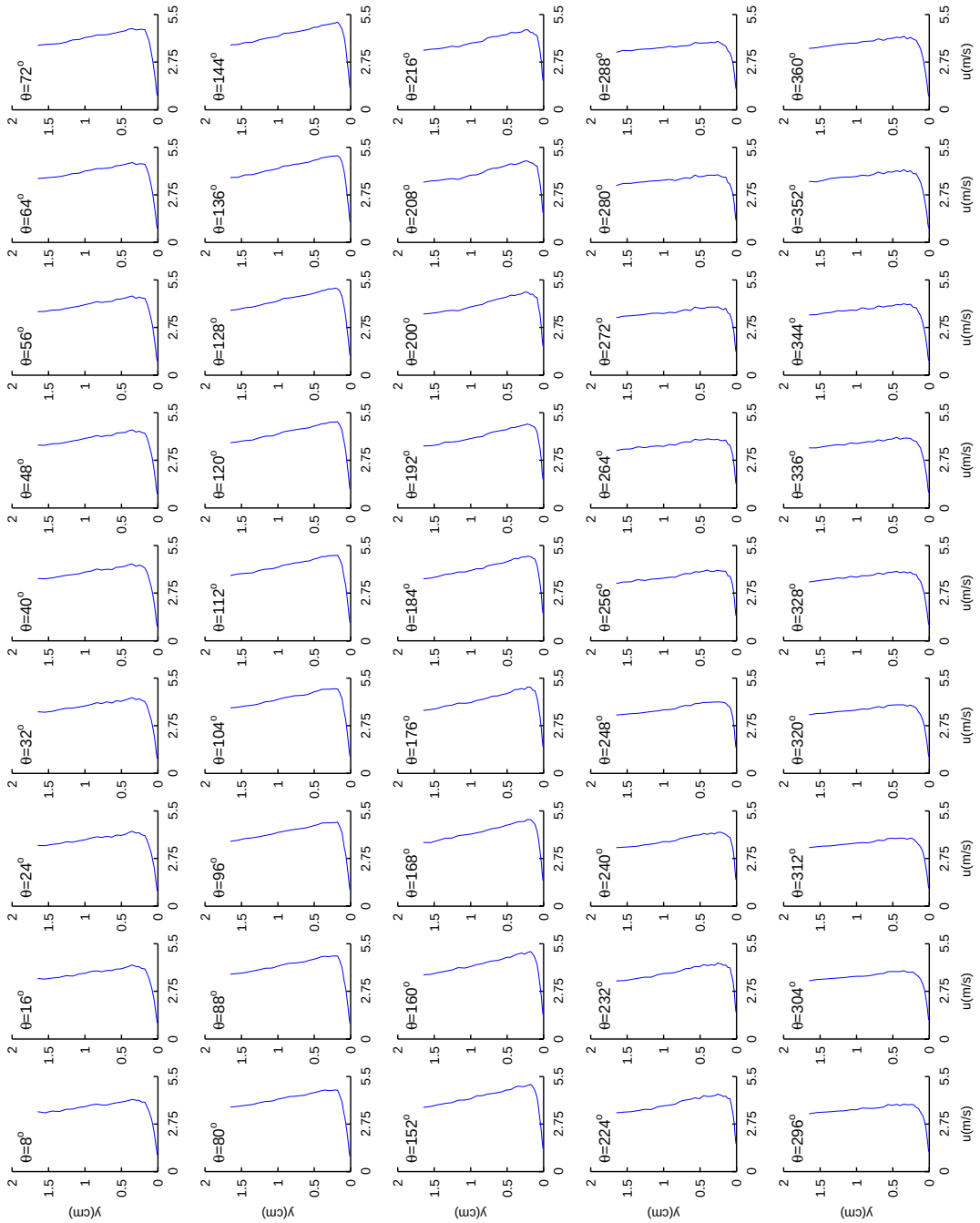

Figure 5.41: Phase average velocity $\tilde{u}(y, \theta)$ at p05, $s/L_{ss} = 37.35\%$, presented as a function of θ.

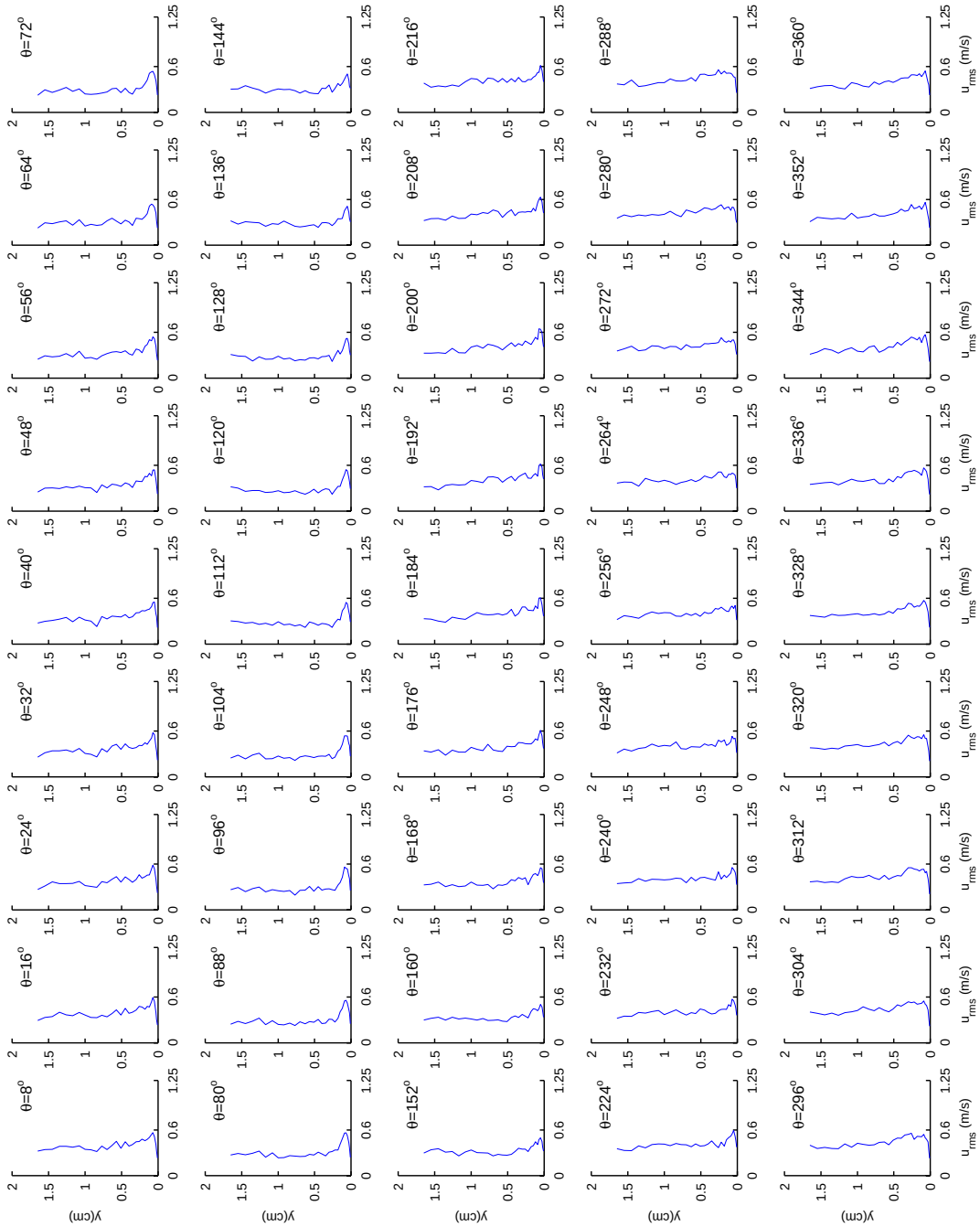

Figure 5.42: Phase average rms velocity fluctuation $\widetilde{u_{rms}}(y, \theta)$ at p05, $s/L_{ss} = 37.35\%$, presented as a function of θ.

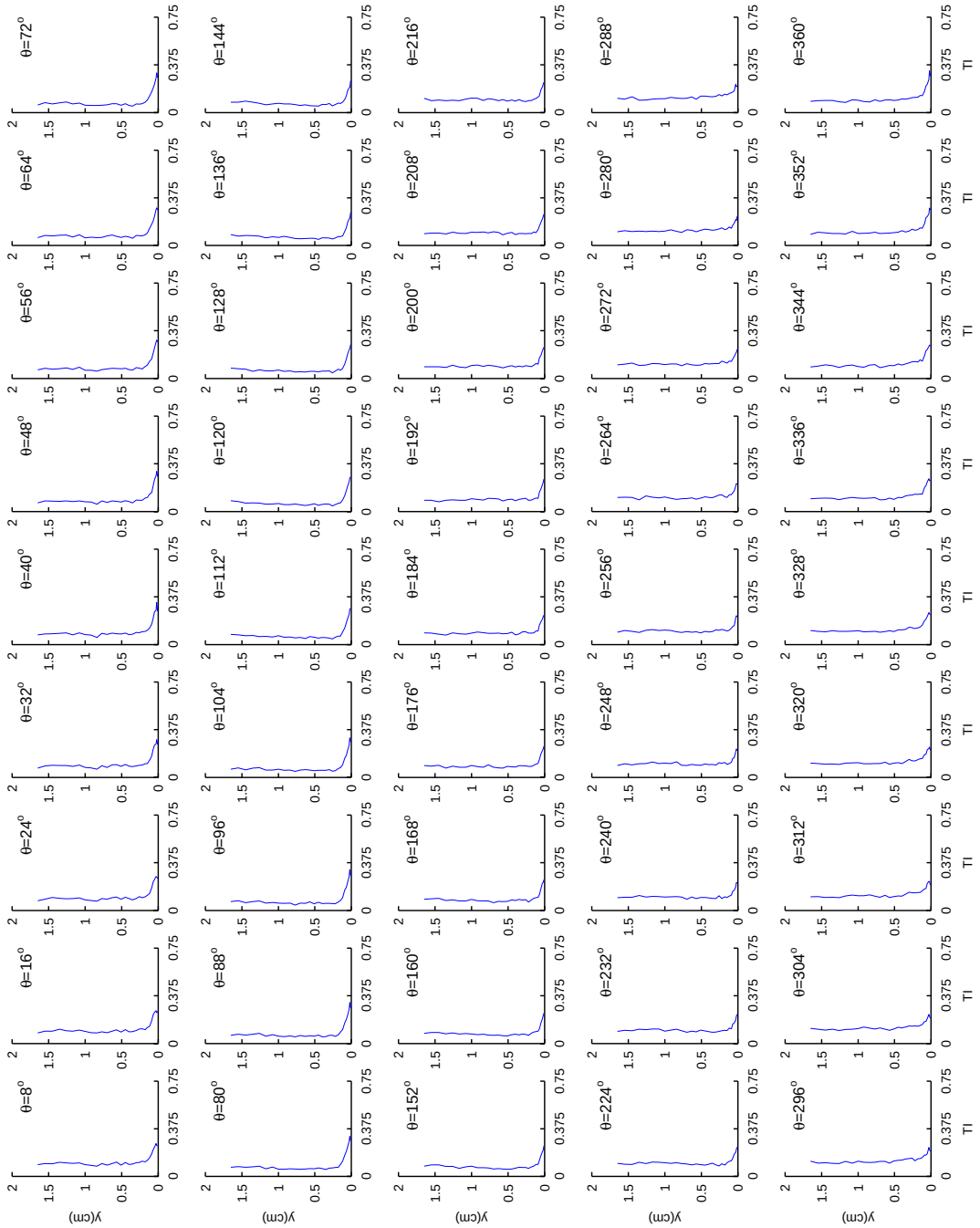

Figure 5.43: Phase average turbulence intensity $\widetilde{TI}(y,\theta)$ at p05, $s/L_{ss} = 37.35\%$, presented as a function of θ.

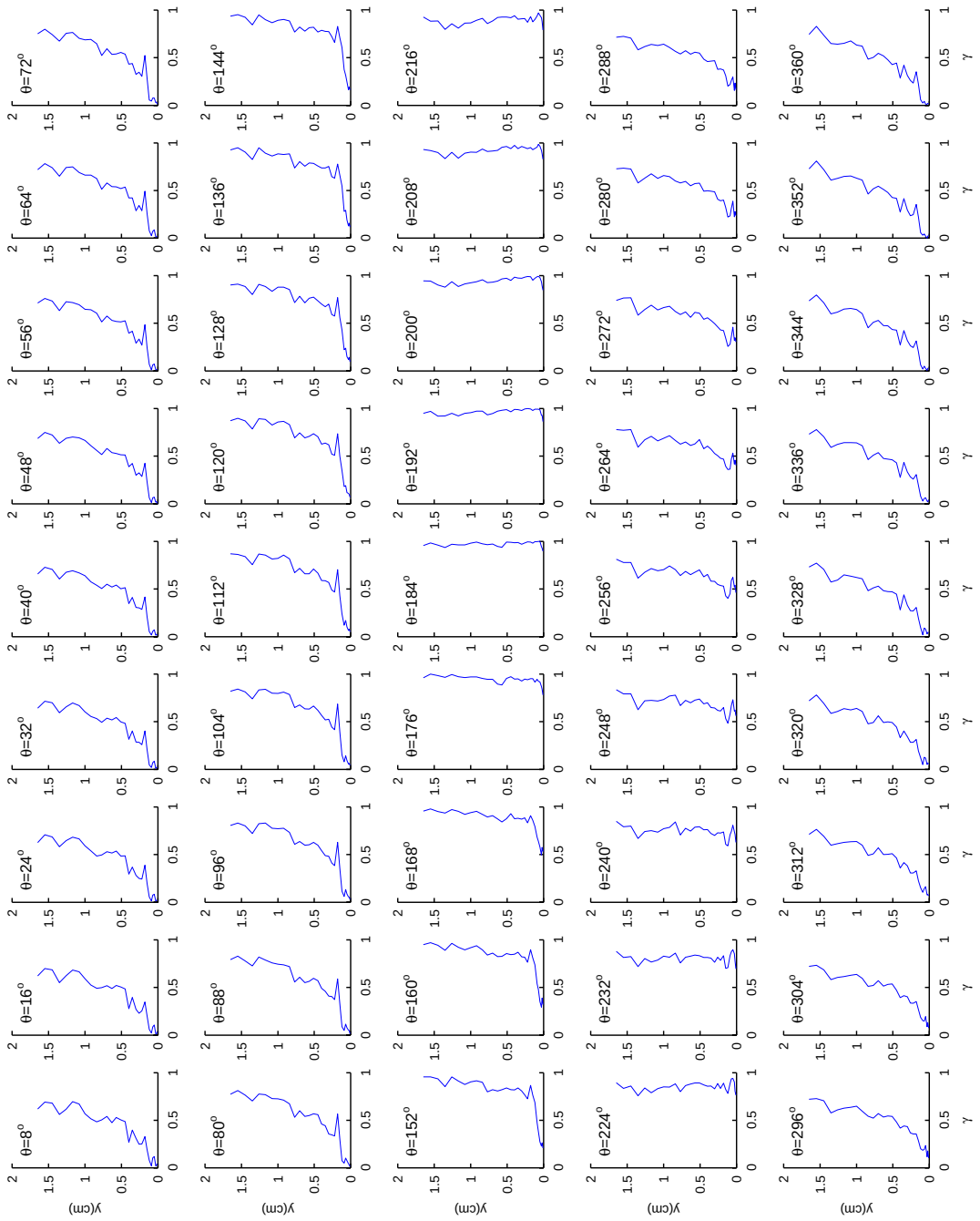

Figure 5.44: Phase average intermittency $\tilde{\gamma}(y, \theta)$ at p05, $s/L_{ss} = 37.35\%$, presented as a function of θ.

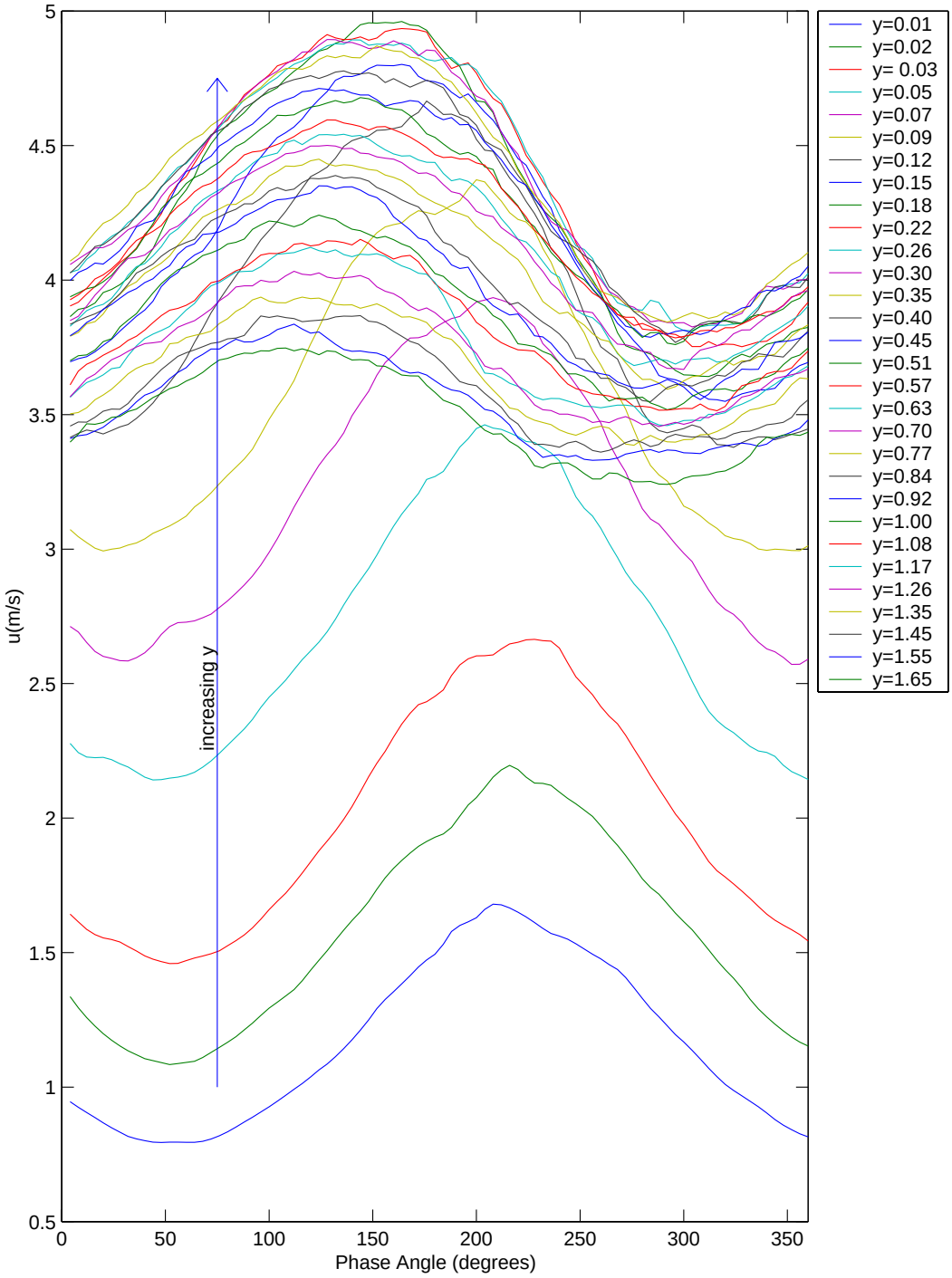

Figure 5.45: Phase average velocity $\tilde{u}(y, \theta)$ at p05, $s/L_{ss} = 37.35\%$, presented as a function of y (y-values are in cm).

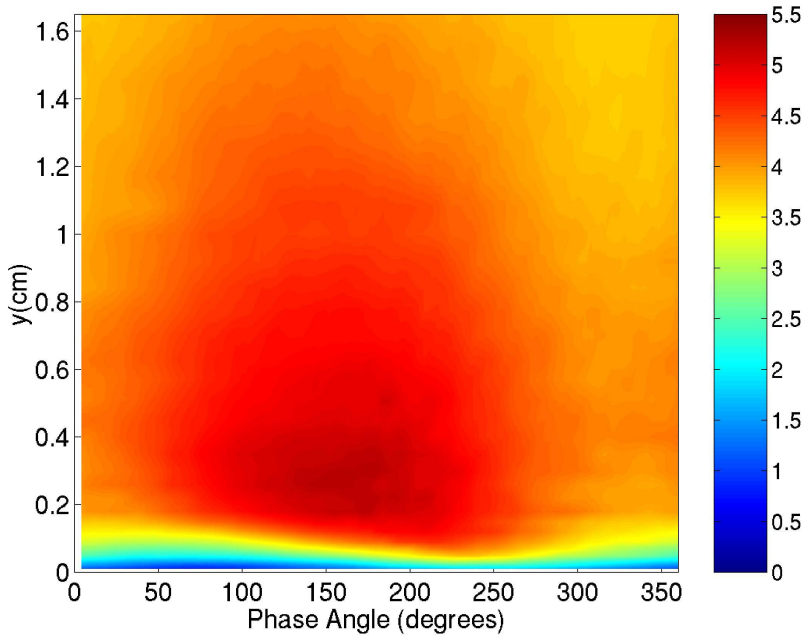

Figure 5.46: Phase average velocity $\tilde{u}(y, \theta)$ at p06, $s/L_{ss} = 43.34\%$.

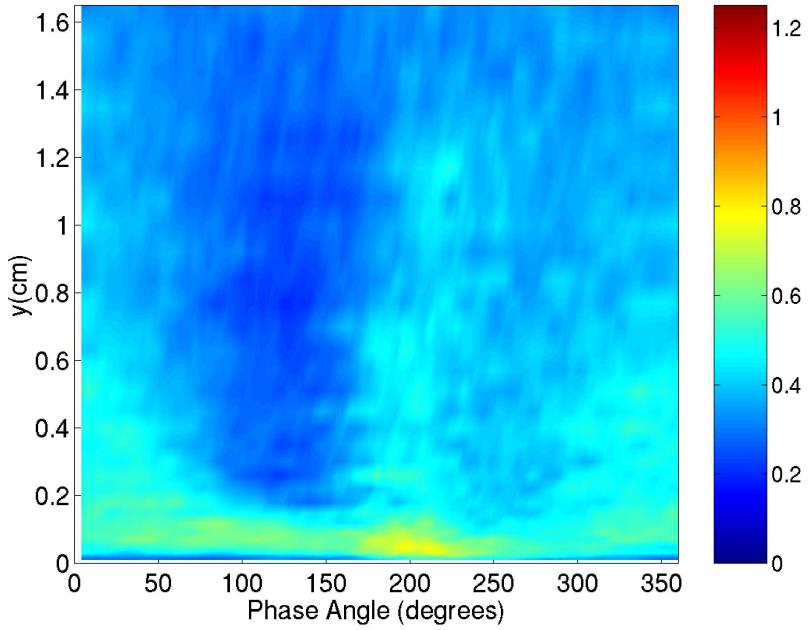

Figure 5.47: Phase average rms velocity fluctuation $\widetilde{u_{rms}}(y, \theta)$ at p06, $s/L_{ss} = 43.34\%$.

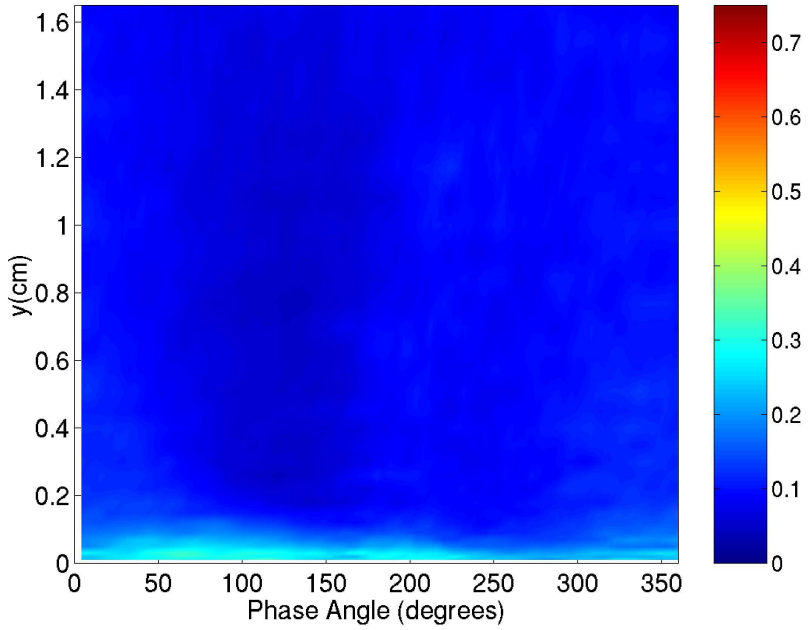

Figure 5.48: Phase average turbulence intensity $\widetilde{TI}(y,\theta)$ at p06, $s/L_{ss} = 43.34\%$.

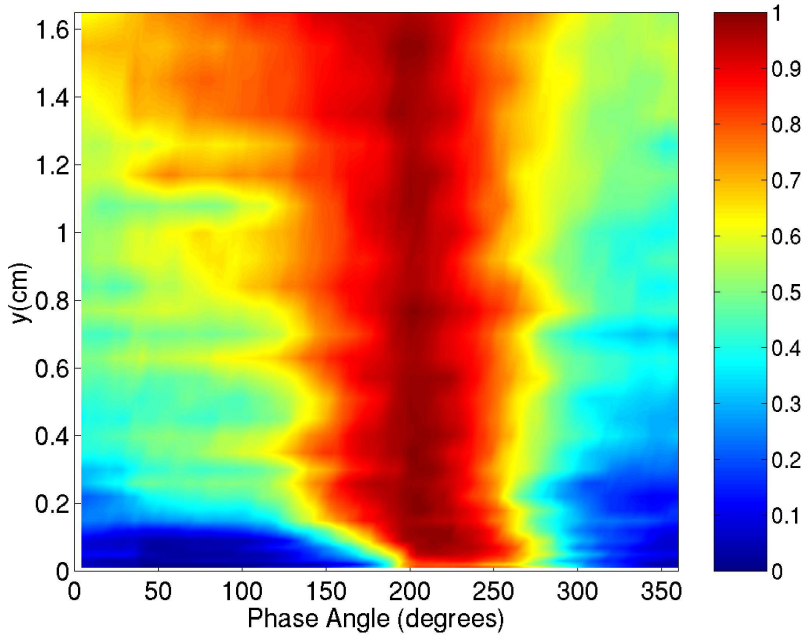

Figure 5.49: Phase average intermittency $\tilde{\gamma}(y,\theta)$ at p06, $s/L_{ss} = 43.34\%$.

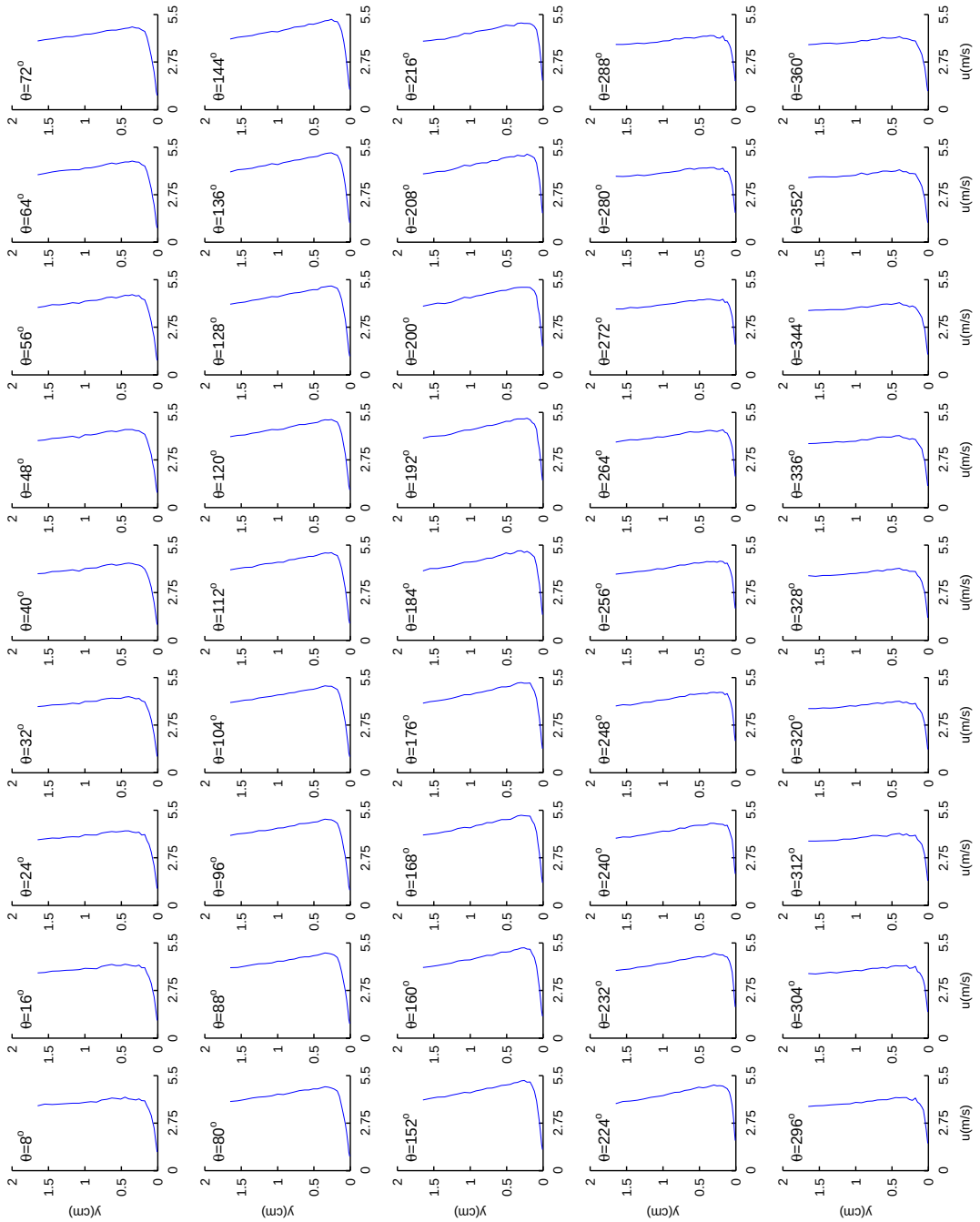

Figure 5.50: Phase average velocity $\tilde{u}(y, \theta)$ at p06, $s/L_{ss} = 43.34\%$, presented as a function of θ.

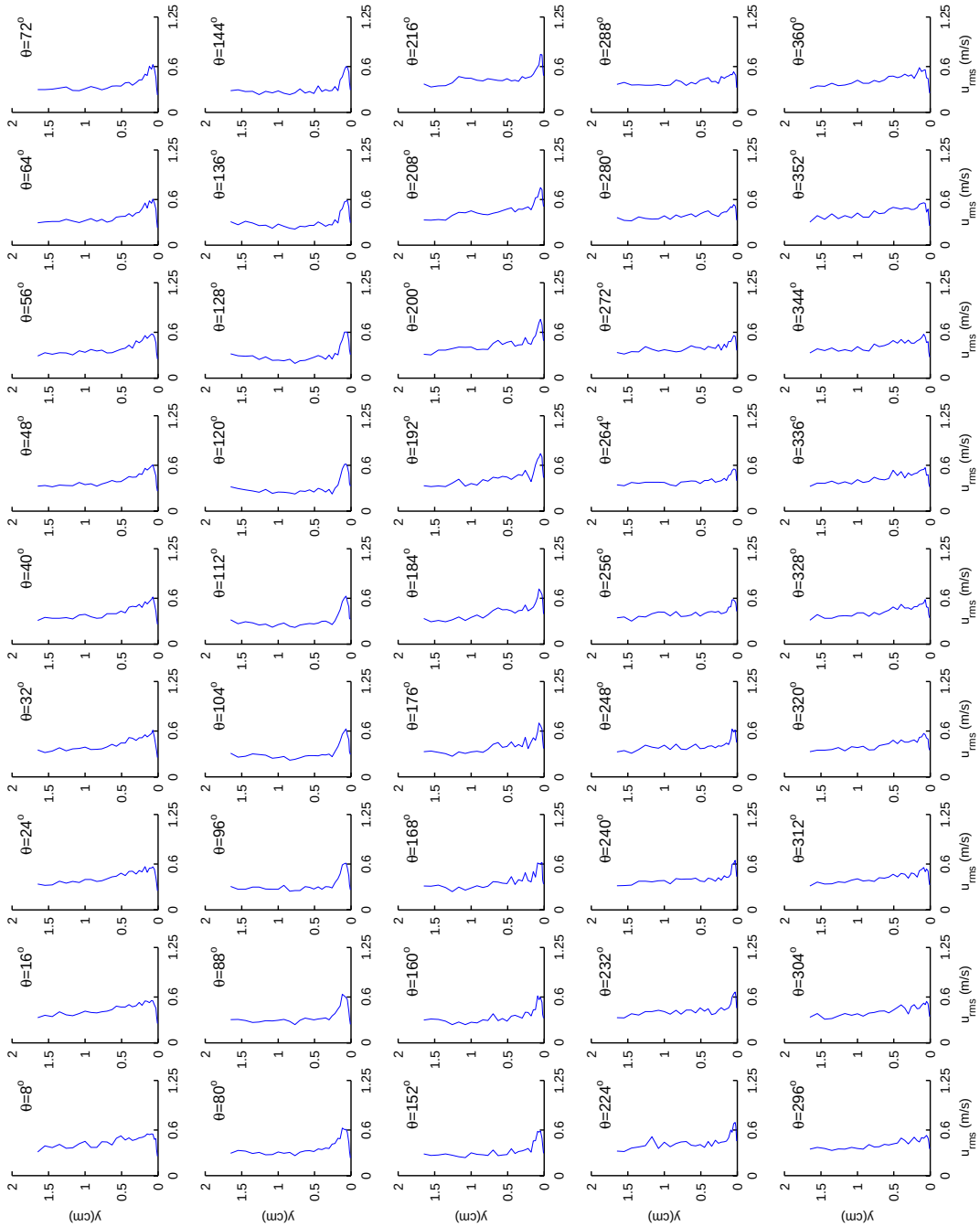

Figure 5.51: Phase average rms velocity fluctuation $\widetilde{u_{rms}}(y, \theta)$ at p06, $s/L_{ss} = 43.34\%$, presented as a function of θ.

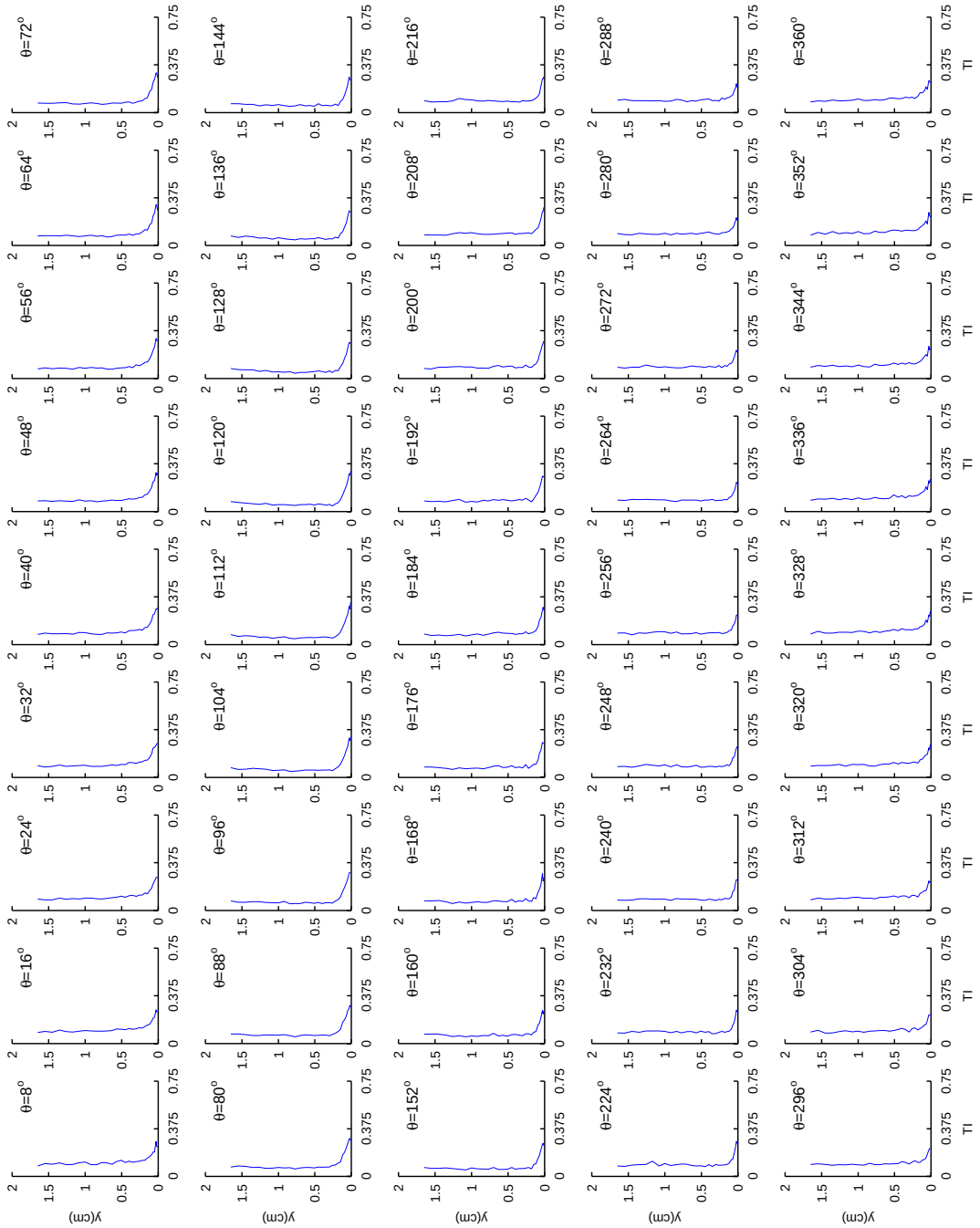

Figure 5.52: Phase average turbulence intensity $\widetilde{TI}(y,\theta)$ at p06, $s/L_{ss} = 43.34\%$, presented as a function of θ.

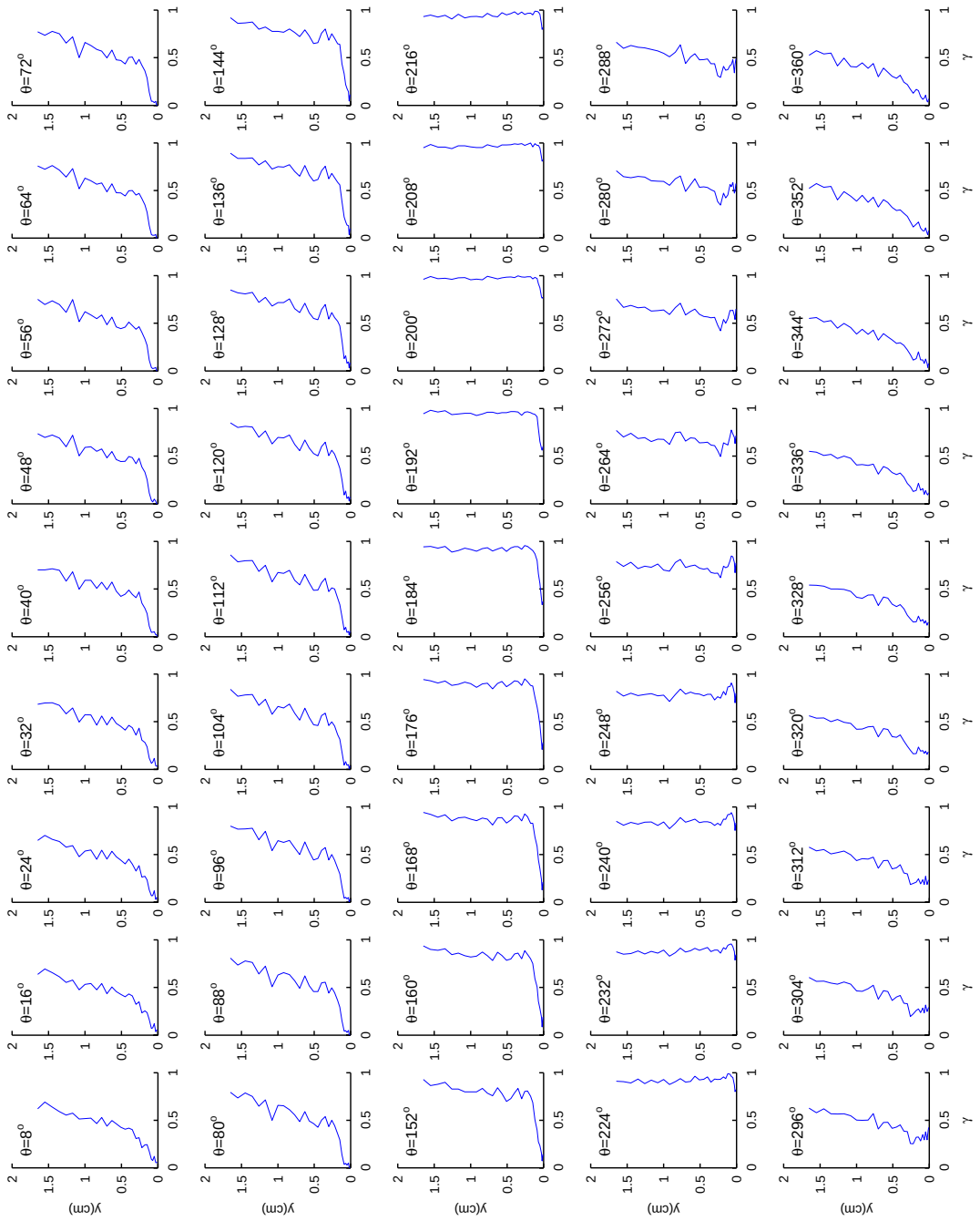

Figure 5.53: Phase average intermittency $\tilde{\gamma}(y, \theta)$ at p06, $s/L_{ss} = 43.34\%$, presented as a function of θ.

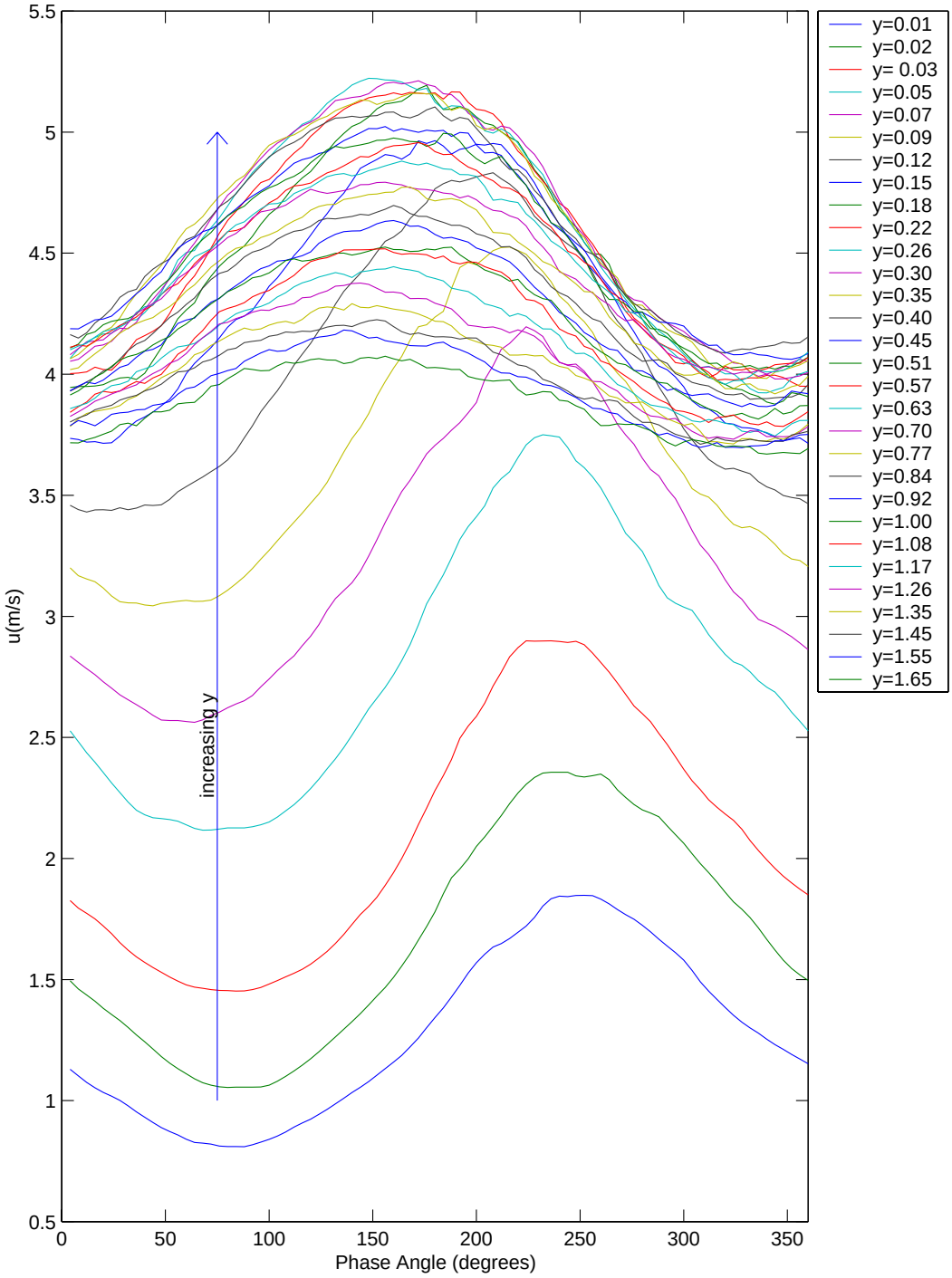

Figure 5.54: Phase average velocity $\tilde{u}(y, \theta)$ at p06, $s/L_{ss} = 43.34\%$, presented as a function of y (y-values are in cm).

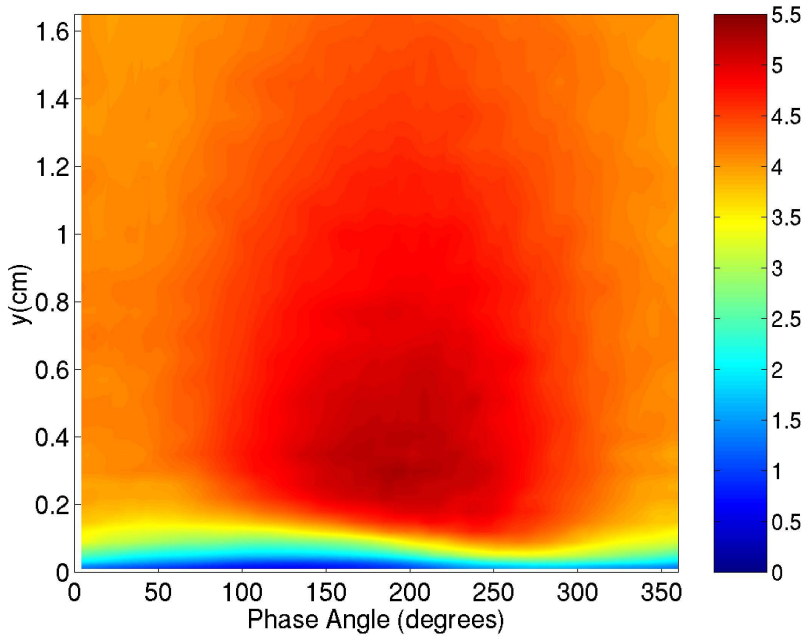

Figure 5.55: Phase average velocity $\tilde{u}(y, \theta)$ at p07, $s/L_{ss} = 49.33\%$.

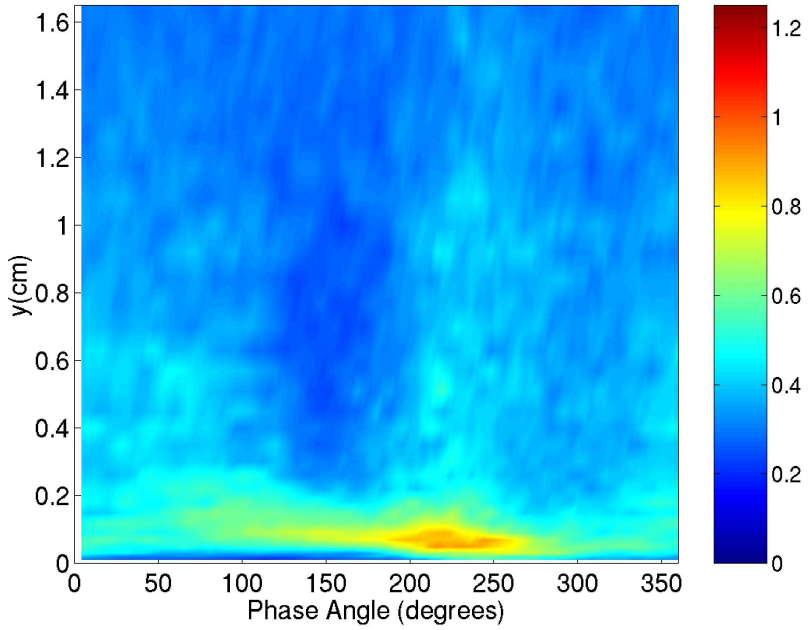

Figure 5.56: Phase average rms velocity fluctuation $\widetilde{u_{rms}}(y, \theta)$ at p07, $s/L_{ss} = 49.33\%$.

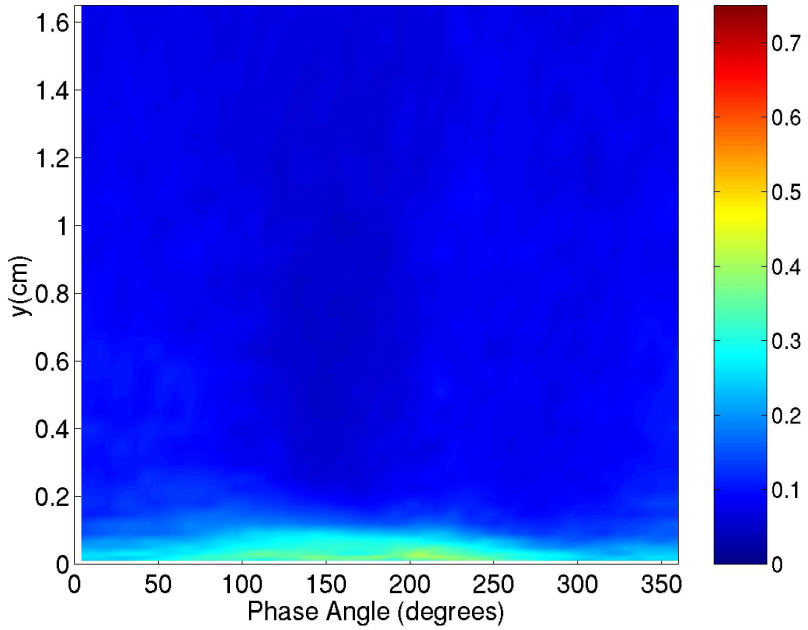

Figure 5.57: Phase average turbulence intensity $\widetilde{TI}(y,\theta)$ at p07, $s/L_{ss} = 49.33\%$.

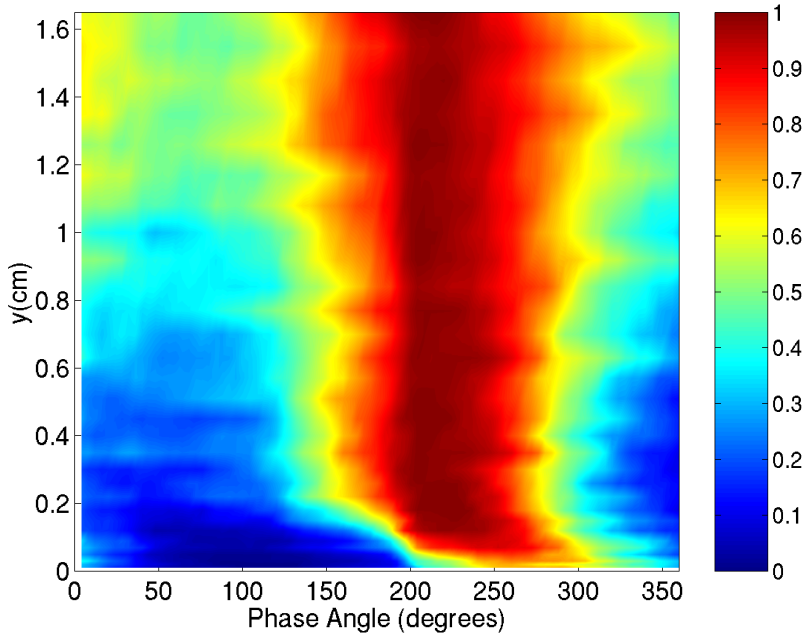

Figure 5.58: Phase average intermittency $\tilde{\gamma}(y,\theta)$ at p07, $s/L_{ss} = 49.33\%$.

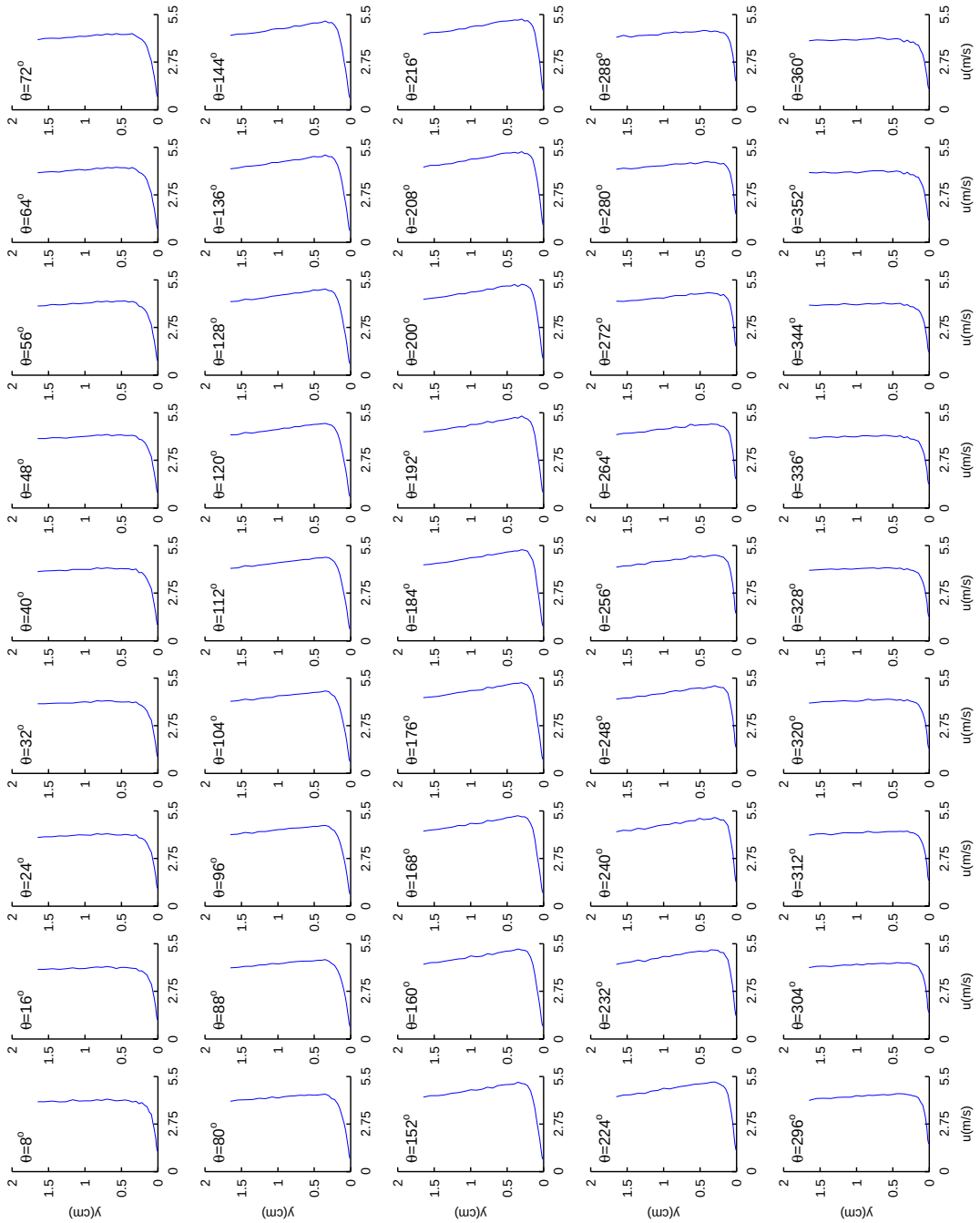

Figure 5.59: Phase average velocity $\tilde{u}(y, \theta)$ at p07, $s/L_{ss} = 49.33\%$, presented as a function of θ.

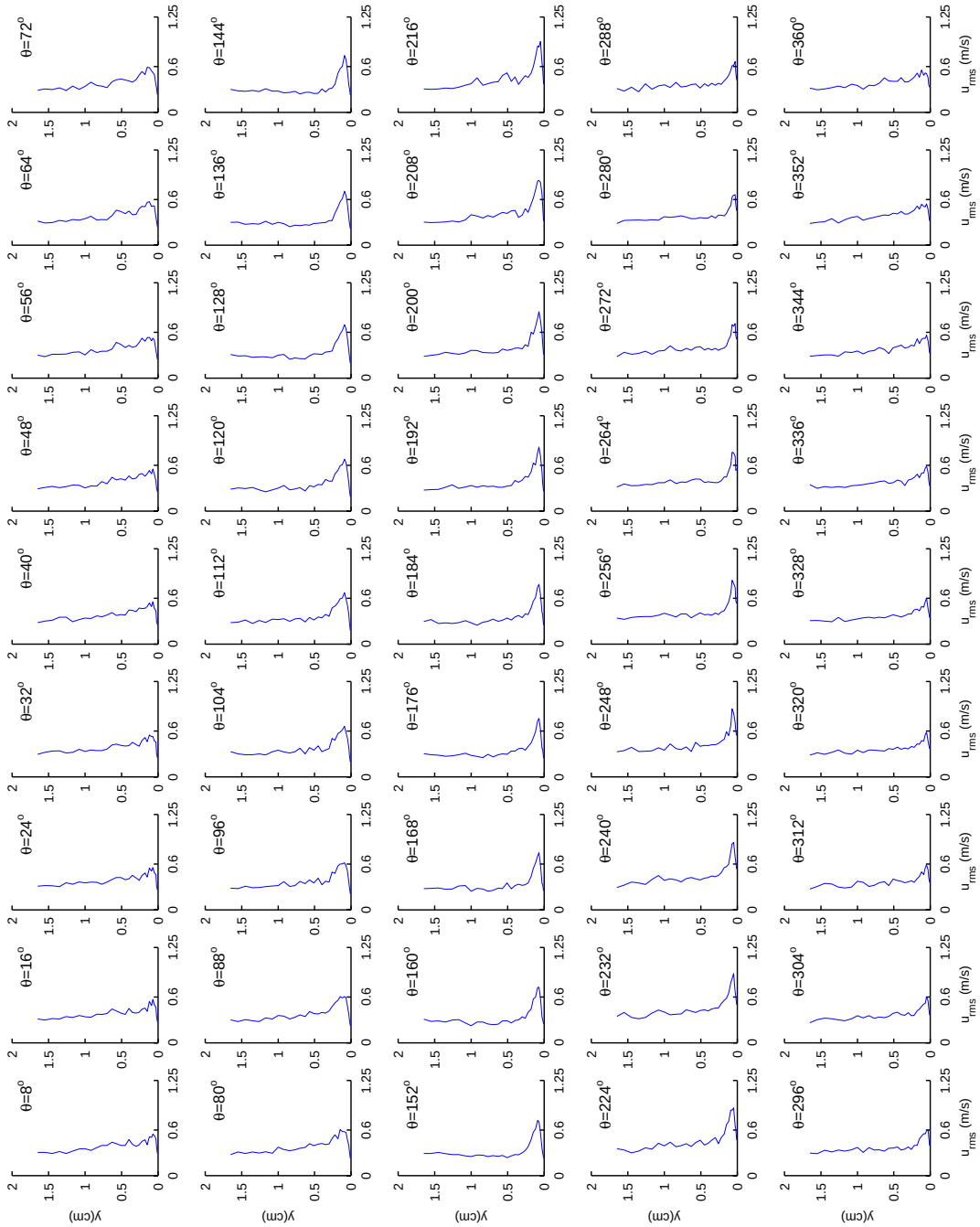

Figure 5.60: Phase average rms velocity fluctuation $\widetilde{u_{rms}}(y, \theta)$ at p07, $s/L_{ss} = 49.33\%$, presented as a function of θ.

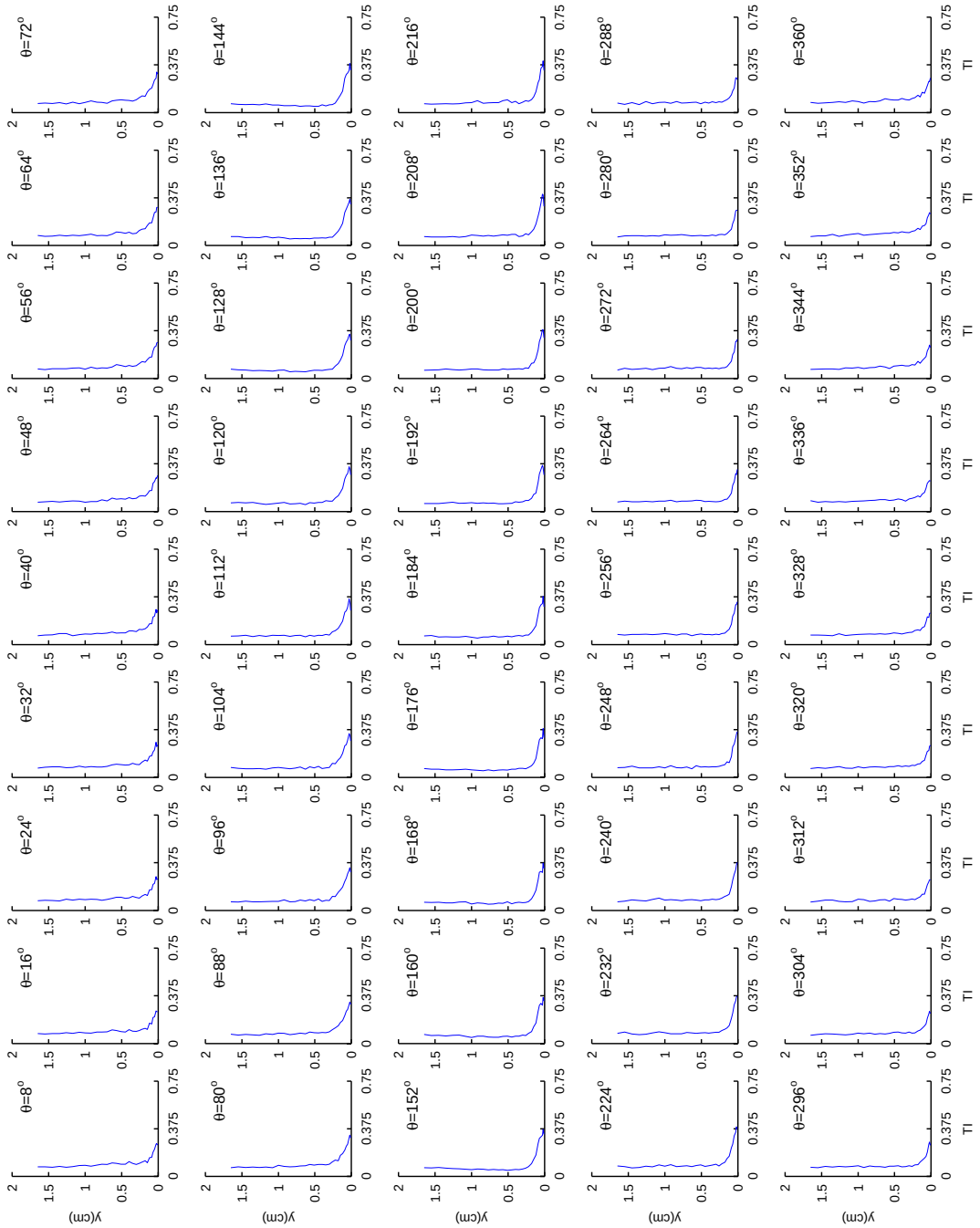

Figure 5.61: Phase average turbulence intensity $\widetilde{TI}(y,\theta)$ at p07, $s/L_{ss} = 49.33\%$, presented as a function of θ.

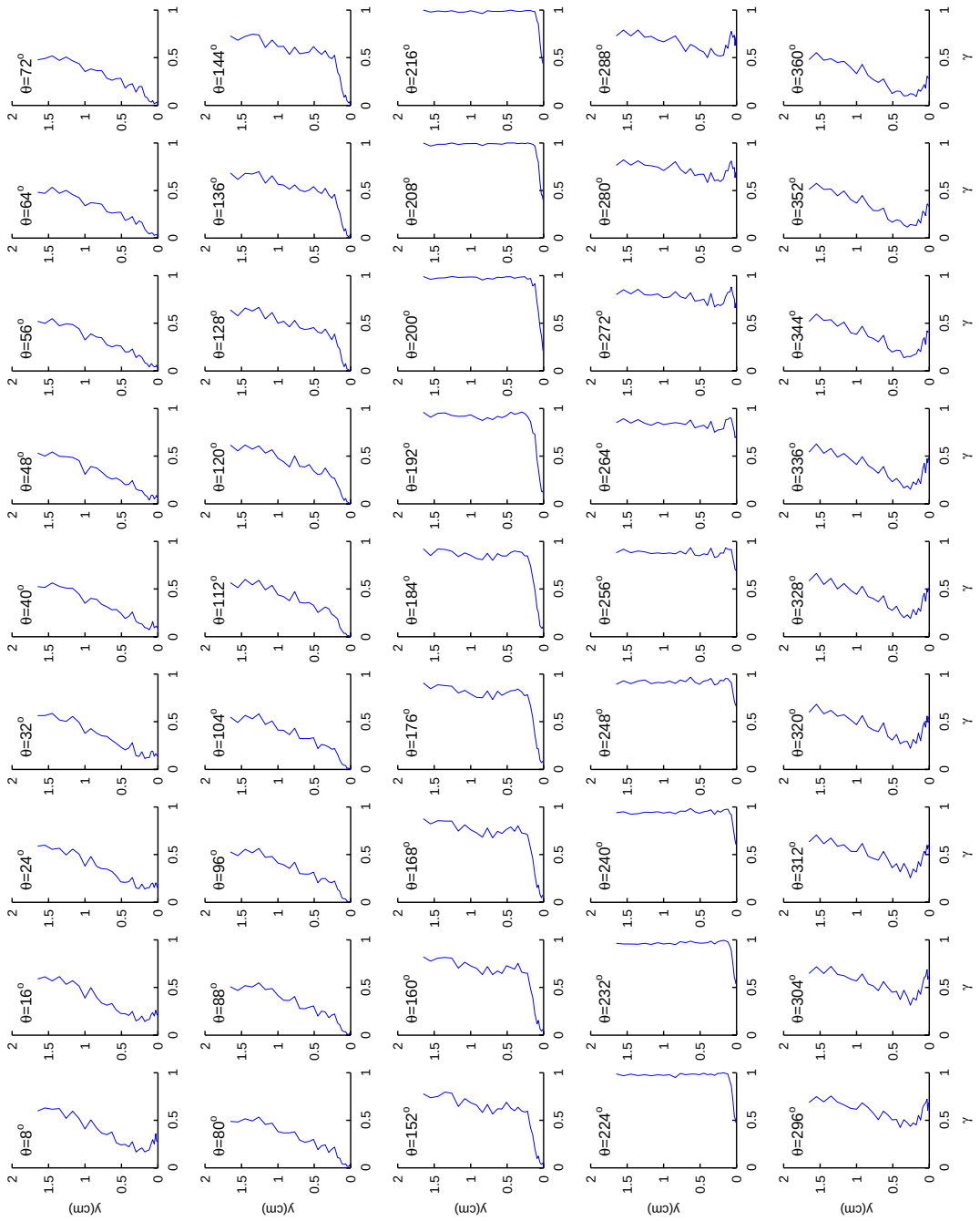

Figure 5.62: Phase average intermittency $\tilde{\gamma}(y, \theta)$ at p07, $s/L_{ss} = 49.33\%$, presented as a function of θ.

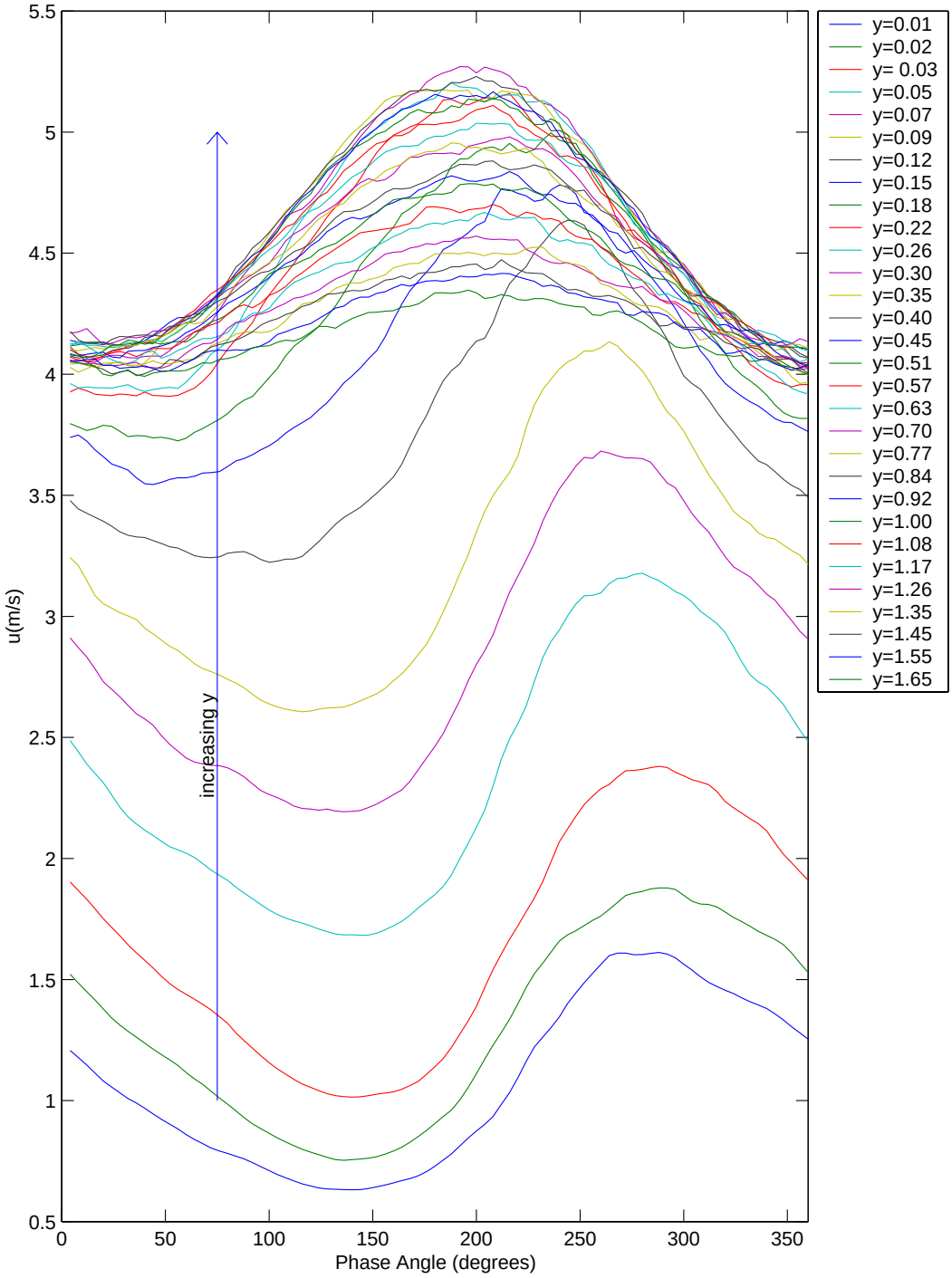

Figure 5.63: Phase average velocity $\tilde{u}(y, \theta)$ at p07, $s/L_{ss} = 49.33\%$, presented as a function of y (y-values are in cm).

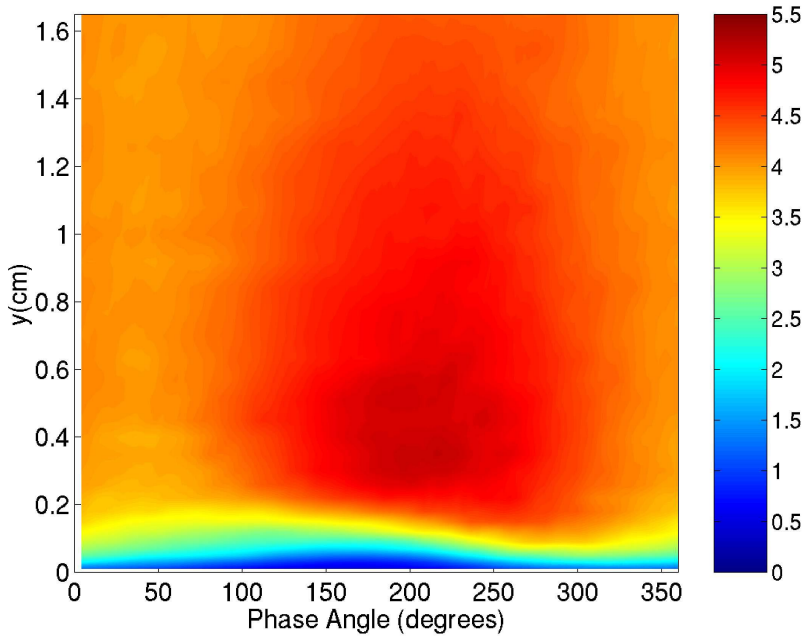

Figure 5.64: Phase average velocity $\tilde{u}(y, \theta)$ at p08, $s/L_{ss} = 55.33\%$.

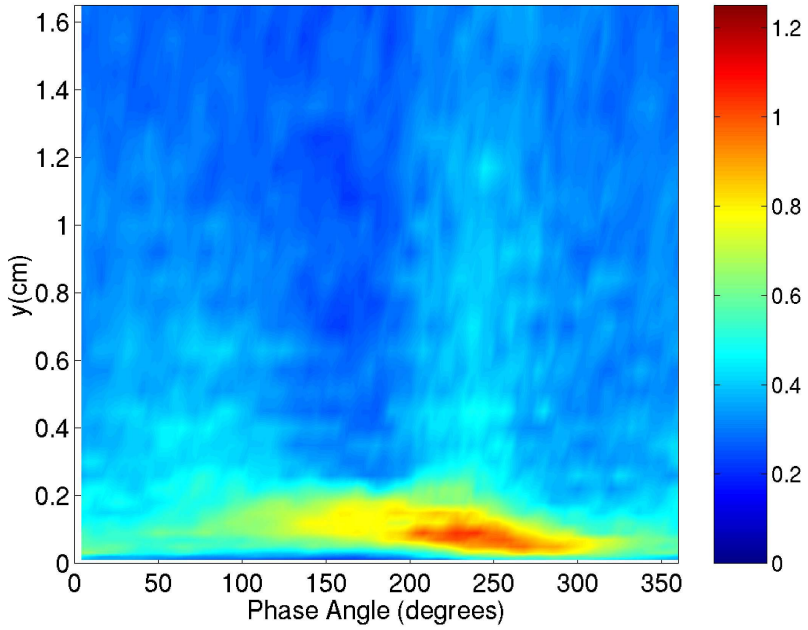

Figure 5.65: Phase average rms velocity fluctuation $\widetilde{u_{rms}}(y, \theta)$ at p08, $s/L_{ss} = 55.33\%$.

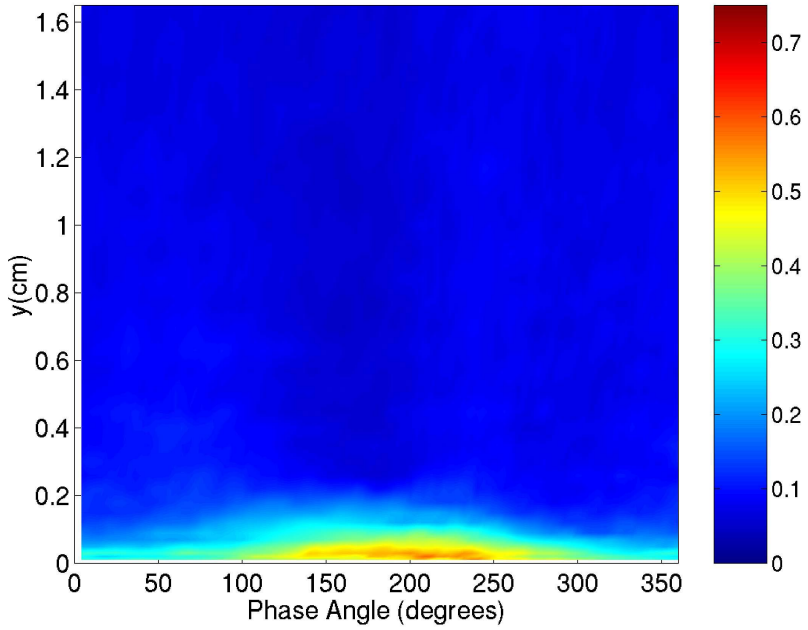

Figure 5.66: Phase average turbulence intensity $\widetilde{TI}(y,\theta)$ at p08, $s/L_{ss} = 55.33\%$.

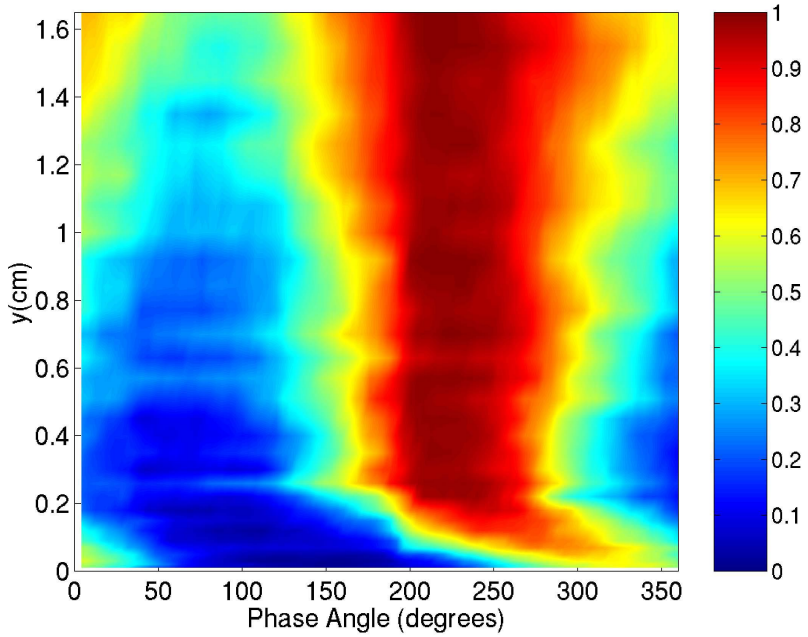

Figure 5.67: Phase average intermittency $\tilde{\gamma}(y,\theta)$ at p08, $s/L_{ss} = 55.33\%$.

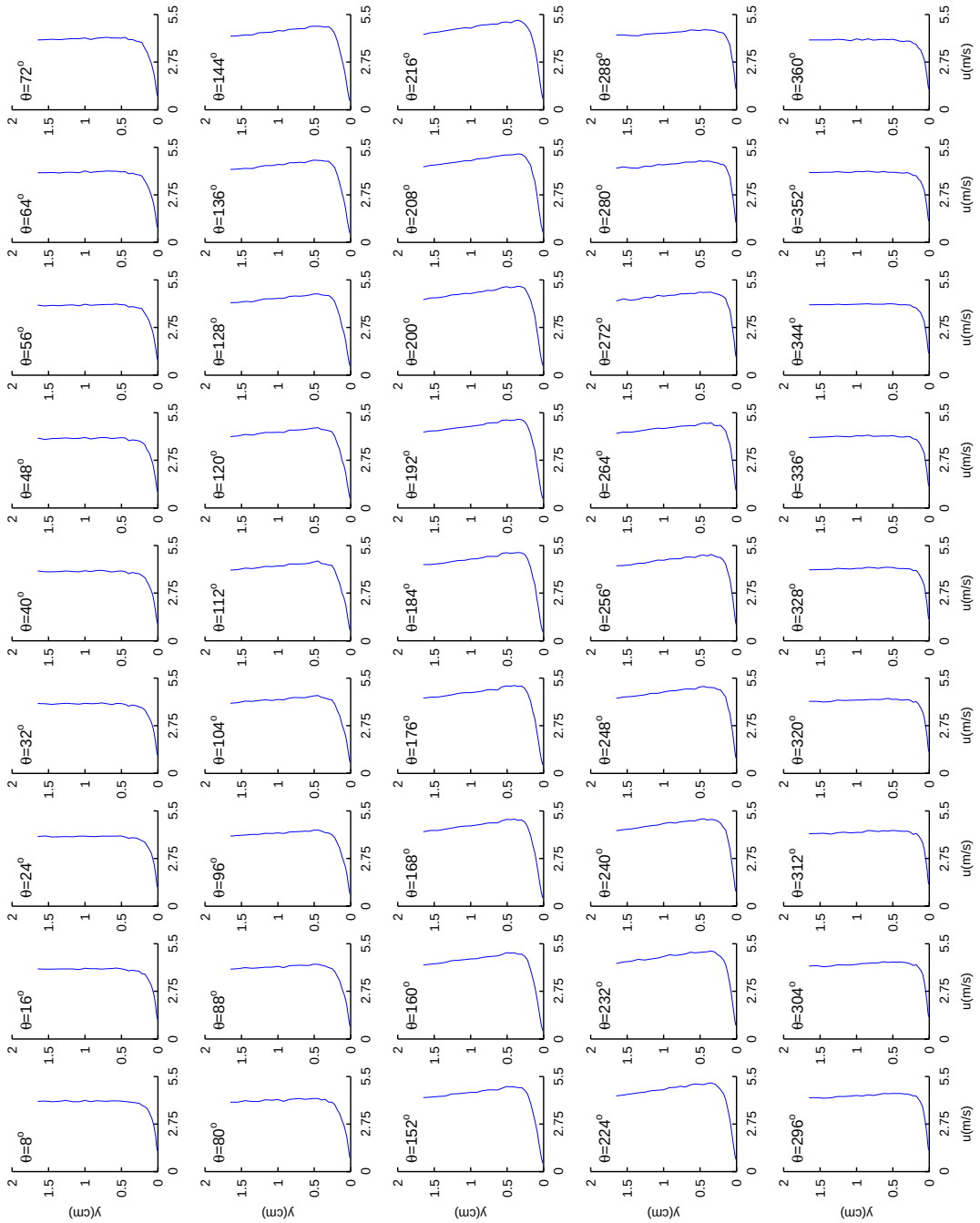

Figure 5.68: Phase average velocity $\tilde{u}(y, \theta)$ at p08, $s/L_{ss} = 55.33\%$, presented as a function of θ.

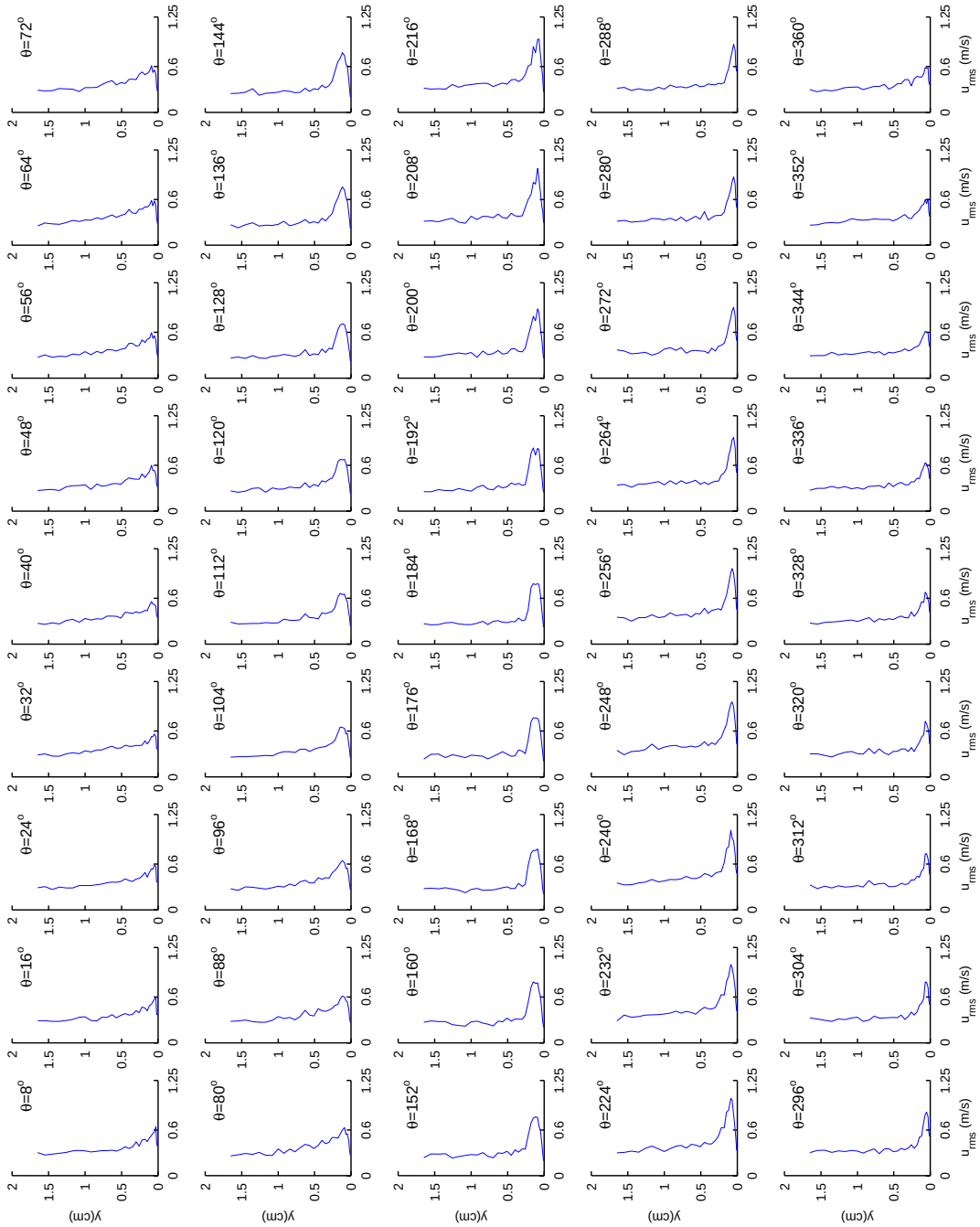

Figure 5.69: Phase average rms velocity fluctuation $\widetilde{u_{rms}}(y, \theta)$ at p08, $s/L_{ss} = 55.33\%$, presented as a function of θ.

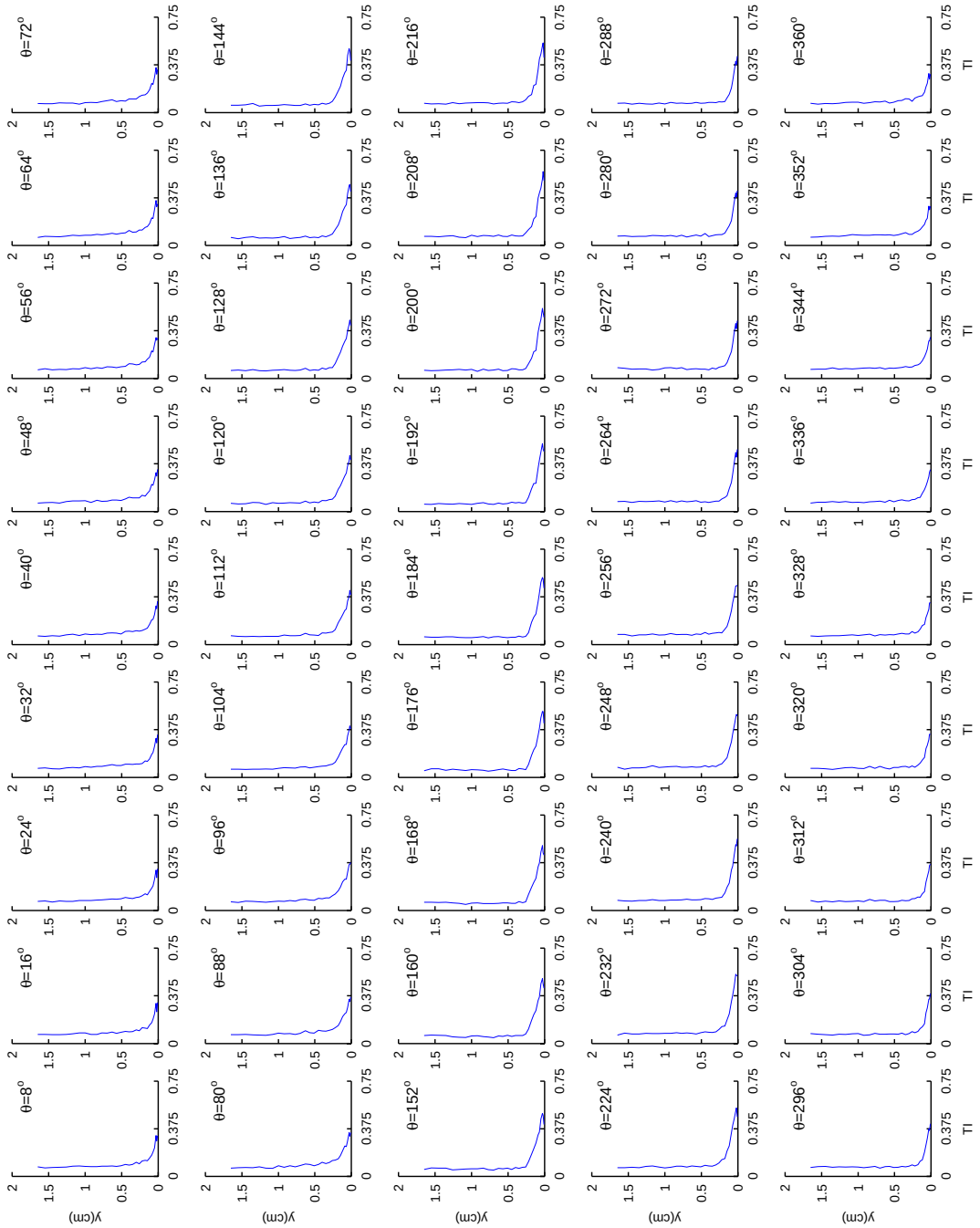

Figure 5.70: Phase average turbulence intensity $\widetilde{TI}(y,\theta)$ at p08, $s/L_{ss} = 55.33\%$, presented as a function of θ.

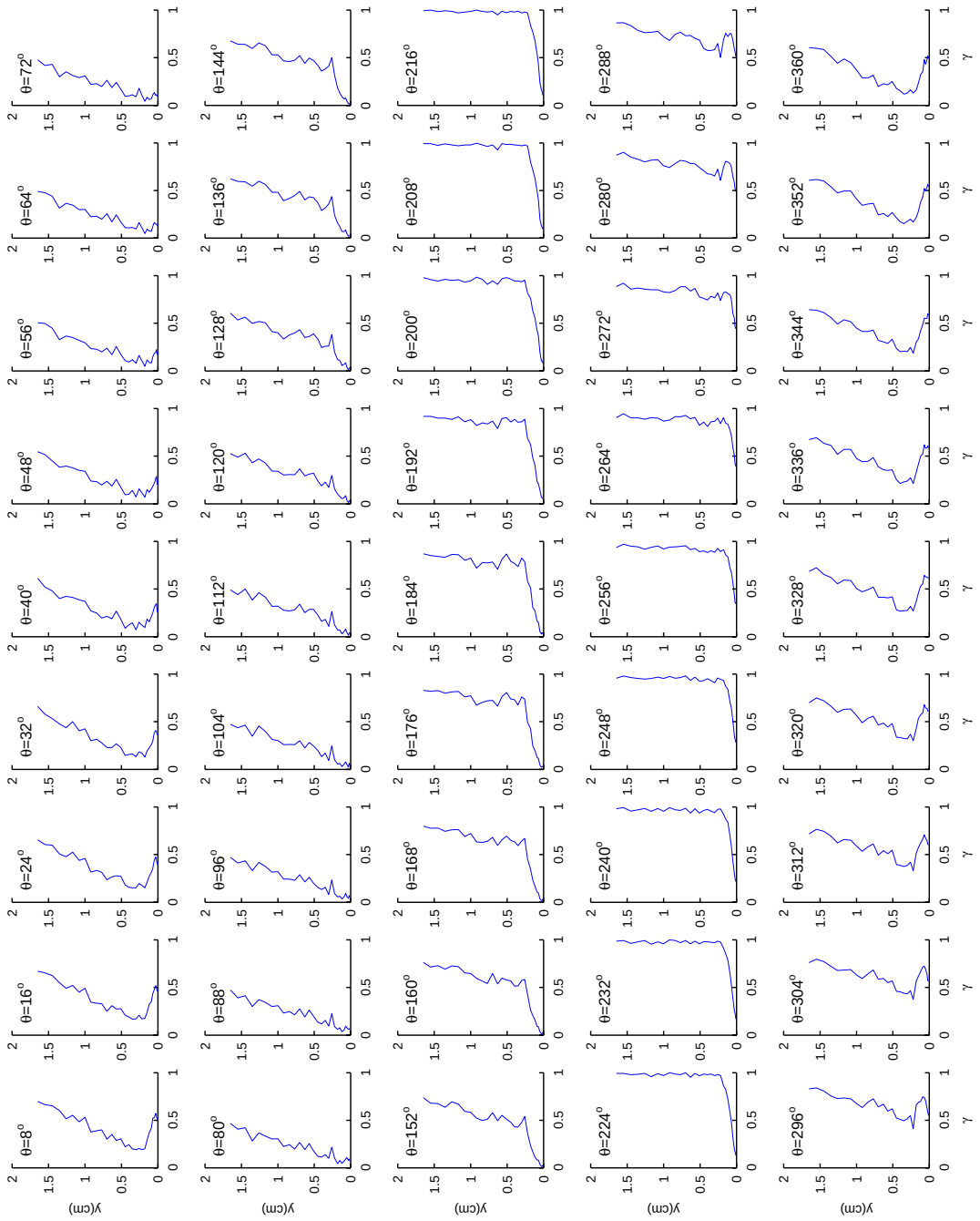

Figure 5.71: Phase average intermittency $\tilde{\gamma}(y, \theta)$ at p08, $s/L_{ss} = 55.33\%$, presented as a function of θ.

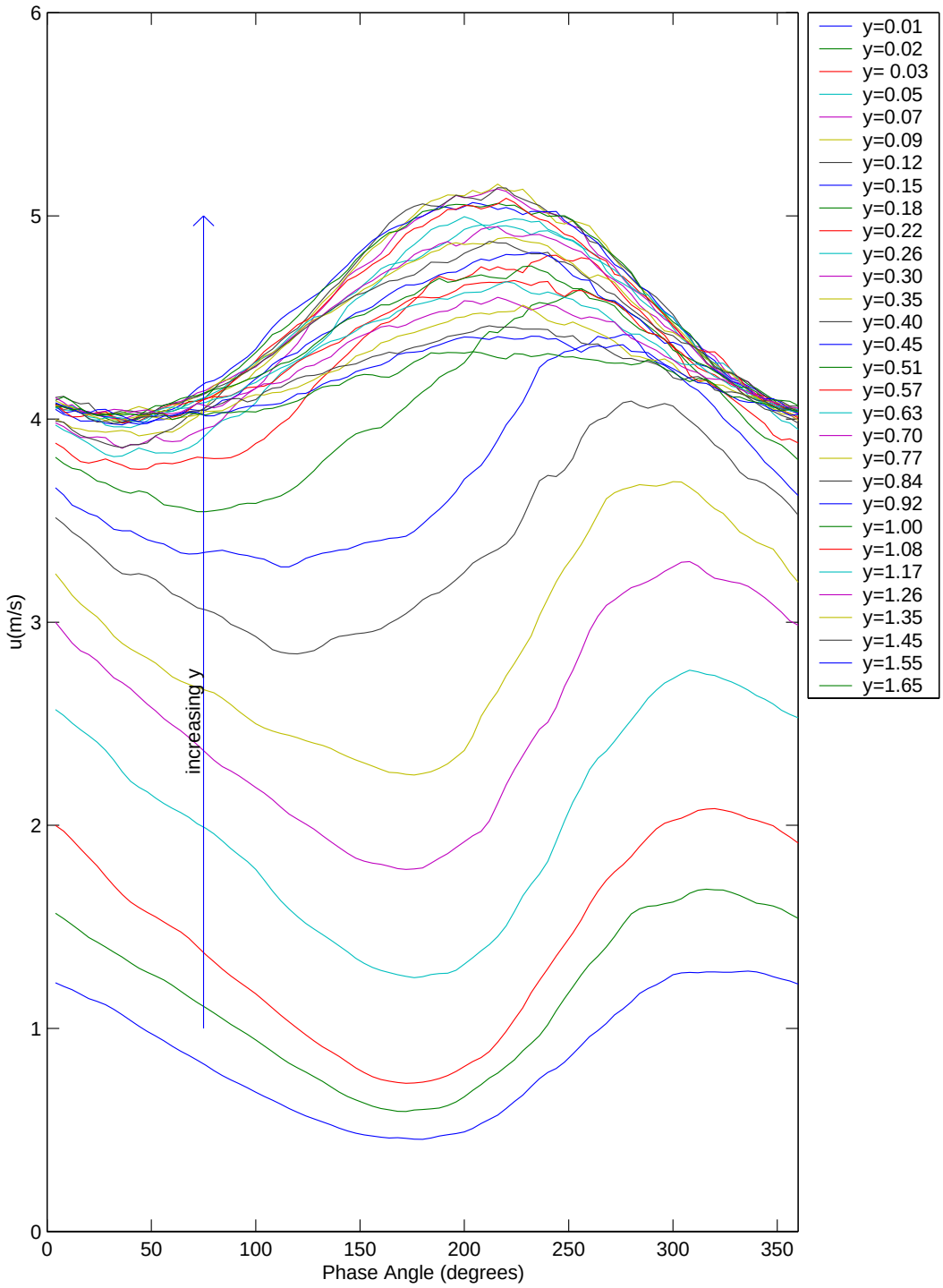

Figure 5.72: Phase average velocity $\tilde{u}(y, \theta)$ at p08, $s/L_{ss} = 55.33\%$, presented as a function of y (y-values are in cm).

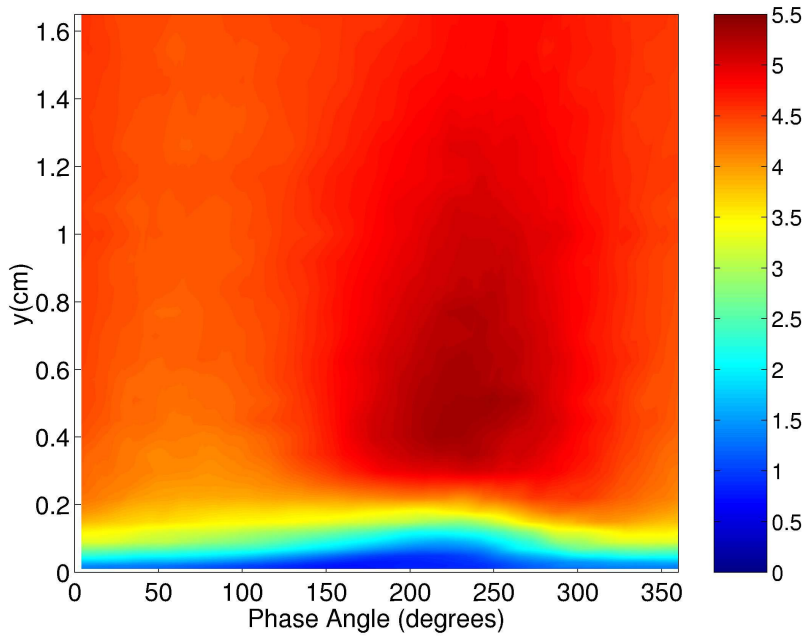

Figure 5.73: Phase average velocity $\tilde{u}(y,\theta)$ at p09, $s/L_{ss} = 61.32\%$.

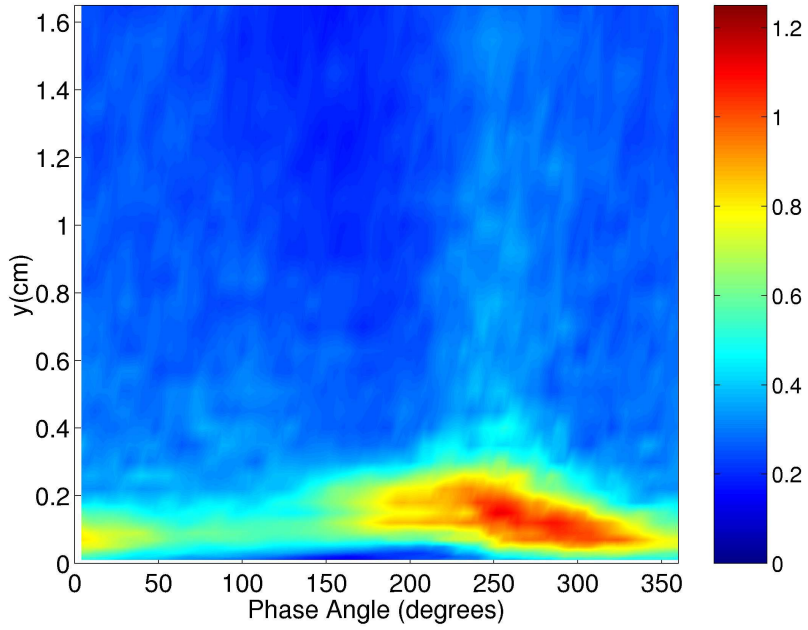

Figure 5.74: Phase average rms velocity fluctuation $\widetilde{u_{rms}}(y,\theta)$ at p09, $s/L_{ss} = 61.32\%$.

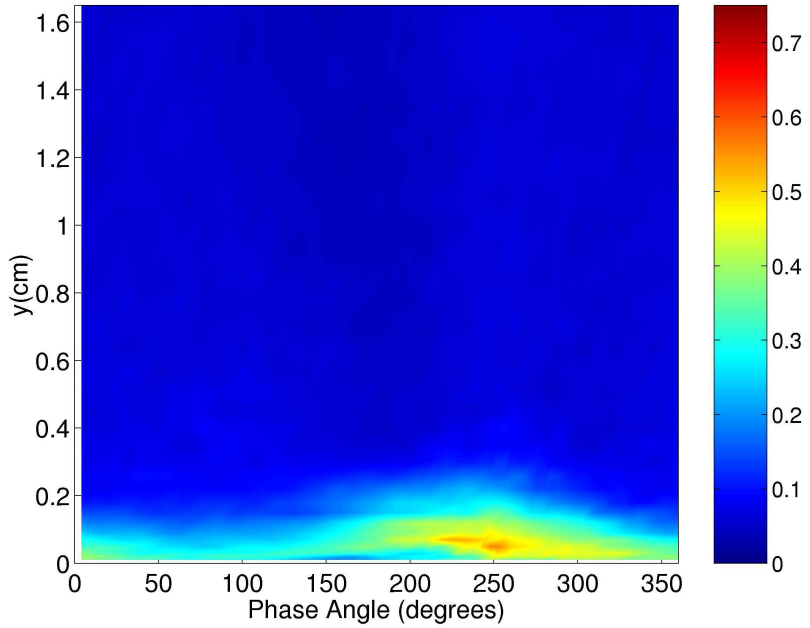

Figure 5.75: Phase average turbulence intensity $\widetilde{TI}(y,\theta)$ at p09, $s/L_{ss} = 61.32\%$.

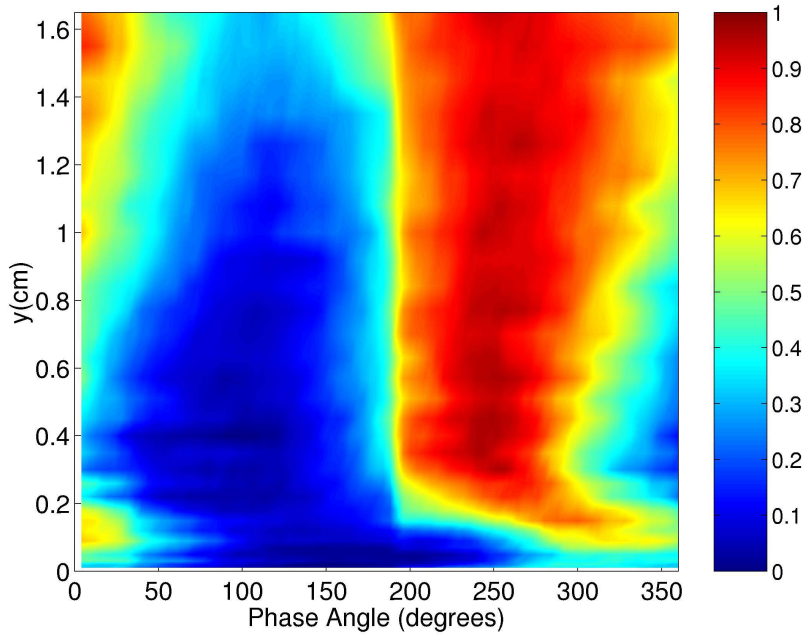

Figure 5.76: Phase average intermittency $\tilde{\gamma}(y,\theta)$ at p09, $s/L_{ss} = 61.32\%$.

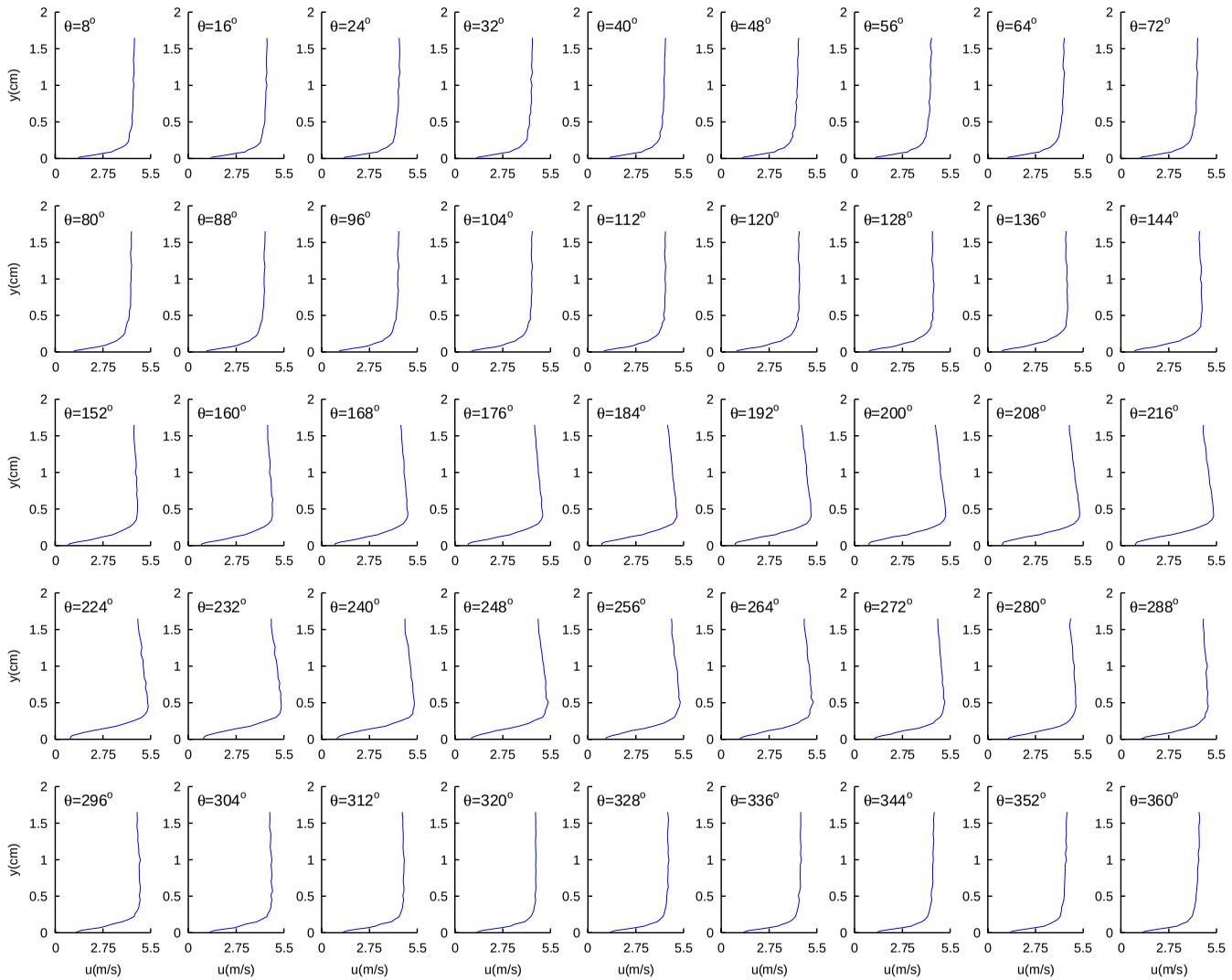

Figure 5.77: Phase average velocity $\tilde{u}(y, \theta)$ at p09, $s/L_{ss} = 61.32\%$, presented as a function of θ.

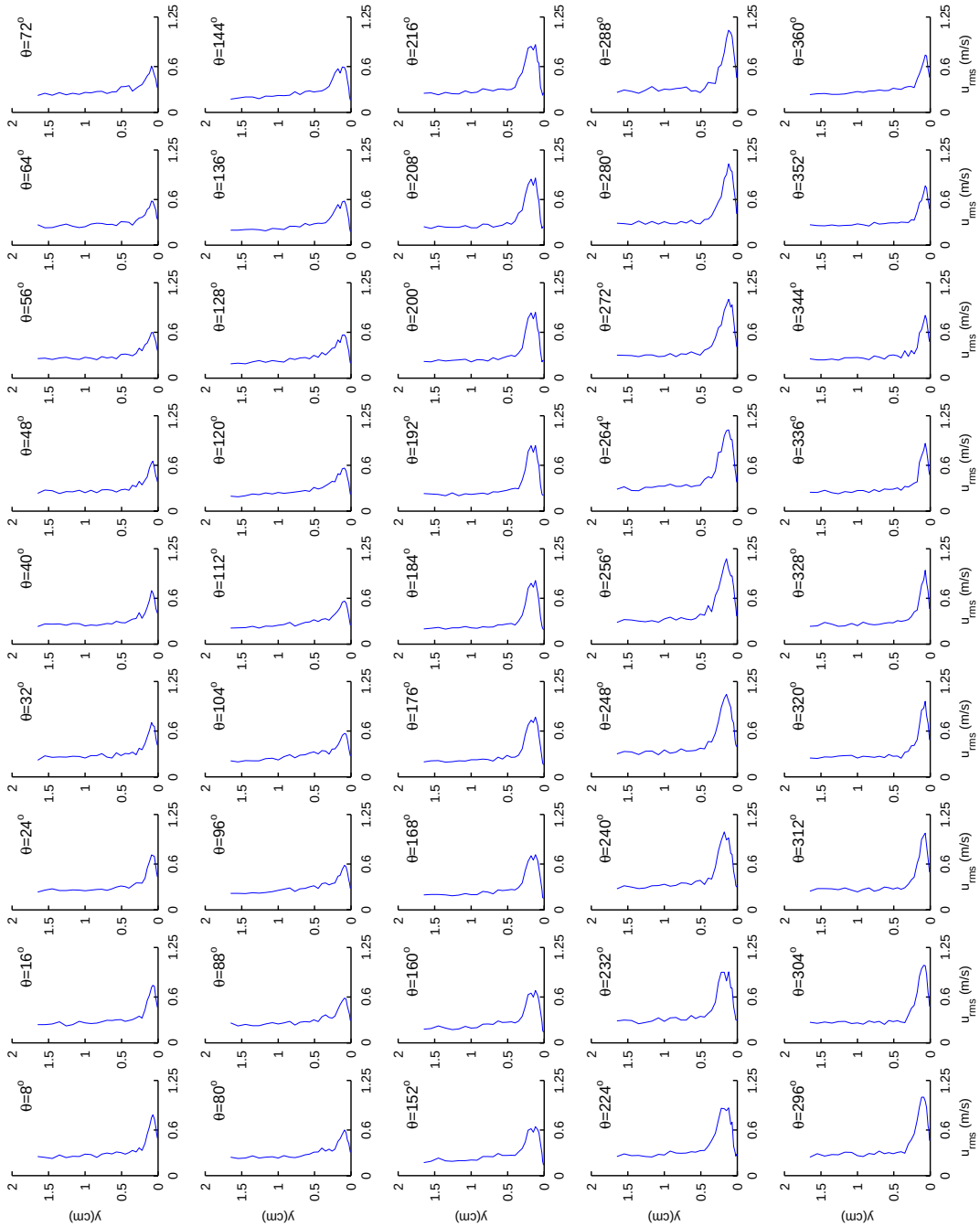

Figure 5.78: Phase average rms velocity fluctuation $\widetilde{u_{rms}}(y, \theta)$ at p09, $s/L_{ss} = 61.32\%$, presented as a function of θ.

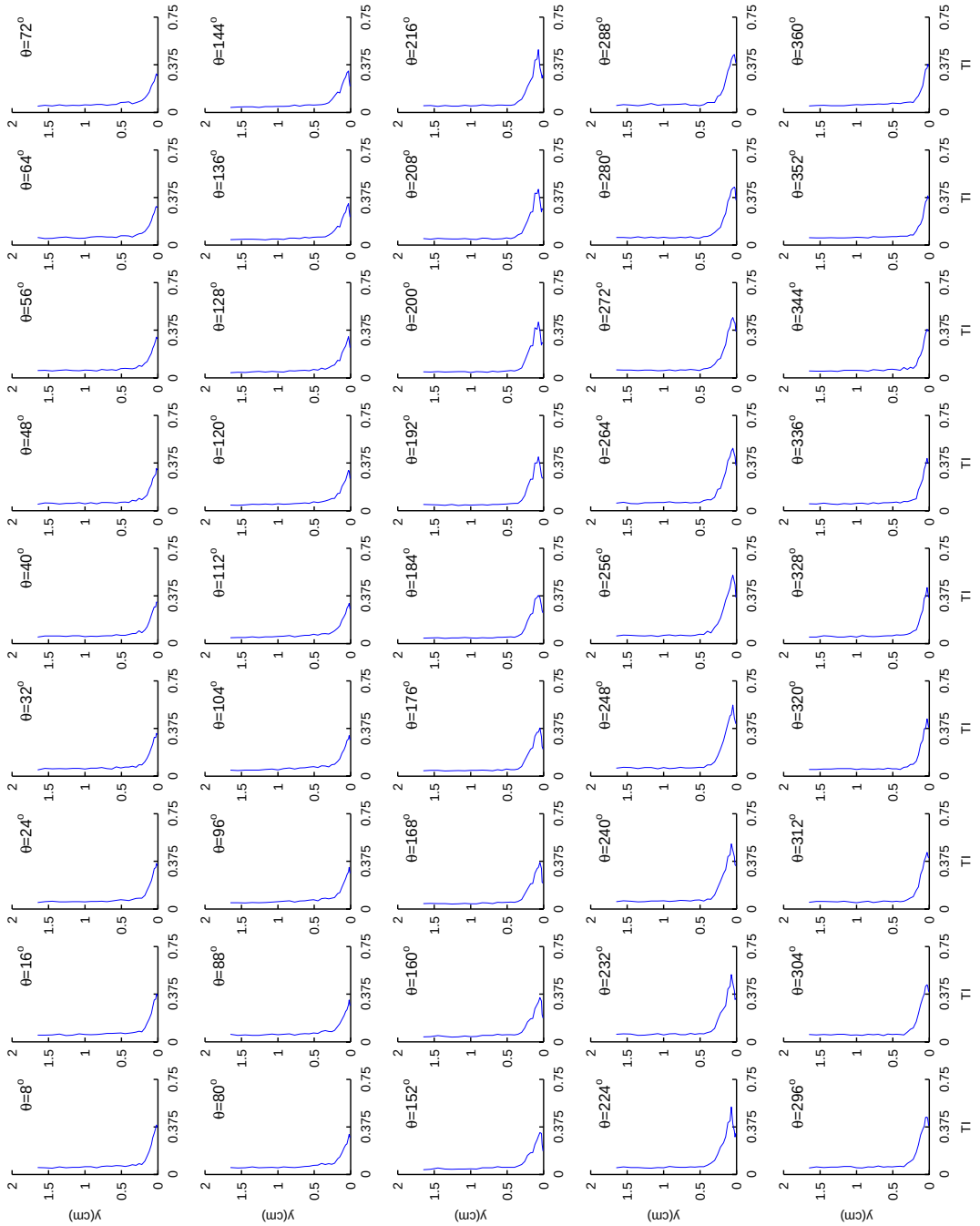

Figure 5.79: Phase average turbulence intensity $\widetilde{TI}(y,\theta)$ at p09, $s/L_{ss} = 61.32\%$, presented as a function of θ.

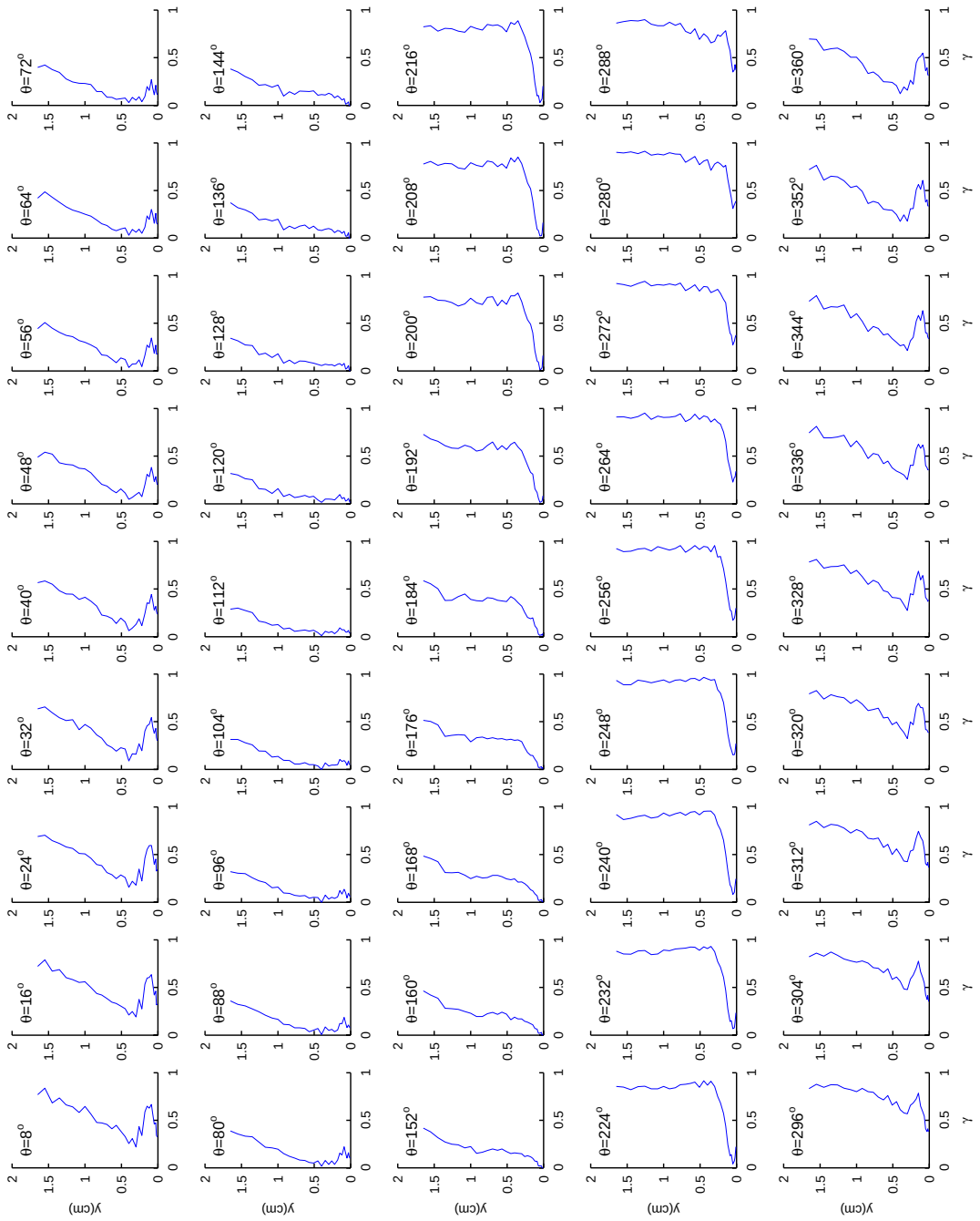

Figure 5.80: Phase average intermittency $\tilde{\gamma}(y, \theta)$ at p09, $s/L_{ss} = 61.32\%$, presented as a function of θ.

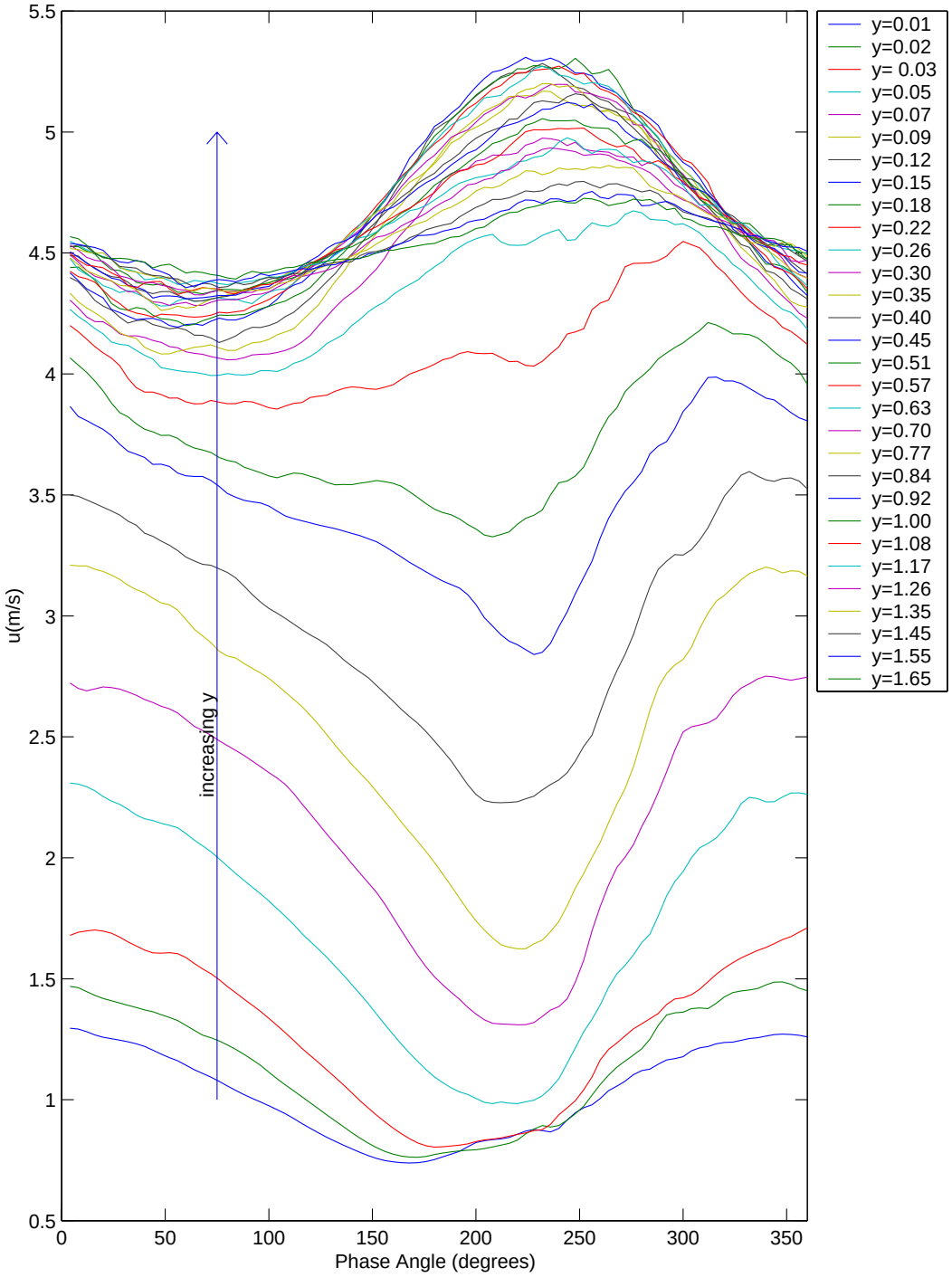

Figure 5.81: Phase average velocity $\tilde{u}(y, \theta)$ at p09, $s/L_{ss} = 61.32\%$, presented as a function of y (y-values are in cm).

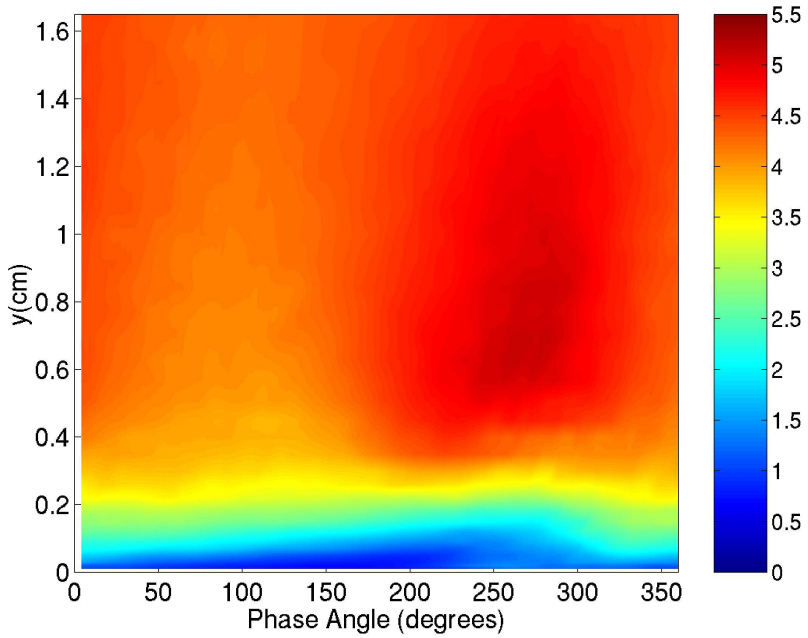

Figure 5.82: Phase average velocity $\tilde{u}(y,\theta)$ at p10, $s/L_{ss} = 70.31\%$.

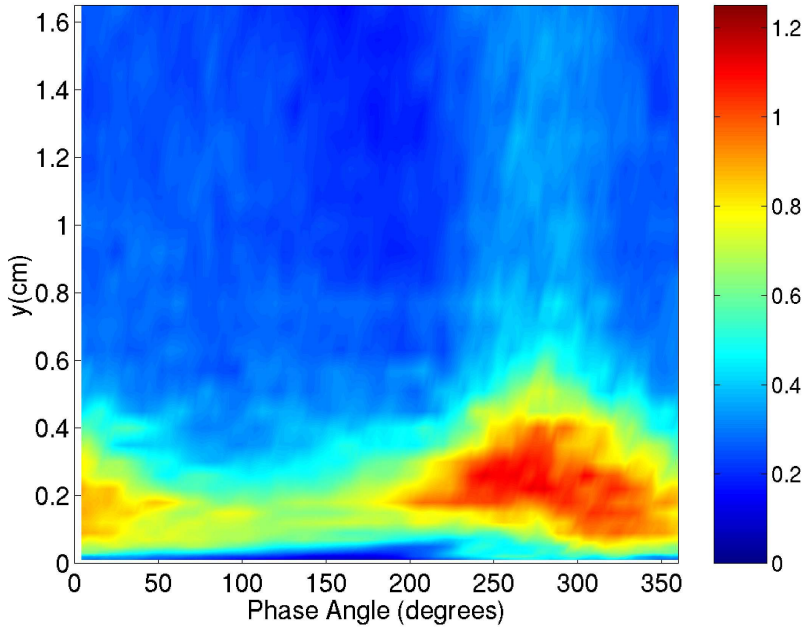

Figure 5.83: Phase average rms velocity fluctuation $\widetilde{u_{rms}}(y,\theta)$ at p10, $s/L_{ss} = 70.31\%$.

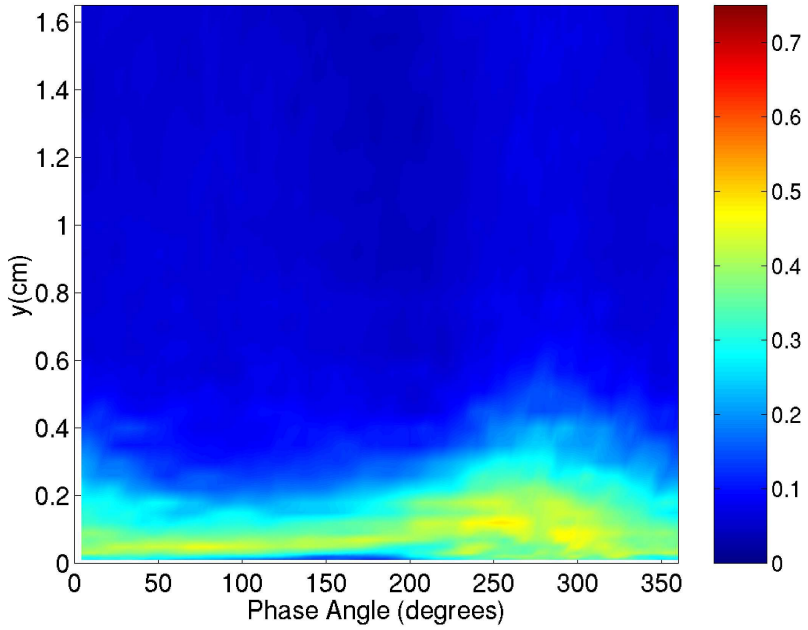

Figure 5.84: Phase average turbulence intensity $\widetilde{TI}(y,\theta)$ at p10, $s/L_{ss} = 70.31\%$.

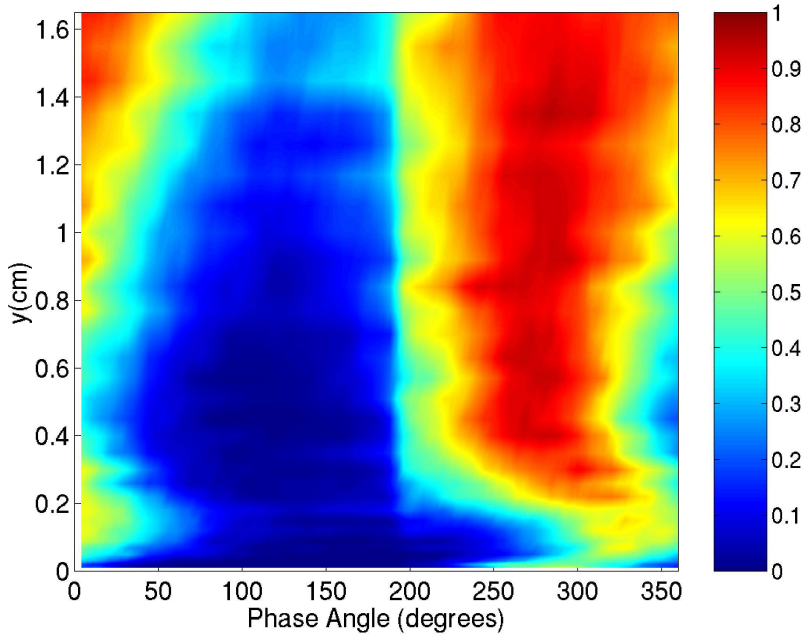

Figure 5.85: Phase average intermittency $\tilde{\gamma}(y,\theta)$ at p10, $s/L_{ss} = 70.31\%$.

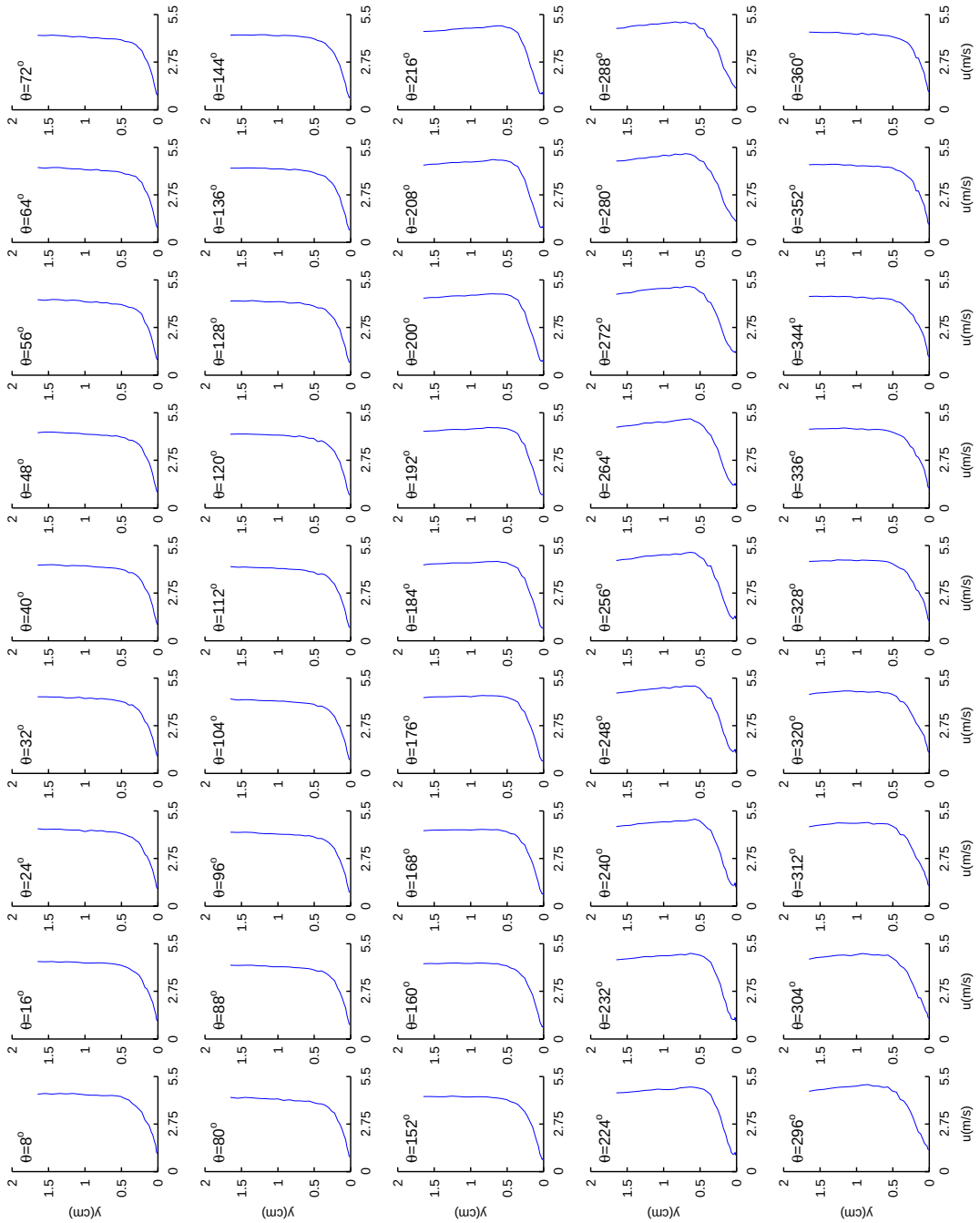

Figure 5.86: Phase average velocity $\tilde{u}(y, \theta)$ at p10, $s/L_{ss} = 70.31\%$, presented as a function of θ.

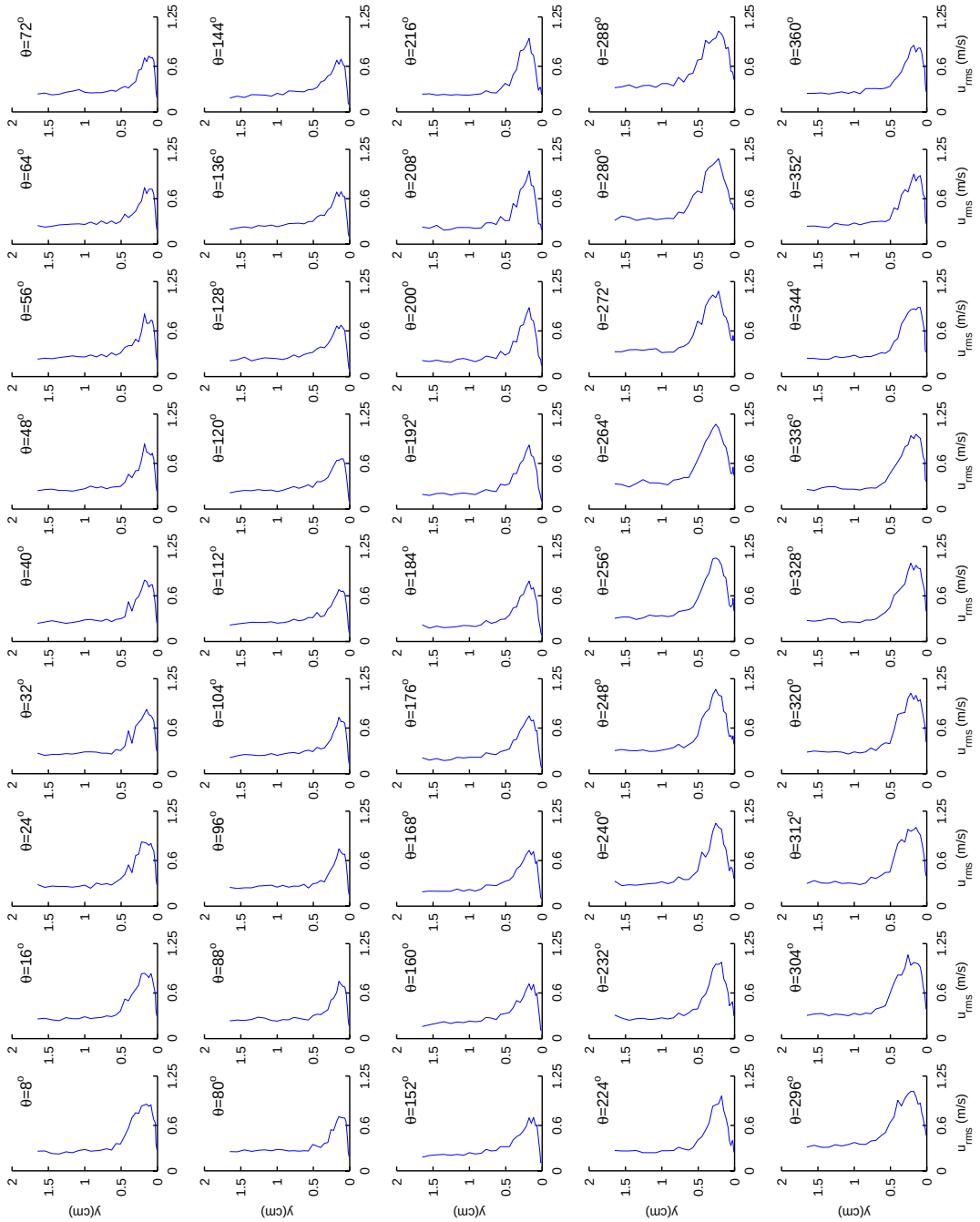

Figure 5.87: Phase average rms velocity fluctuation $\widetilde{u_{rms}}(y, \theta)$ at p10, $s/L_{ss} = 70.31\%$, presented as a function of θ.

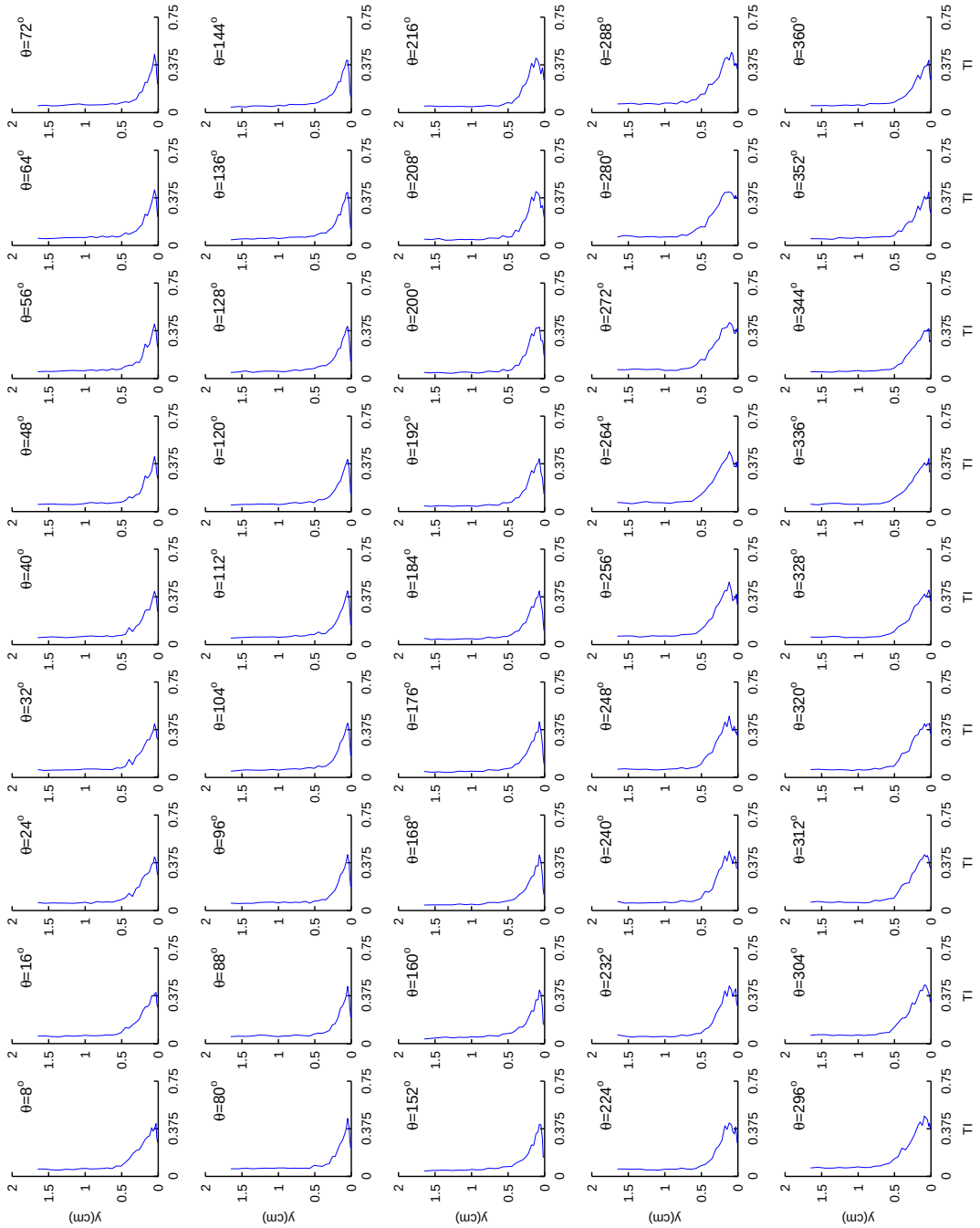

Figure 5.88: Phase average turbulence intensity $\widetilde{TI}(y,\theta)$ at p10, $s/L_{ss} = 70.31\%$, presented as a function of θ.

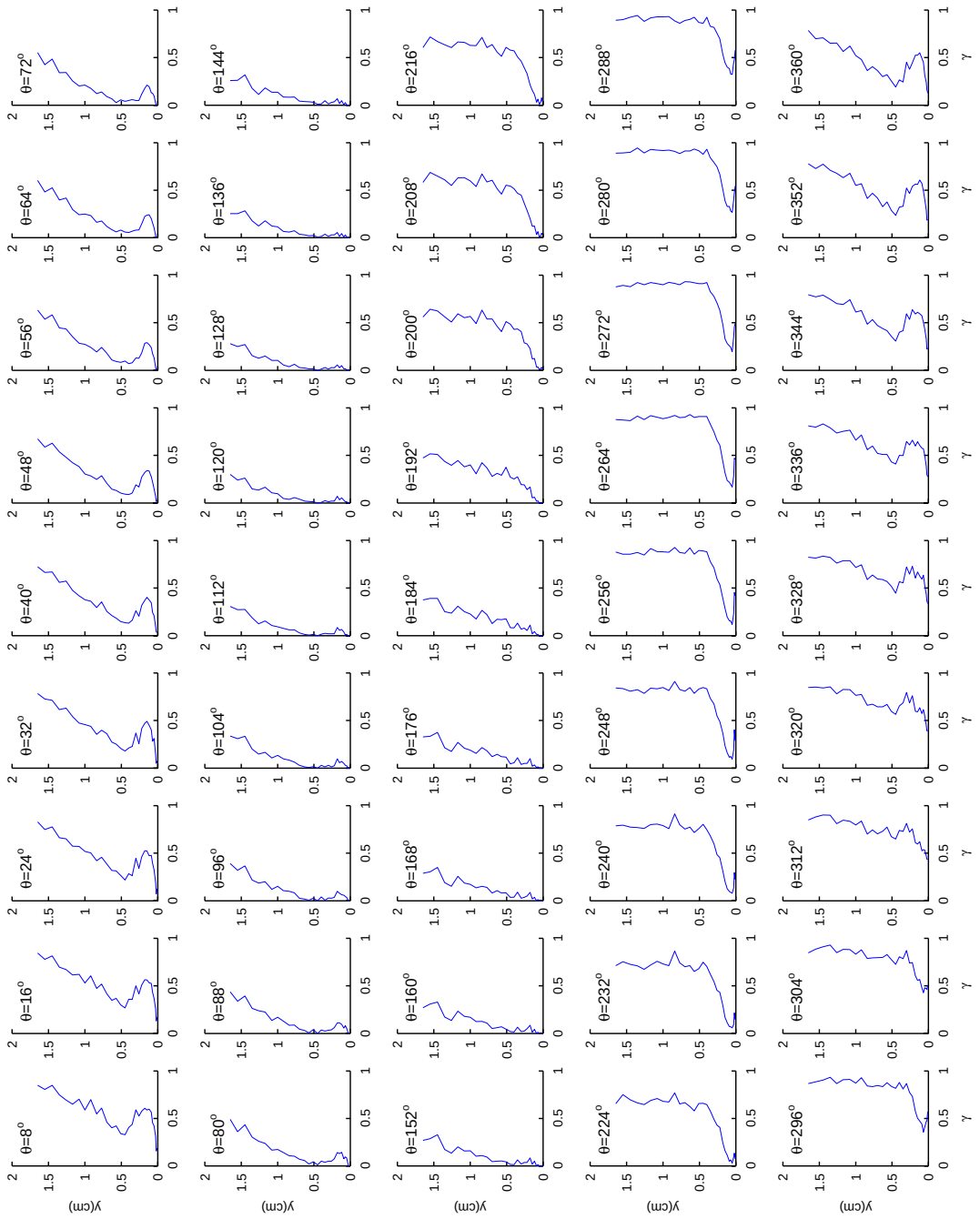

Figure 5.89: Phase average intermittency $\tilde{\gamma}(y, \theta)$ at p10, $s/L_{ss} = 70.31\%$, presented as a function of θ.

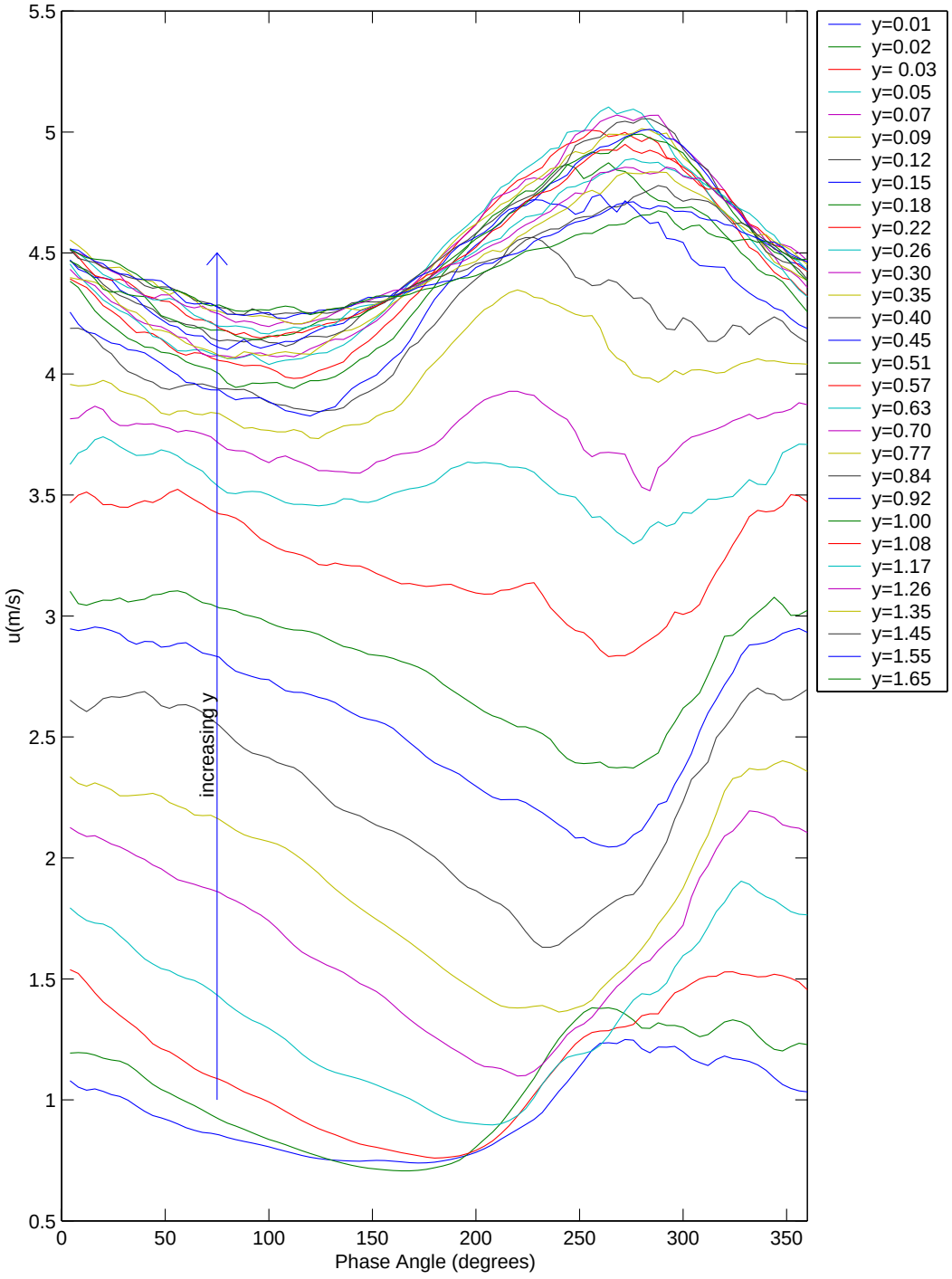

Figure 5.90: Phase average velocity $\tilde{u}(y, \theta)$ at p10, $s/L_{ss} = 70.31\%$, presented as a function of y (y-values are in cm).

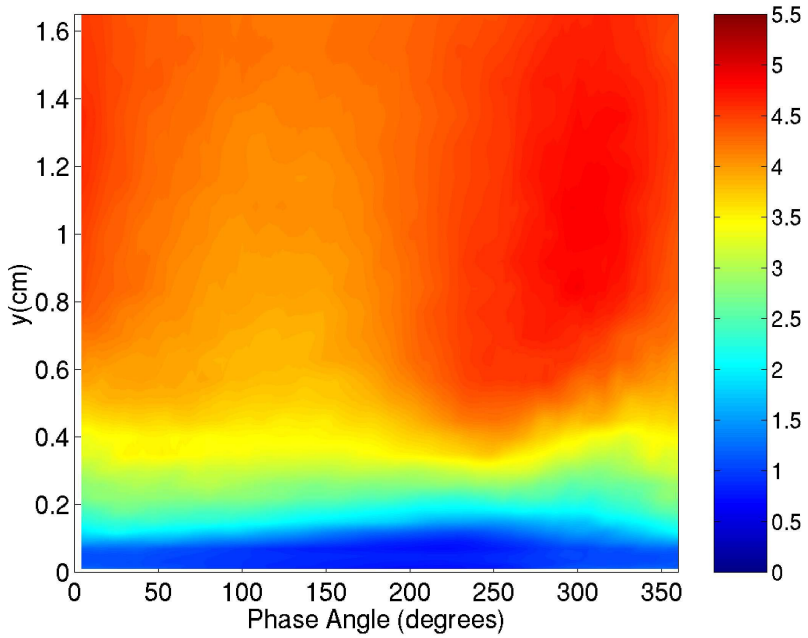

Figure 5.91: Phase average velocity $\tilde{u}(y,\theta)$ at p11, $s/L_{ss} = 76.11\%$.

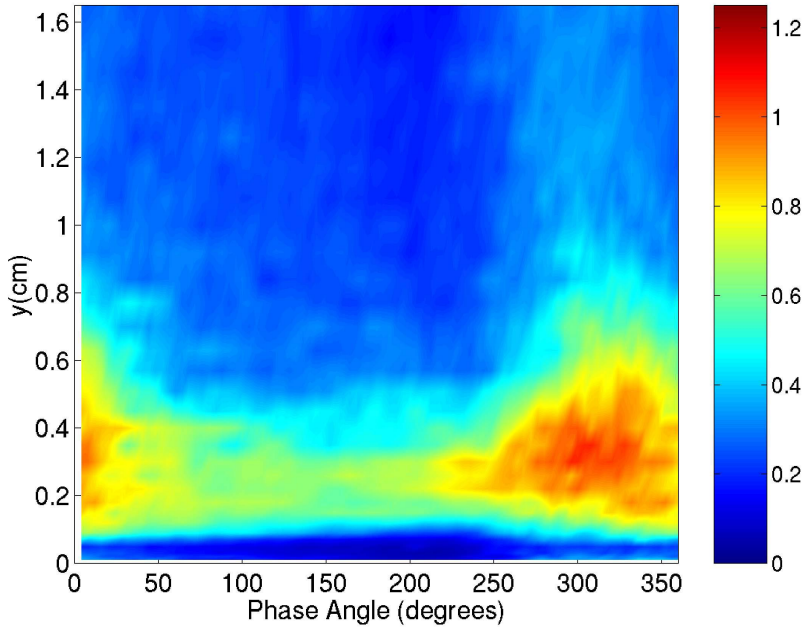

Figure 5.92: Phase average rms velocity fluctuation $\widetilde{u_{rms}}(y,\theta)$ at p11, $s/L_{ss} = 76.11\%$.

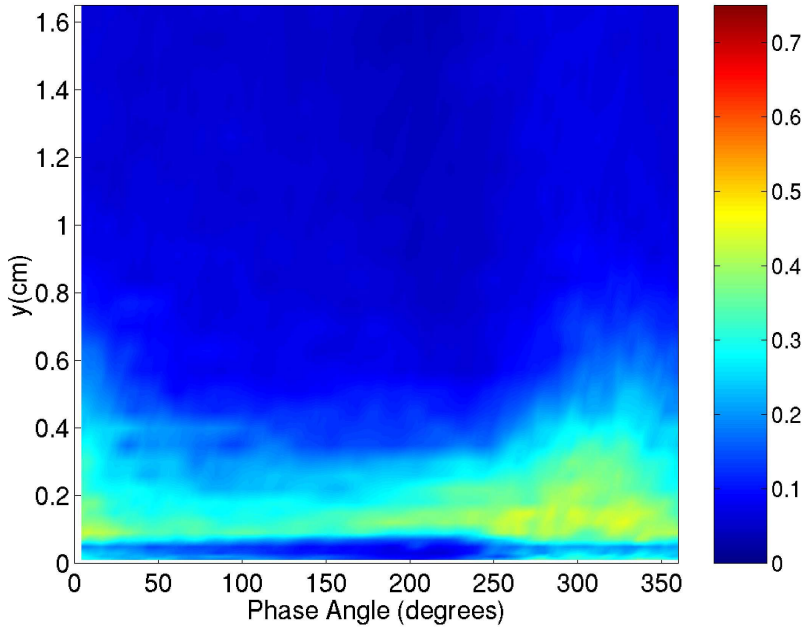

Figure 5.93: Phase average turbulence intensity $\widetilde{TI}(y,\theta)$ at p11, $s/L_{ss} = 76.11\%$.

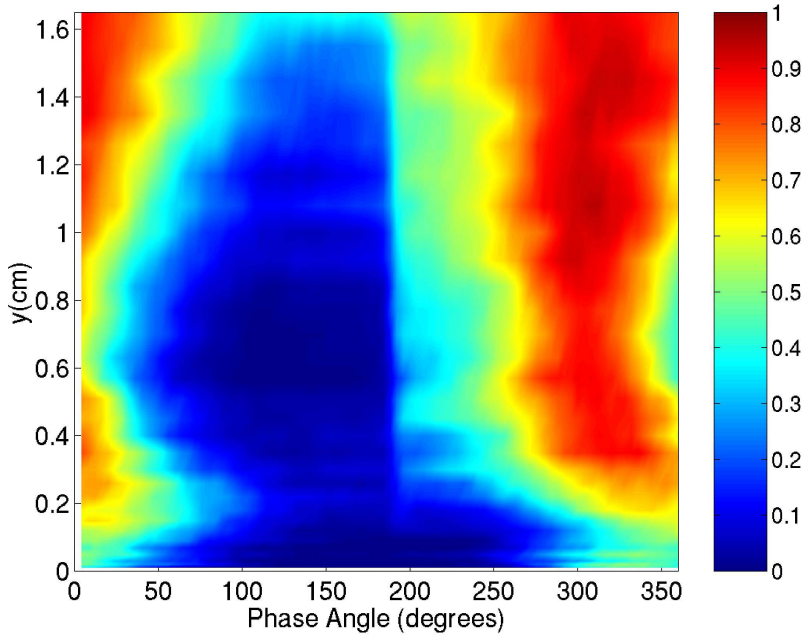

Figure 5.94: Phase average intermittency $\tilde{\gamma}(y,\theta)$ at p11, $s/L_{ss} = 76.11\%$.

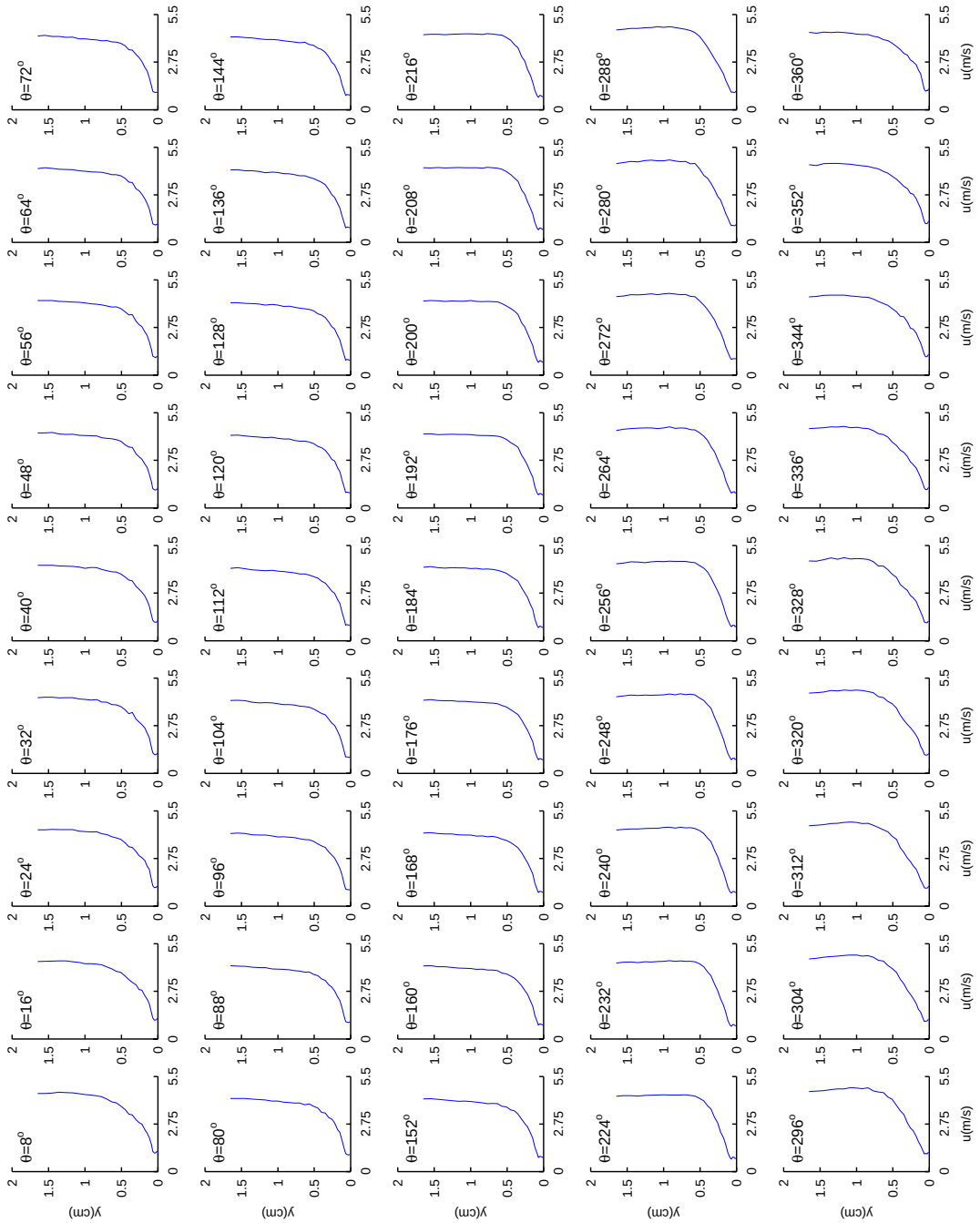

Figure 5.95: Phase average velocity $\tilde{u}(y, \theta)$ at p11, $s/L_{ss} = 76.11\%$, presented as a function of θ.

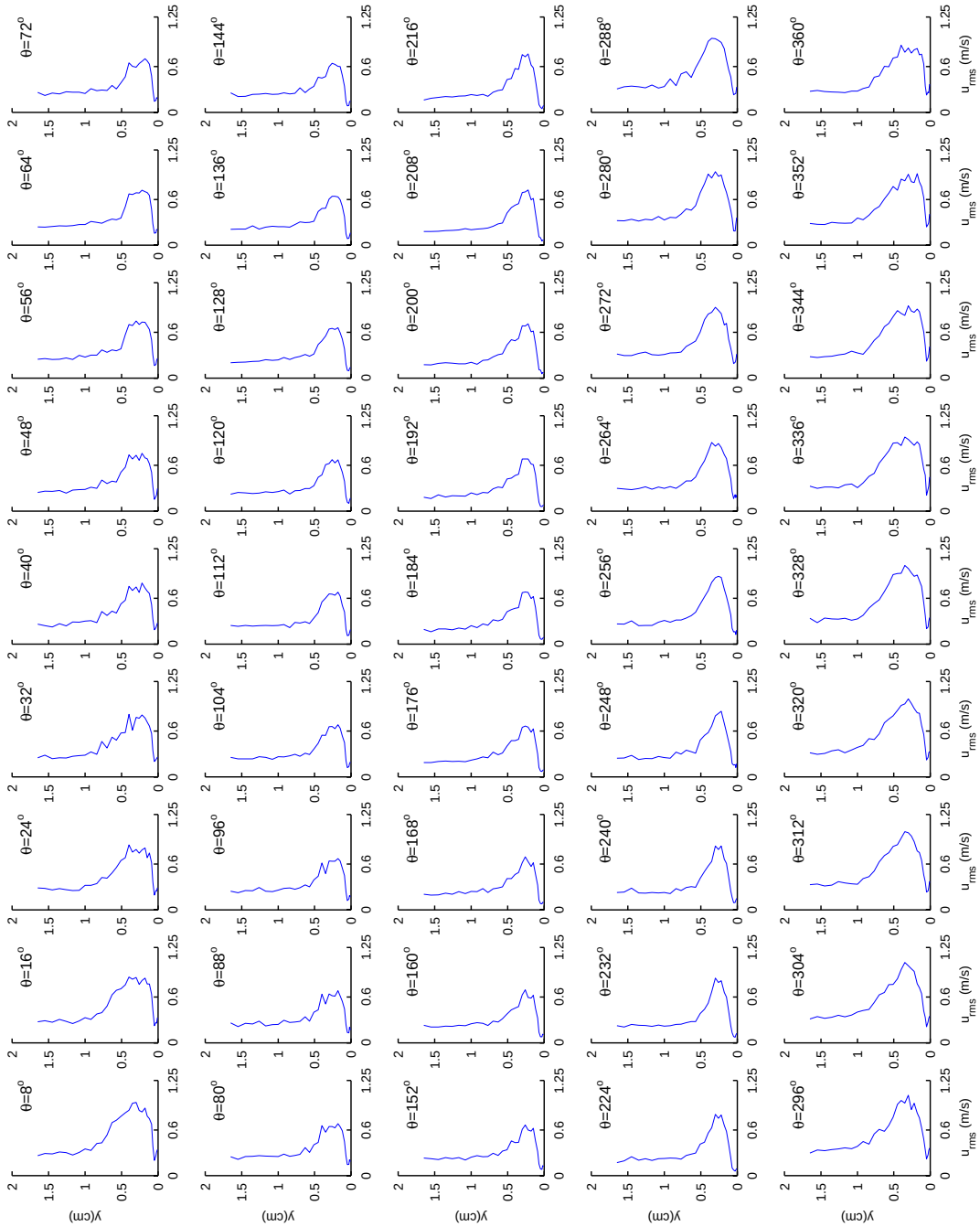

Figure 5.96: Phase average rms velocity fluctuation $\widetilde{u_{rms}}(y, \theta)$ at p11, $s/L_{ss} = 76.11\%$, presented as a function of θ.

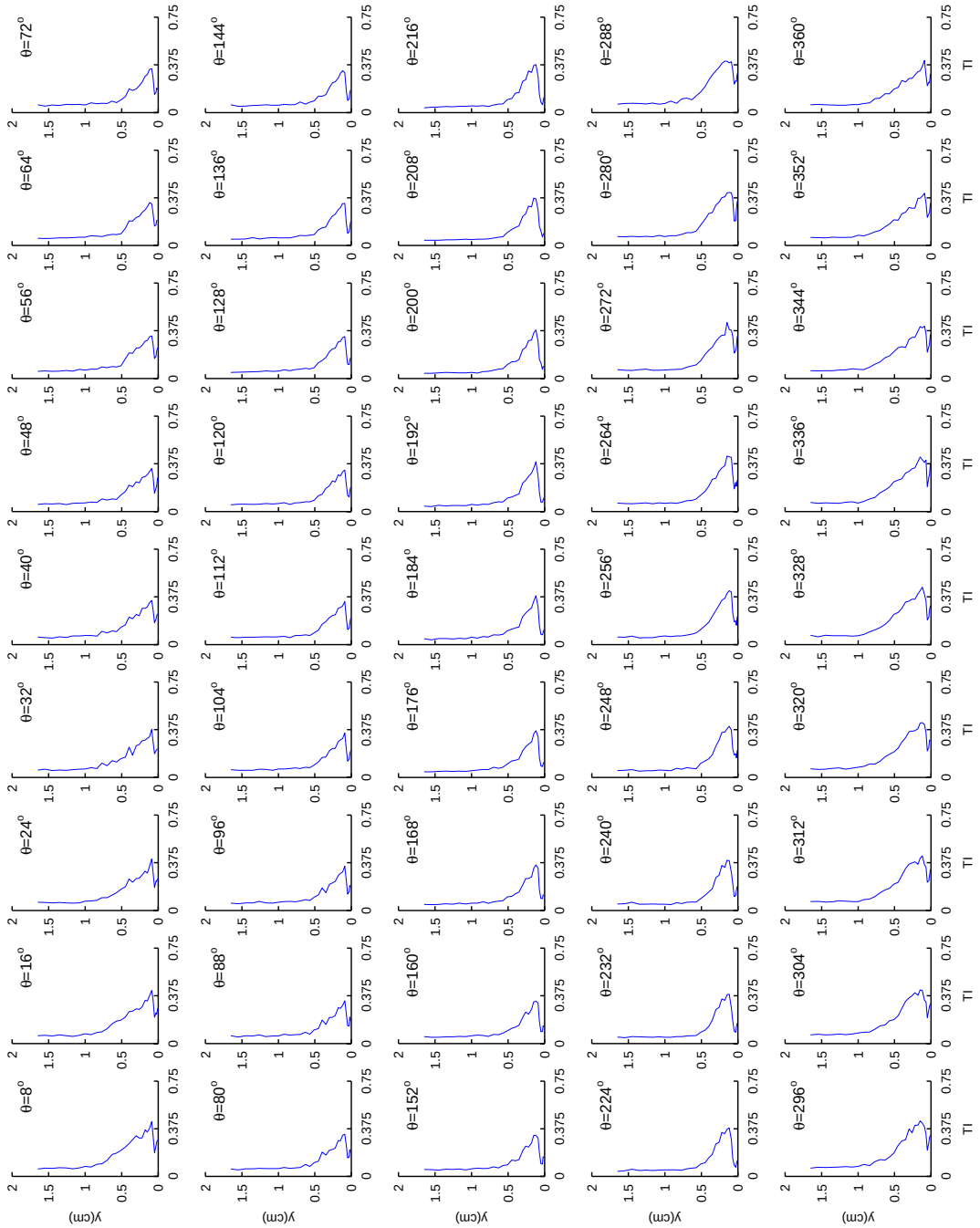

Figure 5.97: Phase average turbulence intensity $\widetilde{TI}(y,\theta)$ at p11, $s/L_{ss} = 76.11\%$, presented as a function of θ.

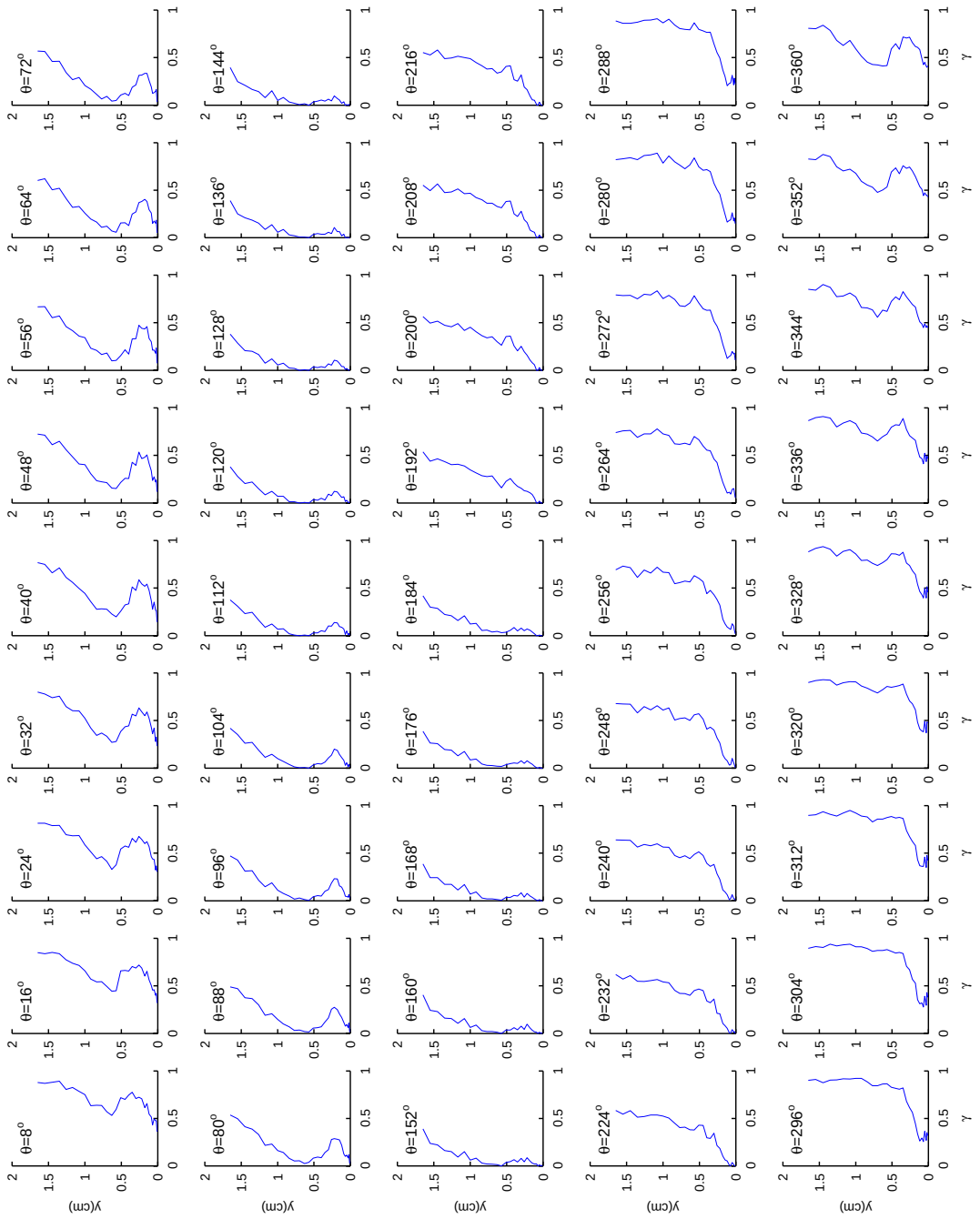

Figure 5.98: Phase average intermittency $\tilde{\gamma}(y, \theta)$ at p11, $s/L_{ss} = 76.11\%$, presented as a function of θ.

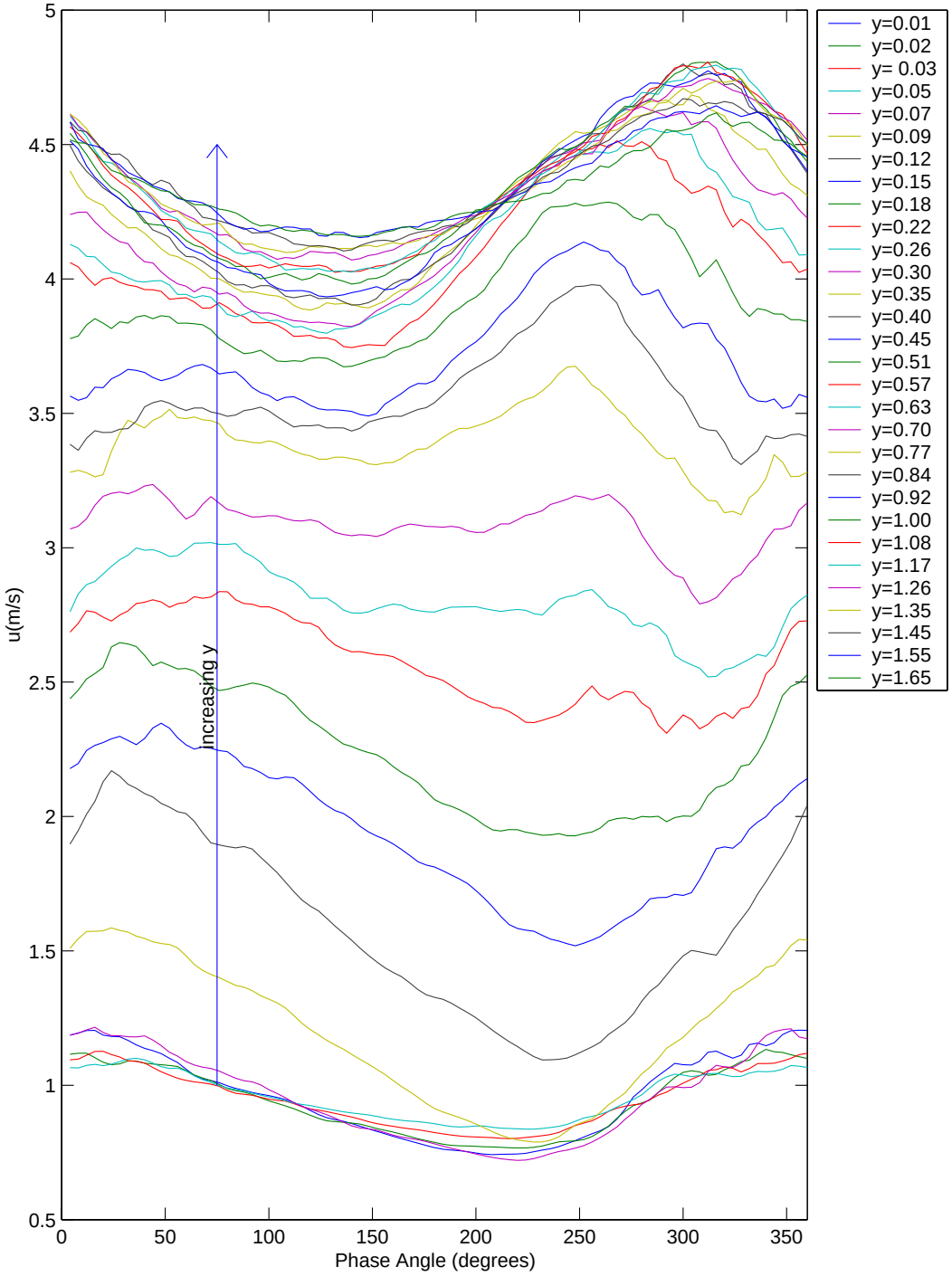

Figure 5.99: Phase average velocity $\tilde{u}(y, \theta)$ at p11, $s/L_{ss} = 76.11\%$, presented as a function of y (y-values are in cm).

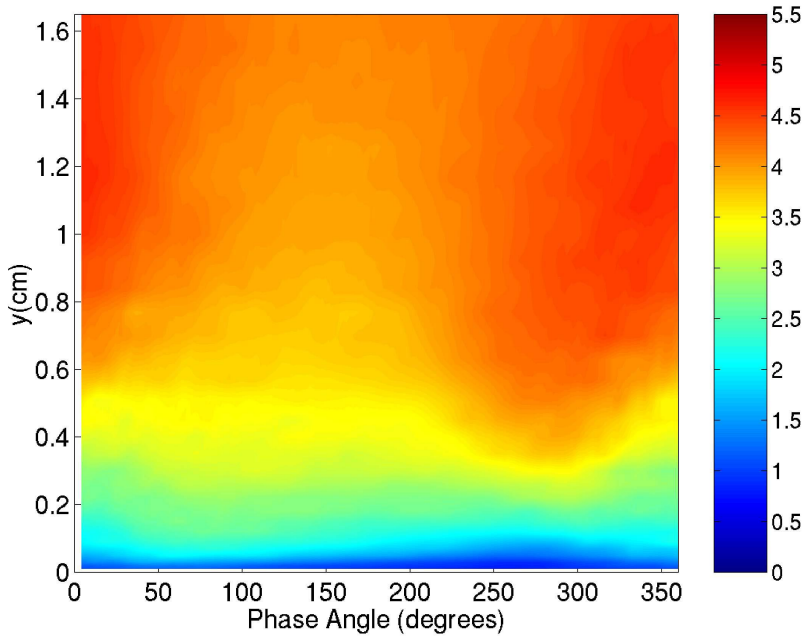

Figure 5.100: Phase average velocity $\tilde{u}(y, \theta)$ at p12, $s/L_{ss} = 84.00\%$.

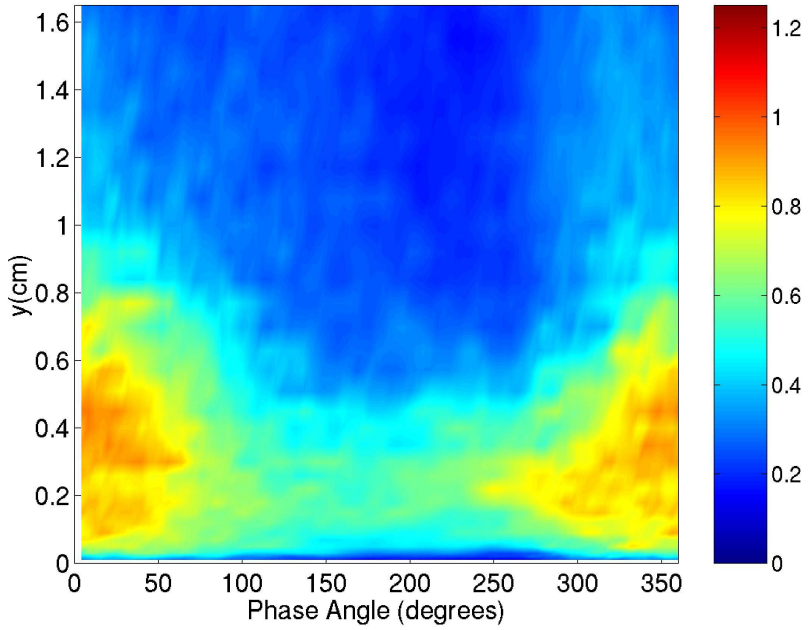

Figure 5.101: Phase average rms velocity fluctuation $\widetilde{u_{rms}}(y, \theta)$ at p12, $s/L_{ss} = 84.00\%$.

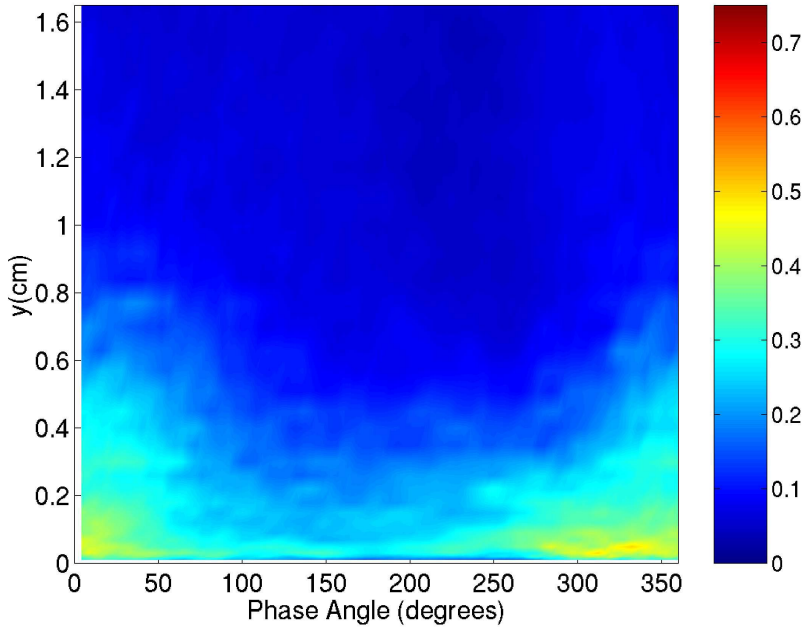

Figure 5.102: Phase average turbulence intensity $\widetilde{TI}(y,\theta)$ at p12, $s/L_{ss} = 84.00\%$.

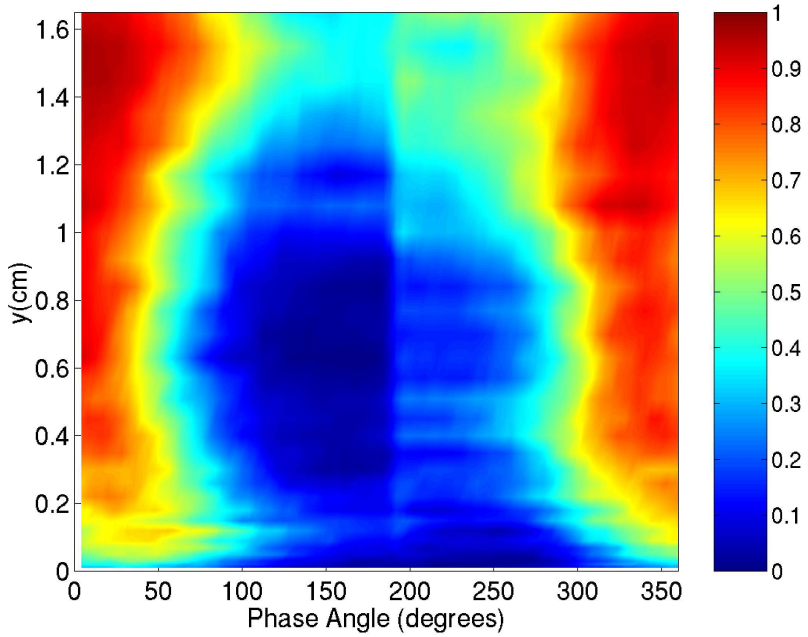

Figure 5.103: Phase average intermittency $\tilde{\gamma}(y,\theta)$ at p12, $s/L_{ss} = 84.00\%$.

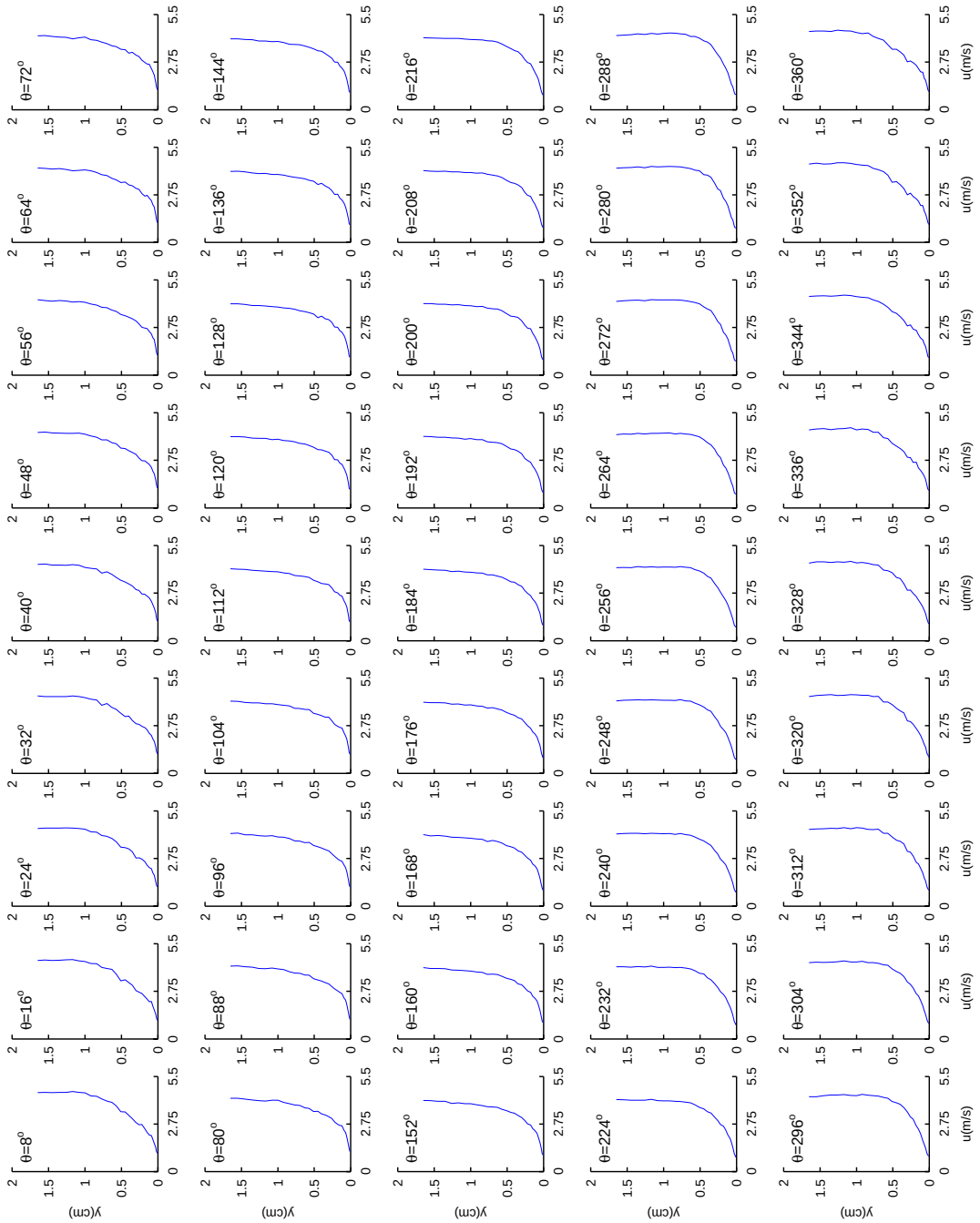

Figure 5.104: Phase average velocity $\tilde{u}(y, \theta)$ at p12, $s/L_{ss} = 84.00\%$, presented as a function of θ.

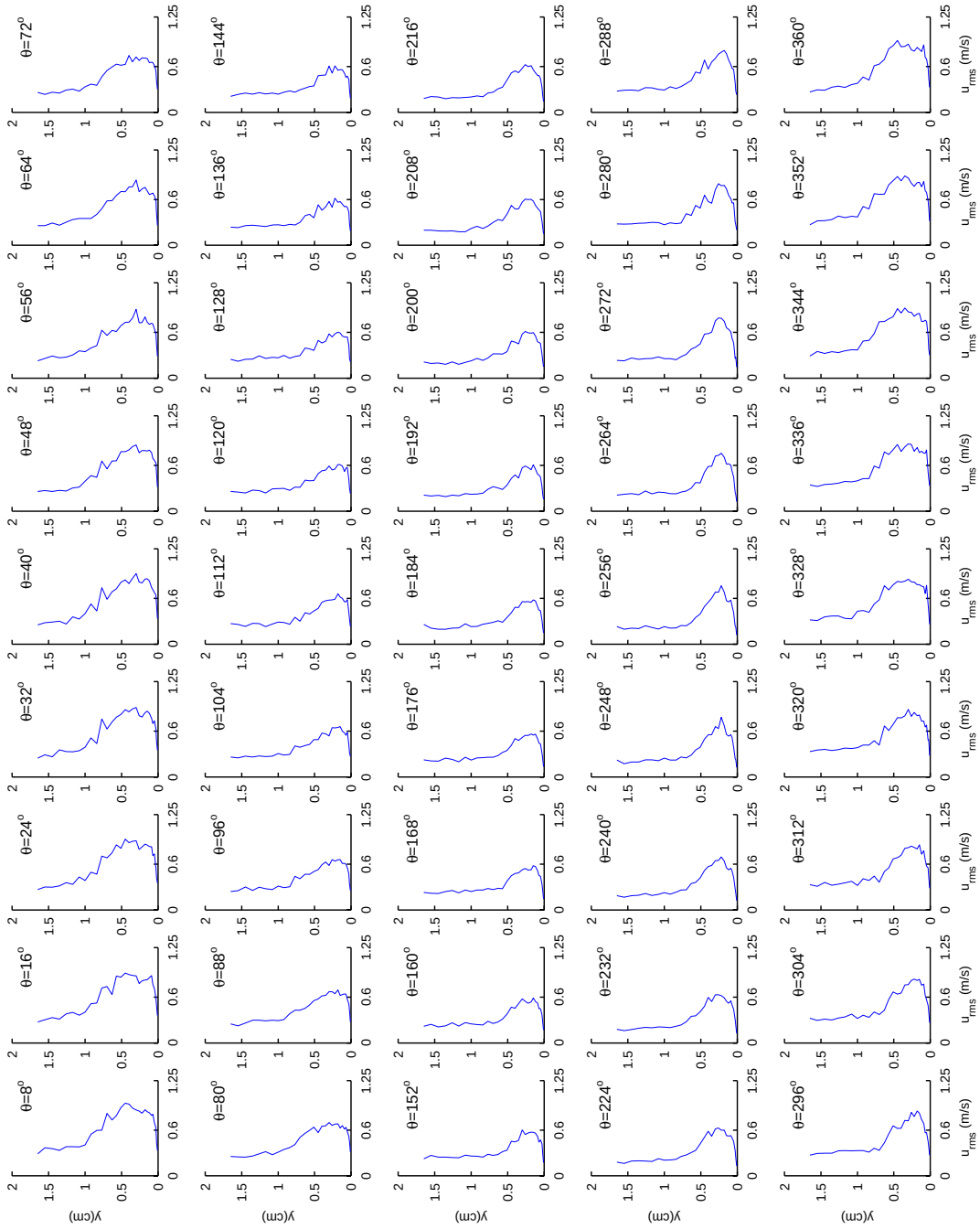

Figure 5.105: Phase average rms velocity fluctuation $\widetilde{u_{rms}}(y,\theta)$ at p12, $s/L_{ss} = 84.00\%$, presented as a function of θ.

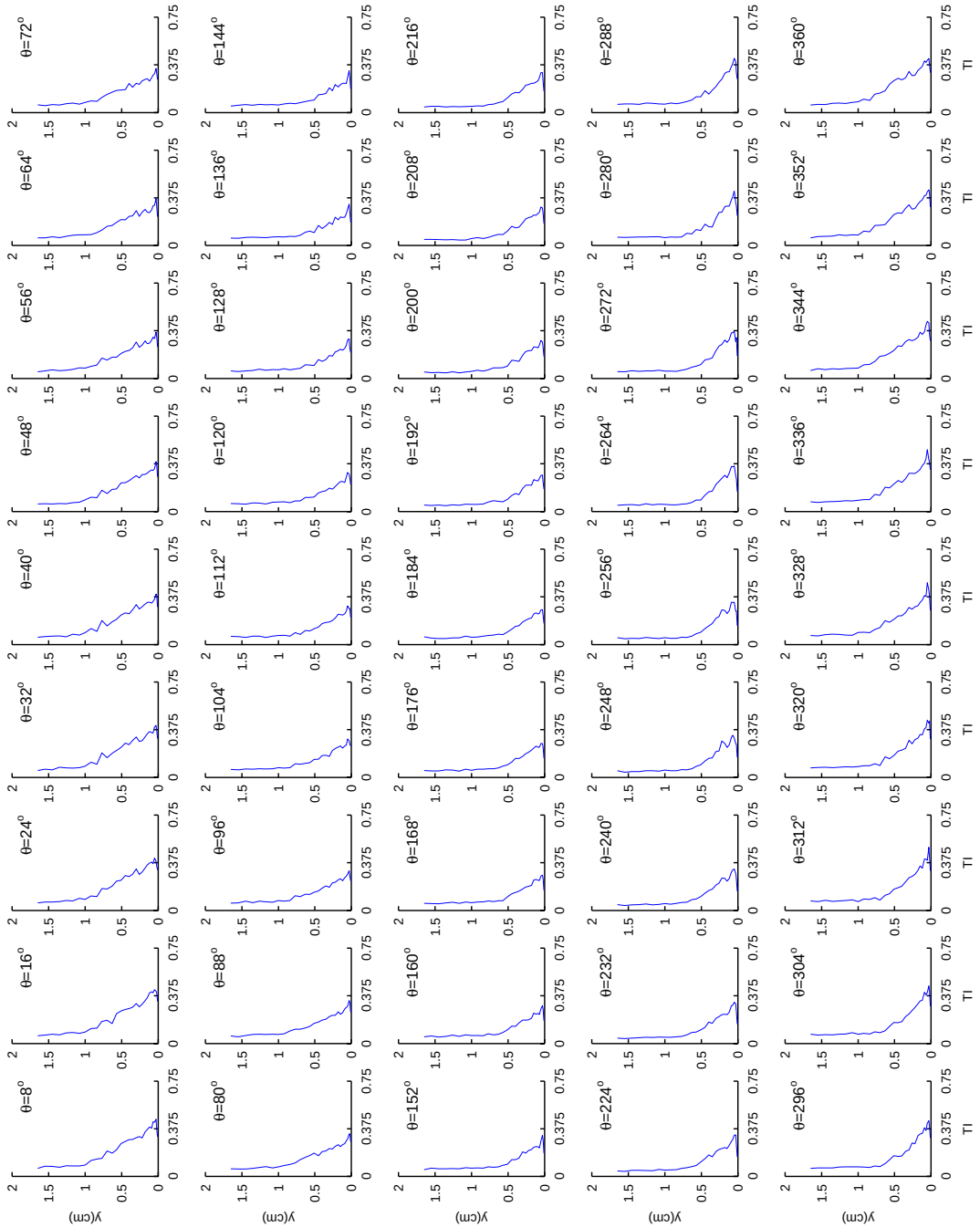

Figure 5.106: Phase average turbulence intensity $\widetilde{TI}(y,\theta)$ at p12, $s/L_{ss} = 84.00\%$, presented as a function of θ.

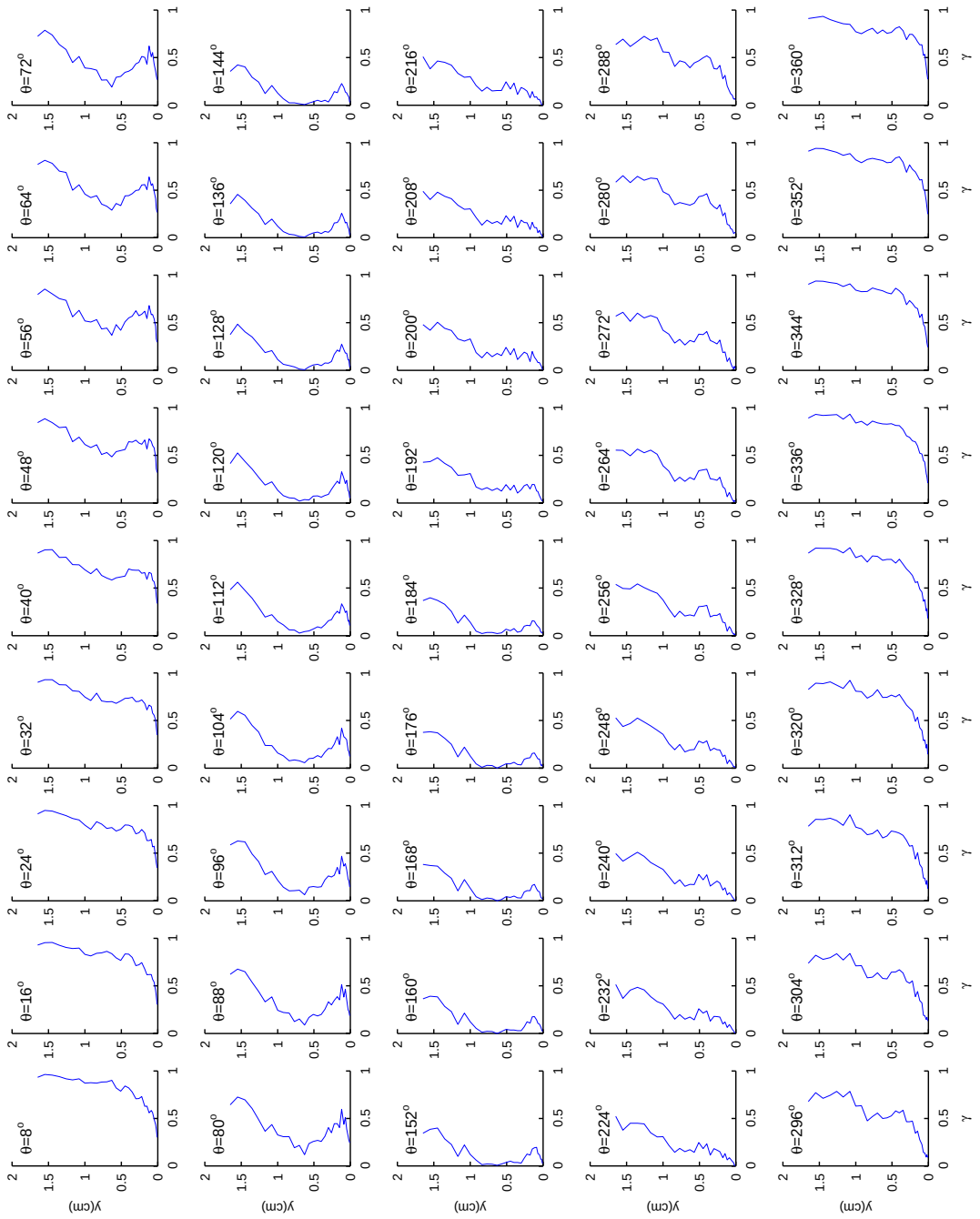

Figure 5.107: Phase average intermittency $\tilde{\gamma}(y, \theta)$ at p12, $s/L_{ss} = 84.00\%$, presented as a function of θ.

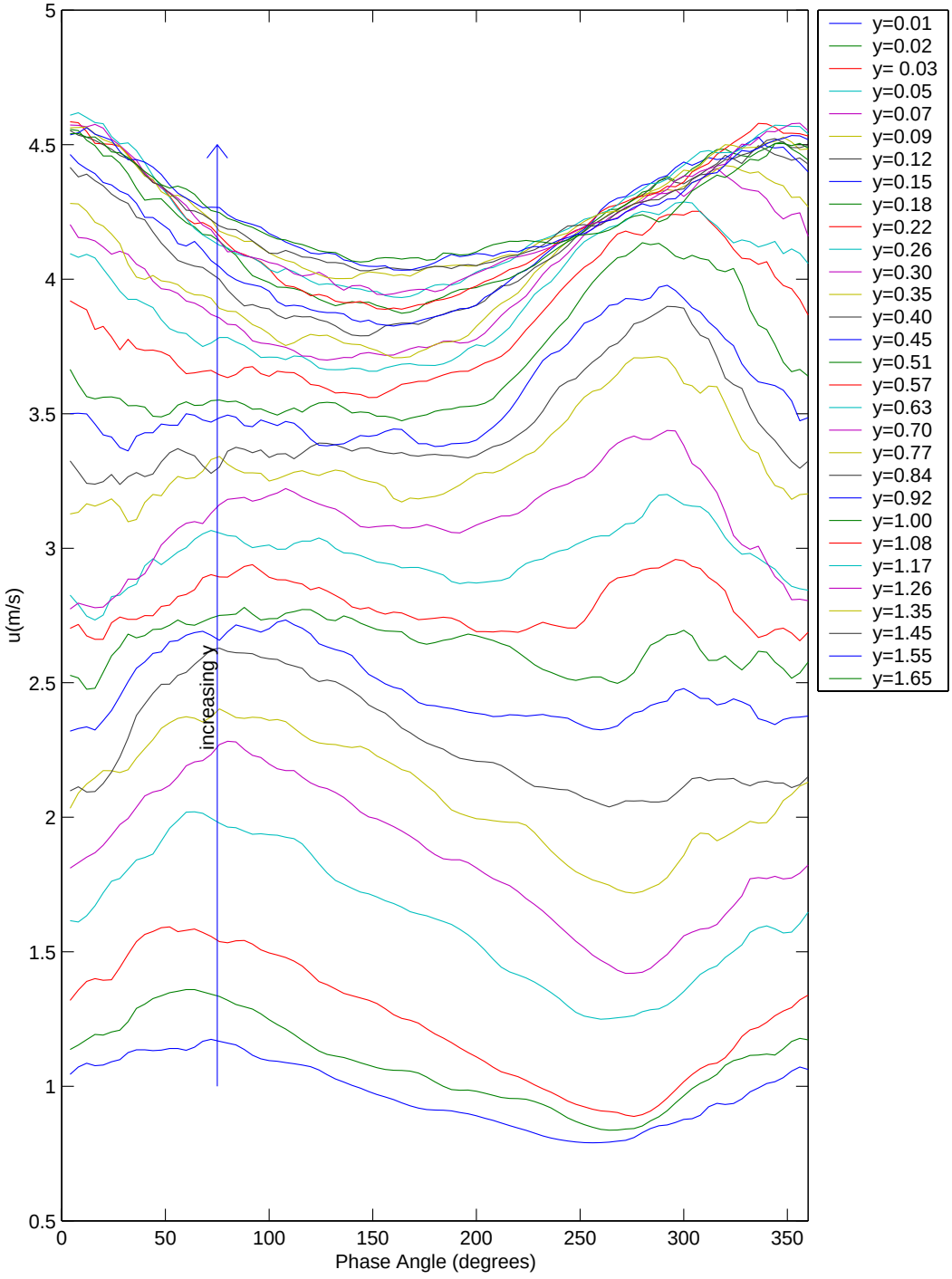

Figure 5.108: Phase average velocity $\tilde{u}(y, \theta)$ at p12, $s/L_{ss} = 84.00\%$, presented as a function of y (y-values are in cm).

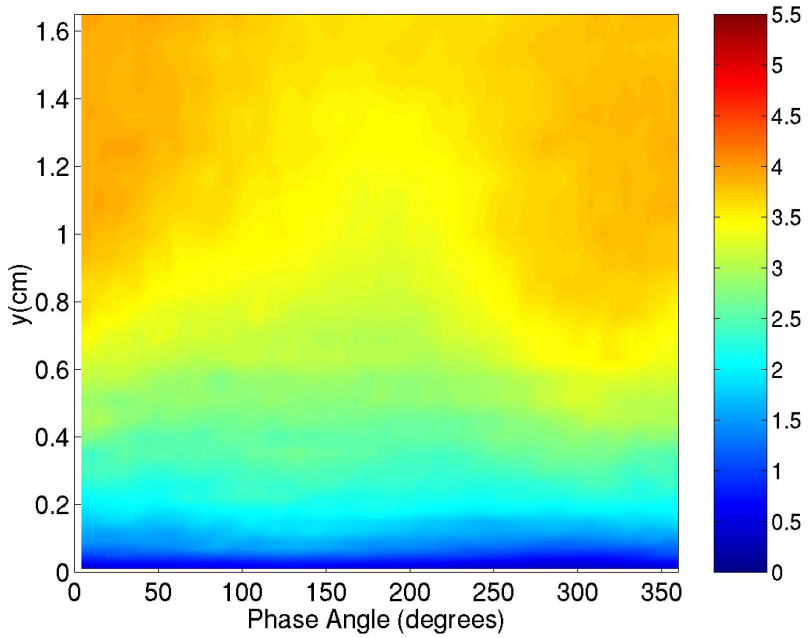

Figure 5.109: Phase average velocity $\tilde{u}(y, \theta)$ at p13, $s/L_{ss} = 93.49\%$.

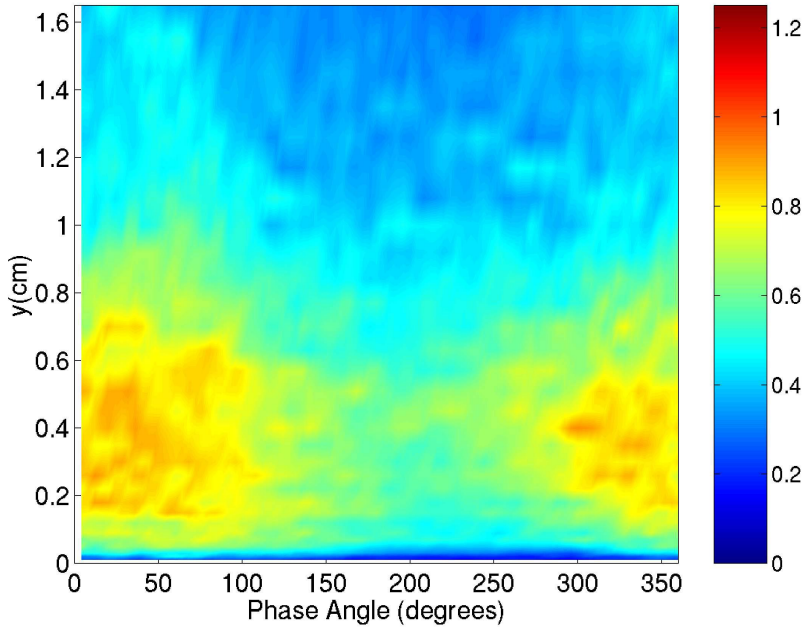

Figure 5.110: Phase average rms velocity fluctuation $\widetilde{u_{rms}}(y, \theta)$ at p13, $s/L_{ss} = 93.49\%$.

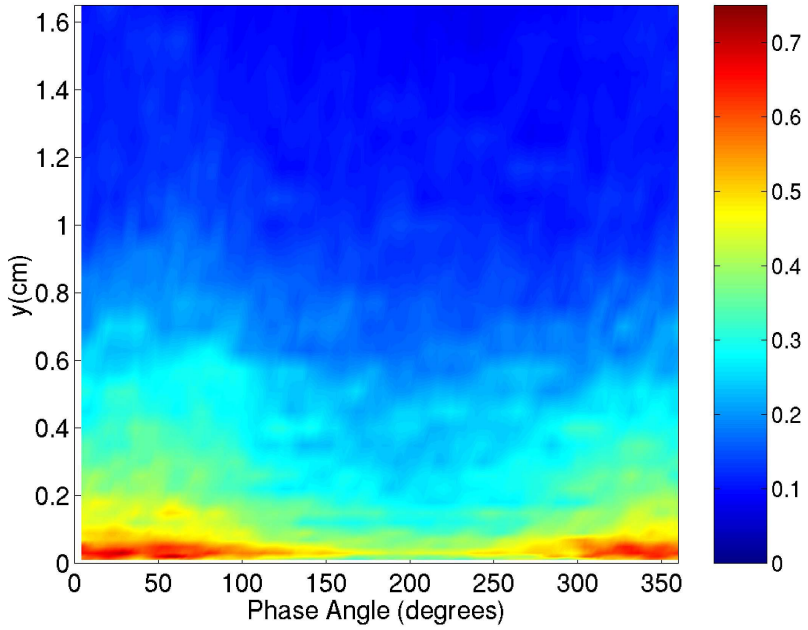

Figure 5.111: Phase average turbulence intensity $\widetilde{TI}(y,\theta)$ at p13, $s/L_{ss} = 93.49\%$.

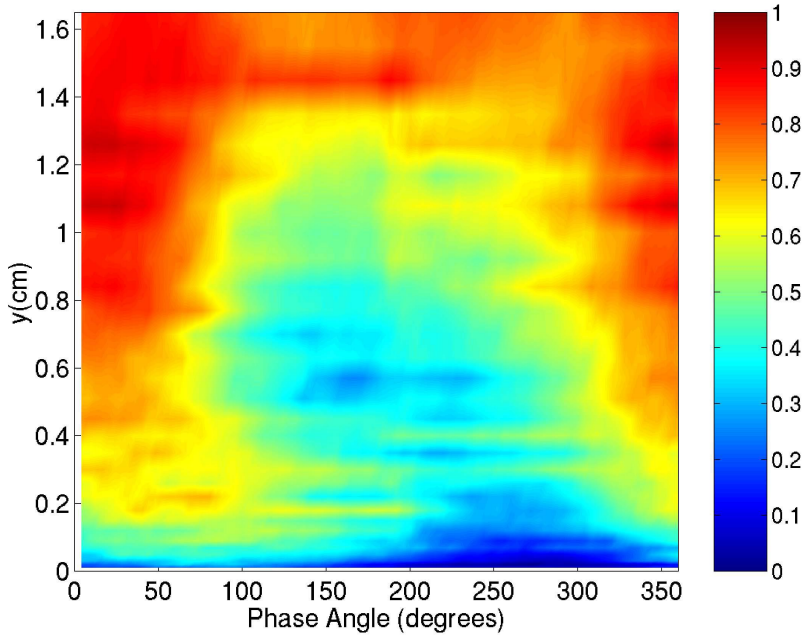

Figure 5.112: Phase average intermittency $\tilde{\gamma}(y,\theta)$ at p13, $s/L_{ss} = 93.49\%$.

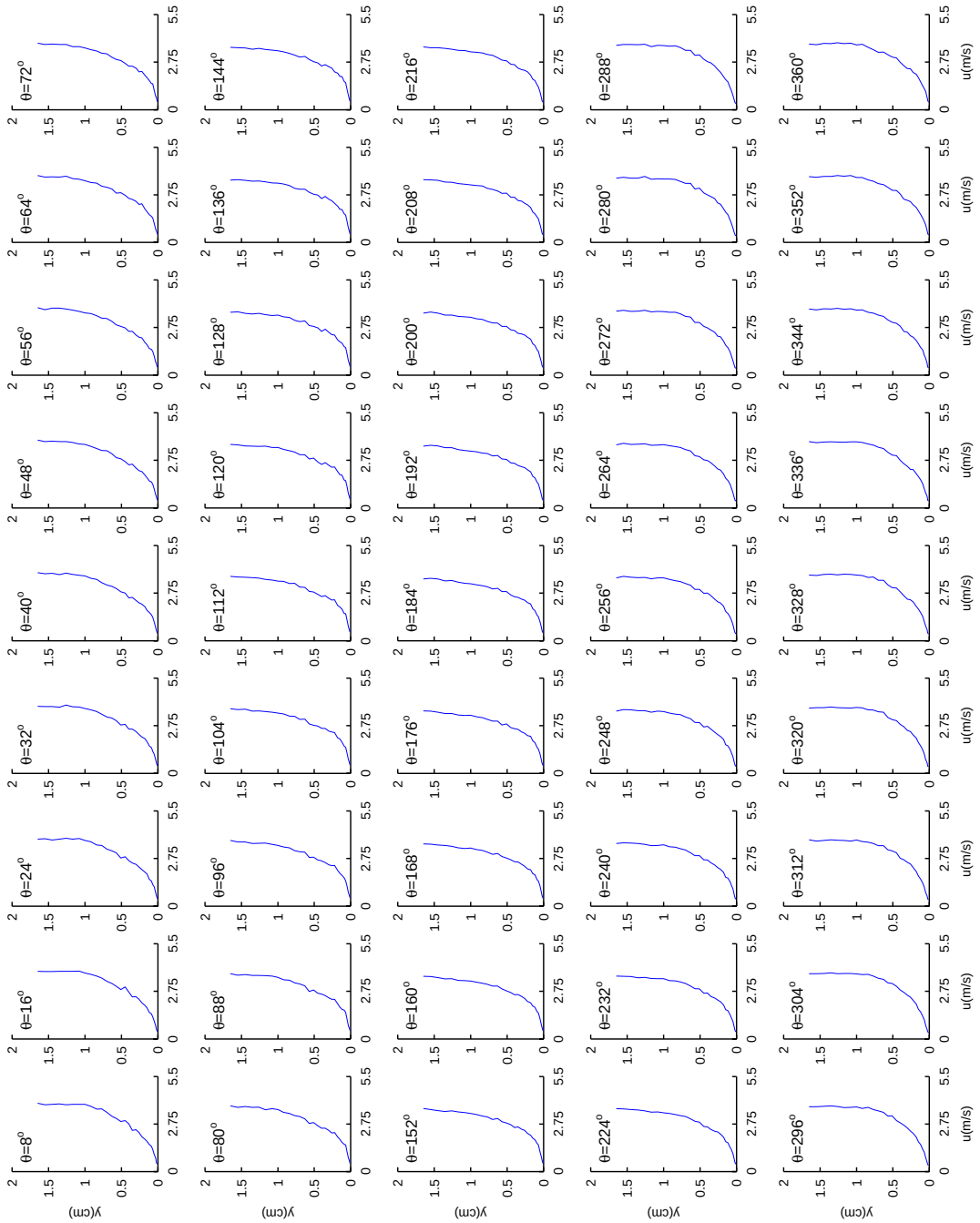

Figure 5.113: Phase average velocity $\tilde{u}(y, \theta)$ at p13, $s/L_{ss} = 93.49\%$, presented as a function of θ.

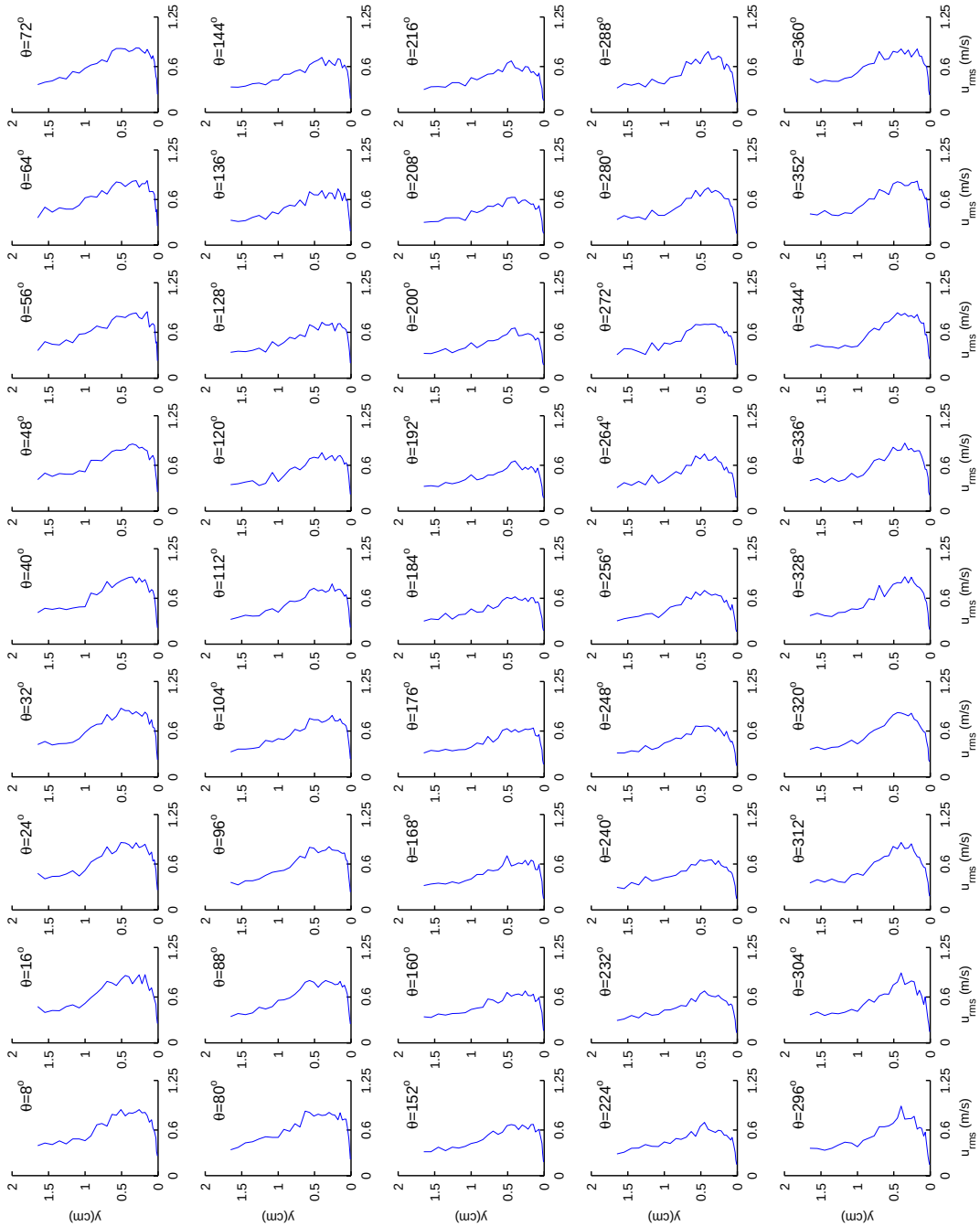

Figure 5.114: Phase average rms velocity fluctuation $\widetilde{u_{rms}}(y,\theta)$ at p13, $s/L_{ss} = 93.49\%$, presented as a function of θ.

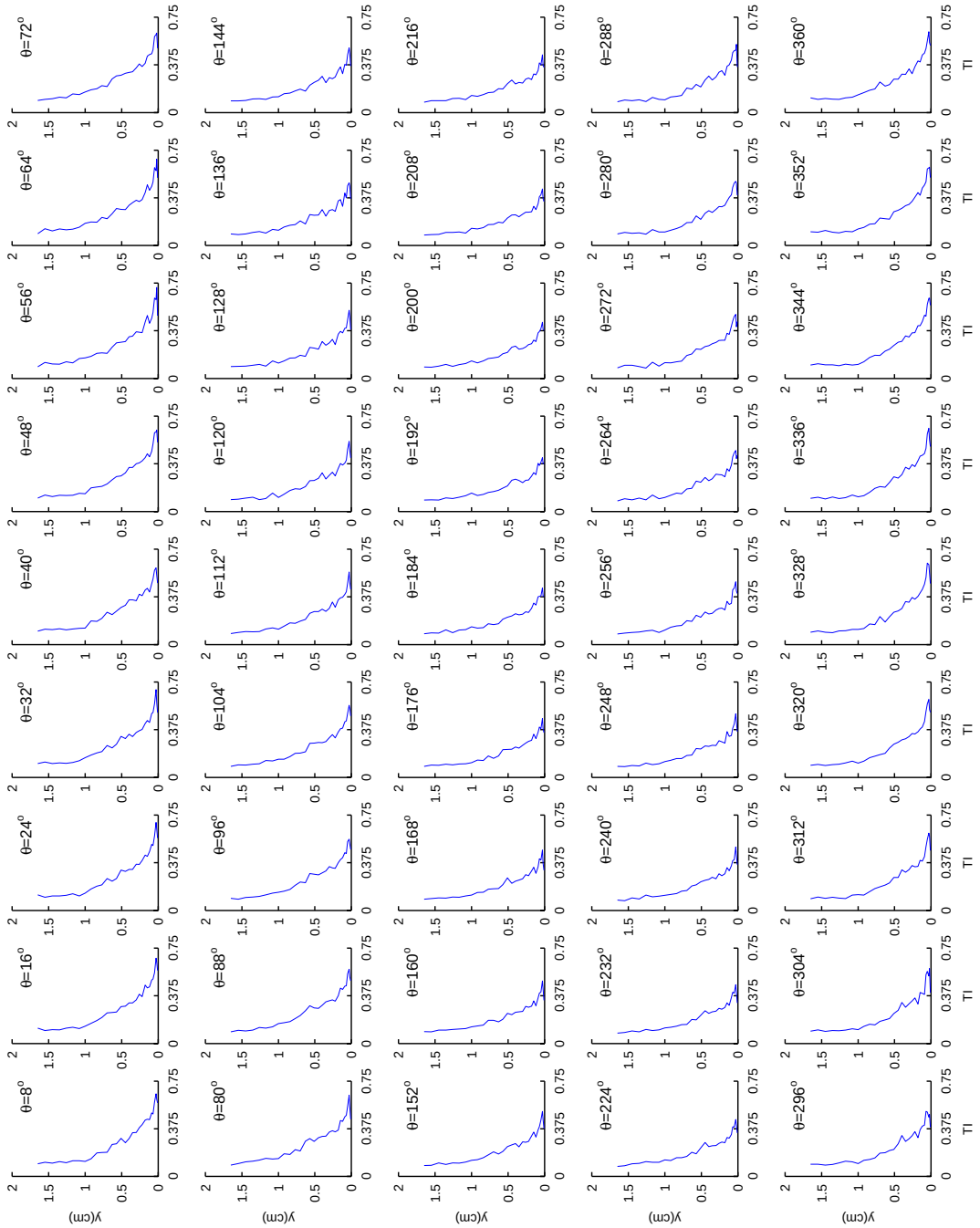

Figure 5.115: Phase average turbulence intensity $\widetilde{TI}(y,\theta)$ at p13, $s/L_{ss} = 93.49\%$, presented as a function of θ.

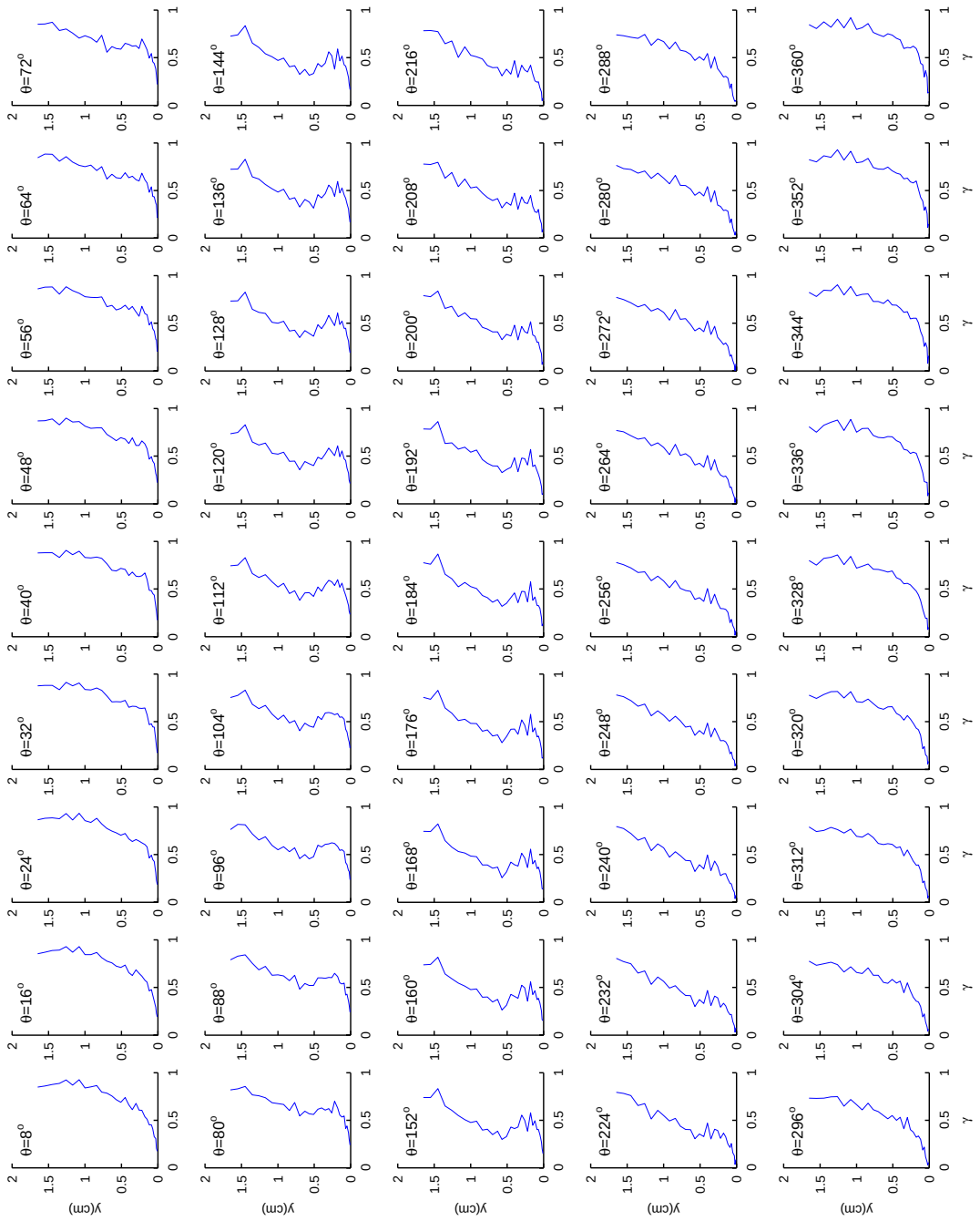

Figure 5.116: Phase average intermittency $\tilde{\gamma}(y, \theta)$ at p13, $s/L_{ss} = 93.49\%$, presented as a function of θ.

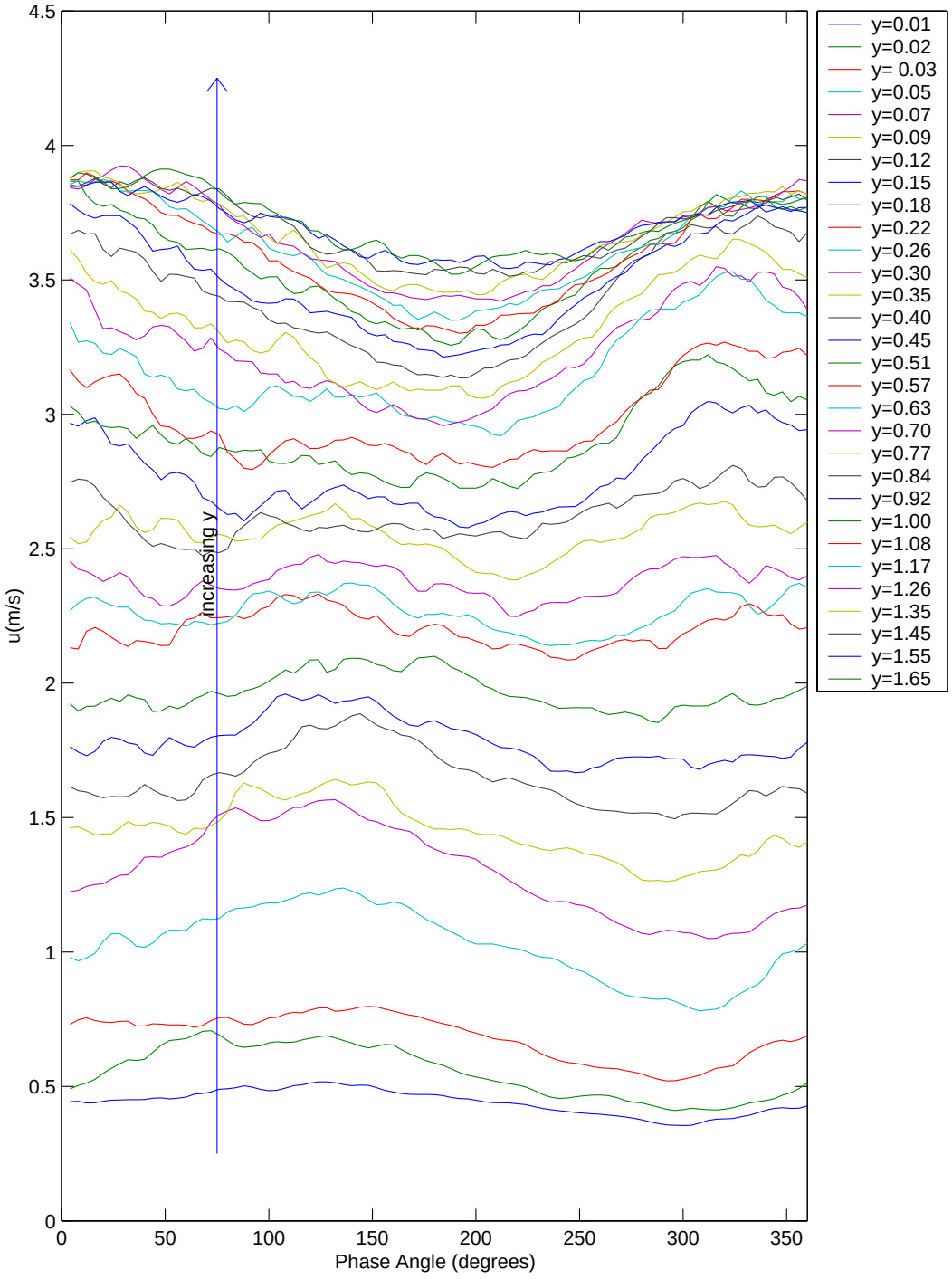

Figure 5.117: Phase average velocity $\tilde{u}(y, \theta)$ at p13, $s/L_{ss} = 93.49\%$, presented as a function of y (y-values are in cm).

Chapter 6

Conclusions

6.1 General Significance and Applicability of the Results

These results represent detailed documentation of the effects periodically passing wakes have upon laminar-to-turbulent transition in a low-pressure turbine passage. These results represent the first documentation of wall-normal, time-resolved velocity distributions inside such a periodic-unsteady flow. Because all the raw velocity measurements obtained in these studies were retained, the results are amenable to further processing such as using frequency-based techniques, including wavelet analysis.

The combination of the velocity profiles and the simplified turbine passage geometry create a flow which is amenable to computational simulation, which should assist in the development and testing of turbine flow calculations and transition models.

Also, the results seem to support some of the existing transition modeling theories, particularly those of Johnson and Ercan (1996) and Mayle and Schulz (1997), who suggest that transition to turbulence in bypass transition flows is due not to the direct introduction of turbulence to the boundary layer, but is due to the response of the near-wall boundary layer to fluctuations of the free-stream flow. Instabilities so generated eventually grow into turbulence. Examining the results presented in sections 5.2.1 through 5.2.3, we can see that the current study shows that fluctuations in the freestream flow seem to induce fluctuations in the near-wall boundary layer which cause the boundary layer thickness to undulate. It is reasonable to assume that the temporal adverse pressure gradient would have a significant effect on transition

to turbulence. This assumption is supported by the documented strong sensitivity of transition to spatial adverse pressure gradients. Thus, the current data appear to support the theories of Johnson and Ercan and Mayle and Schulz. However, whether the near-wall transition is influenced more strongly by low-frequency oscillations of the freestream (as proposed by Johnson and Ercan) or more strongly by high-frequency oscillations (as proposed by Mayle and Schulz) cannot be determined from these results without further analysis. The analysis also shows that the near-wall transition process does not begin immediately upon being disturbed by the free-stream flow, but must first undergo a process of slow amplification before higher-order modes of instability begin to affect the flow, a factor not included in present transition models. Evidence of this delay is a lag of the near-wall intermittency behind the wake.

Finally, a comparison of this information with our previous study without wakes (Simon et al., 2000) highlights to both designers and researchers the significant differences between the wake-free and wake-disturbed turbine flows, and may provide insight into the development of better transition prediction techniques which incorporate unsteadiness effects.

6.2 Specific Conclusions

1. The basic flow field of the wake-disturbed turbine passage flow is similar to that shown for the steady-state flow by Simon et al. (2000): boundary layer growth, followed by separation of the flow. At the Reynolds number studied, the presence of wakes in the flow does not eliminate separation, however it does seem to reduce the length of the separation zone in the boundary layer. The primary difference between the steady flow and the unsteady flow is an overall increase in turbulence level due to the turbulence generated by the wakes, and the movement of the location of separation due to the oscillatory free-stream flow and the wake turbulence.

2. An analysis of the rms velocity and intermittency profiles appears to support the models of Johnson and Ercan (1996) and Mayle and Schulz (1997) for bypass transition in which transition to turbulence in bypass transition flows is due not to the direct introduction of turbulence to the boundary layer, but is due to the response of the near-wall boundary layer to pressure fluctuations in the free-stream flow. Fluctuations in the freestream flow seem to induce fluctuations in

the near-wall boundary layer, which cause the boundary layer to transition to turbulence.

3. Due to the time delay between events happening in the freestream and the boundary-layer's response to these events, for wake-disturbed flows, integral parameters, such as the momentum thickness, energy thickness, or displacement thickness, may not give a proper representation of the boundary layer state. At any moment, they will be simultaneously representing a free-stream and near-wall flow. However, the near-wall flow is retarded in time from the free-stream flow and has not yet had a chance to respond to changing free-stream conditions. Thus, transition models based upon correlations which use local Re_θ values must be examined and tested before being applied to wake-disturbed flows.

6.3 Considerations for Further Study

During the data collection, reduction, and analysis stages of this study, a number of directions for further study on this topic were considered.

First, the flow parameters used in this study, particularly the low suction surface length Reynolds number, $Re_{L_{ss}}$, were representative only of the extreme values seen in turbomachinery flows (typically, $Re_{L_{ss}} \approx 50{,}000$ is seen only in small turbine engines operating at cruise conditions, or engines operating at very high cruise altitudes). A study similar to this one should be repeated with a higher $Re_{L_{ss}}$. Also, studies made with less aggressive blade curvature, or higher *FSTI* (to decrease the likelihood of separation) would provide valuable comparisons with previous studies. Currently, a higher-*FSTI* case is being investigated.

Similarly, the combination of the wake Strouhal number and the rod velocity to axial velocity ratio of the present facility combined to create wakes which were spaced together tightly enough that the flow did not have sufficient time to recover, and the turbulence intensity between wakes did not drop to the background level. A variation of this case with greater wake spacing would allow a study of the calming and re-growth of boundary layers expected with a longer period between wakes. Our current research efforts include a "sparse rod" case, in which the spacing between rods has been doubled, effectively halving the wake Strouhal number, though the rod velocity to approach flow velocity ratio of 0.7 (Figure 2.12) is maintained.

Approximate surface shear stress maps computed from near-wall flow velocities were presented in this study. Previous measurements without wakes (Qiu and Simon, 1997; Simon et al., 2000) showed that separation and reattachment points taken from such shear stress distribution maps which were computed from near-wall flow velocities differed, somewhat, from the more reliable separation and reattachment measurements taken directly from surface shear direction measurements. The problem stems from the difficulty in deducing wall shear stress from near-wall velocity data in thin and rapidly-changing boundary layers. Thus, separation and reattachment values from these approximate surface shear stress maps should be replaced by values measured directly at the wall. Presently, we are developing means for taking such measurements by using thin-film sensors on the airfoil surface as shear stress direction sensors.

Also, the techniques of ensemble averaging and intermittency calculation do not document the wide ranges of time scales that influence the transition processes present in turbomachinery flows. A re-processing of the experimental data using frequency analysis techniques, such as wavelets, may help identify the time scales present in the flow, and further identify the nature of transition in unsteady boundary layers. Some preliminary work on applying this technique to our data has already been done with wavelet analysis of a subset of these data, as presented in Appendix B.

As the effect of spatial and temporal pressure gradients, surface curvature, background turbulence intensity and wakes become better known, there will be opportunity for flow control with surface injection, passive modifications of surface geometry, and active surface geometry changes with Micro Electrical Mechanical (MEMs) activation. Some activity along this line has already begun (Bons et al., 2000; Van Treuren et al., 2001).

Appendix A

Facility Geometry

All of the important dimensions of the wake generator facility are shown in Figures A.1 and A.2. The dimensions themselves are listed in Table A.1.

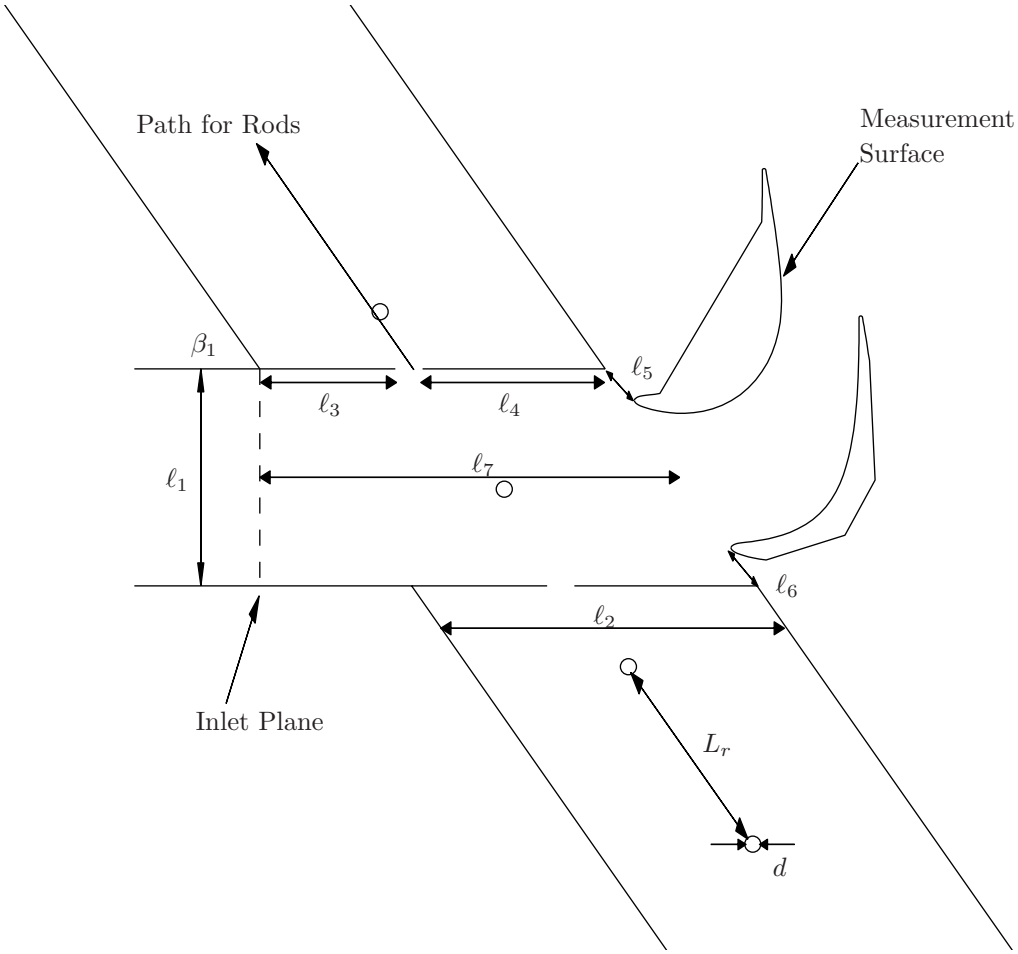

Figure A.1: Wake generator dimensions and geometry

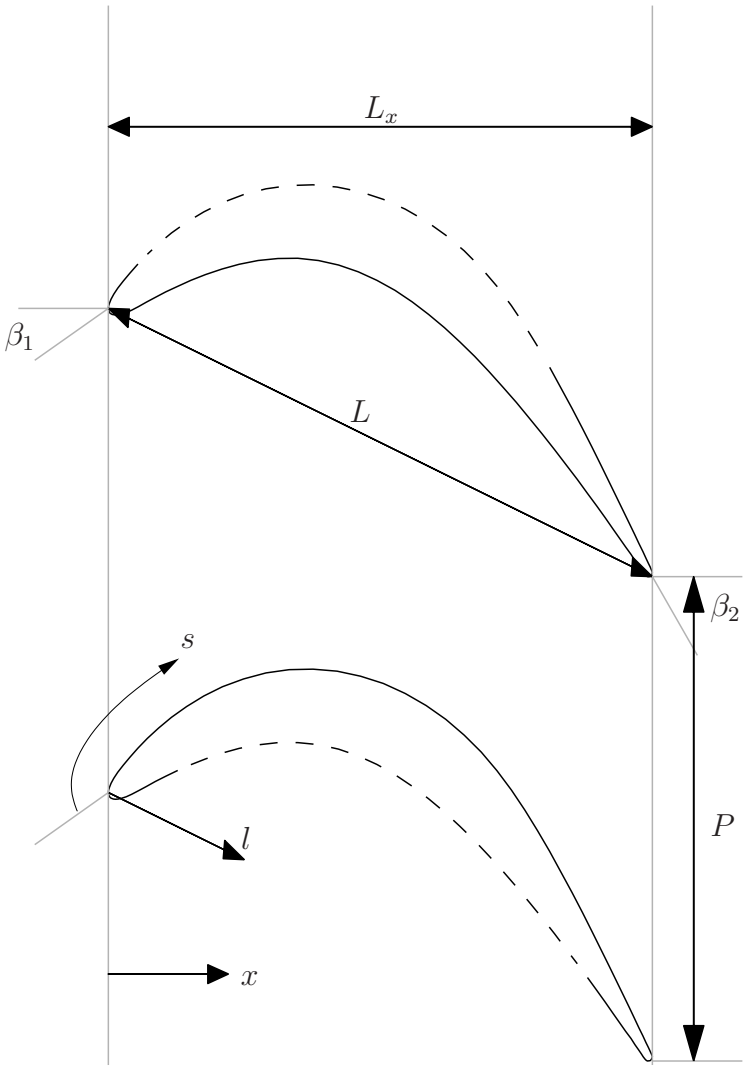

Figure A.2: Turbine passage dimensions and geometry

Table A.1: Wake generator and turbine passage dimensions

Dimension:	**Value:**
Chord length, L:	114.3 mm
Axial chord length, L_x:	103.57 mm
Suction surface length, L_{ss}:	152.76 mm
Axial chord to chord ratio, L_x/L:	0.906
Pitch to chord ratio, P/L:	0.8
Aspect ratio (span/chord), L_z/L:	6.0
Blade inlet angle, β_1:	35°
Blade outlet angle, β_2:	−60°
Rod diameter, d:	3.175 mm
Rod spacing, L_r:	91.44 mm
Inlet channel width, ℓ_1:	114.3 mm
Wake generator streamwise length, ℓ_2:	142.24 mm
Wake generator upstream flap length, ℓ_3:	50.8 mm
Wake generator downstream flap length, ℓ_4:	79.375 mm
Suction surface bleed slot width, ℓ_5:	24.047 mm
Pressure surface bleed slot width, ℓ_6:	24.047 mm
Distance from the inlet plane to the point mid-span between the leading edges, ℓ_7:	182.25 mm

Appendix B

Wavelet Analysis

The techniques of ensemble averaging and intermittency calculation do not allow us to document the unsteady nature of the wide ranges of time scales that influence the transition processes present in turbomachinery flows. We have considered alternate means, and would propose that more be done than is documented in this report. For this study, the complete set of velocity waveforms collected from the wake generator were preserved, which would allow re-processing of the data.

By using wavelet techniques, we can analyze the frequency scales present in the data, providing a wavelet map of the energy content of the velocity signal resolved on both a frequency and time basis. The technique has been used frequently in the literature to analyze turbulence signals, as described by Farge (1992). More recently, wavelet studies in bypass transition flow have been conducted by Lewalle and Ashpis (1995), Lewalle et al. (1997), and Volino (1998).

A fairly complete treatment of the wavelet technique is presented by Farge, but the wavelet process can be summarized as:

1. A wavelet shape is selected, and expressed in the time domain. The wavelet is characterized by its particular shape and frequency.
2. The FFT of the wavelet is calculated.
3. The FFT of the wavelet is multiplied by the FFT of the velocity signal.

4. The inverse FFT is taken of this result, and multiplied by it's complex conjugate to yield a wavelet map of the streamwise component of turbulent energy, $(f)(-u'u'(t,f))$.

This process is repeated until all relevant frequencies of the waveform have been processed.

The result of this process is a wavelet spectral map, which identifies the frequencies present in the signal as a function of time. The overall wavelet map is best analyzed by considering it to be similar to a FFT, but still resolved in the time domain.

For the results presented here, the Sombrero wavelet,

$$w(t) = (t^2 - 1)e^{-t^2/2} \tag{B.1}$$

is used. Wavelet maps are presented for two locations in the flow. Figure B.1 shows the wavelet map at the location nearest the wall at pressure station p07 ($s/L_{ss} = 46.7\%$), while Figure B.2 shows the wavelet map in the freestream flow at the same location (the MATLAB code used to generate these figures is included in Appendix C as `ml.m`). As described in Section 2.1.2, the wake generator operates by moving a rack of seven rods through the flow upstream of our test section.

Examining Figure B.1(a), in which the near-wall velocity signal collected at $y = 0.01\,\text{cm}$ and $s/L_{ss} = 46.7\%$ is presented, we can see that the flow starts out as a quiescent flow, the rods enter the channel, generating a series of wakes, and then the flow returns to steady flow after the last rod has left the channel. Examining the corresponding wavelet map (Figure B.1(b)), we can again see that the flow starts out as a quiescent flow (no significant peaks in the wavelet map), the rods enter the channel (grouping of broad peaks at the 23 Hz level from $0.3 < t < 0.375$), and returns to quiescent, steady flow after the last rod has left the channel. Turbulent flow is characterized by a wide spectrum of time scales. If the flow at a given time is turbulent we would expect to see peaks distributed over a wide range of frequencies at that instant. Examining Figure B.1(b), we can see that in the near-wall region of the flow, wall damping appears to damp out any of the higher frequency oscillations, resulting in only a few small regions of higher frequency activity (for example, 200 to 900 Hz activity is seen at $t \approx 0.10\,\text{s}$ and $t \approx 0.275\,\text{s}$).

However, examining Figure B.2(a), in which we show the freestream velocity at $y = 1.65\,\text{cm}$ and $s/L_{ss} = 46.7\%$, we can see some differences from the near-wall case. In general, the wavelet map for this location (Figure B.2(b)) shows the same overall pattern as seen in the near-wall flow (Figure B.1(b)), with a series of wide peaks centered at 23 Hz during the wake passage portion of the waveform. However, unlike the near-wall flow, there is significant higher-frequency activity (in the range $0.06\,\text{s} < t < 0.375\,\text{s}$) associated with the wakes, suggesting that we are seeing the turbulent strips associated with the wake passage (in the near-wall case, these turbulent strips never penetrated the boundary layer, and, hence, the higher frequency activity was not observed).

The results presented here are preliminary, but suggest that further investigation of this flow using wavelet techniques might provide a technique for better identifying transition to turbulence in this flow, as well as identifying the important time-scales involved in the transition process.

We learned in this processing that the type of wavelet form chosen influenced whether the time resolution was improved at the expense of the frequency resolution (using the Sombrero wavelet) or whether the frequency resolution was enhanced at the expense of the time resolution (using Morlet[1] wavelets, for example). We also learned that these compromises were rather severe, making the processing less fruitful than we had hoped in determining when certain frequencies emerged in the flow.

[1]The Morlet wavelet is a commonly used complex-valued wavelet function defined as $w(t) = [\cos(nt) - i \cdot \sin(nt)]e^{-t^2/2}$.

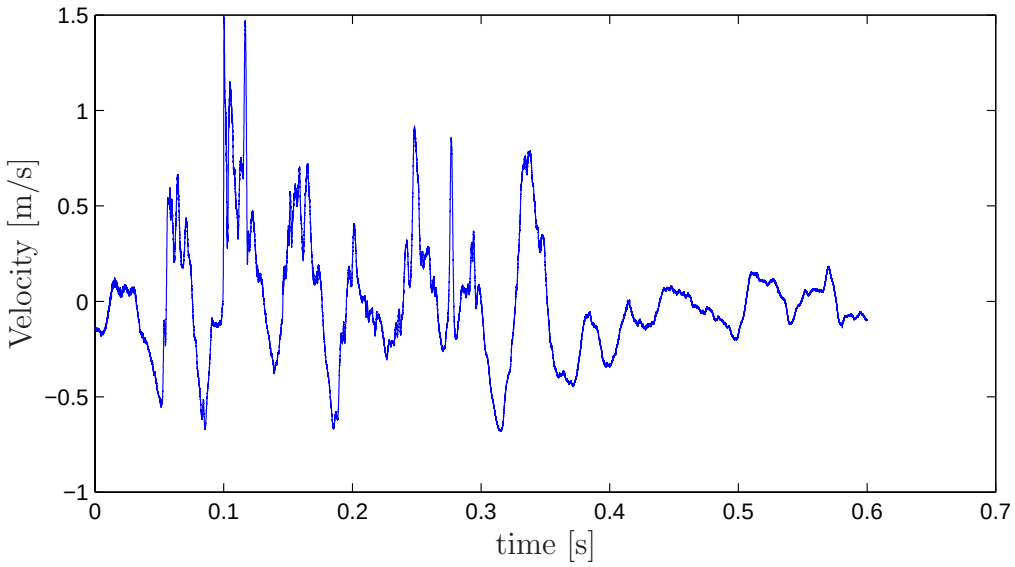

(a) Velocity Signal

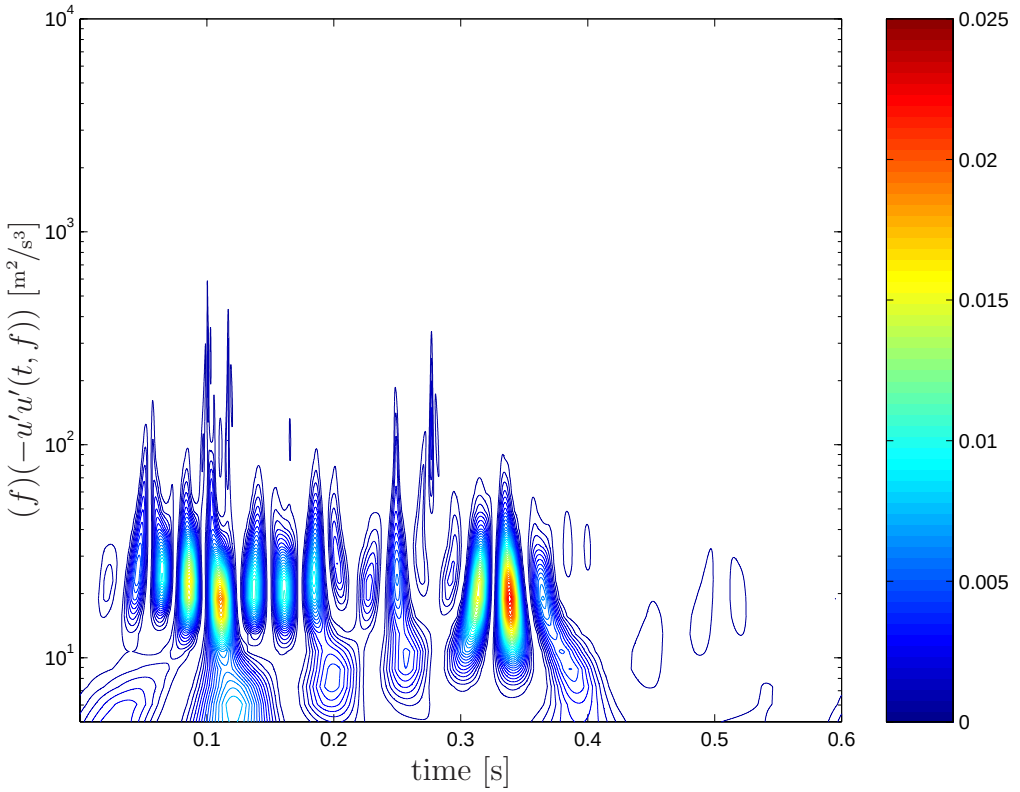

(b) Wavelet Map

Figure B.1: $u'u'$ Sombrero wavelet map at $y = 0.01\,\text{cm}$ at $s/L_{ss} = 46.7\%$

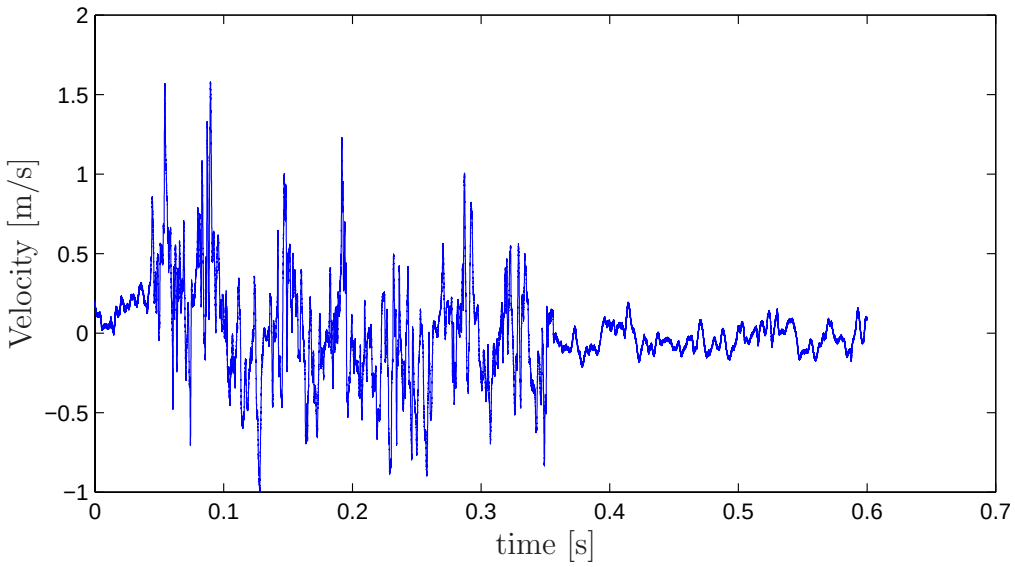

(a) Velocity Signal

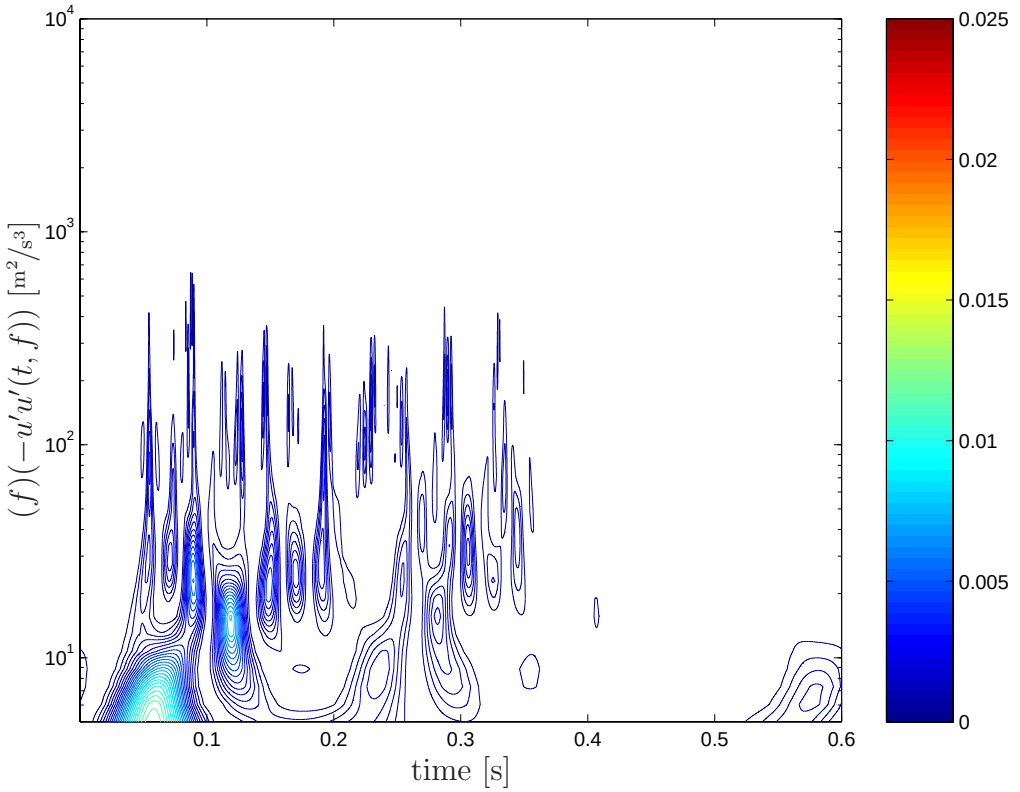

(b) Wavelet Map

Figure B.2: $u'u'$ Sombrero wavelet map at $y = 1.65\,\text{cm}$ at $s/L_{ss} = 46.7\%$

Appendix C

Source Code Listings

This appendix includes a number of programs, written in both C and MATLAB, used in collecting and processing the data. A description of each program is given in table C.1.

Table C.1: Included programs

Program	Language	Description
`automate2.c`	C	Data Collection program for the single-wire anemometer and wake generator.
`superior.c`	C	Data automation program controlling the Superior Electric stepper motor.
`pitotsingle-cal.c`	C	Calibration program for the single-wire anemometer.
`pitottriple-cal.c`	C	Calibration program for the triple-wire anemometer.
`p09.m`	MATLAB	Sample Data Reduction Script which decomposes the velocity and photogate data into individual wakes and calculates ensemble-average velocity and turbulence intensity.
`p09inter.m`	MATLAB	Sample Data Reduction Script which calculates intermittency.
`monte.m`	MATLAB	Monte Carlo script used to estimate experimental uncertainties.
`lengthscale.m`	MATLAB	Script used to calculate power spectral densities and integral length scales.
`wl.m`	MATLAB	Script used to calculate wavelet maps.

C.1 automate2.c

```
#include<stdio.h>
#include<unistd.h>
#include<stdlib.h>
#include<ugpib.h>
#include<math.h>

/* Number of data points collected by the iotech */
#define DATAPOINTS 60000
/* Threshold voltage for determining photogate blockage */
#define THRESHOLD 2.5
/* Ideal length of each wake */
#define IDEALLENGTH 4520
/* Number of data points to shift waveform by */
#define LEADPOINTS 4125
/* Number of trials */
#define TRIALS 35
/* Gain on hotwire bridge */
#define GAIN 4.0

/* Platinum RTD Coefficients: */

#define R0 500.88
#define T0 0.0
#define alpha 0.003859

void main(int argc, char * argv[]) {
  int i,j;                          /* Counter Variables */

  int iotech1;                      /* Hotwire Iotech */
  int iotech2;                      /* Photogate Iotech */
  int dvm;                          /* Fluke DVM with Platinum RTD */
  int powersupply;                  /* HP Power Supply */

  int opt;                          /* Command line option handling */

  FILE * velocitydatafile;          /* Velocity Data (whole record)*/
  FILE * photogatedatafile;         /* Photogate Data */

  FILE * calfile;                   /* Calibration data */
  char * calfilename;               /* The name of the calibration file */

  char mkdirhier[80];
  char banner[80];

  char trialdatafilename[120];      /* The name of the trial data file */
  char photogatedatafilename[120]; /* The name of the photogate data file */

  int pressurelocation;             /* Which pressure location are we at? */
  int ylocation;                    /* Which y-location are we at? */

  char resiststring[200];           /* String read from Fluke */
  double resist;                    /* Measured Resistance */

  double T_dry;                     /* dry temperature */
  double T_ref;                     /* Reference temperatures, stored in calfile */
  double T_sensor=250;              /* Sensor runs at 250 */
  double vcorr,volt;                /* Temperature correction */
  short velocitydata[DATAPOINTS]; /* Velocity Data in 16-bit integer format */
  short photogatedata[DATAPOINTS]; /* Photogate Data in 16-bit integer format */
  short flagdata[4];                /* 4 data points, one for each flag
                                       and two extras*/
  double m,b;                       /* Hotwire Calibration values */
  static double voltage[DATAPOINTS];
                                    /* The velocity voltage data, one channel */
```

```
static double u[DATAPOINTS];
                                /* The velocity data, one channel */
static double photogate[DATAPOINTS];
                                /* The photogate voltage data, one channel */

double startflagvoltage;        /* Photogate voltages */
double endflagvoltage;
double encoderflagvoltage;
int outcount;

/* Parse command line options */
calfilename="calfile.single";

/* Set Reasonable defaults */

pressurelocation=0;
ylocation=0;

while(1) {
  opt=getopt(argc,argv,"y:p:");
  if (opt == -1) break;
  switch (opt) {
  case 'y':                     /* Override default y location */
    ylocation=atoi(optarg);
    break;
  case 'p':                     /* Override default pressure tap location */
    pressurelocation=atoi(optarg);
    break;
  case ':':
    printf("missing argument\n");
    break;
  case '?':
    printf("Unknown option\n");
  }
}

/* Get calibration data */
calfile=fopen(calfilename,"r"); /* Open the calibration file for reading */
fscanf(calfile,"%lf",&T_ref); /* Get the reference temperature */
fscanf(calfile,"%lf %lf\n",&m,&b); /* get calib constants */

/* Find GPIB devices */
iotech1=ibfind("dev13");
iotech2=ibfind("dev14");
powersupply=ibfind("dev4");
dvm=ibfind("dev8");

/* Status report */
printf("Collecting Data at Pressure Location %d and Y location %d\n",
       pressurelocation, ylocation);

/* Find local temperature */
ibclr(dvm);                     /* Clear Fluke */
ibwrt(dvm,"*F4R0S0?",8);        /* Set to 4-wire mode */
sleep(4);                       /* Let it settle out */
ibrd(dvm,resiststring,40);      /* Read the resistance */
resist=atof(resiststring);
T_dry=(resist/R0-1)/alpha+T0;
printf("Temperature is %f degrees C\n",T_dry);

/* Set up velocity iotech. This we only need to do once, since it never
   changes through the run */
ibclr(iotech1);                 /* Clear iotech */
ibtmo(iotech1,T30s);            /* Set a timeout */
ibwrt(iotech1,"M4X",3);         /* Clear Error Mask */
```

```
ibwrt(iotech1,"C1X",3);        /* Use channel 1 only */
ibwrt(iotech1,"R2X",3);        /* +/- 5 volts Range */
ibwrt(iotech1,"G11X",4); /* set up binary little-endian transfer */
ibwrt(iotech1,"I0X",3);        /* Set timing interval */
printf("Velocity Iotech set up\n"); fflush(stdout);

/* Set up photogate iotech.  This we only need to be careful with,
   since at some points in the code we read single points from
   single channels, other times we read a full sequence. */
ibclr(iotech2);                /* Clear iotech */
ibtmo(iotech2,T30s);           /* Set a timeout */
ibwrt(iotech2,"M4X",3);        /* Clear Error Mask */
ibwrt(iotech2,"G11X",4);       /* set up binary little-endian transfer */
ibwrt(iotech2,"I0X",3);        /* Set timing interval */
printf("Photogate Iotech set up\n"); fflush(stdout);

/* Turn off power supply */
printf("Turning off power..."); fflush(stdout);
ibwrt(powersupply,"2000",4);
printf("done (%d bytes written)\n",ibcnt); fflush(stdout);

/* Make storage directory */
sprintf(mkdirhier,"/bin/mkdir -p p%02d/velocity/y%02d\n",
        pressurelocation,ylocation);
printf("%s",mkdirhier);    fflush(stdout);
system(mkdirhier);
sprintf(mkdirhier,"/bin/mkdir -p p%02d/photogate/y%02d\n",
        pressurelocation,ylocation);
printf("%s",mkdirhier);    fflush(stdout);
system(mkdirhier);

/* Do each trial */
for(i=0;i<TRIALS;i++) {        /* Each trial */

  /* First determine that the return flag is triggered */
  ibwrt(iotech2,"C1,2,3,4X",9); /* Use channels 1, 2, 3, and 4  only */
  ibwrt(iotech2,"R#1,2X",6);  /* +/- 5 volts Range */
  ibwrt(iotech2,"R#2,2X",6);  /* +/- 5 volts Range */
  ibwrt(iotech2,"R#3,2X",6);  /* +/- 5 volts Range */
  ibwrt(iotech2,"R#4,2X",6);  /* +/- 5 volts Range */
  ibwrt(iotech2,"N1X",3);     /* Single data point */
  ibwrt(iotech2,"T6X",3);     /* One-shot Trigger on talk */
  sleep(1);
  printf("Reading flags..."); fflush(stdout);
  ibrd(iotech2,(char*)flagdata,8);
  printf("Done (%d bytes read)\n",ibcnt); fflush(stdout);

  encoderflagvoltage=(10.0/60000.0)*flagdata[0];
  startflagvoltage=(10.0/60000.0)*flagdata[2];
  endflagvoltage=(10.0/60000.0)*flagdata[1];

  printf("Flag Voltages:\nEncoder: %f\nStart: %f\nEnd: %f\n",
         encoderflagvoltage,startflagvoltage,endflagvoltage);

  /* Check flag status.  Start flag should be set, and
     end flag and encoder shouldn't be.  If error, exit. */
  if(!((startflagvoltage<THRESHOLD)
       &&(endflagvoltage>THRESHOLD)
       &&(encoderflagvoltage>THRESHOLD))) {
    printf("FATAL PHOTOGATE ERROR.  Exiting...\007\n");
    fflush(stdout);
    exit(1);
  }

  /* Prepare both iotechs for work */
```

```
    ibwrt(iotech1,"N0X",3);       /* Put iotech in FIFO mode */
    ibwrt(iotech1,"T3X",3);       /* Trigger on falling external trigger */

    /* For second iotech, must reset channels, too */
    ibwrt(iotech2,"C1X",3);       /* Channel 1 only */
    ibwrt(iotech2,"R#1,2X", 6);   /* +/- 5 volts Range */
    ibwrt(iotech2,"N0X",3);       /* Put iotech in FIFO mode */
    ibwrt(iotech2,"T3X",3);       /* Trigger on falling external trigger */

    /* Sleep */
    sleep(1);

    /* Turn on power */
    printf("Turning on power..."); fflush(stdout);
    ibwrt(powersupply,"2999",4);
    printf("done (%d bytes written)\n",ibcnt); fflush(stdout);

    /* Read both iotechs */
    printf("Reading %d bytes from velocity iotech...",2*DATAPOINTS);
    fflush(stdout);
    ibrd(iotech1, (char *)velocitydata, DATAPOINTS*2);
    printf("done. (%d bytes read)\n",ibcnt); fflush(stdout);
    printf("Reading %d bytes from photogate iotech...",2*DATAPOINTS);
    fflush(stdout);
    ibrd(iotech2, (char *)photogatedata, DATAPOINTS*2);
    printf("done. (%d bytes read)\n",ibcnt); fflush(stdout);

  /* Recycle the wake generator */

  /* First determine that the end flag is triggered */
    ibwrt(iotech2,"C1,2,3,4X", 9); /* Use channels 1, 2, 3, and 4 only */
    ibwrt(iotech2,"R#1,2X", 6);   /* +/- 5 volts Range */
    ibwrt(iotech2,"R#2,2X", 6);   /* +/- 5 volts Range */
    ibwrt(iotech2,"R#3,2X", 6);   /* +/- 5 volts Range */
    ibwrt(iotech2,"R#4,2X", 6);   /* +/- 5 volts Range */
    ibwrt(iotech2,"N1X", 3);      /* Single data point */
    ibwrt(iotech2,"T6X", 3);      /* One-shot Trigger on talk */
    sleep(1);
    printf("Reading flags..."); fflush(stdout);
    ibrd(iotech2, (char *)flagdata, 8);
    printf("Done (%d bytes read)\n",ibcnt); fflush(stdout);

    encoderflagvoltage=(10.0/60000.0)*flagdata[0];
    startflagvoltage=(10.0/60000.0)*flagdata[2];
    endflagvoltage=(10.0/60000.0)*flagdata[1];

    printf("Flag Voltages:\nEncoder: %f\nStart: %f\nEnd: %f\n",
           encoderflagvoltage,startflagvoltage,endflagvoltage);

    /* Check flag status. Start flag should be set, and
       end flag and encoder shouldn't be. If error, exit. */
    if(!((startflagvoltage>THRESHOLD)
       &&(endflagvoltage<THRESHOLD)
       )) {
      printf("FATAL PHOTOGATE ERROR.  Exiting...\007\n");
      fflush(stdout);
      exit(1);
    }

    /* Prepare both iotechs for work */
    ibwrt(iotech1,"N0X",3);       /* Put iotech in FIFO mode */
    ibwrt(iotech1,"T3X",3);       /* Trigger on falling external trigger */

    /* For second iotech, must reset channels, too */
    ibwrt(iotech2,"C1X",3);       /* Channel 1 only */
```

```
    ibwrt(iotech2,"R#1,2X", 6);  /* +/- 5 volts Range */
    ibwrt(iotech2,"N0X",3);      /* Put iotech in FIFO mode */
    ibwrt(iotech2,"T3X",3);      /* Trigger on falling external trigger */

    /* Sleep */
    sleep(1);

    /* Turn off power */
    printf("Turning off power..."); fflush(stdout);
    ibwrt(powersupply,"2000",4);
    printf("done (%d bytes written)\n",ibcnt); fflush(stdout);

    /* Convert Binary Readings to voltages */
    for(j=0;j<DATAPOINTS;j++)   /* For each reading */
      {
        voltage[j]=((10.0/GAIN)/60000.0)*velocitydata[j];
        photogate[j]=(10.0/60000.0)*photogatedata[j];
      }

    /* Convert Voltage data to the effective velocity seen by each wire */
    vcorr=(T_sensor-T_ref)/(T_sensor-T_dry); /* 1st order
                                                temperature correction */
    for(j=0;j<DATAPOINTS;j++)   /* each datapoint */
      {
        volt=voltage[j]*voltage[j]*vcorr;
        u[j]=pow((b+m*volt),2.29885);
      }

    /* Form the filenames for the velocity and photogate data */
    sprintf(trialdatafilename,"p%02d/velocity/y%02d/p%02dy%02dt%03dvelocity",
            pressurelocation,ylocation,pressurelocation,ylocation,i);
    sprintf(photogatedatafilename,
            "p%02d/photogate/y%02d/p%02dy%02dt%03dphotogate",
            pressurelocation,ylocation,pressurelocation,ylocation,i);

    /* Write velocity data to file */
    printf("Writing u data to file %s...",trialdatafilename); fflush(stdout);
    velocitydatafile=fopen(trialdatafilename,"w");
    outcount=fwrite(u,8,DATAPOINTS,velocitydatafile);
    fflush(velocitydatafile); fclose(velocitydatafile);
    printf("(%d records written)\n",outcount); fflush(stdout);

    /* Write photogate data to file */
    printf("Writing photogate data to file %s...",
           photogatedatafilename); fflush(stdout);
    photogatedatafile=fopen(photogatedatafilename,"w");
    fwrite(photogate,8,DATAPOINTS,photogatedatafile);
    fflush(photogatedatafile); fclose(photogatedatafile);
    printf("(%d records written)\n",outcount); fflush(stdout);

    printf("Total number of trials: %d\n",i+1);
    sprintf(banner,"/usr/bin/figlet -c -f banner3 %d\n",i+1);
    system(banner);


    usleep(1750000);

  }
}
```

C.2 superior.c

```
#include<ugpib.h>
#include<string.h>
#include<stdio.h>
```

```
#include<stdlib.h>
#include<unistd.h>

/* Program to test the superior electric motor controller.  Mostly
   reverse-engineering from Songgang Qiu's experiment.c code.

   Modified to take two command line options, "start" and "finish"

 */

#define writeib(a,b) ibwrt(a,b,strlen(b))

void main(int argc, char * argv[]) {
  int opt;                      /* Command line option handling  */
  int trav;                     /* GPIB pointer for the traverse */
  double y=0.0;                 /* Current location, defaults to 0.0 */
  int ysteps;                   /* Location, in terms of motor steps */
  double ynew;                  /* New location */
  int ystepsnew;                /* New location, in terms of motor steps */
  int steps;                    /* Number of steps to new location */
  char stepstring[30];          /* String representation of steps */
  char ibcommand[50];           /* String for building IB commands */
  double start=0.0;             /* Starting location */
  double finish=0.0;            /* Ending location */
  int startset=0,endset=0;

  /* Parse command line options */
  while(1) {
    opt=getopt(argc,argv,"s:f:e:");
    if (opt == -1) break;
    switch(opt) {
    case 's':                   /* Override default  */
      start=atof(optarg);
      printf("Start at %f cm\n", start);
      startset=1;
      break;
    case 'f':                   /* Override default  */
      finish=atof(optarg);
      printf("End at %f cm\n", finish);
      endset=1;
      break;
    case 'e':                   /* Override default  */
      finish=atof(optarg);
      printf("End at %f cm\n", finish);
      endset=1;
      break;
    case ':':
      printf("missing argument\n");
      break;
    case '?':
      printf("Unknown option\n");
    }
  }

  if(!(startset&&endset)) {
    printf("Must enter both start and finish locations!\n");
    exit(1);
  }

  /* Initialize Traverse */
  trav=ibfind("dev11");         /* Initialize the traverse */

  /* Set starting position */

  y=start;
```

```
  ynew=finish;

  printf("Current Probe Location: %f\n",y);
  printf("New Probe Location:     %f\n",ynew);
  /* We do all calculations in terms of steps to prevent rounding errors.
     2000 is 2000 steps/cm */
  ysteps=2000*y;
  ystepsnew=2000*ynew;
  steps=ystepsnew-ysteps;

  /* Move Probe to the new location */
  ibwrt(trav,"Y.D.\n",5);         /* Send current to the windings */
  ibwrt(trav,"Y.B2000.\n",9); /* Set base speed to 2000 pulse/sec */
  sprintf(stepstring,"%d.",steps); /* Convert steps to string */
  /* Build up command string */
  strcpy(ibcommand,"Y.M");        /* Store value in move register */
  strcat(ibcommand,stepstring); /* The number of steps */
  strcat(ibcommand,"G.\n");       /* Index the motor */
  printf("Moving %d steps to y=%f from y=%f ...",steps,ynew,y);
  ibwrt(trav,ibcommand,strlen(ibcommand)); /* Do it */
  printf("Done! (%d characters of %d written)\n",ibcnt,strlen(ibcommand));
  ibwrt(trav,"Y.B320.\n",8); /* Reset base speed to default 320 */
  ibwrt(trav,"Y.E.\n",5);         /* Remove current from windings */

}
```

C.3 pitotsingle-cal.c

```
#include<ugpib.h>
#include<math.h>
#include<stdio.h>
#include<unistd.h>
#include<pressure.h>

/* Modified 27 October 1999 with corrections for using elliptical
   telescoping Pitot tube. */

#define DATAPOINTS 262144

void main(int argc, char * argv[]) {
  int i;                          /* Counter variable */
  int iotech,board,fluke;         /* gpib pointers to the iotech and
                                     interface board */
  int opt;                        /* command line option handling */
  FILE * calfile;                 /* Where the calibration data is stored */
  char * calfilename;             /* The name of the calibration file */
  double T_dry;                   /* dry temperature */
  double mvalue;                  /* Pressure of calibration jet */
  double Pv;                      /* Pressure of jet, in pascals */
  double p_atm;                   /* Atmosphere pressure */
  double ujet;                    /* jet velocity */
  char response[40];              /* y/n response */
  static short data[DATAPOINTS]; /* The waveform data, 256k data points */
  static double voltage[DATAPOINTS]; /* The voltage data, single channel */
  double vtotal;                  /* For averaging */
  double vave;                    /* Average voltage */
  char reiststring[40];           /* The resistance returned by the flike */
  double resist;                  /* Resistance of RTD */
  int trial=1;                    /* Which trial */
  double R0=500.88;               /* RTD Constants */
  double T0=0.0;
  double alpha=0.003859;
  double gain=4.0;

  /* Parse command line options */
```

```
calfilename="calfile.rough.single";    /* Reasonable defaults */

while(1) {
    opt=getopt(argc,argv,"d:");
    if (opt==-1) break;
    switch (opt) {
    case 'd':                  /* Override default datafile name */
      calfilename=optarg;
      printf("Using calfile \"%s\"\n", calfilename);
      break;
    case ':':
      printf("missing argument\n");
      break;
    case '?':
      printf("Unknown option\n");
  }
}

calfile=fopen(calfilename,"a"); /* Open data file for writing */

/* Configure iotech and IEEE board*/
iotech=ibfind("dev13");
board=ibfind("gpib0");
ibclr(iotech);                 /* Clear the iotech */
ibtmo(iotech,T100s);           /* Set timeout to 30 seconds */
ibwrt(iotech,"C1X",3);         /* Use channel 1 */
ibwrt(iotech,"R2X",3);         /* +/-5 volts range */
ibwrt(iotech,"G11X",4);        /* Binary transfer mode */
ibwrt(iotech,"I4X",3);         /* sample rate */
sleep(1);                      /* Give iotech a chance to catch up */

/* Configure fluke and get temperature */
fluke=ibfind("dev8");
ibclr(fluke);                  /* Clear Fluke */
ibwrt(fluke,"*F4R0S0?",8);
sleep(3);
ibrd(fluke,resiststring,40);
resist=atof(resiststring);
T_dry=(resist/R0-1)/alpha+T0;
printf("Air Temperature is %f degrees C\n",T_dry);
/* Convert T to Kelvin */
T_dry+=273.15;
/* Get Atmospheric Pressure from Pressure Server */
p_atm=findpressure_mbar();
printf("Atmospheric pressue in mbar: %f\n",p_atm);

while(1)                       /* Loop repeatedly, gathering data */
  {
    /* Get Pressure Data and calculate jet velocity */
    printf("Input total delta p across jet in inH20:\n");
    scanf("%lf",&mvalue);
    Pv = mvalue*2*249.08891;
    printf("Velocity Pressure in Pa: %f\n",Pv);
    ujet=1.291*sqrt(1000.0/p_atm*T_dry/289.0*Pv);
    printf("Calibration jet velocity: %g\n", ujet);

    /* Acquire Data from Iotech, binary mode */
    ibwrt(iotech,"N0X",3);     /* Put iotech in FIFO mode */
    ibwrt(iotech,"T0X",3);     /* Trigger on talk */
    sleep(1);
    printf("Acquiring data ..."); fflush(stdout);
    ibrd(iotech,(char *)data,2*DATAPOINTS); /* 2 bytes per data point,
                                               1 channels,
                                               256k data points */
    printf("done. (%d bytes collected)\007\n",ibcnt); fflush(stdout);
```

```
      /* Convert Binary Readings to voltages */
      for(i=0;i<DATAPOINTS;i++) /* For each reading */
        {
              voltage[i]=((10.0/gain)/60000.0)*data[i];
        }

      /* Find average voltage seen by each wire */
      vtotal=0.0;
      for(i=0;i<DATAPOINTS;i++) /* each datapoint */
        {
          vtotal+=voltage[i];
        }

      /* Calculate Averages */
      vave=vtotal/DATAPOINTS;

      /* Report Values to screen */
      printf("vave:    %g\n", vave);
      /* Report Values to data file */
      fprintf(calfile,"%d\t%g\t%g\n",
              trial,ujet,vave);
      fflush(calfile);
      /* Continue? */
      printf("Continue?\n");
      scanf("%s",response);
      if((response[0]=='n')||(response[0]=='N')) break;
      trial++;
    }
  fclose(calfile);

}
```

C.4 pitottriple-cal.c

```
#include<ugpib.h>
#include<math.h>
#include<stdio.h>
#include<unistd.h>
#include<stdlib.h>
#include<pressure.h>

#define DATAPOINTS 262144

void main(int argc, char * argv[]) {
  int i,j;                          /* Counter variables */
  int iotech1,fluke;                /* gpib pointers to the iotech and fluke */
  int opt;                          /* command line option handling */
  FILE * calfile;                   /* Where the calibration data is stored */
  char * calfilename;               /* The name of the calibration file */
  double T_dry;                     /* dry temperature */
  double mvalue;                    /* Pressure of calibration jet */
  double p_atm;                     /* Atmosphere pressure */
  double Pv;                        /* Pressure of jet, in pascals */
  double ujet;                      /* jet velocity */
  double ueffn;                     /* effective normal velocity */
  double ueff;                      /* jet velocity seen by wires */
  char response[40];                /* y/n response */
  static short data[DATAPOINTS][4]; /* The waveform data, 256k data points */
  static double voltage[3][DATAPOINTS]; /* The voltage data, three channels */
  double angle=35.26;               /* Angle of hot wires, in degrees */
  double theta;                     /* The same in radians */
  double v1total,v2total,v3total; /* For averaging */
  double v1ave,v2ave,v3ave;         /* Average voltages */
  int trial=1;                      /* Which trial */
```

```
char resiststring[40];          /* The resistance returned by the flike */
double resist;                  /* Resistance of RTD */
double R0=500.88;               /* RTD Constants */
double T0=0.0;
double alpha=0.003859;

/* Parse command line options */
calfilename="calfile.rough";    /* Reasonable defaults */

while(1) {
    opt=getopt(argc,argv,"d:");
    if (opt==-1) break;
    switch (opt) {
    case 'd':                   /* Override default datafile name */
      calfilename=optarg;
      printf("Using calfile \"%s\"\n", calfilename);
      break;
    case ':':
      printf("missing argument\n");
      break;
    case '?':
      printf("Unknown option\n");
  }
}

calfile=fopen(calfilename,"a"); /* Open data file for writing */

/* Configure iotech and IEEE board*/
iotech1=ibfind("dev13");
ibclr(iotech1);                 /* Clear the iotech */
ibtmo(iotech1,T100s);           /* Set timeout to 100 seconds */
ibwrt(iotech1,"M4X",3);         /* Clear buffer overrun mask if set */
ibwrt(iotech1,"C1,2,3,4X",9);   /* Use channels 1-4 */
ibwrt(iotech1,"R1,1,1,1X",9);   /* +/-2.5 volts on each channel */
ibwrt(iotech1,"G11X",4);        /* Binary transfer mode */
ibwrt(iotech1,"I4X",3);         /* sample rate */
sleep(1);                       /* Give iotech a chance to catch up */

/* Configure fluke and get temperature */
fluke=ibfind("dev8");
ibclr(fluke);                   /* Clear Fluke */
ibwrt(fluke,"*F4R0S0?",8);
sleep(3);
ibrd(fluke,resiststring,40);
resist=atof(resiststring);
T_dry=(resist/R0-1)/alpha+T0;
printf("Air Temperature is %f degrees C\n",T_dry);
/* Convert T to Kelvin */
T_dry+=273.15;
/* Get Atmospheric Pressure from Pressure Server */
p_atm=findpressure_mbar();
printf("Atmospheric pressue in mbar: %f\n",p_atm);

/* Calculate theta of wires */
theta=(M_PI/180.)*angle;

while(1)                        /* Loop repeatedly, gathering data */
  {
    /* Get Pressure Data and calculate jet velocity */
    printf("Input halt-column delta p across manometer in inH20:\n");
    scanf("%lf",&mvalue);
    Pv = mvalue*2*249.08891;
    printf("Velocity Pressure in Pa: %f\n",Pv);
    ujet=1.291*sqrt(1000.0/p_atm*T_dry/289.0*Pv);
    printf("Calibration jet velocity: %g\n", ujet);
```

```
        ueffn=ujet*sin(theta);
        ueff=sqrt(2.04*ueffn*ueffn);
        printf("Effective velocity: %g\n", ueff);

        /* Acquire Data from Iotech, binary mode */
        ibwrt(iotech1,"N0X",3);     /* Put iotech in FIFO mode */
        ibwrt(iotech1,"T0X",3);     /* Trigger on talk */
        sleep(1);
        printf("Acquiring data..."); fflush(stdout);
        ibrd(iotech1, (char *)data, 2*4*DATAPOINTS); /* 2 bytes per data point,
                                                        4 channels,
                                                        256k data points */
        printf("done.\007\n"); fflush(stdout);

        /* Convert Binary Readings to voltages */
        for(i=0;i<DATAPOINTS;i++) /* For each reading */
          {
            for(j=0;j<3;j++)              /* For each channel */
              {
                voltage[j][i]=(4.0/60000.0)*data[i][j];
              }
          }

        /* Find average voltage seen by each wire */
        v1total=0.0;
        v2total=0.0;
        v3total=0.0;
        for(i=0;i<DATAPOINTS;i++) /* each datapoint */
          {
            v1total+=voltage[0][i];
            v2total+=voltage[1][i];
            v3total+=voltage[2][i];
          }

        /* Calculate Averages */
        v1ave=v1total/DATAPOINTS;
        v2ave=v2total/DATAPOINTS;
        v3ave=v3total/DATAPOINTS;

        /* Report Values to screen */
        printf("v1ave:     %g\n", v1ave);
        printf("v2ave:     %g\n", v2ave);
        printf("v3ave:     %g\n", v3ave);
        /* Report Values to data file */
        fprintf(calfile,"%d\t%g\t%g\t%g\t%g\n",
                trial,ueff,v1ave,v2ave,v3ave);
        fflush(calfile);
        /* Continue? */
        printf("Continue?\n");
        scanf("%s",response);
        if((response[0]=='n')||(response[0]=='N')) break;
        trial++;
      }
    fclose(calfile);

}
```

C.5 p09.m

```
clear;
clf;

leadpoints=3550;

%Sampling frequency
```

```
frequency=100000;
ideallength=4500;
trials=35;
rods=6;
pressurelocation=9;
phasesegments=90;
ystations=30;
ylocation=1;
y=[0.01 0.02 0.03 0.05 0.07 0.09 0.12 0.15 0.18 0.22 0.26 0.30 0.35 ...
   0.40 0.45 0.51 0.57 0.63 0.70 0.77 0.84 0.92 1.00 1.08 1.17 1.26 ...
   1.35 1.45 1.55 1.65];
wakes=rods*trials;
datapoints=60000;
pulsetime=zeros(1,50);
wakedata=zeros(wakes,ideallength);
uphase=zeros(phasesegments,ystations);
urmsphase=zeros(phasesegments,ystations);
tiphase=zeros(phasesegments,ystations);

% For each trial, we load in the photogate data and the velocity
% data.  We find each state change in the photogate data, and use that
% to find the center of each wake.  We then extract the wakes from
% each velocity data file

% For each y location
for ylocation=1:ystations,
  ylocation
  % For each trial
  for i=1:trials,
    velocityfilename=sprintf('p%02d/velocity/y%02d/p%02dy%02dt%03dvelocity',...
                             pressurelocation,ylocation,pressurelocation,...
                             ylocation,i-1);
    velocityfid=fopen(velocityfilename);
    velocitydata=fread(velocityfid,inf,'double');
    fclose(velocityfid);
    photogatefilename=sprintf('p%02d/photogate/y%02d/p%02dy%02dt%03dphotogate',...
                              pressurelocation,ylocation,...
                              pressurelocation,ylocation,i-1);
    photogatefid=fopen(photogatefilename);
    photogatedata=fread(photogatefid,inf,'double');
    fclose(photogatefid);
    % Find state changes
    pulses=0;
    lastpoint=5.0;
    for j=1:datapoints,
      if((lastpoint>2.5)&(photogatedata(j)<2.5))
        pulsetime(pulses+1)=j;
        pulses=pulses+1;
      end
      if((lastpoint<2.5)&(photogatedata(j)>2.5))
        pulsetime(pulses+1)=j;
        pulses=pulses+1;
      end
      lastpoint=photogatedata(j);
      if(pulses==28)
        break;
      end
    end
    % For each of the six wakes, take the ideallength points
    % around the center of the wake
    for j=1:6,
      thiswake=(i-1)*rods+j;
      centerpulse=pulsetime(7+4*(j-1));
      centerwake=centerpulse+leadpoints;
      wake=velocitydata((centerwake-ideallength/2):...
```

```
                        (centerwake+ideallength/2-1));
      wakedata(thiswake,:)=wake';
    end
  end
  % For each phase segment, find the mean velocity and the
      % rms fluctuation
  segmentlength=ideallength/phasesegments;
  for i=1:phasesegments,
    startsegment=(i-1)*(segmentlength*1)+1;
    endsegment=startsegment+segmentlength-1;
    segment=reshape(wakedata(:,[startsegment:endsegment]),1,...
                    segmentlength*wakes);
    uphase(i,ylocation)=mean(segment);
    urmsphase(i,ylocation)=std(segment);
  end
plot(uphase(:,[1:ylocation]));
pause(0.05);
end
tiphase=urmsphase./uphase;
phase=360*([1:phasesegments]/phasesegments);

savefilename=sprintf('p%02d.mat',pressurelocation);
save(savefilename,'uphase','urmsphase','tiphase','y',...
     'phase','pressurelocation');
```

C.6 p09inter.m

```
clear;
clf;

% Second pass---this one uses the profile results from the first pass
% calculate intermittency. (To calculate the windowing time and
% threshold values, we need to have a fairly decent estimate of the
% freestream velocity)

leadpoints=3550;

%Sampling frequency
frequency=100000;
ideallength=4500;
trials=35;
rods=6;
pressurelocation=9;
phasesegments=90;
ystations=30;
ylocation=1;
y=[0.01 0.02 0.03 0.05 0.07 0.09 0.12 0.15 0.18 0.22 0.26 0.30 0.35 0.40 ...
   0.45 0.51 0.57 0.63 0.70 0.77 0.84 0.92 1.00 1.08 1.17 1.26 1.35 1.45 ...
   1.55 1.65];
wakes=rods*trials;
datapoints=60000;
pulsetime=zeros(1,50);
uphase=zeros(phasesegments,ystations);
urmsphase=zeros(phasesegments,ystations);
tiphase=zeros(phasesegments,ystations);
rod1wakes=linspace(1, 205, 35);
rod2wakes=linspace(2, 206, 35);
rod3wakes=linspace(3, 207, 35);
rod4wakes=linspace(4, 208, 35);
rod5wakes=linspace(5, 209, 35);
rod6wakes=linspace(6, 210, 35);
uphase1=zeros(phasesegments,ystations);
urmsphase1=zeros(phasesegments,ystations);
tiphase1=zeros(phasesegments,ystations);
interphase1=zeros(phasesegments,ystations);
```

```
uphase2=zeros(phasesegments,ystations);
urmsphase2=zeros(phasesegments,ystations);
tiphase2=zeros(phasesegments,ystations);
interphase2=zeros(phasesegments,ystations);
uphase3=zeros(phasesegments,ystations);
urmsphase3=zeros(phasesegments,ystations);
tiphase3=zeros(phasesegments,ystations);
interphase3=zeros(phasesegments,ystations);
uphase4=zeros(phasesegments,ystations);
urmsphase4=zeros(phasesegments,ystations);
tiphase4=zeros(phasesegments,ystations);
interphase4=zeros(phasesegments,ystations);
uphase5=zeros(phasesegments,ystations);
urmsphase5=zeros(phasesegments,ystations);
tiphase5=zeros(phasesegments,ystations);
interphase5=zeros(phasesegments,ystations);
uphase6=zeros(phasesegments,ystations);
urmsphase6=zeros(phasesegments,ystations);
tiphase6=zeros(phasesegments,ystations);
interphase6=zeros(phasesegments,ystations);

interdata=zeros(wakes,ideallength);
interphase=zeros(phasesegments,ystations);
t=[0:(datapoints-1)]'/frequency;
deltat=1/frequency;
threshfactor=2.75;
ds=4e-6;
nu=15.75;

firststagefilename=sprintf('p%02d.mat',pressurelocation);

load(firststagefilename,'uphase');

% For each trial, we load in the photogate data and the velocity
% data.  We find each state change in the photogate data, and use that
% to find the center of each wake.  We then calculate the
% intermittency for each velocity trace, and use the photogate data to
% break this into wakes and ensemble average it like we did in the
% first pass

% For each y location
for ylocation=1:ystations,
  ylocation
        % Calculate correction factor
  ycur=y(ylocation)
  yscale=2*y(ylocation)*1e-2/ds
  if yscale<50,
          kw=0.9-7.2e-2*yscale+2.89e-3*yscale.^2-6.15E-5*yscale.^3 ...
              +6.51e-7*yscale.^4
  else
          kw=0.54-2.42e-2*yscale+5.01e-4*yscale.^2-5.36E-6*yscale.^3 ...
              +2.85e-8*yscale.^4
  end
  % For each trial
  for i=1:trials,
    i
    velocityfilename=sprintf( ...
      'p%02d/velocity/y%02d/p%02dy%02dt%03dvelocity',...
      pressurelocation,ylocation,pressurelocation,ylocation,i-1);
    velocityfid=fopen(velocityfilename);
    velocitydata=fread(velocityfid,inf,'double');
    fclose(velocityfid);
    photogatefilename=sprintf( ...
      'p%02d/photogate/y%02d/p%02dy%02dt%03dphotogate',...
      pressurelocation,ylocation,pressurelocation,ylocation,i-1);
```

```
photogatefid=fopen(photogatefilename);
photogatedata=fread(photogatefid,inf,'double');
fclose(photogatefid);
% calcule u and du/dt
u=velocitydata;
dudt=[diff(u)./diff(t); 0];
% Calculate the criterion function and the threshold
criterion=u.*dudt;
threshold=threshfactor*std(criterion([3550:35050]));
criterion=abs(criterion);
threshline=threshold*ones(datapoints,1);
% Calculate the windowing time from the BL scale
delta=0.0165; % approximated BL thickness
Ufs=mean(uphase(:,30)); % approximated mean freestream velocity
tbl=delta/Ufs;
tw=tbl*2.5; % as suggested by Blair(1983)
% Initialize gamma, td, and jend
gamma=zeros(datapoints,1);
td=0;
jend=1;
j=1;
eventcontinues=1;
while j<(datapoints+1),
  % March through criterion, comparing each point to the threshold
  if (criterion(j)>threshold)
    td = (j-jend)*deltat;
  if (td>tw)
    % assume a new event is starting
    jstart=j;
  else
    % assume this is a continuation of a previous event
    jstart=jend;
  end
  while (eventcontinues>0),
          % Calculate average value of criterion since jstart
    criterionave=mean(criterion(jstart:j));
    if (criterionave>threshold) | (criterion(j)>threshold)
            eventcontinues=1;
    else
            jend=j;
      eventcontinues=0;
    end
          j=j+1;
  end
  td=(jstart-jend)*deltat;
  if (td<tw)
    gamma([jstart:j])=ones(j-jstart+1,1);
    jend=j;
  else
    jend=jstart;
       end
  end
       j=j+1;
end
     gamma2=ceil((criterion-threshold)/max(criterion));
% Find state changes
pulses=0;
lastpoint=5.0;
for j=1:datapoints,
  if ((lastpoint>2.5)&(photogatedata(j)<2.5))
    pulsetime(pulses+1)=j;
    pulses=pulses+1;
  end
  if ((lastpoint<2.5)&(photogatedata(j)>2.5))
    pulsetime(pulses+1)=j;
```

```
      pulses=pulses+1;
    end
    lastpoint=photogatedata(j);
    if (pulses==28)
      break;
    end
  end
  % For each of the six wakes, take the ideallength points
  % of intermittency around the center of the wake
  for j=1:6,
    thiswake=(i-1)*rods+j;
    centerpulse=pulsetime(7+4*(j-1));
    centerwake=centerpulse+leadpoints;
    wake=velocitydata((centerwake-ideallength/2):...
                      (centerwake+ideallength/2-1));
    wakedata(thiswake,:)=wake';
    interwake=gamma((centerwake-ideallength/2):...
                    (centerwake+ideallength/2-1));
    interdata(thiswake,:)=interwake';
  end
% For each wake, calculate the velocity correction if required
if y<0.04,
wakedataraw=wakedata;
for i=1:wakes
  for j=1:ideallength
    if interdata(i,j)<1
            wakedata(i,j)=(wakedataraw(i,j).^0.45-...
                           ((nu/ds)^.45)*kw).^(1/.45);
    else
            wakedata(i,j)=0.84*(wakedataraw(i,j).^0.45-...
              ((nu/ds)^.45)*kw).^(1/.45)+0.16*wakedataraw(i,j);
    end
  end
end
end
end
% For each phase segment, find the mean velocity and the
      % rms fluctuation
segmentlength=ideallength/phasesegments;
for i=1:phasesegments,
  startsegment=(i-1)*(segmentlength*1)+1;
  endsegment=startsegment+segmentlength-1;
  segment=reshape(interdata(:,[startsegment:endsegment]),...
                  1,segmentlength*wakes);
  segment1=reshape(interdata(rod1wakes,[startsegment:endsegment]),...
                   1,segmentlength*wakes/6);
  segment2=reshape(interdata(rod2wakes,[startsegment:endsegment]),...
                   1,segmentlength*wakes/6);
  segment3=reshape(interdata(rod3wakes,[startsegment:endsegment]),...
                   1,segmentlength*wakes/6);
  segment4=reshape(interdata(rod4wakes,[startsegment:endsegment]),...
                   1,segmentlength*wakes/6);
  segment5=reshape(interdata(rod5wakes,[startsegment:endsegment]),...
                   1,segmentlength*wakes/6);
  segment6=reshape(interdata(rod6wakes,[startsegment:endsegment]),...
                   1,segmentlength*wakes/6);
  interphase(i,ylocation)=mean(segment);
  interphase1(i,ylocation)=mean(segment1);
  interphase2(i,ylocation)=mean(segment2);
  interphase3(i,ylocation)=mean(segment3);
  interphase4(i,ylocation)=mean(segment4);
  interphase5(i,ylocation)=mean(segment5);
  interphase6(i,ylocation)=mean(segment6);
  segment=reshape(wakedata(:,[startsegment:endsegment]),...
                  1,segmentlength*wakes);
```

```
    segment1=reshape(wakedata(rod1wakes,[startsegment:endsegment]),...
                     1,segmentlength*wakes/6);
    segment2=reshape(wakedata(rod2wakes,[startsegment:endsegment]),...
                     1,segmentlength*wakes/6);
    segment3=reshape(wakedata(rod3wakes,[startsegment:endsegment]),...
                     1,segmentlength*wakes/6);
    segment4=reshape(wakedata(rod4wakes,[startsegment:endsegment]),...
                     1,segmentlength*wakes/6);
    segment5=reshape(wakedata(rod5wakes,[startsegment:endsegment]),...
                     1,segmentlength*wakes/6);
    segment6=reshape(wakedata(rod6wakes,[startsegment:endsegment]),...
                     1,segmentlength*wakes/6);
    uphase(i,ylocation)=mean(segment);
    urmsphase(i,ylocation)=std(segment);
    uphase1(i,ylocation)=mean(segment1);
    urmsphase1(i,ylocation)=std(segment1);
    uphase2(i,ylocation)=mean(segment2);
    urmsphase2(i,ylocation)=std(segment2);
    uphase3(i,ylocation)=mean(segment3);
    urmsphase3(i,ylocation)=std(segment3);
    uphase4(i,ylocation)=mean(segment4);
    urmsphase4(i,ylocation)=std(segment4);
    uphase5(i,ylocation)=mean(segment5);
    urmsphase5(i,ylocation)=std(segment5);
    uphase6(i,ylocation)=mean(segment6);
    urmsphase6(i,ylocation)=std(segment6);
  end
end
tiphase=urmsphase./uphase;
tiphase1=urmsphase1./uphase1;
tiphase2=urmsphase2./uphase2;
tiphase3=urmsphase3./uphase3;
tiphase4=urmsphase4./uphase4;
tiphase5=urmsphase5./uphase5;
tiphase6=urmsphase6./uphase6;
phase=360*([1:phasesegments]/phasesegments);
fullphase=[phase,360+phase,720+phase,1080+phase,1440+phase,1800+phase];
ubyrod=[uphase1;uphase2;uphase3;uphase4;uphase5;uphase6];
urmsbyrod=[urmsphase1;urmsphase2;urmsphase3;...
           urmsphase4;urmsphase5;urmsphase6];
tibyrod=[tiphase1;tiphase2;tiphase3;tiphase4;tiphase5;tiphase6];
interbyrod=[interphase1;interphase2;interphase3;...
            interphase4;interphase5;interphase6];

%recalculate uphase, urmsphase, tiphase, and interphase
uphase=(uphase1+uphase2+uphase3+uphase4)/4;
urmsphase=(urmsphase1+urmsphase2+urmsphase3+urmsphase4)/4;
interphase=(interphase1+interphase2+interphase3+interphase4)/4;
tiphase=urmsphase./uphase;


savefilename=sprintf('p%02dfourrod.mat',pressurelocation);
save(savefilename,'interphase','uphase','urmsphase',...
     'tiphase','y','phase','pressurelocation','fullphase',...
     'ubyrod','urmsbyrod','tibyrod','interbyrod');
```

C.7 monte.m

```
clear;
clf;
N=1000000;
conf=0.95;
confint=[(1-conf)/2 (1+conf)/2];
% For normals, relate delta to sigma
prob=norminv(confint);
```

```
probscale=1/(prob(2));
% We want to calculate the uncertainty in velocity based upon
% uncertainties in voltage

% First, here are the mean values of all the quanties
voltage_mean=1.06314;
b_mean=-1.2784;
m_mean=2.8611;
Tsensor_mean=250;
Tref_mean=24.8;
Tdry_mean=25.2;

% And approximated uncertainties
voltage_delta=.001;
b_delta=.04;
m_delta=.004;
Tsensor_delta=10;
Tref_delta=0.2;
Tdry_delta=0.2;

% Create a matrix of N random values for each value,
voltage=random('norm',voltage_mean,voltage_delta*probscale,N,1);
b=random('norm',b_mean,b_delta*probscale,N,1);
m=random('norm',m_mean,m_delta*probscale,N,1);
Tsensor=random('norm',Tsensor_mean,Tsensor_delta*probscale,N,1);
Tref=random('norm',Tref_mean,Tref_delta*probscale,N,1);
Tdry=random('norm',Tdry_mean,Tdry_delta*probscale,N,1);

% Calculate the velocity from the given parameters

velocity=volt2vel(voltage,b,m,Tsensor,Tref,Tdry);
%hist(velocity,100);
%velocity_sigma=std(velocity)
%velocity_delta=velocity_sigma/probscale
%velocity_delta/mean(velocity)
hist(voltage,100);
xlabel('voltage (V)');
print -deps voltage;
hist(b,100);
xlabel('b');
print -deps b;
hist(m,100);
xlabel('m');
print -deps m;
hist(Tsensor,100);
xlabel('T_{sensor} (\circC)');
print -deps Tsensor;
hist(Tref,100);
xlabel('T_{ref} (\circC)');
print -deps Tref;
hist(Tdry,100);
xlabel('T_{dry} (\circC)');
print -deps Tdry;
hist(velocity,100);
xlabel('Velocity (m/s)');
print -deps velocity;
```

C.8 lengthscale.m

```
clear;
clf;

%Sampling frequency
freq=2000;
```

```
ufid=fopen('uraw');
vfid=fopen('vraw');
wfid=fopen('wraw');
u=fread(ufid,inf,'double');
v=fread(vfid,inf,'double');
w=fread(wfid,inf,'double');

ubar=mean(u);
vbar=mean(v);
wbar=mean(w);

urms=sqrt(var(u));
vrms=sqrt(var(v));
wrms=sqrt(var(w));

u=u-ubar;
v=v-vbar;
w=w-wbar;

% Calculate a -5/3 power law for comparison
fcompare=logspace(1.5,3);
PSDcompare=fcompare.^(-5/3);

%Choose appropriate windowing function:

window=boxcar(512);

%Calculate the PSDs

[Pu,fu]=psd(u,512,freq,window,'none');
[Pv,fv]=psd(v,512,freq,window,'none');
[Pw,fw]=psd(w,512,freq,window,'none');
W=norm(window)^2/sum(window)^2; % Normalize as per matlab email
Pu=4*Pu*W/(fu(2)-fu(1)); % Scale on df
Pv=4*Pv*W/(fv(2)-fv(1)); % Scale on df
Pw=4*Pw*W/(fw(2)-fw(1)); % Scale on df

loglog(fu,Pu,'r-',fu,Pv,'g--',fu,Pw,'b-.',fcompare,0.25*PSDcompare,'k--');
legend('uprime','vprime','wprime','-5/3 power relation');

%title('PSD of u\prime, v\prime, and w\prime, sampled at 2 kHz for 1049 seconds');
xlabel('frequency (Hz)');
ylabel('PSD');
hold off;

% Calculate Length Scales via the PSD
LambdauxPSD=ubar*Pu(1)/(4*(urms.*urms))
LambdavxPSD=ubar*Pv(1)/(4*(vrms.*vrms))
LambdawxPSD=ubar*Pw(1)/(4*(vrms.*vrms))
% Calculate Length Scales via the Autocorrelation
```

C.9 wl.m

```
clear;
clf;

fs=100000;
deltat=1/fs;
samples=60000;

lowf=5;
highf=10000;

numfreqs=41;
f=logspace(log10(lowf),log10(highf),numfreqs);
```

```
% Load the data:
fid=fopen('velocity','r','l');
velocity=fread(fid,inf,'double');
% Convert to u'
velocity=velocity-mean(velocity);
time=deltat*(1:samples)';
%velocity=2*sin(2*pi*23*time);
waveletmap=zeros(samples,numfreqs);

subplot(3,1,1);
plot(time,velocity);

% Calculate the fft of the velocity signal
velocityf=fft(velocity);
b=sqrt(4/pi);

% For each frequency...
for i=1:numfreqs,
        f(i)
        % calculate the wavelet dilation factor
        c=((2*pi)/sqrt(2.5))*f(i);
        % Construct the mexican hat wavelett in time space,
        % placing it smack dab in the middle of the time record
        y=(c*(time-time(samples/2))).^2;
        wavefunc=(y-1).*exp(-y/2);
        subplot(3,1,2);
        plot(time,wavefunc);
        % Calculate the fft of the wavelet function
        wavefuncf=fft(wavefunc);
        % Multiply ffts of velocity and wavelet
        convolution=wavefuncf.*velocityf;
        % Convert back into time space
        wlmap=ifft(convolution);
        % Time shift it back to the origin
        wlmap=fftshift(wlmap);
        % Scale it---
        wlmapscaled=wlmap*sqrt(c)*b/fs;
        % Multiply by the conjugate to get u'^2
        upsqwlmapscaled=wlmapscaled.*conj(wlmapscaled);
        waveletmap(:,i)=upsqwlmapscaled;
        subplot(3,1,3);
        plot(time,upsqwlmapscaled);
        pause(0.001);
end

upsqt=mean(velocity.*velocity); % time average of uprime^2
upsqf=trapz(f,mean(waveletmap)); % From time-averaged wavelet map.
```

References

Abu-Ghannam, B. J. and Shaw, R., 1980. "Natural Transition of Boundary Layers—The Effects of Pressure Gradient and Flow History." *Journal of Engineering Science*, vol. 22, no. 5, pp. 213–228.

Alam, M. and Sandham, N. D., 2000. "Direct Numerical Simulation of 'Short' Laminar Separation Bubbles with Turbulent Reattachment." *Journal of Fluid Mechanics*, vol. 403, pp. 223–250.

Alfredsson, R. H. and Matsubara, M., 2000. "Free-stream Turbulence, Streaky Structures and Transition in Boundary Layer Flows." AIAA Paper 2000-2534.

Baughn, J. W., Butler, R. J., Byerley, A. R., and Rivir, R. B., 1995. "An Experimental Investigation of Heat Transfer, Transition, and Separation on Turbine Blades at Low Reynolds Number and High Turbulence Intensity." Presented at the 1995 ASME Winter Annual Meeting. ASME Paper 95-WA/HT-25.

Berlin, S. and Henningson, D. S., 1999. "A Nonlinear Mechanism for Receptivity of Free-Stream Disturbances." *Physics of Fluids*, vol. 11, no. 12, pp. 3749–3760.

Blair, M. F., 1982. "Influence of Free-Stream Turbulence on Boundary Layer Transition in Favorable Pressure Gradients." *ASME Journal of Heat Transfer*, vol. 105, pp. 33–40.

Blair, M. F., 1991. "Boundary Layer Transition in Accelerating Flows with Intense Freestream Turbulence." Tech Report UTRC91-1, UTRC, East Hartford, CT.

Bons, J. P., Sondergaard, R., and Rivir, R. B., 2000. "Turbine Separation Control Using Pulsed Vortex Generator Jets." Presented at the 2000 International Gas Turbine and Aeroengine Congress and Exposition, Munich, Germany. ASME Paper 2000-GT-262.

Boyle, R. J., Lucci, B. L., Verhoff, V. G., Camperchioli, W., and La, H., 1998. "Aerodynamics of a Transitioning Turbine Stator Over a Range of Reynolds Numbers." Presented at the 1998 International Gas Turbine and Aeroengine Congress and Exposition, Stockholm, Sweden. ASME Paper 98-GT-285, also NASA/TM-1998-208408.

Brunner, S., Fottner, L., and Schiffer, H.-P., 2000. "Comparison of Two Highly Loaded Low Pressure Turbine Cascades Under the Influence of Wake-Induced Transition." Presented at the 2000 International Gas Turbine and Aeroengine Congress and Exposition, Munich, Germany. ASME Paper 2000-GT-268.

Chakka, P. and Schobeiri, M. T., 1999a. "Modeling Unsteady Boundary Layer Transition on a Curved Plate under Periodic Unsteady Flow Conditions: Aerodynamic and Heat Transfer Investigations." *ASME Journal of Turbomachinery*, vol. 121, pp. 88–97.

Chakka, P. and Schobeiri, M. T., 1999b. "Scales of Turbulence During Boundary Layer Transition Under Steady and Unsteady Flow Conditions." Presented at the 1999 International Gas Turbine and Aeroengine Congress and Exposition, Indianapolis, Indiana. ASME Paper 99-GT-221.

Chew, Y. T., Shi, S. X., and Khoo, B. C., 1995. "On the Numerical Near-Wall Corrections of Single-Wire Measurements." *International Journal of Heat and Fluid Flow*, vol. 16, pp. 471–476.

Cho, J. R. and Chung, M. K., 1992. "A k-Epsilon-Gamma Equation Turbulence Model." *Journal of Fluid Mechanics*, vol. 237, pp. 301–322.

Davies, M. R. D., O'Donnell, F. K., and Niven, A. J., 2000. "Turbine Blade Entropy Generation Rate, Part 1: The Boundary Layer Defined." Presented at the 2000 International Gas Turbine and Aeroengine Congress and Exposition, Munich, Germany. ASME Paper 2000-GT-265.

Deutsch, S. and Zierke, W. C., 1987. "The Measurement of Boundary Layers on a Compressor Blade in Cascade: Part 2: Suction Surface Boundary Layers." Presented at the 1987 International Gas Turbine and Aeroengine Congress and Exposition. ASME Paper 87-GT-249.

Dietz, A. J., 1999. "Local Boundary-Layer Receptivity to a Convected Free-Stream Disturbance." *Journal of Fluid Mechanics*, vol. 378, pp. 291–317.

Dong, Y. and Cumpsty, N. A., 1990a. "Compressor Blade Boundary Layers: Part 1—Test Facility and Measurements with No Incident Wakes." *ASME Journal of Turbomachinery*, vol. 112, pp. 221–230.

Dong, Y. and Cumpsty, N. A., 1990b. "Compressor Blade Boundary Layers: Part 2—Measurements with Incident Wakes." *ASME Journal of Turbomachinery*, vol. 112, pp. 231–240.

Dorney, D. J., Ashpis, D. E., Halstead, D. E., and Wisler, D. C., 1999. "Study of Boundary Layer Development in Two-Stage Low-Pressure Turbine." AIAA Paper 99-0742, also NASA TM-1999-208913.

Dorney, D. J., Flitan, H. C., Ashpis, D. E., and Solomon, W. J., 2000a. "Effects of Blade Count on Boundary Layer Development in a Low-Pressure Turbine." AIAA Paper 2000-0742.

Dorney, D. J., Lake, J. P., King, P. I., and Ashpis, D. E., 2000b. "Experimental and Numerical Investigation of Losses in Low-Pressure Turbine Blade Rows." AIAA Paper 2000-0737.

Dullenkopf, K., Schulz, A., and Wittig, S., 1991. "The Effects of Incident Wake Condition on the Mean Heat Transfer of an Airfoil." *ASME Journal of Turbomachinery*, vol. 113, pp. 412–418.

Emmons, H. W., 1951. "The Laminar-Turbulent Transition in a Boundary Later—Part I." *J. Aero. Science*, pp. 490–498.

Enomoto, S., Hah, C., and Hobson, G. V., 2000. "Numerical and Experimental Investigation of Low Reynolds Number Effects on Laminar Flow Separation and Transition in a Cascade of Compressor Blades." Presented at the 2000 International Gas Turbine and Aeroengine Congress and Exposition, Munich, Germany. ASME Paper 2000-GT-276.

Evans, R. L., 1978. "Boundary-Layer Development on an Axial-Flow Compressor Stator Blade." *Journal of Engineering for Power*, vol. 100, pp. 287–293.

Falco, R. E. and Gendrich, C. P., 1990. "The Turbulence Burst Detection Algorithm of Z. Zarić." In S. J. Kline and N. H. Afgan, editors, *Near-Wall Turbulence 1988 Z. Zarić Memorial Conference*, pp. 911–931. Hemisphere.

Farge, M., 1992. "Wavelet Transforms and Their Application to Turbulence." *Annu. Rev. Fluid Mech*, vol. 24, pp. 395–457.

Funazaki, K. and Aoyama, Y., 2000. "Studies on Turbulence Structure of Boundary Layers Disturbed by Moving Wakes." Presented at the 2000 International Gas Turbine and Aeroengine Congress and Exposition, Munich, Germany. ASME Paper 2000-GT-272.

Funazaki, K. and Kitazawa, T., 1997. "Boundary Layer Transition Induced by Periodic Wake Passage: Measurements of the Boundary Layer by Hot Wire Anemometry." Bulletin of the GTSJ.

Funazaki, K., Tetsuka, N., and Tanuma, T., 1999a. "Effects of Periodic Wake Passing upon Aerodynamic Loss of a Turbine Cascade, Part I." Presented at the 1999 International Gas Turbine and Aeroengine Congress and Exposition, Indianapolis, Indiana. ASME Paper 99-GT-93.

Funazaki, K., Tetsuka, N., and Tanuma, T., 1999b. "Effects of Periodic Wake Passing upon Aerodynamic Loss of a Turbine Cascade, Part II." Presented at the 1999 International Gas Turbine and Aeroengine Congress and Exposition, Indianapolis, Indiana. ASME Paper 99-GT-94.

Gostelow, J. P. and Walker, G. J., 1990. "Similarity Behavior in Transitional Boundary Layers over a Range of Adverse Pressure Gradients and Turbulence Levels." Presented at the 1990 International Gas Turbine and Aeroengine Congress and Exposition. ASME Paper 90-GT-130.

Hall, D. J. and Gibbings, J. C., 1972. "Influence of Stream Turbulence and Pressure Gradient on Boundary Layer Transition." *Journal of Mechanical Engineering Science*, vol. 14, pp. 134–146.

Halstead, D. E., 1996. *Boundary Layer Development in Multi-Stage Low Pressure Turbines*. Ph.D. Thesis, Iowa State University, Ames, IA.

Halstead, D. E., Wisler, D. C., Okiishi, T. H., Walker, G. J., Hodson, H. P., and Shin, H.-W., 1997a. "Boundary Layer Development in Axial Compressors and Turbines: Part 1 of 4: Composite Picture." *ASME Journal of Turbomachinery*, vol. 119, pp. 114–127. Also ASME Paper 95-GT-461.

Halstead, D. E., Wisler, D. C., Okiishi, T. H., Walker, G. J., Hodson, H. P., and Shin, H.-W., 1997b. "Boundary Layer Development in Axial Compressors and Turbines: Part 2 of 4: Compressors." *ASME Journal of Turbomachinery*, vol. 119, pp. 426–444. Also ASME Paper 95-GT-462.

Halstead, D. E., Wisler, D. C., Okiishi, T. H., Walker, G. J., Hodson, H. P., and Shin, H.-W., 1997c. "Boundary Layer Development in Axial Compressors and Turbines: Part 3 of 4: Low Pressure Turbines." *ASME Journal of Turbomachinery*, vol. 119, pp. 225–237. Also ASME Paper 95-GT-463.

Halstead, D. E., Wisler, D. C., Okiishi, T. H., Walker, G. J., Hodson, H. P., and Shin, H.-W., 1997d. "Boundary Layer Development in Axial Compressors and Turbines: Part 4 of 4: Computations and Analyses." *ASME Journal of Turbomachinery*, vol. 119, pp. 128–139. Also ASME Paper 95-GT-464.

Hedley, T. B. and Keller, J. F., 1974. "Some Turbulent/Non-Turbulent Properties of The Outer Intermittent Region of a Boundary Layer." *Journal of Fluid Mechanics*, vol. 64, pp. 645–678.

Hinze, J. O., 1975. *Turbulence*. McGraw-Hill, New York, 2nd edn.

Hobson, G. V. and Weber, S., 2000. "Prediction of a Laminar Separation Bubble over a Controlled-Diffusion Compressor Blade." Presented at the 2000 International Gas Turbine and Aeroengine Congress and Exposition, Munich, Germany. ASME Paper 2000-GT-277.

Hodson, H. P., 1984. "Boundary Layer and Loss Measurements on the Rotor of an Axial Flow Turbine." *ASME Journal of Engineering for Gas Turbines and Power*, vol. 106.

Hourmouziadis, J., 1989. "Blading Design for Axial Turbomachines." In L. Fottner, editor, *AGARD Lecture Series No. 167*, pp. 8.1–8.40. AGARD.

Johnson, M. W. and Dris, A., 2000. "The Origin of Turbulent Spots." *ASME Journal of Turbomachinery*, vol. 122, pp. 88–92. Also ASME Paper 99-GT-32.

Johnson, M. W. and Ercan, A. H., 1996. "A Boundary Layer Transition Model." Presented at the 1996 International Gas Turbine and Aeroengine Congress and Exposition, Birmingham, UK. ASME Paper 96-GT-444.

Jonas, P., 1997. "Experimental Investigation of By-Pass Transition in the Institute of Thermomechanics in Prague." Minnowbrook Workshop Proceedings.

Kang, D. J. and Lakshminarayana, B., 1997. "Numerical Prediction of Unsteady Transitional Boundary Layer Flow Due to Rotor-Stator Interaction." AIAA Paper 97-2752.

Kaszeta, R. W., Simon, T. W., and Ashpis, D. E., 2001. "Experimental Investigation of Transition to Turbulence as Affected by Passing Wakes." To be presented at the 2001 International Gas Turbine and Aeroengine Congress and Exposition, New Orleans, Louisiana. ASME Paper 2001-GT-195.

Kays, W. M. and Crawford, M. E., 1993. *Convective Heat and Mass Transfer*. McGraw-Hill, New York, 3rd edn.

Keller, F. J. and Wang, T., 1995. "Effects of Criterion Function on Intermittency in Heated Transitional Boundary Layers With and Without Streamwise Acceleration." *ASME Journal of Turbomachinery*, vol. 117, pp. 154–165. Also ASME Paper 93-GT-67.

Kim, J., 1990. *Freestream Turbulence and Concave Curvature Effects on Heated, Transitional Boundary Layers*. Ph.D. Thesis, University of Minnesota, Mechanical Engineering Department, Minneapolis, MN.

Kim, J., Simon, T. W., and Russ, S. G., 1992. "Free-Stream Turbulence and Concave Curvature Effects on Heated, Transitional Boundary Layers." *ASME Journal of Heat Transfer*, vol. 114, pp. 338–347.

Kim, K. and Crawford, M. E., 2000. "Prediction of Transitional Heat Transfer Characteristics of Wake-Affected Boundary Layers." *ASME Journal of Turbomachinery*, vol. 122, pp. 78–87.

Kittichaikarn, C., Ireland, P. T., Zhong, S., and Hodson, H. P., 1999. "An Investigation of the Onset of Wake-Induced Transition and Turbulent Spot Production Using Thermochromic Liquid Crystals." Presented at the 1999 International Gas Turbine and Aeroengine Congress and Exposition, Indianapolis, Indiana. ASME Paper 99-GT-126.

Kost, F., Hummel, F., and Tiedemann, M., 2000. "Investigation of the Unsteady Rotor Flow Field in a Single HP Turbine Stage." Presented at the 2000 International Gas Turbine and Aeroengine Congress and Exposition, Munich, Germany. ASME Paper 2000-GT-432.

Lake, J. P., 1999. *Flow Separation Prevention on a Turbine Blade in Cascade at Low Reynolds Number*. Ph.D. Thesis, Air Force Institute of Technology.

Lake, J. P., King, P. I., and Rivir, R. B., 2000. "Low Reynolds Number Loss Reduction on Turbine Blades with Dimples and V-Grooves." AIAA Paper 2000-0738.

Lewalle, J. and Ashpis, D. E., 1995. "Transport in Bypass Transition: Mapping Active Times Scales Using Wavelet Techniques." Presented at the Tenth Symposium on Turbulent Shear Flows, Pennsylvania State University, vol. 2, pp. P2-37–P2-42.

Lewalle, J., Ashpis, D. E., and Sohn, K.-H., 1997. "Demonstration of Wavelet Techniques in the Spectral Analysis of Bypass Transition Data." NASA TP-3555.

Lou, W. and Hourmouziadis, J., 2000. "Separation Bubbles Under Steady and Periodic-Unsteady Main Flow Conditions." Presented at the 2000 International Gas Turbine and Aeroengine Congress and Exposition, Munich, Germany. ASME Paper 2000-GT-270.

Madavan, N. K. and Rai, M. M., 1995. "Direct Numerical Simulation of Boundary Layer Transition on a Heated Flat Plate with Elevated Freestream Turbulence." AIAA Paper 95-0771.

Matsubara, M., Alfredsson, P. H., and Westin, K. J. A., 1998. "Boundary Layer Transition at High Levels of Free Stream Turbulence." Presented at the 1998 International Gas Turbine and Aeroengine Congress and Exposition, Stockholm, Sweden. ASME Paper 98-GT-248.

Mayle, R. E., 1991. "The Role of Laminar-Turbulent Transition in Gas Turbine Engines." *ASME Journal of Turbomachinery*, vol. 113, pp. 509–537. The 1991 IGTI Scholar Lecture, also presented as ASME Paper 91-GT-261.

Mayle, R. E., 1998. "A Theory for Predicting The Turbulent-Spot Production Rate." Presented at the 1998 International Gas Turbine and Aeroengine Congress and Exposition, Stockholm, Sweden. ASME Paper 98-GT-256.

Mayle, R. E. and Schulz, A., 1997. "The Path to Predicting Bypass Transition." *ASME Journal of Turbomachinery*, vol. 119, pp. 405–411.

McDaniel, R. D. and Hassan, H. A., 2000. "Study of Bypass Transition Using the k-zeta Framework." AIAA Paper 2000-2310.

Morkovin, M. V., 1978. "Instability, Transition to Turbulence and Predictability." NATO AGARDograph No. 236.

Müller, M., Gallus, H. E., and Niehuis, R., 2000. "A Study on Models to Simulate Boundary Layer Transition in Turbomachinery Flows." Presented at the 2000 International Gas Turbine and Aeroengine Congress and Exposition, Munich, Germany. ASME Paper 2000-GT-274.

Murawski, C. G., Vafai, K., Simon, T. W., and Volino, R. J., 1997. "Experimental Study of the Unsteady Aerodynamics in a Linear Cascade with Low Reynolds Number Low Pressure Turbine Blades." Presented at the 1997 International Gas Turbine and Aeroengine Congress and Exposition, Orlando, Florida. ASME Paper 97-GT-95.

Narasimha, R., 1985. "The Laminar-Turbulent Transition Zone in the Boundary Layer." *Prog. Aerospace Science*, vol. 22, pp. 29–80.

O'Donnell, F. K. and Davies, M. R. D., 2000. "Turbine Blade Entropy Generation Rate, Part 2: The Measured Loss." Presented at the 2000 International Gas Turbine and Aeroengine Congress and Exposition, Munich, Germany. ASME Paper 2000-GT-266.

Ou, S., Han, J. C., Mehendale, A. B., and Lee, C. P., 1994. "Unsteady Wake Over a Linear Turbine Blade Cascade with Air and CO2 Film Injection: Part I—Effects on Heat Transfer Coefficients." *ASME Journal of Turbomachinery*, vol. 116, pp. 721–729.

Qiu, S., 1996. *An Experimental Study of Laminar to Turbulent Flow Transition with Temporal And Spatial Acceleration Effects*. Ph.D. Thesis, University of Minnesota, Department of Mechanical Engineering.

Qiu, S. and Simon, T. W., 1997. "An Experimental Investigation of Transition as Applied to Low Pressure Turbine Suction Surface Flows." Presented at the 1997 International Gas Turbine and Aeroengine Congress and Exposition, Orlando, Florida. ASME Paper 97-GT-455.

Rai, M. M. and Moin, P., 1993. "Direct Numerical Simulation of Transition and Turbulence in a Spatially Evolving Boundary Layer." *Journal of Computational Physics*, vol. 109, no. 2, pp. 169–192.

Roach, P. E. and Brierley, D. H., 2000. "Bypass Transition Modeling: A New Method Which Accounts for Free-Stream Turbulence Intensity and Length Scale." Presented at the 2000 International Gas Turbine and Aeroengine Congress and Exposition, Munich, Germany. ASME Paper 2000-GT-278.

Russ, S. and Simon, T. W., 1990. "Signal Processing Using the Orthogonal Triple-Wire Equations." *Flow Lines*, the TSI quarterly magazine, Winter 1990.

Savill, A. M., 1993a. "Further Progress in the Turbulence Modeling of By-Pass Transition." In R. M. C. So, C. G. Speziale, and B. E. Launder, editors, *Near-Wall Turbulent Flows*, pp. 583–592. Elsevier Science Pub.

Savill, A. M., 1993b. "Some Recent Progress in the Turbulence Modeling of By-Pass Transition." In R. M. C. So, C. G. Speziale, and B. E. Launder, editors, *Near-Wall Turbulent Flows*, pp. 829–848. Elsevier Science Pub.

Schlichting, H., 1979. *Boundary Layer Theory*. McGraw-Hill, New York, 7th edn.

Schobeiri, M. T., Chakka, P., and Pappu, K., 1998. "Unsteady Wake Effects on Boundary Layer Transition and Heat Transfer Characteristics of a Turbine Blade." Presented at the 1998 International Gas Turbine and Aeroengine Congress and Exposition, Stockholm, Sweden. ASME Paper 98-GT-291.

Schobeiri, M. T., Read, K., and Lewalle, J., 1995. "Effect of Unsteady Wake Passing Frequency on Boundary Layer Transition, Experimental Investigation and Wavelet Analysis." Presented at the 1995 International Gas Turbine and Aeroengine Congress and Exposition, Houston, Texas. ASME Paper 95-GT-437.

Schreiber, H.-A., Steinert, W., and Küsters, B., 2000. "Effects of Reynolds Number and Free-Stream Turbulence on Boundary Layer Transition in a Compressor Cascade." Presented at the 2000 International Gas Turbine and Aeroengine Congress and Exposition, Munich, Germany. ASME Paper 2000-GT-0263.

Simon, F. F. and Ashpis, D. E., 1996. "Progress in Modeling of Laminar to Turbulent Transition on Turbine Vanes and Blades." Presented at the Intl. Conference on Turbulent Heat Transfer, San Diego, California. NASA TM-107180.

Simon, T. W. and Kaszeta, R. W., 2000. "Transition to Turbulence Under Low-Pressure Turbine Conditions." To be published, Proceedings of the International Symposium on Heat Transfer in Gas Turbine Systems, Cesme, Turkey, 13-18 August 2000, *Annals of the New York Academy of Sciences*.

Simon, T. W., Qiu, S., and Yuan, K., 2000. "Measurements in a Transitional Boundary Layer Under Low-Pressure Turbine Airfoil Conditions." NASA Contractor Report NASA/CR-2000-209957.

Sohn, K. H., Shyne, R. J., and Dewitt, K. J., 1998. "Experimental Investigation of Boundary Layer Behavior in a Simulated Low Pressure Turbine." Presented at the 1998 International Gas Turbine and Aeroengine Congress and Exposition, Stockholm, Sweden. ASME Paper 98-GT-34, also NASA/TM-1999-207921.

Solomon, W. J., 1996. *Unsteady Boundary Layer Transition on Axial Compressor Blades*. Ph.D. Thesis, University of Tasmania, Department of Civil and Mechanical Engineering.

Solomon, W. J., 2000. "Effects of Turbulence and Solidity on the Boundary Layer Development in a Low Pressure Turbine." Presented at the 2000 International Gas Turbine and Aeroengine Congress and Exposition, Munich, Germany. ASME Paper 2000-GT-273.

Stadtmüller, P., Fottner, L., and Fiala, A., 2000. "Experimental and Numerical Investigation of Wake-Induced Transition on a Highly Loaded Low Pressure Turbine at Low Reynolds Numbers." Presented at the 2000 International Gas Turbine and Aeroengine Congress and Exposition, Munich, Germany. ASME Paper 2000-GT-269.

Steelant, J. E. and Dick, E., 1996a. "Calculation of Transition in Adverse Pressure Gradient Flow by Conditioned Equations." Presented at the 1996 International Gas Turbine and Aeroengine Congress and Exposition, Birmingham, UK. ASME Paper 96-GT-160.

Steelant, J. E. and Dick, E., 1996b. "Modeling of Bypass Transition with Conditioned Navier-Stokes Equations Coupled to an Intermittency Transport Equation." *Intl. Journal for Numerical Methods in Fluids*, vol. 26, pp. 193–220.

Steelant, J. E. and Dick, E., 1999a. "Prediction of By-Pass Transition by Means of a Turbulence Weighting Factor, Part I." Presented at the 1999 International Gas Turbine and Aeroengine Congress and Exposition, Indianapolis, Indiana. ASME Paper 99-GT-29.

Steelant, J. E. and Dick, E., 1999b. "Prediction of By-Pass Transition by Means of a Turbulence Weighting Factor, Part II." Presented at the 1999 International Gas Turbine and Aeroengine Congress and Exposition, Indianapolis, Indiana. ASME Paper 99-GT-30.

Suzen, Y. B. and Huang, P. G., 2000a. "An Intermittency Transport Equations for Modeling Flow Transition." AIAA Paper 2000-0287.

Suzen, Y. B. and Huang, P. G., 2000b. "Modeling of Flow Transition Using an Intermittency Transport Equation." *Journal of Fluids Engineering*, vol. 123, no. 2.

Teusch, R., Brunner, S., Fottner, L., and Swoboda, M., 2000. "The Influence of Multimode Transition Initiated by Periodic Wakes on the Profile Loss of a Linear Compressor Cascade." Presented at the 2000 International Gas Turbine and Aeroengine Congress and Exposition, Munich, Germany. ASME Paper 2000-GT-271.

Tiedemann, M. and Kost, F., 1999. "Unsteady Boundary Layer Transition on a High Pressure Turbine Rotor Blade." Presented at the 1999 International Gas Turbine and Aeroengine Congress and Exposition, Indianapolis, Indiana. ASME Paper 99-GT-194.

Townsend, A. A., 1949. "The Fully-Developed Turbulent Wake of a Circular Cylinder." *Australian Journal of Scientific Research, Series A: Physical Sciences*, vol. 2, no. 4, pp. 451–468.

TSI, Inc., 1999. Thermal Anemometry Product Catalog. St Paul, MN.

Van Treuren, K. W., Simon, T. W., von Koller, M., Byerly, A. R., Baughn, J. W., and Rivir, R., 2001. "Measurements in a Turbine Cascade Flow under Under Low Reynolds Number Conditions." To be presented at the 2001 International Gas Turbine and Aeroengine Congress and Exposition, New Orleans, Louisiana. ASME Paper 2001-GT-164.

Volino, R. J., 1998. "Wavelet Analysis of Transitional Flow Data under High Free-Stream Turbulence Conditions." Presented at the 1998 International Gas Turbine and Aeroengine Congress and Exposition, Stockholm, Sweden. ASME Paper 98-GT-194.

Volino, R. J. and Hultgren, L. S., 2000. "Measurements in Separated and Transitional Boundary Layers Under Low-Pressure Turbine Airfoil Conditions." Presented at the 2000 International Gas Turbine and Aeroengine Congress and Exposition, Munich, Germany. ASME Paper 2000-GT-0260.

Volino, R. J. and Simon, T. W., 1994. "An Application of Octant Analysis to Turbulent and Transitional Flow Data." *ASME Journal of Turbomachinery*, vol. 166, no. 4, pp. 752–758.

Volino, R. J. and Simon, T. W., 1995a. "Bypass Transition in Boundary Layers Including Curvature and Favorable Pressure Gradient Effects." *ASME Journal of Turbomachinery*, vol. 117, pp. 166–174.

Volino, R. J. and Simon, T. W., 1995b. "Measurements of Turbulent Transport in Transitional Boundary Layers under High Free-Stream Turbulence and Strong Acceleration Conditions." *Proc. of the Tenth Symposium on Turbulent Shear Flows*. University Park, PA.

Volino, R. J. and Simon, T. W., 1997a. "Boundary Layer Transition under High Free-Stream Turbulence and Strong Acceleration Conditions: Part 1, Mean Flow Results." *ASME Journal of Heat Transfer*, vol. 119, no. 3, pp. 420–426.

Volino, R. J. and Simon, T. W., 1997b. "Boundary Layer Transition under High Free-Stream Turbulence and Strong Acceleration Conditions: Part 2, Turbulent Transport Results." *ASME Journal of Heat Transfer*, vol. 119, no. 3, pp. 427–432.

Volino, R. J. and Simon, T. W., 1997c. "Measurements in a Transitional Boundary Layer with Görtler Vortices." *Journal of Fluids Engineering*, vol. 119, pp. 562–568.

Walker, G. J. and Solomon, W. J., 1992. "Turbulent Intermittency Measurement on an Axial Compressor Blade." In M. R. Davis and G. J. Walker, editors, *Eleventh Australasian Fluid Mechanics Conference*, pp. 1277–1280. Hobart, Australia.

Walker, G. J., Subroto, P. H., and Platzer, M. F., 1988. "Transition Modeling Effects on Viscous/Inviscid Interaction Analysis of Low Reynolds Number Airfoil Flows Involving Laminar Separation Bubbles." Presented at the 1988 International Gas Turbine and Aeroengine Congress and Exposition. ASME Paper 88-GT-32.

Wang, T., 1984. *An Experimental Investigation of Curvature and Freestream Turbulence Effects on Heat Transfer and Fluid Mechanics in Transitional Boundary Layer Flows*. Ph.D. Thesis, University of Minnesota.

Wills, J. A. B., 1962. "The Correction of Hot-Wire Readings for Proximity to a Solid Boundary." *Journal of Fluid Mechanics*, vol. 12, pp. 388–396.

Wu, X. and Durbin, P. A., 2000a. "Evidence of Longitudinal Vortices Evolved From Distorted Wakes in a Turbine Passage." Submitted to the *Journal of Fluid Mechanics*.

Wu, X. and Durbin, P. A., 2000b. "Numerical Simulation of Heat Transfer in a Transitional Boundary Layer with Passing Wakes." *ASME Journal of Heat Transfer*, vol. 122, pp. 248–257.

Wu, X. H., Jacobs, R. G., Hunt, J. C. R., and Durbin, P. A., 1999. "Simulation of Boundary Layer Transition Induced by Periodically Passing Wakes." *Journal of Fluid Mechanics*, vol. 398, pp. 109–153.

Yuan, K., 1999. *Simulation of Wakes: The Development of a Linear Cascade Wake Generator*. Master's Thesis, University of Minnesota. Department of Mechanical Engineering.

REPORT DOCUMENTATION PAGE

Form Approved
OMB No. 0704-0188

1. AGENCY USE ONLY (*Leave blank*)	2. REPORT DATE	3. REPORT TYPE AND DATES COVERED
	December 2002	Final Contractor Report

4. TITLE AND SUBTITLE

Experimental Investigation of Transition to Turbulence as Affected by Passing Wakes

5. FUNDING NUMBERS

WBS–22–719–10–03
WBS–22–708–28–07
NCC3–652

6. AUTHOR(S)

Richard W. Kaszeta and Terrence W. Simon

7. PERFORMING ORGANIZATION NAME(S) AND ADDRESS(ES)

University of Minnesota
100 Church Street S.E.
Minneapolis, Minnesota 55455

8. PERFORMING ORGANIZATION REPORT NUMBER

E–12858–1

9. SPONSORING/MONITORING AGENCY NAME(S) AND ADDRESS(ES)

National Aeronautics and Space Administration
Washington, DC 20546–0001

10. SPONSORING/MONITORING AGENCY REPORT NUMBER

NASA CR—2002-212104

11. SUPPLEMENTARY NOTES

The accompanying CD-ROM includes tabulated data, animations, higher resolution plots, and an electronic copy of this report. Project Manager, David E. Ashpis, Turbomachinery and Propulsion Systems Division, NASA Glenn Research Center, organization code 5820, 216–433–8317, David.E.Ashpis@nasa.gov.

12a. DISTRIBUTION/AVAILABILITY STATEMENT

Unclassified - Unlimited
Subject Categories: 01 and 34 Distribution: Nonstandard

Available electronically at http://gltrs.grc.nasa.gov

This publication is available from the NASA Center for AeroSpace Information, 301–621–0390.

12b. DISTRIBUTION CODE

13. ABSTRACT ***(Maximum 200 words)***

Experimental results from a study of the effects of passing wakes upon laminar-to-turbulent transition in a low-pressure turbine passage are presented. The test section geometry is designed to simulate the effects of unsteady wakes resulting from rotor-stator interaction upon laminar-to-turbulent transition in turbine blade boundary layers and separated flow regions over suction surfaces. Single-wire, thermal anemometry techniques were used to measure time-resolved and phase-averaged, wall-normal profiles of velocity, turbulence intensity, and intermittency at multiple streamwise locations over the turbine airfoil suction surface. These data are compared to steady-state, wake-free data collected in the same geometry to identify the effects of wakes upon laminar-to-turbulent transition. Results are presented for flows with a Reynolds number based on suction surface length and exit velocity of 50,000 and an approach flow turbulence intensity of 2.5 percent. From these data, the effects of passing wakes and associated increased turbulence levels and varying pressure gradients on transition and separation in the near-wall flow are presented. The results show that the wakes affect transition both by virtue of their difference in turbulence level from that of the free-stream but also by virtue of their velocity deficit relative to the free-stream velocity, and the concomitant change in angle of attack and temporal pressure gradients. The results of this study seem to support the theory that bypass transition is a response of the near-wall viscous layer to pressure fluctuations imposed upon it from the free-stream flow. The data also show a significant lag between when the wake is present over the surface and when transition begins. The accompanying CD-ROM includes tabulated data, animations, higher resolution plots, and an electronic copy of this report.

14. SUBJECT TERMS

Turbulent flow; Transition; Wakes; Turbulent spots; Turbomachinery; Turbine; Anemometry

15. NUMBER OF PAGES

250

16. PRICE CODE

17. SECURITY CLASSIFICATION OF REPORT	18. SECURITY CLASSIFICATION OF THIS PAGE	19. SECURITY CLASSIFICATION OF ABSTRACT	20. LIMITATION OF ABSTRACT
Unclassified	Unclassified	Unclassified	